Late Quaternary and Holocene paleoclimate and paleoenvironmental reconstruction - a multi-proxy approach on Swiss speleothems

Inauguraldissertation
der Philosophisch-naturwissenschaftlichen Fakultät
der Universität Bern

vorgelegt von

Anamaria Diana Häuselmann

von Bistrița (Rumänien)

Leiter der Arbeit:

Prof. Dr. Dominik Fleitmann
Institut für Geologie und Oeschger Centre for Climate Change Research
Universität Bern

Co-Leiter der Arbeit:

Prof. Dr. Markus Leuenberger
Abteilung für Klima- und Umweltphysik
Physikalisches Institut der Universität Bern

Late Quaternary and Holocene paleoclimate and paleoenvironmental reconstruction - a multi-proxy approach on Swiss speleothems

Inauguraldissertation
der Philosophisch-naturwissenschaftlichen Fakultät
der Universität Bern

vorgelegt von

Anamaria Diana Häuselmann
von Bistrița (Rumänien)

Leiter der Arbeit:

Prof. Dr. Dominik Fleitmann

Co-Leiter der Arbeit:

Prof. Dr. Markus Leuenberger

Von der Philosophisch-naturwissenschaftlichen Fakultät angenommen.

Der Dekan:
Bern, den 14. Juli 2015 Prof. Dr. G. Colangelo

TABLE OF CONTENTS

LIST OF FIGURES AND TABLES

SUMMARY

Detailed knowledge of the past climate and environmental variability is vital in order to predict future scenarios with more confidence. High resolution and highly-resolved natural archives are therefore in growing demand (PAGES report, 2009).

This thesis is part of a coordinated effort, STALCLIM project, where a series of state-of-the-art methods in speleothems proxies were used in order to develop the full potential of speleothemsas paleoclimate and paleoenvironmental archive. The thesis investigates climate variations as recorded by speleothems from Schafsloch and Milandre caves, spanning time intervals of high scientific interest: 0 to 14 550 years BP and 130 000 to 230 000 years BP. The locations of the caves, Jura Mountains and the Alpstein Mountains (Swiss Alps) are regions highly sensitive to climate-induced changes in temperature, atmospheric pathways and/or environment evolution. In order to establish new climate records and resolve the paleoclimate questions, continuous geochemical analyses were applied, with high resolution stable isotopic and trace elements analysis and ^{230}Th age measurements, and these were combined with thin section analysis of the calcite petrology. Where possible, we conducted continuous and temporal measurements in the caves where the samples were collected, to provide a better understanding of the cave environment.

Chapters 2 and 3 highlight the sensitivity of high altitude speleothem proxies to small changes in temperature and water availability, both induced by internal and external climate drivers. The MF3 stalagmite, from Schafsloch Cave, provides a unique opportunity to investigate a regional expression of millennial-scale climate variability in Central Europe during MIS 6 and Late MIS 7. The sample records in high detail the structure of the penultimate deglaciation in the Alps, and brings new evidence regarding the nature of this important climatic transition.

Chapters 4 and 5 show the high resolution composite δ^{18}O record and elemental composition of speleothems from Milandre Cave, covering the Lateglacial- Holocene interval. A detailed comparison with Greenland ice cores and Gerzensee lake sediments (Central Switzerland) indicates similarities in the long timescale changes of atmospheric circulation patterns in the whole North Atlantic region after the last deglaciation. In contrast, during the Holocene, the signature pattern in the isotopic calcite δ^{18}O data differs to that seen in Central Europe. This provides important insights into the regional teleconnections and local environmental reaction to changes in the temperature, seasonality of precipitation and atmospheric processes. The use of a robust δ^{18}O/temperature transfer function has enabled a high resolution temperature reconstruction of the autumn to spring temperatures at the Milandre site for the last 14 550 y BP.

In summary, this thesis provides new results on environmental and climatic variability in Switzerland during specific intervals over the last 230 000 years. It suports large teleconnections over the northern hemisphere and emphasizes the role of insolation and obliquity as important climate triggers in the region. These new high-resolution and precisely dated records of δ^{18}O and cold season temperature reconstruction for the Jura Mountains over the last 14 550 y BP, are proposed as being representative for Central Europe.

ZUSAMMENFASSUNG

Das Wissen um das Klima der Vergangenheit und der Umweltariabilität ist eminent wichtig, um zukünftige Szenarien besser vorauszusagen. Dementsprechend sind hochauflösende natürliche Archive immer mehr gefragt (PAGES report, 2009).

Diese Dissertation ist ein Teil eines koordinierten Projektes (STALCLIM), in welchem moderne Methoden an Speläothem-Proxies benutzt wurden, um das volle Potential der Tropfsteine als paläoklimatisches Archiv zu entwickeln. Die Arbeit untersucht Klimavariationen, die in Tropfsteinen vom Schafsloch und der Milandre-Höhle gespeichert wurden und die zeitlich hochinteressant sind: 0-14 550 Jahre sowie 130 000 -250 000 Jahre vor heute. Der Jura und der Alpstein, wo die Höhlen liegen, sind Regionen, die sensibel auf klimabedingte Änderungen in Temperatur, atmosphärische Zirkulationen und/oder Entwicklungen der Umwelt reagieren. Um neue Klimadaten zu erhalten, wurden kontinuierliche geochemische Analysen, hochauflösende Stabilisotopen- und Spurenelement-Analysen sowie ^{230}Th-Altersbestimmungen durchgeführt. Diese wurden mit Dünnschliffanalysen der Petrologie kombiniert. Wo möglich, führten wir kontinuierliche und diskrete Messungen an den Probenahmestellen durch, um ein besseres Verständnis für das Höhlenklima zu erhalten.

Kapitel 2 und 3 beleuchten die Sensitivität von hochgelegenen Tropfsteinen auf Temperatur und Verfügbarkeit von Wasser, die beide durch interne und externe Klimavariationen beeinflusst werden. Der Tropfstein MF3 aus dem Schafsloch erlaubt einzigartige Einblicke in die regionale Auswirkung von Klimavariabilität in Zentraleuropa im MIS 6 und MIS 7. Die Probe bildet die Struktur der vorletzten Vergletscherung der Alpen hochauflösend ab und bringt neue Erkentnisse über die Art dieses wichtigen klimatischen Übergangs.

Kapitel 4 und 5 beschreiben die hochauflösenden δ^{18}O-Werte und elementare Zusammensetzung von Tropfsteinen aus der Milandre-Höhle, die das Spätglazial-Holozän abdecken. Ein detaillierter Vergleich mit Eisbohrkernen von Grönland und Sediment aus dem Gerzensee (Zentralschweiz) zeigt Ähnlichkeiten in Langzeit-Änderungen von atmosphärischen Zirkulationsmustern in der gesamten Region des Nordatlantiks nach der letzten Eiszeit. Im Gegensatz dazu ist die Signatur des δ^{18}O im Holozän unterschiedlich zu derjenigen Zentraleuropas. Dies ergibt wichtige Erkenntnisse zu regionalen Verbindungen und lokalen Reaktionen auf Temperaturänderungen, Niederschlagsvariabilität in Funktion der Jahreszeit und atmosphärischen Prozessen. Die Nutzung einer robusten δ^{18}O/Temperatur-Transferfunktion erlaubte die Erstellung einer hochaufgelösten Temperaturrekonstruktion der Herbst-Winter-Frühlingstemperaturen bei der Milandre.-Höhle innerhalb der letzten 14 550 Jahre.

Zusammenfassend zeigt die vorliegende Arbeit neue Resultate zur klimatischen Variabilität in der Schweiz in zwei Intervallen der letzten 230 000 Jahre. Sie postuliert grosse Fernverbindungen in der nördlichen Hemisphäre und betont die Rolle der Besonnung und Obliquität als wichtige klimabeeinflussende Faktoren. Die neuen hochauflösenden, genau datierten δ^{18}O-Zeitreihen und Wintertemperaturrekonstruktionen aus dem Jura in den letzten 14 550 a werden als repräsentativ für Zentraleuropa angesehen.

*"If we knew what it was we were doing,
it would not be called research, would it?"*

ALBERT EINSTEIN

CHAPTER 1.

INTRODUCTION

1.1. Objectives and structure of the thesis

1.1.1. Tasks and importance within the STALCLIM project

This PhD thesis is part of the Sinergia STALCLIM project “STALCLIM - Multi-proxy climatic and environmental reconstructions from stalagmites from Switzerland, Turkey, Arabia and India”. The STALCLIM project includes disciplines of Physical, Chemical and Geological Sciences, involving six groups based at Bern University and ETH Zürich (Fig.1.1).

The goal of this sub-group (STALCLIM A) was to construct highly resolved and precisely dated paleoclimate records from stalagmites sampled in Swiss caves and provide new information regarding the paleoclimatic and paleoenvironmental variability in the region. This was achieved by using a broad array of analytical techniques (determine growth intervals, stable isotopes analysis, calcite petrology observation) and combining the information with a suite of temperature sensitive speleothem proxies (fluid inclusion stable isotopes, gas inclusions and trace elements) as well as paleo-precipitation proxies (trace elements, water content). This PhD thesis is an integral part of STALCLIM having sampled and tested the quality of newly collected stalagmites. Through this work, the group has obtained established chronologies, initial geochemical data sets ($\delta^{18}O$ and $\delta^{13}C$) and first environmental interpretations, used to decide and coordinate the analysis strategy for the other sub-groups. With the exception of laboratory and coordination tasks, STALCLIM A was responsible for the organization of field trips, not only for sampling campaigns but equally to monitor present-day conditions in the selected caves, which is a key-aspect for the calibration of multiple speleothem proxies.

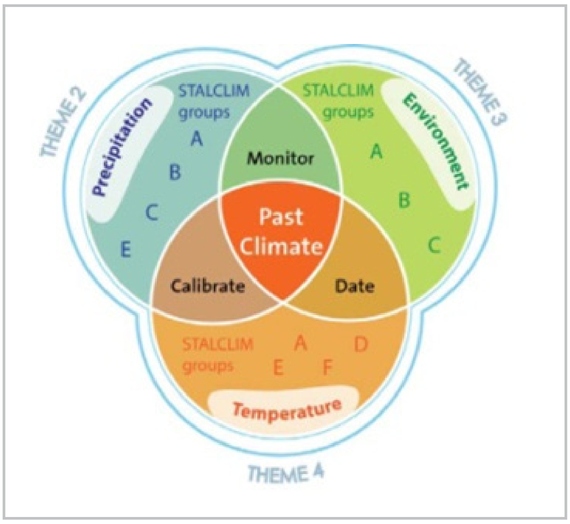

Figure 1.1. Organization and tasks within the STALCLIM project. This study is the contribution of the STALCLIM_A group

1.1.2. Structure of this thesis

This thesis, *Late Quaternary and Holocene paleoclimate and paleoenvironmental reconstruction – a multi-proxy approach on Swiss speleothems,* comprises six chapters, with each chapter comprising its own reference list. Chapter 1 provides a general introduction to the thesis topic, the study area and the applied methodologies. Chapters 2 to 5 represent four individual manuscripts, either submitted or in preparation, for publication in peer-reviewed scientific journals. Chapter 6 presents an overall conclusion of the thesis and provides an outlook for future research in this field.

These four manuscripts represent the major tasks that contribute to this PhD thesis, and can be summarized as follows:

- Chapter 2: *Alpine climate variability during MIS 7 and MIS 6 as recorded in growth intervals of a stalagmite from Alpstein Mts. (Swiss Alps)* investigates the MF3 speleothem growth in Schafsloch Cave (Alpstein Mts., Appenzell), based on precise dating, petrography, stable isotopes, organic matter and trace elements content. Intervals of calcite formation are described with regard to regional geomorphological and environmental (at the surface and in cave) settings. Furthermore, information regarding internal and external climate factors that induced interstadial and interglacial conditions in this high alpine area is presented, together with a novel indication of glacier dynamics in the region during the penultimate glaciation.
- Chapter 3: *Timing and nature of the penultimate deglaciation in a high alpine stalagmite from Switzerland"; detailed study of the structure and triggers of penultimate deglaciation as recorded in speleothem MF3 (Alpstein Mts., Appenzell).* This chapter provides the first highly- resolved isotopic-age profile for the penultimate deglaciation from the northern fringe of the Alps. Petrography, ultra-high stable isotopes and trace element analysis highlight the importance of internal and external climate triggers responsible for deglaciations in high alpine areas, and display a regional and hemispheric teleconnection over this interval.
- Chapter 4: *Lateglacial environmental and temperature reconstruction in Central Europe: a multi-proxy and multi-techniques approach on speleothems from Milandre Cave (Swiss Jura Mountains),* presents Lateglacial high-resolution quantitative and qualitative paleoclimate reconstructions in Central Europe based on stable isotopes and trace elements from three coeval speleothems from Milandre Cave (Swiss Jura Mountains). A new temperature transfer function was developed based on three independent lines of evidence.
- Chapter 5: *Preliminary results on Holocene cold temperature reconstructions, as recorded in speleothem M6 (Milandre Cave, Swiss Jura Mountains),* presents highly-resolved and precise Holocene $\delta^{18}O$ and $\delta^{13}C$ records from sample M6 (Milandre Cave, Swiss Jura Mts.) and the first results of cold-season temperature reconstructions at the site. An extensive analysing and dating campaign aimed to establish precise chronologies and high resolution long-term climate variability at the cave site, with results which are representative for the Central European region.

1.2. General setting and previous speleothem studies in Switzerland

Climatologically, the northern side of the Swiss Alps and Jura Mountains shows a temperate climate with a considerable Atlantic influence. The Alpine chain and Jura Mountains are located on the southern fringe of the extra-tropical westerlies and form an orographic border between the Mediterranean and the North Atlantic climatic zones (Sodemann and Zubler, 2010). The climate is strongly tied to processes over the North Atlantic Ocean and its sea-ice system, making this region very suitable for the study of climatic and atmospheric processes over the North Atlantic region (Wanner et al., 1997). Cave speleothems offer an advantage, when compared to other natural archives, in recording regional to hemispheric scale climate processes due to their i) high resolution stratigraphy (up to seasonal scale), ii) high preservation potential over long time intervals, iii) high resistance to post depositional processes that may alter their proxy quality (Turgon and Lundberg, 2007).

Almost 20 % of the surface of Switzerland is represented by karst areas which host more than 9000 caves, including two of the most extensive cave systems in the world (Hölloch and Siebenhengste cave system). Distribution of the caves, both in areas that were glaciated or ice-free during the Quaternary history of Switzerland (Fig. 1.2), allows the unique potential to improve our knowledge with regard to the presence and/or dynamics of glaciers over long time intervals (e.g. Spötl et al., 2007).

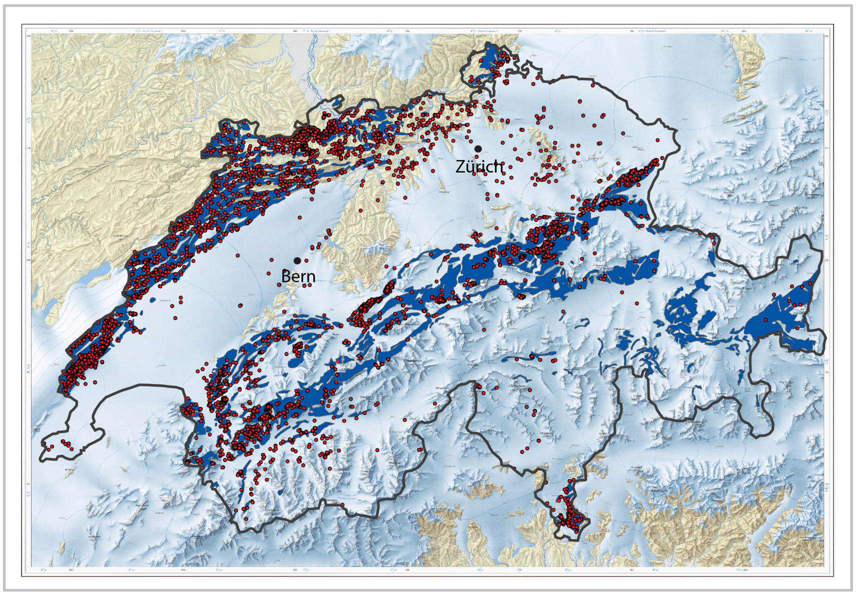

Figure 1.2. *Swiss caves distribution (dots, data from SISKA and Atlas der Schweiz 2.0) and spatial extension of glaciers during the Last Glacial Maximum interval in Switzerland (blue color, data from map.geo.admin.ch).*

Until now, speleothems from the Swiss caves were primarily used to reconstruct growing intervals, cave evolution, geomorphologic surface evolution (e.g. valley incision) and seismic and neotectonic events (please refer to Fig. 1.3). More recently however, new high resolution analyses of the calcite isotopic composition of samples has been published for Swiss speleothems (Luetscher et al., 2011, 2015; Boch et al., 2011).

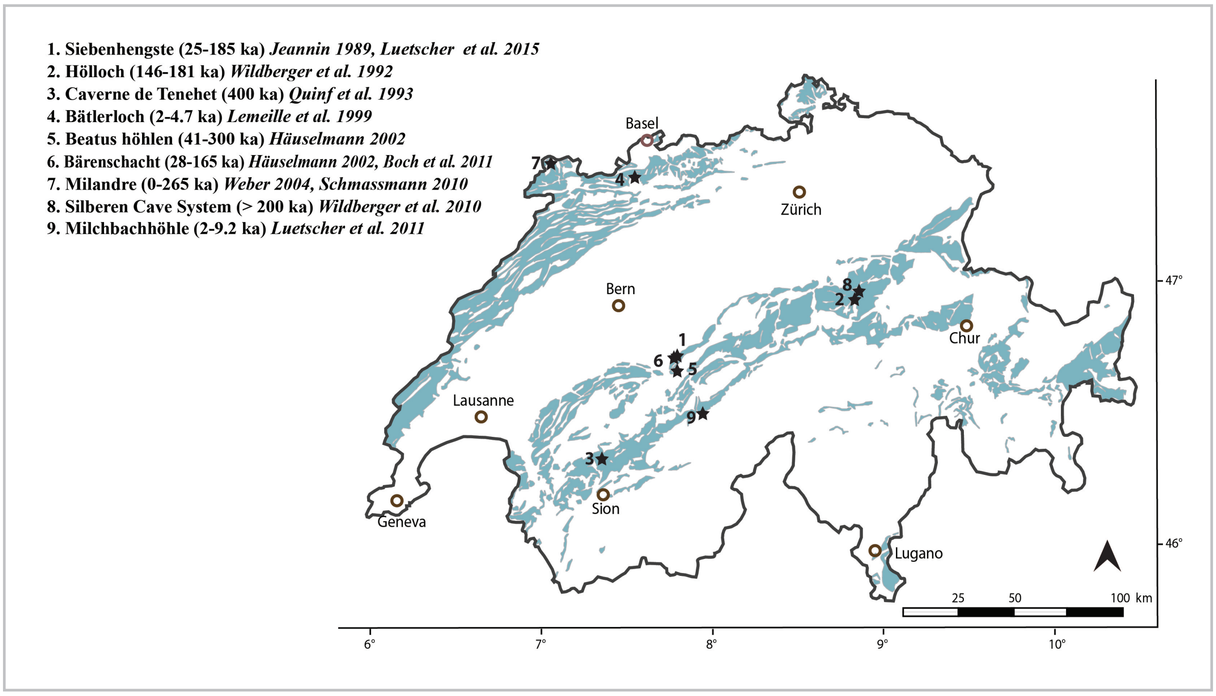

Figure 1.3*. Karst areas in Switzerland (blue, data from SISKA and Atlas der Schweiz 2.0) and previous studies of speleothems from Swiss caves (modified from Häuselmann et al., 2013).*

1.3. SPELEOTHEMS AS CLIMATE AND ENVIRONMENTAL ARCHIVES

1.3.1. SPELEOTHEM FORMATION

Speleothems are secondary carbonate deposits found in natural caves (large scale solution cavities) or artificial (man-made) tunnels. Among calcium carbonate minerals commonly found in caves (calcite, aragonite, vaterite, huntite, magnesite and dolomite, Hill and Forti, 1997), calcite is the most abundant due to its stable form under the physical conditions (temperature, total pressure and partial P_{CO2}) found in the cave environment (White, 2007).

The mechanisms of speleothem formation are simple (see review in Fairchild et al., 2006). Three main stages characterize their deposition, as summarized in the reactions listed below (Roques, 1962):

$$H_2O_{(l)} + CO_{2(g)} \longrightarrow H_2CO_{3(aq)}$$

$$H_2CO_{3(aq)} + CaCO_{3(s)} \longrightarrow Ca^{2+}_{(aq)} + 2HCO_3^-$$

$$Ca^{2+}_{(aq)} + 2HCO_{3\ (aq)}^- \longrightarrow CO_{2(g)} + H_2O_{\ (l)} + CaCO_{3(s)}$$

Carbonic acid is produced as a result of meteoric water mixing with additional soil CO_2 (produced as a result of decaying organic matter, microbial processes and plants root respiration. Meteoric water has a P_{CO2} of $10^{-3.5}$ bar (White, 2007), as the absorbtion of additional CO_2 during its percolation downward in the soil column brings it into equilibrium with the P_{CO2} in the soil, reachings a P_{CO2} of 10^{-1} bar (White, 2007). The dissolution capacity of the resulting solution is increased and becomes undersaturated with respect to $CaCO_3$ ("aggressive water", Ford and Williams, 1989). During its percolation through the pores and fractions of the carbonatic rock, this weak carbonic acid reacts with $CaCO_3$ and will produce a calcium bicarbonate solution. The solution will continue to dissolve $CaCO_3$ and hold more Ca^{2+} ions until saturation is reached. As higher P_{CO2} levels are produced in the soils, higher concentrations of Ca^{2+} will be required for the solution to reach saturation. As the saturated solution reaches the cave gallery, in the form of saturated $CaCO_3$- bearing drip waters, CO_2 degasses as it is out of equilibrium with that of the cave atmosphere which has a lower P_{CO2} (around $10^{-2.5}$ bar, White, 2007). As a result of degassing, the solution becomes supersaturated with respect to calcite and as a result carbonate minerals precipitate out of solution, forming different speleothem formations in the spelean environment. Most caves have high humidity, typically 95-100% (Tanner, 2010), minimizing the evaporation of drip water (Hendy, 1971). Therefore CO_2 degassing and not evaporation will be the dominant factor in calcite precipitation (McDermott, 2004). Speleothems can also form without the presence of soil and vegetation above the cave. If pyrite in present in the host rock and under oxidizing condition, sulfuric acid forms and dissolves the host rock and produce excess CO_2 (Atkinson, 1983). It has been also suggested that warming up of water while percolating through the host rock or entering the cave, or by dissolving Ca-bearing minerals ("common-ion effect") can cause calcite supersaturation and calcite may subsequently precipitate in the caves (Dreybrodt, 1982; Atkinson, 1983).

1.3.2. GEOCHEMISTRY OF SPELEOTHEMS

The climatic and environmental changes at the surface are transmitted to the cave through the chemical and physical properties of the drip water, and preserved in the speleothem calcite. In order to reconstruct these changes, this study combined information from the following speleothem proxies: growth intervals and growth rates, petrography of the calcite, calcite stable isotopes (oxygen and carbon), trace elements and organic matter concentration in calcite (Fig. 1.4, Frisia and Borsato, 2010).

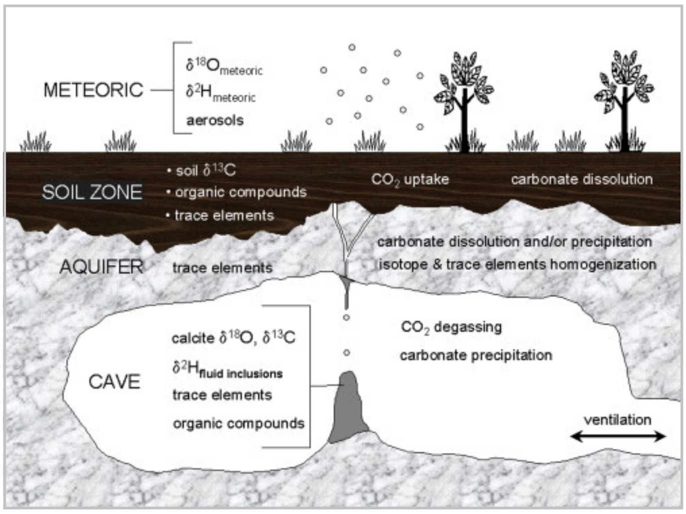

Figure 1.4. *Transfer of climate proxies in the speleothem calcite (Frisia and Borsato, 2010)*

1.3.2.1. U-SERIES DATING

The Uranium disequilibrium dating method is widely used in dating speleothems. Isotopes of uranium leached from the bedrock are co-precipitated in the calcite structure as uranyl carbonate ($UO_2(CO_3)_{(s)}$). The ^{238}U ($t_{0.5}$=4.47 Ga) decay chain begins with an alpha decay to ^{234}Th ($t_{0.5}$=24.1 days), which will be followed by a decay to ^{234}Pa ($t_{0.5}$=6.69 hours), ^{234}U ($t_{0.5}$=245 ka), ^{230}Th ($t_{0.5}$=75 ka), ^{226}Ra ($t_{0.5}$=1.6 ka), followed by a number of short-lived nuclides until it reaches the stable ^{206}Pb (Richards and Dorale, 2003). Ages are calculated based on measurements of $^{230}Th/^{234}U$ and $^{234}U/^{238}U$ in speleothem calcite (Fig. 1.5), which is considered to initially be deficient in thorium, as thorium is essentially insoluble and not transported by the parent water in the cave environment. An indication of detrital contamination in the sample is given by the presence of ^{232}Th in the Th spectrum. ^{232}Th is a non-radiogenic isotope that only occurs in water as a trace impurity. Nevertheless, the $^{230}Th/^{232}Th$ ratio can be used as a basis to correct the ages for detrital contamination (Richards and Dorale, 2003). Special attention should be given to samples where a $^{230}Th/^{232}Th$ activity ratio < 200 is measured (Richards and Dorale, 2003). The isochron methodology (measuring coeval subsamples of calcite) can be used to control both the detrital contamination and for any petrographic indications of "open system" activity in the sample (e.g. recrystallization of calcite, mobilization of nuclides, Schwarcz, 1989; Richards and Dorale, 2003).

A sub-sampling strategy for age determination should include: i) measurement of overview samples to determine the age range of the sample and its uranium concentration, ii) avoidence of dirty (detrital contaminated) and hiatuses sections, recrystallized and open pores areas of the sample. Detrital contamination of the sample and remobilization of uranium lead to older ages than the real age, while mobilization of fresh drip water within older speleothem layers (via pores) and precipitation of fresh calcite in pores results in younger ages.

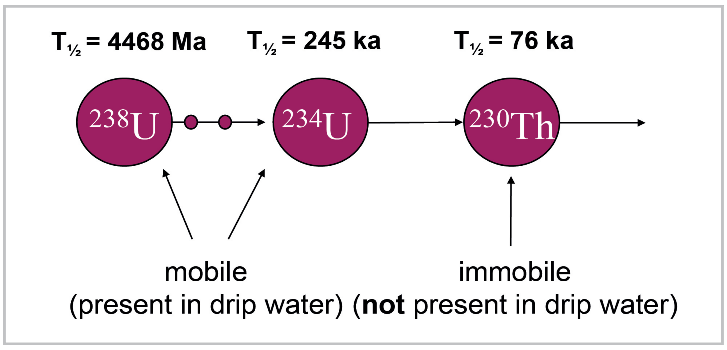

Figure 1.5. *Nuclides of U-decay chain used to calculate calcite ^{230}Th ages*

Important advances have been made both in accurately constraining the decay constants and in measuring of daughter-to-parent nuclide ratio (Cheng et al., 2013). The method provides precise ^{230}Th ages for calcite precipitated in the last 500 ka (e.g. Cheng et al., 2009, 2012; Badertscher et al., 2011), limited by the secular equilibrium conditions caused by the decay rate of ^{230}Th.

1.3.2.2. Petrography of the calcite

Variations in calcite crystals fabrics are mostly related to variations in drip rates and departures from equilibrium growth (high-supersaturation levels of the cave drip water, Frisia et al., 2000). Columnar and microcrystaline fabrics form in low-supersaturation conditions (quasi-equilibrium conditions), whereas dendritic fabrics form in disequilibrium conditions as a result of low and irregular drip rates (prolonged outgassing, Frisia et al., 2000). The dense close columnar fabric is suggested to be formed at low supersaturation and regular flow conditions, with negligible presence of impurities (Frisia et al., 2000). Open columnar fabric could form during faster growth rates, high supersaturation conditions, presence of impurities and high discharge variability (Frisia and Borsato, 2010; Boch et al., 2011).

1.3.2.3. Stable isotopes in speleothem calcite

Stable isotopes are atoms of the same element exhibiting different atomic masses. The natural abundance of oxygen (O) stable isotopes is: ^{16}O (99.763 %), ^{17}O (0.0375 %) and ^{18}O (0.1995 %), and of carbon (C) stable isotopes: ^{12}C (98.89 %) and ^{13}C (1.11 %).

The stable isotopic composition of oxygen and carbon are not measured in absolute terms, but are reported as enrichments and depletions relative to a standard of known composition. Isotopic composition is usually reported against the Vienna PeeDee Belemnite (VPDB) standard for calcite samples and Vienna Standard Mean Ocean Water (VSMOW) standard for water samples, using the δ notation and following equation:

$$\delta^{18}O_{\text{sample}}\ (‰) = [\ (^{18}O/^{16}O)_{\text{sample}} - (^{18}O/^{16}O)_{\text{standard}}] * 1000/\ (^{18}O/^{16}O)_{\text{standard}}$$
$$\delta^{13}C_{\text{sample}}\ (‰) = [\ (^{14}C/^{13}C)_{\text{sample}} - (^{14}C/^{13}C)_{\text{standard}}] * 1000/\ (^{14}C/^{13}C)_{\text{standard}}$$

If the δ^{18}O values are more negative, the term ^{18}O depleted or ^{16}O enriched are used. Conversely, if the δ^{18}O values are more positive, these are referred to as ^{18}O enriched or ^{16}O depleted.

The $\delta^{18}O_{\text{precipitation}}$ decreases with increasing latitude, altitude, distance from coast, increasing rainfall (tropics) and with a drop in temperature (mid-latitudes, Fig. 1.6). In mid-latitude regions, the season of precipitation recharge of the karst aquifer is during winter to spring seasons, with infiltration during summer less likely to infiltrate due to higher evapotranspiration rates (Genty et al., 2006).

Under favorable conditions (calcite is deposited in conditions close to equilibrium) $\delta^{18}O$ of speleothems will be dominated by the i) $\delta^{18}O$ signature of precipitation above the cave and ii) isotopic fractionation occurring during the calcite precipitation (controlled by the temperature at the moment of calcite precipitation). As widely discussed in literature, variations in $\delta^{18}O$ of precipitation and drip water depend on several factors such as i) changes in the source of the moisture, ii) isotopic composition of the moisture (namely North Atlantic Ocean for our region of interest), iii) the "amount effect", and iv) surface and cave air temperature. Excellent reviews on the subject were published by McDermott (2004), Fairchild et al. (2006) and Lachniet (2009). As well as this, local complex processes (in hydrologic cycle, soil, epikarst and cave environment) can influence the incorporation of oxygen isotopes, and consequently, the variability of $\delta^{18}O$ values in the stalagmite layers deposited at different times. To overcome the complexity of processes that can overprint the climatic signal in speleothems, it is highly recommended to analyze coeval speleothems from the same cave and/or region.

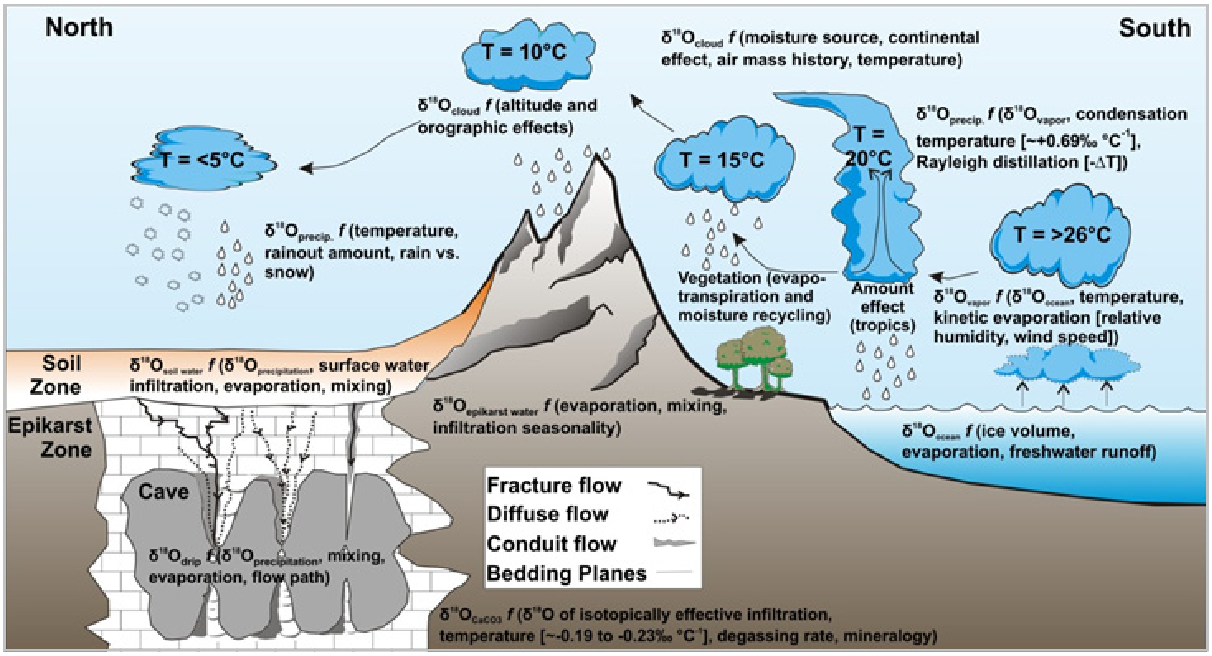

Fig. 1.6. *Overview on the primary controls on variations in the $\delta^{18}O$ of precipitation and $\delta^{18}O$ of speleothem calcite (Lachniet, 2009).*

The main influencing factors of calcite $\delta^{13}C$ include changes in i) the density and type of vegetation (proportion of C3 and C4 plants), ii) microbial processes in the soil zone, iii) recharge conditions (closed versus open system dissolution) and iv) CO_2 degassing. In general, $\delta^{13}C$ calcite values of -14 to -6‰ and -6 to +2‰ can be indicative of C3 and C4 vegetation respectively (McDermott, 2004; Frisia and Borsato, 2010). Recharge conditions and equilibration of infiltrating water with soil CO_2 (closed versus open system dissolution) can be an additional parameter determining $\delta^{13}C$ values in speleothems, particularly when soils are thin or absent. Finally, low drip rates and enhanced CO_2 degassing during calcite precipitation and ventilation can lead to elevated calcite $\delta^{13}C$ values (Baker et al., 1997, 2011; Mühlinghaus et al., 2009, Deininger et al., 2012). Spötl et al., (2005) and references therein, stressed about the importance of air circulation in dynamically ventilated caves, which may result in an enhanced carbon kinetic fractionation factor.

1.3.2.4. TRACE ELEMENTS AND ORGANIC MATTER CONCENTRATION

Trace elements are transported as particles, solutes or adsorbed onto colloids, and incorporated into speleothem calcite according to their concentration in drip water (Fairchild and Treble, 2009). They are incorporated within the calcite crystal lattice by substitution of a major ion, at defect sides, or as colloids and detrital particles (Fairchild and Treble, 2009). Their concentrations provide additional information on recharge conditions, groundwater residence time, soil conditions, and help reduce uncertainties associated with the interpretation of $\delta^{18}O$ and $\delta^{13}C$ (Fairchild and Baker, 2012, Fig. 1.7).

Elements such as Mg, Sr, U and Ba are well-established indicators for effective rainfall and groundwater residence time in the karst aquifer above the cave (Fairchild and McMillan, 2007; McDonald et al., 2004; Roberts et al., 1998; Zhou et al., 2005). In addition, Mg and U contents are also related to prior calcite precipitation at times of low effective moisture (Fairchild and McMillan, 2007; Drysdale et al., 2009) and rock weathering (Ayalon et al., 1999).

Along with $\delta^{13}C$, P concentration is used as an indicator for soil activity and vegetation (Borsato et al., 2007; Fairchild et al., 2001; Treble et al., 2003). Rare earth elements such as Y and Ti are indicators for enhanced weathering of the overlying soil layer and the host rock (Richter et al., 2004; Zhou et al., 2008). Schimpf et al. (2011) used Y as a tracer for detrital (including colloidal) transport and used it as a proxy for rainfall. Ti is often used as a tracer for detritus, due to its extremely low solubility (Fairchild and Baker, 2012). Another element typically incorporated in the fine-grained detrital layers deposited on speleothems during flooding events is Al, which has been used as a paleohydrological indicator (Borsato et al., 2007).

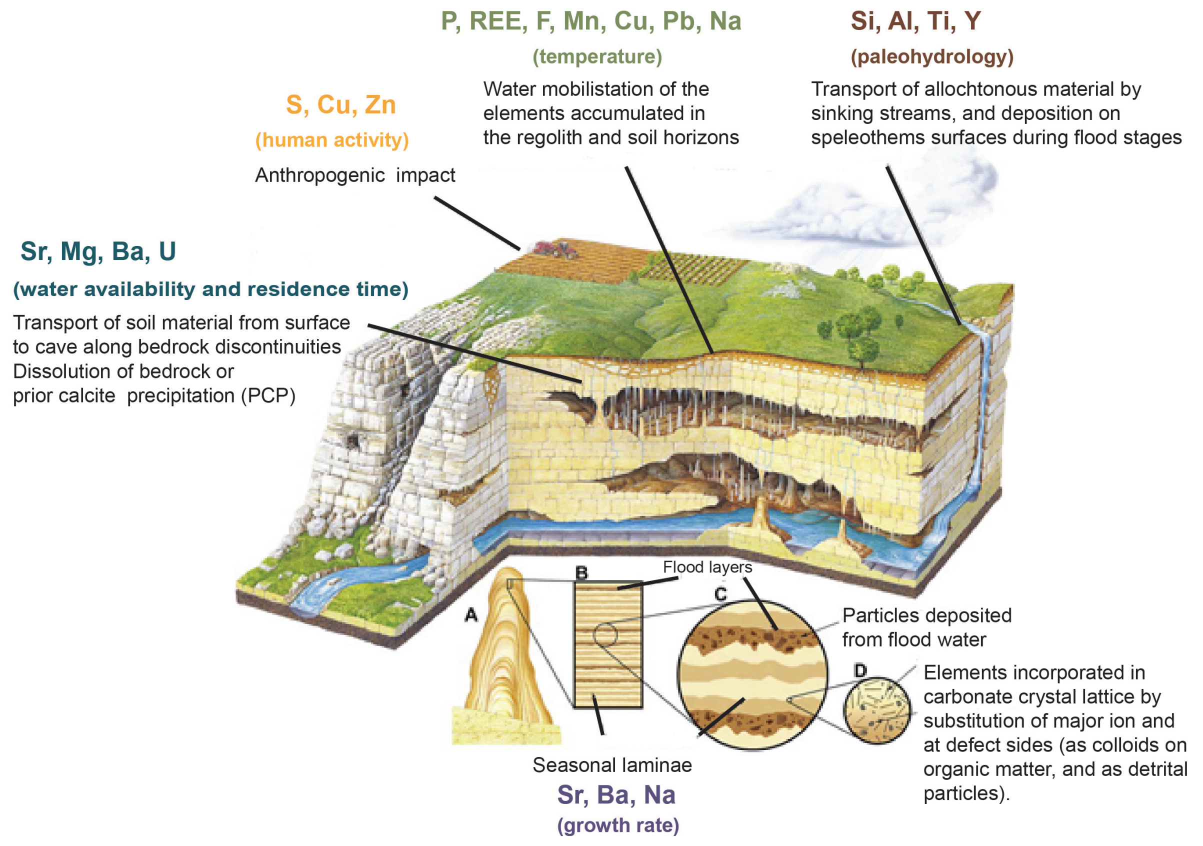

Figure 1.7. *Overview on trace element incorporation mechanisms into stalagmite structure (figure modified from Lascu and Feinberg, 2011), based on data from Fairchild et al. (2007), Fairchild and Treble (2009), Stoll et al. (2012), and Hartland et al. (2012). Please refer to the text for further details.*

Organic matter is also incorporated as a trace component either between or within the mineral crystals (Ramseyer et al., 1997). Organic matter preserved in speleothems, detected as fluorescence intensity, is used to identify climate and hydrological-induced changes in the rate of organic matter turnover and its release into the groundwater system (Proctor et al., 2000, Linge et al., 2009).

1.4. METHODS

1.4.1. FIELD CAMPAIGNS AND CAVE PARAMETERS

For this study, we collected and/or received samples from the Jura Mountains and the northern side of the Swiss Alps. Actively growing stalagmites were collected from Milandre Cave, St. Beatus Cave, Grotte aux Fees du Vallorbe. Samples remobilized from their growing place were collected from Hobbit Cave, Haglätsch Cave, Chammfluhöhle, Romontberghöhle and Schafsloch Cave. The overview with growing intervals for each sample is presented in Table 1.1 and Fig. 1.8.

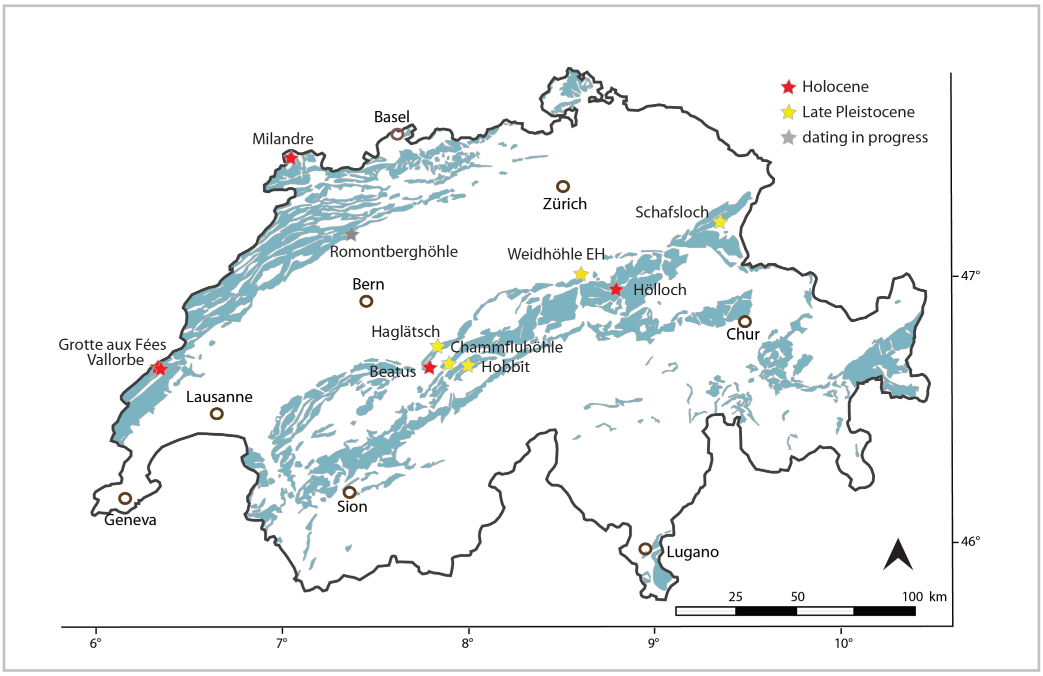

Figure 1.8. *Karst areas in Switzerland (blue, Atlas der Schweiz) and cave locations of samples studied in the STALCLIM project (modified from Häuselmann et al., 2013)*

Cave (region)	Alt. (m asl)	Sample	Type	Length (mm)	Growing interval
St. Beatus Cave (BE)	690	BHN_1	stalagmite	535	MIS 1
Hölloch (SZ)	740	Höll_A	soda straw	600	MIS 1
Schafsloch (AI)	1890	MF_3	stalagmite	210	MIS 5-7
Milandre Cave (NE)	400	M2	stalagmite	250	MIS 1
Milandre Cave (NE)	400	M6	stalagmite	1450	MIS 1
Milandre Cave (NE)	400	M8	stalagmite	135	MIS 1
Grotte aux Fees (VD)	895	GEF_1	stalagmite	695	MIS 1
Hobbit Cave (BE)	2000	Ho_1	stalagmite	210	MIS 5
Haglätsch Cave (BE)	1660	HAG_01	stalagmite	230	MIS 5
Weidhöhle bei EH (SZ)	780	WEH_1	core	300	MIS 2-3
Chammfluehöhle (BE)	650	CHAM_1	stalagmite	540	MIS 1
Romontberghöhle (BE)	1156	ROM_01	stalagmite	670	?

Table 1.1. *Inventory of the Swiss samples collected/studied during the STALCLIM project (see Appendix for data)*

The in-situ stalagmites were collected in deep parts of the cave (away from the entrance) were temperature is constant and equal to the multi-annual temperature average, with a high relative humidity (RH > 95%) and from cave passages protected from ventilation and/or close to underground rivers. A good understanding of the cave genesis and evolution is also important, in order to avoid areas frequently exposed to flooding in the past, or within the vicinity of a former entrance to the cave. We chose caves with galleries close to the surface, to minimize the buffering of the isotopic signal in the aquifer over long time intervals.

Before removing a stalagmite we have observed:

- the calcite texture and porosity of stalagmites in the gallery (ideally done on samples detached from their initial growing place, or drilling "reconnaissance cores" in the stalagmites, photo Fig. 8A).
- under certain circumstances (large diameter stalagmites or flowstone) a 30 cm long cores were drilled (Fig. 8B)
- the feeding point of the stalagmite (soda straws are preferred)
- the distance from stalagmite to the feeding point (at high distances the drip water will splash and more calcite will be deposited on the flanks of the sample)
- the shape and height of the sample (stalagmites with cylindrical growth geometry are favoured due to their faster growth rate and tendency to form in close isotopic equilibrium with the parental drip water.

To monitor present day conditions at the Milandre sampling site, the following equipment was installed: a STALAGMATE drip logger (Stalagmate Plus Mk2b, Driptych, UK, Mattey and Collister, 2008); a temperature logger (UTL-3 Scientific Dataloggers, GEOTEST, Zollikofen and Snow and Avalanche Research SFL, Davos) and glass watches in order to precipitate fresh calcite. Relative humidity was measured over time using an Aspirationspsychrometer Hänni device (Jegensdorf, CH). P_{CO2} was measured using a Dräger X-am 5600 device, and air flow speed measured with a Dräger X-am 5600.

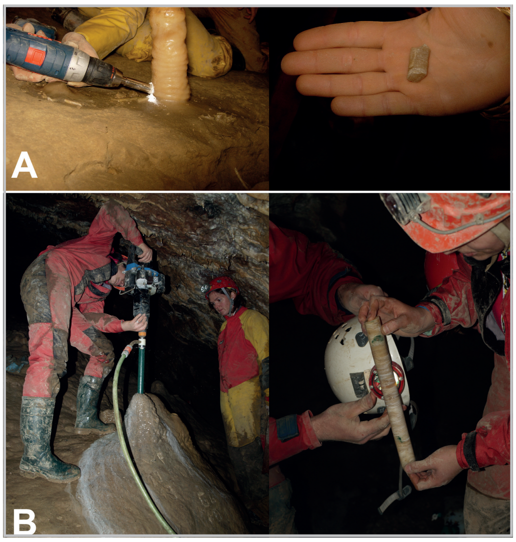

Figure 1.9. ***A.*** *Drilling "reconnaissance core" in sample BHL_01 (St. Beatus Cave, photos: A.D. Häuselmann).* ***B.*** *stalagmite core WHL_01 (Weidhöhle EH, photo: R. Graf).*

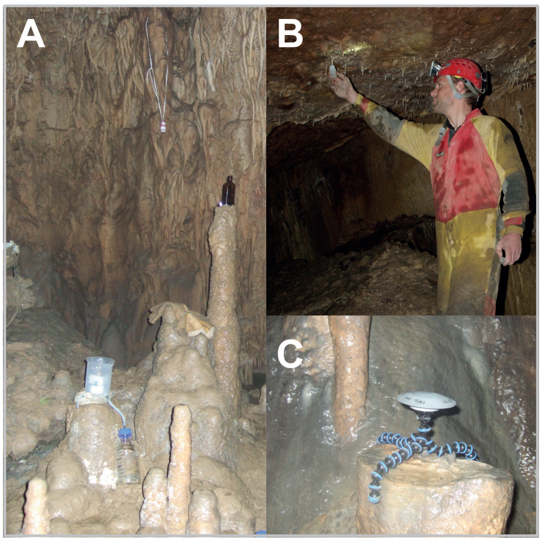

Figure 1.10. ***A*** *and* ***C****. Monitoring present conditions in Milandre cave (photo: A.D. Häuselmann)* ***A.*** *Drip water and temperature loggers, punctual and continuous water sampling at M6 site* ***B.*** *Glass watch at M4 site (C).* ***C.*** *Punctual drip-water sampling in Weidhöhle EH (photo: R. Graf).*

1.4.2. LABORATORY ANALYSIS

For Uranium-series dating (^{230}Th hereinafter), approximately 200 mg of powder was drilled along discrete growth horizons. Overview age determination was performed at the Institute for Geological Sciences, University of Bern, Switzerland, with a a detailed description of the method available in Fleitmann et al. (2007). Isotope analysis was conducted using a Nu Instruments MC-ICP-MS at the Institute for Geological Sciences, University of Bern.

Most of ^{230}Th analysis were performed in the laboratory of Dr. L. Edwards at the Department of Earth Sciences, University of Minnesota, and are kindly provided for this thesis. Element separation was done using the procedure of Edwards et al. (1987). The ^{230}Th ages were determined on a multi-collector inductively coupled plasma mass spectrometer (MC-ICP-MS, Thermo-Finnigan Neptune) at the Department of Earth Sciences, University of Minnesota. Details of the methods, including standards used for mass fractionation and yield correction can be found in Cheng et al. (2013).

In order to construct stalagmite age models the calculated ages were plotted versus their distance from the top of the stalagmite. Linear interpolation was applied where only two ages were available between two hiatuses in the sample, and statistical age models (StalAge, Scholz and Hoffmann, 2011; COPRA, Breitenbach et al., 2012) were used where more ages were available. We stress the importance of providing as many ages as possible for each sample, in order to correctly assess the presence of hiatuses and changes in the growth rate of the samples.

Calcite stable isotope (δ^{18}O and δ^{13}C) measurements were performed in the laboratory of the Institute for Geological Sciences, University of Bern. Calcite powder was micromilled continuously, using an electronically controlled micromill equipped with a 0.5 mm diameter drilled head. About 150-200 µg of powdered sample was placed in 12 ml vacutainers, flushed with He, and reacted with 5 drops of 99 % P_5O_5 at 70°C for 80 minutes. The samples were measured using a Finnigan Delta V Advantage mass spectrometer equipped with an automated carbonate preparation system (Gas Bench II) at the Institute of Geological Sciences, University of Bern, Switzerland. The analytical reproducibility based on repeated measurement of the internal standard for δ^{18}O and δ^{13}C is lower than 0.07 and 0.06 ‰ VPDB (1σ).

Methods development and raw-data analyses of calcite trace elements and fluid inclusions were performed by the other groups of the STALCLIM project, and were kindly provided for use in this thesis, in order to construct age models, compare results and/or provide a climatological and environmental data interpretation. Determination of minor and major trace element concentration in the samples, using a laser ablation technique, was performed in the Department of Chemistry and Applied Biosciences, Laboratory of Inorganic Chemistry, ETH Zürich. We used a 193 nm ArF excimer laser (GeoLas Pro, Lambda Physik) coupled to a quadrupole ICP-MS (ELAN 6100 DRC+, Perkin Elmer). A detailed description of the experimental setup is given in Kovacs et al. (2010) and optimized as described in Tabersky et al. (2013). The method is nondestructive, does not require an ablation cell, and analyses can be performed at a speed of 1.2 cm/min. Noble gases in fluid inclusions (NG) were measured at the Department of Water Resources and Drinking Water, Eawag, using a recently developed combined vacuum crushing and sieving (CVCS) system'. The setup and operation conditions are described in Vogel et al. (2013). δ^{18}O and δD of speleothem fluid inclusions were measured using a wavelength scanned cavity ring down spectroscopy (WS-CRDS) instrument, following the set up and procedure described in Affolter et al. (2014).

BIBLIOGRAPHY

Affolter, S., Fleitmann, D., Leuenberger, M., 2014. New online method for water isotope analysis of speleothem fluid inclusions using laser absorption spectroscopy (WS-CRDS). Clim. Past 10, 1291-1304.

Affolter, S., Häuselmann, A.D., Fleitmann, D., Häuselmann, Ph., Leuenberger, M., in review. Triple isotope (δD, $\delta^{18}O$, $\delta^{17}O$) study on precipitation, drip water and speleothem fluid inclusions for a central European cave (NW Switzerland). Quaternary Science Reviews.

Atkinson, T.C., 1983. Growth Mechanisms of Speleothems in Castleguard Cave, Columbia Icefields, Alberta, Canada. Arctic and Alpine Research 15, 523-536.

Atkinson, T.C., Harmon, R.S., Smart, P.L. and Waltham, A.C., 1978. Palaeoclimate and geomorphic implications of 230 Th/234U dates on speleothems from Britain. Nature 272, 24-28.

Ayalon, A., Bar-Matthews, M., Kaufman, A., 1999. Petrography, strontium, barium and uranium concentrations, and strontium and uranium isotope ratios in speleothems as palaeoclimatic proxies: Soreq Cave, Israel. Holocene 9, 715-722.

Badertscher, S., Fleitmann, D., Cheng, H., Edwards, R.L., Göktürk, O.M., Zumbühl, A., Leuenberger, M., Tüysüz, O., 2011. Pleistocene water intrusions from the Mediterranean and Caspian seas into the Black Sea. Nature Geoscience 4, 236-239.

Baker, A., Ito, E., Smart, P.L., McEwan, R.F., 1997. Elevated and variable values of C-13 in speleothems in a British cave system. Chem Geol 136, 263-270.

Baker, A., Wilson, R., Fairchild, I.J., Franke, J., Spötl, C., Mattey, D., Trouet, V., Fuller, L., 2011. High resolution δ18O and δ13C records from an annually laminated Scottish stalagmite and relationship with last millennium climate. Global and Planetary Change.

Boch, R., Cheng, H., Spötl, C., Edwards, R.L., Wang, X., Ph, H., 2011a. NALPS: A precisely dated European climate record 120-60 ka. Climate of the Past 7, 1247-1259.

Boch, R., Spotl, C., Frisia, S., 2011b. Origin and palaeoenvironmental significance of lamination in stalagmites from Katerloch Cave, Austria. Sedimentology 58, 508-531.

Borsato, A., Frisia, S., Fairchild, I.J., Somogyi, A., Susini, J., 2007. Trace element distribution in annual stalagmite laminae mapped by micrometer-resolution X-ray fluorescence: Implications for incorporation of environmentally significant species. Geochimica Et Cosmochimica Acta 71, 1494-1512.

Breitenbach, S.F.M., Rehfeld, K., Goswami, B., Baldini, J.U.L., Ridley, H.E., Kennett, D.J., Prufer, K.M., Aquino, V.V., Asmerom, Y., Polyak, V.J., Cheng, H., Kurths, J., Marwan, N., 2012. Constructing proxy records from age models (COPRA). Climate of the Past 8, 1765-1779.

Cheng, H., Lawrence Edwards, R., Shen, C.-C., Polyak, V.J., Asmerom, Y., Woodhead, J., Hellstrom, J., Wang, Y., Kong, X., Spötl, C., Wang, X., Calvin Alexander Jr, E., 2013. Improvements in 230Th dating, 230Th and 234U half-life values, and U–Th isotopic measurements by multi-collector inductively coupled plasma mass spectrometry. Earth and Planetary Science Letters 371–372, 82-91.

Deininger, M., Fohlmeister, J., Scholz, D., Mangini, A., 2012. Isotope disequilibrium effects: The influence of evaporation and ventilation effects on the carbon and oxygen isotope composition of speleothems – A model approach. Geochimica Et Cosmochimica Acta 96, 57-79.

Dreybrodt, W., 1982. A possible mechanism for growth of calcite speleothems without participation of biogenic carbon dioxide. Earth and Planetary Science Letters 58, 293-299.

Drysdale, R.N., Hellstrom, J.C., Zanchetta, G., Fallick, A.E., Goni, M.F.S., Couchoud, I., McDonald, J., Maas, R., Lohmann, G., Isola, I., 2009. Evidence for Obliquity Forcing of Glacial Termination II. Science 325, 1527-1531.

Edwards, R.L., Chen, J.H., Wasserburg, G.J., 1987. U-238, U-234, Th-230, TH-232 systematics and the precise measurement of time over the past 500 000 years. Earth and Planetary Science Letters 81, 175-192.

Fairchild, I.J., Baker, A., 2012. Speleothem Science: From Process to Past Environments. Wiley-Blackwell.

Fairchild, I.J., Baker, A., Borsato, A., Frisia, S., Hinton, R.W., McDermott, F., Tooth, A.F., 2001. Annual to sub-annual resolution of multiple trace-element trends in speleothems. J Geol Soc London 158, 831-841.

Fairchild, I.J., McMillan, E.A., 2007. Speleothems as indicators of wet and dry periods. Int J Speleol 36, 69-74.

Fairchild, I.J., Smith, C.L., Baker, A., Fuller, L., Spötl, C., Mattey, D., McDermott, F., 2006. Modification and preservation of environmental signals in speleothems. Earth-Science Reviews 75, 105-153.

Fairchild, I.J., Treble, P.C., 2009. Trace elements in speleothems as recorders of environmental change. Quaternary Science Reviews 28, 449-468.

Fleitmann, D., Burns, S.J., Mangini, A., Mudelsee, M., Kramers, J., Villa, I., Neff, U., Al-Subbary, A.A., Buettner, A., Hippler, D., Matter, A., 2007. Holocene ITCZ and Indian monsoon dynamics recorded in stalagmites from Oman and Yemen (Socotra). Quaternary Science Reviews 26, 170-188.

Frisia, S., Borsato, A., 2010. Karst, In: Alonso-Zarza, A.M., Tanner, L.H. (Eds.), Carbonates in Continental Settings: Facies, Environments, and Processes. Elsever, Amsterdam, pp. 269-318.

Frisia, S., Borsato, A., Fairchild, I.J., McDermott, F., 2000. Calcite fabrics, growth mechanisms, and environments of formation in speleothems from the Italian Alps and southwestern Ireland. J Sediment Res 70, 1183-1196.

Genty, D., Blamart, D., Ghaleb, B., Plagnes, V., Causse, C., Bakalowicz, M., Zouari, K., Chkir, N., Hellstrom, J., Wainer, K., Bourges, F., 2006. Timing and dynamics of the last deglaciation from European and North African δ13C stalagmite profiles-comparison with Chinese and South Hemisphere stalagmites. Quaternary Science Reviews 25, 2118-2142.

Hai, C., Ashish, S., Xianfeng, W., Francisco, W.C., Edwards, R.L., 2012. The Global Paleomonsoon as seen through speleothem records from Asia and the Americas. Climate Dynamics 39, 1045-1062.

Hai, C., Edwards, R.L., Wallace, S.B., George, H.D., Xinggong, K., Yongjin, W., Rong, Z., Xianfeng, W., 2009. Ice age terminations. Science 326, 248-252.

Hasenfratz, A., 2012. Temperature reconstruction over the past two millenia based on stalagmite $\delta^{18}O$ record from the Jura Swiss Mountains, Institute of Geological Sciences. Bern University, p. 79.

Hasenfratz, A., Fleitmann, D., Häuselmann, A.D., Lehner, F., Cheng, H., Edwards, R.L., Leuenberger, M., Affolter, S., Raible, C.C., Breitenbach, S.F.M., Luterbacher, J., in prep. Central European temperature variations over the past two millennia based on a stalagmite oxygen isotope record from the Swiss Jura Mountains.

Häuselmann, A.D., Breitenbach, S, Hasenfratz, A., Fleitmann, D., 2013. Project STALCLIM Switzerland: where, how and what for?, Proceedings of the 13th Swiss National Congress of Speleology, Muotantal

Häuselmann, Ph., 2002. Cave Genesis and its relationship to surface processes: Investigations in the Siebenhengste region (BE, Switzerland), PhD thesis, Institut de géographie, Université de Fribourg, 168 p.

Hendy, C.H., 1971. The isotopic geochemistry of speleothems: The calculations of the effects of different modes of Formation on the isotopic composition of speleothems and their applicability as palaeclimate indicators. Geochimica et Cosmochimica Acta 35, 801-824.

Hill, C., Forti, P., 1997. Cave minerals of the world. 2nd Edition. NSS, Huntsville., 463 p.

Jeannin, P.Y., 1996. Structure et comportement hydraulique des aquifères karstiques. - Thèse de doctorat, Université de Neuchâtel, Centre d' hydrogéologie, 237 pages.

Kovacs, R., Nishiguchi, K., Utani, K., Gunther, D., 2010. Development of direct atmospheric sampling for laser ablation-inductively coupled plasma-mass spectrometry. Journal of Analytical Atomic Spectrometry 25, 142-147.

Lachniet, M.S., Denniston, R.F., Asmerom, Y., Polyak, V.J., 2014. Orbital control of western North America atmospheric circulation and climate over two glacial cycles. Nature Communications 5.

Lascu, I. and Fainberg, J., 2011. Speleothem magnetism, Quaternary Science Reviews 30, 3306-3320.

Lemeille, F., Cushing, M., Carbon, D., Grellet, B., Bitterli, Th., Flehoc, C., Innocent, C., 1999. Co-seismic ruptures and deformations recorded by speleothems in the epicentral zone of the Basel earthquake, Geodinamica Acta 12, 3-4, 179-191

Linge, H., Lauritzen, S.E., Andersson, C., Hansen, J.K., Skoglund, R.Ø., Sundqvist, H.S., 2009. Stable isotope records for the last 10 000 years from Okshola cave (Fauske, northern Norway) and regional comparisons. Clim. Past 5, 667-682.

Luetscher, M., Boch, R., Sodemann, H., Spötl, C., Cheng, H., Edwards, R.L., Frisia, S., Hof, F., Müller, W., 2015.

North Atlantic storm track changes during the Last Glacial Maximum recorded by Alpine speleothems. Nature Communications 6.

Luetscher, M., Hoffmann, D.L., Frisia, S., Spotl, C., 2011. Holocene glacier history from alpine speleothems, Milchbach cave, Switzerland. Earth and Planetary Science Letters 302, 95-106.

Mattey, D., Collister, C., 2008. High resolution measurements of drip discharge rates in caves using an acustic drip counter. Cave Radio and Electronics Journal 70, 11-13.

McDermott, F., 2004. Palaeo-climate reconstruction from stable isotope variations in speleothems: a review. Quaternary Science Reviews 23, 901-918.

McDonald, J., Drysdale, R., Hill, D., 2004. The 2002-2003 El Nino recorded in Australian cave drip waters: Implications for reconstructing rainfall histories using stalagmites. Geophys Res Lett 31.

Mühlinghaus, C., Scholz, D., Mangini, A., 2009. Modelling fractionation of stable isotopes in stalagmites. Geochimica Et Cosmochimica Acta 73, 7275-7289.

Quinif, Y., Leroy, J., Morverand, Ph., and Pahud, A., 1993. Datation d`une stalagmite dans la Caverne de Tenehet (Wildhorn, Valais-Suisse), Karstologia 22, 2, 48-51.

PAGES, 2009. Past Global Changes:Science Plan and Implementation Strategy, IGBP Report 57, Stockholm, p. 67.

Proctor, C.J., Baker, A., Barnes, W.L., Gilmour, R.A., 2000. A thousand year speleothem proxy record of North Atlantic climate from Scotland. Climate Dynamics 16, 815-820.

Ramseyer, K., Miano, T.M., D'Orazio, V., Wildberger, A., Wagner, T. and Geister, J., 1997. Nature and origin of organic matter in carbonates from speleothems, marine cements and coaral skeletons. Organic Geochemistry 26, 361-378.

Richards, D.A., Dorale, J.A., 2003. Uranium-series chronology and environmental applications of speleothems. Rev Mineral Geochem 52, 407-460.

Richter, D.K., Gotte, T., Niggemann, S., Wurth, G., 2004. REE3+ and Mn2+ activated cathodoluminescence in lateglacial and Holocene stalagmites of central Europe: evidence for climatic processes? Holocene 14, 759-767.

Roberts, M.S., Smart, P.L., Baker, A., 1998. Annual trace element variations in a Holocene speleothem. Earth and Planetary Science Letters 154, 237-246.

Roques, H., 1862. Considerations theoretiques sur la chemie des carbonates. Ann. Spéléologiques 17 (1-4): 1-41, 241-248, 463-467.

Schimpf, D., Kilian, R., Kronz, A., Simon, K., Spötl, C., Wörner, G., Deininger, M., Mangini, A., 2011. The significance of chemical, isotopic, and detrital components in three coeval stalagmites from the superhumid southernmost Andes (53°S) as high-resolution palaeo-climate proxies. Quaternary Science Reviews 30, 443-459.

Scholz, D., Hoffmann, D.L., 2011. StalAge – An algorithm designed for construction of speleothem age models. Quaternary Geochronology 6, 369-382.

Schwarcz, H.P.a.F., D.C., 1986. Geochronology and isotopic geochemistry of speleothems, In: Fontes, P.F.a.J.C. (Ed.), Handbook of Environmental Isotope Geochemistry. Elsevier, Amsterdam, pp. 271-303.

Sodemann, H., Zubler, E., 2010. Seasonal and inter-annual variability of the moisture sources for Alpine precipitation during 1995-2002. Int J Climatol 30, 947-961.

Spötl, C., Fairchild, I.J., Tooth, A.F., 2005. Cave air control on dripwater geochemistry, Obir Caves (Austria): Implications for speleothem deposition in dynamically ventilated caves. Geochimica Et Cosmochimica Acta 69, 2451-2468.

Spötl, C., Holzkämper, S., Mangini, A., 2007. 31. The last and the penultimate interglacial as recorded by speleothems from a climatically sensitive high-elevation cave site in the alps, In: Frank Sirocko, M.C.M.F.S.G., Thomas, L. (Eds.), Developments in Quaternary Sciences. Elsevier, pp. 471-491.

Tanner, L.H., 2010. Chapter 4 Continental Carbonates as Indicators of Paleoclimate, In: Alonso-Zarza, A.M., Tanner, L.H. (Eds.), Developments in Sedimentology. Elsevier, pp. 179-214.

Tabersky, D., Nishiguchi, K., Utani, K., Ohata, M., Dietiker, R., Fricker, M.B., de Maddalena, I.M., Koch, J., Gunther, D., 2013. Aerosol entrainment and a large-capacity gas exchange device (Q-GED) for laser ablation inductively coupled plasma mass spectrometry in atmospheric pressure air. Journal of Analytical Atomic Spectrometry 28, 831-842.

Treble, P., Shelley, J.M.G., Chappell, J., 2003. Comparison of high resolution sub-annual records of trace elements in a modern (1911-1992) speleothem with instrumental climate data from southwest Australia. Earth and Planetary Science Letters 216, 141-153.

Turgeon, S., Lundberg, J., 2007. Establishing A Speleothem Chronology For Southwestern Oregon, In: Sasowsky, I., Mylroie, J. (Eds.), Studies of Cave Sediments. Springer Netherlands, pp. 273-302.

Vogel, N., Scheidegger, Y., Brennwald, M.S., Fleitmann, D., Figura, S., Wieler, R., Kipfer, R., 2013. Stalagmite water content as a proxy for drip water supply in tropical and subtropical areas. Clim. Past 9, 1-12.

Wanner, H., Rickli, R., Salvisberg, E., Schmutz, C., Schuepp, M., 1997. Global climate change and variability and its influence on Alpine climate - Concepts and observations. Theor Appl Climatol 58, 221-243.

Weber, E., 2004. Etude des mouvements récents dans les karst de Melchsee-Frutt: modélisation 3D et comparaison avec la grotte de Milandre et le réseau des Siebenhengste, Diplom thesis, Neuchatel.

Wildberger, A., Geyh, M.A. & Henning, G. (1992): Datierungsversuche an Tropfsteinen aus dem Hölloch (Zentralschweiz). - Actes du 9e congrès national de spéléologie, Charmey (Suisse), 113-119.

White, W.B., 2007. Paleoclimate records from speleothems in limestone caves, Studies of Cave Sediments: Physical and Chemical Records of Paleoclimate, pp. 135-175.

Zhou, H.Y., Chi, B.Q., Lawrence, M., Zhao, J.X., Yan, J., Greig, A., Feng, Y.X., 2008. High-resolution and precisely dated record of weathering and hydrological dynamics recorded by manganese and rare-earth elements in a stalagmite from Central China. Quaternary Res 69, 438-446.

Zhou, J.Z., Lundstrom, C.C., Fouke, B., Panno, S., Hackley, K., Curry, B., 2005. Geochemistry of speleothem records from southern Illinois: Development of (U-234)/(U-238) as a proxy for paleoprecipitation. Chem Geol 221, 1-20.

CHAPTER 2.

ALPINE CLIMATE VARIABILITY DURING MIS 7 AND MIS 6 AS RECORDED IN GROWTH INTERVALS OF A STALAGMITE FROM ALPSTEIN MTS. (SWISS ALPS)

In collaboration with Tabersky Daniel[1], Günther Detlef [1] ,Cheng Hai[2,3], Edwards Lawrence R.[3], Fleitmann Dominik[4,5]

[1] Department of Chemistry and Applied Biosciences, Laboratory of Inorganic Chemistry, ETH Zürich, Wolfgang-Pauli-Strasse 10, CH-8093 Zürich

[2] Institute of Global Environmental Change, Xi'an Jiaotong University, Xi'an 710049, China

[3] Department of of Geology and Geophysics, University of Minnesota, Minneapolis, Minnesota 55455, USA

[4] Institute of Geological Sciences and Oeschger Centre for Climate Change Research, University of Bern, Baltzerstrasse 1+3, CH-3012 Bern

[5] Department of Archaeology, School of Archaeology, Geography and Environmental Science, University of Reading, Whiteknights, PO Box 227, Reading

2.1. Introduction

Temperature is the key factor controlling landscape evolution and vegetation development in alpine areas (Meyer et al., 2012). It has been shown that speleothems from high alpine caves are one of the rare climate archives that can provide long and continuous records of temperature changes over several glacial and interglacial cycles (Spötl and Mangini, 2010; Luetscher et al., 2015 and references therein). Although many factors may contribute to speleothem deposition, there are two dominant conditions that must be met: i) elevated CO_2 levels above atmospheric values must be generated (generally in the soil zone), and ii) water must be available for recharge (Fairchild and Baker, 2012 and references therein). Both are highly dependent on the climate at the cave site and therefore, major depositional hiatuses represent significant spatial and temporal shifts in environmental and/or climatic conditions in the region (Spötl et al., 2008). More importantly, the timing and the duration of these hiatuses can be precisely characterized within speleothems.

If, during glacial intervals, a glacier body is present at the cave surface, changes in its state from cold- to warm - based glacier is reflected as a new calcite generation, and provides evidence of the relationship of alpine glaciers respons to internal and external climate triggers. To date, the classical approach is to correlate Quaternary Alpine stratigraphy (along with phases of glaciers advance and retreat) with low-latitude and low-altitude oxygen isotope records (e.g. marine sediment records, mainly proxy for global ice volume, Preusser et al., 2011). Independently dated records from this region are essential for our understanding of local and regional geomorphologic and climatic evolution, and will also enable a meaningful correlation of events between different environments and sites.

In the Alpine region, Marine Isotopic Stages (MIS) 7 and 6 are a major topic of scientific interest due to the rare high resolution records covering this time interval (Spötl et al., 2008, Preusser et al., 2005). The goal of this work is to document climatic variability during both these stages by applying a multi-proxy approach on a stalagmite collected from the high alpine Schafsloch Cave. The information preserved in stalagmite MF3 will aid in expanding our knowledge of the environmental and climatic conditions in the region between 130 to 230 ka BP. This new independently-dated terrestrial record can provide further insights into the response of alpine climate and glacier dynamics, with respect to external and internal climate forcing, as well as its regional and hemispheric connections.

2.2. Site and sample description

Schafsloch Cave is located in the Appenzell Alps (47°14’N, 9°23’E, 1890 masl), a mountain range slightly detached from the main alpine body (Fig. 2.1A). The northern Alpine climate is strongly influenced by processes over the Atlantic Ocean and its sea-ice system (Wanner et al., 1997). The Alps are located on the southern side of the extra-tropical westerlies, acting as a border between the Mediterranean and the North Atlantic climatic zones. Climatically, the region has a negligible Mediterranean influence (Sodemann and Zubler, 2009), with moisture sourced in the Mediterranean region accounting for a maximum of 20% of the total moisture budget mainly during the winter months. Mean annual air temperature (MAAT) and precipitation rate between 1961 and 1990 measured at Säntis meteorological station (47°24’N, 9°34’E, 2500 masl) is 2.6 °C and 2200 mm/year, respectively (Fig. 2.1B). In these high alpine conditions, average temperature of the warm months (April to September) is 5.8 °C, and of the cold months (October to March) is -1.0 °C, allowing the presence of snow until late spring. The area is karstified, with alpine grassland and a soil depth of only several centimeters.

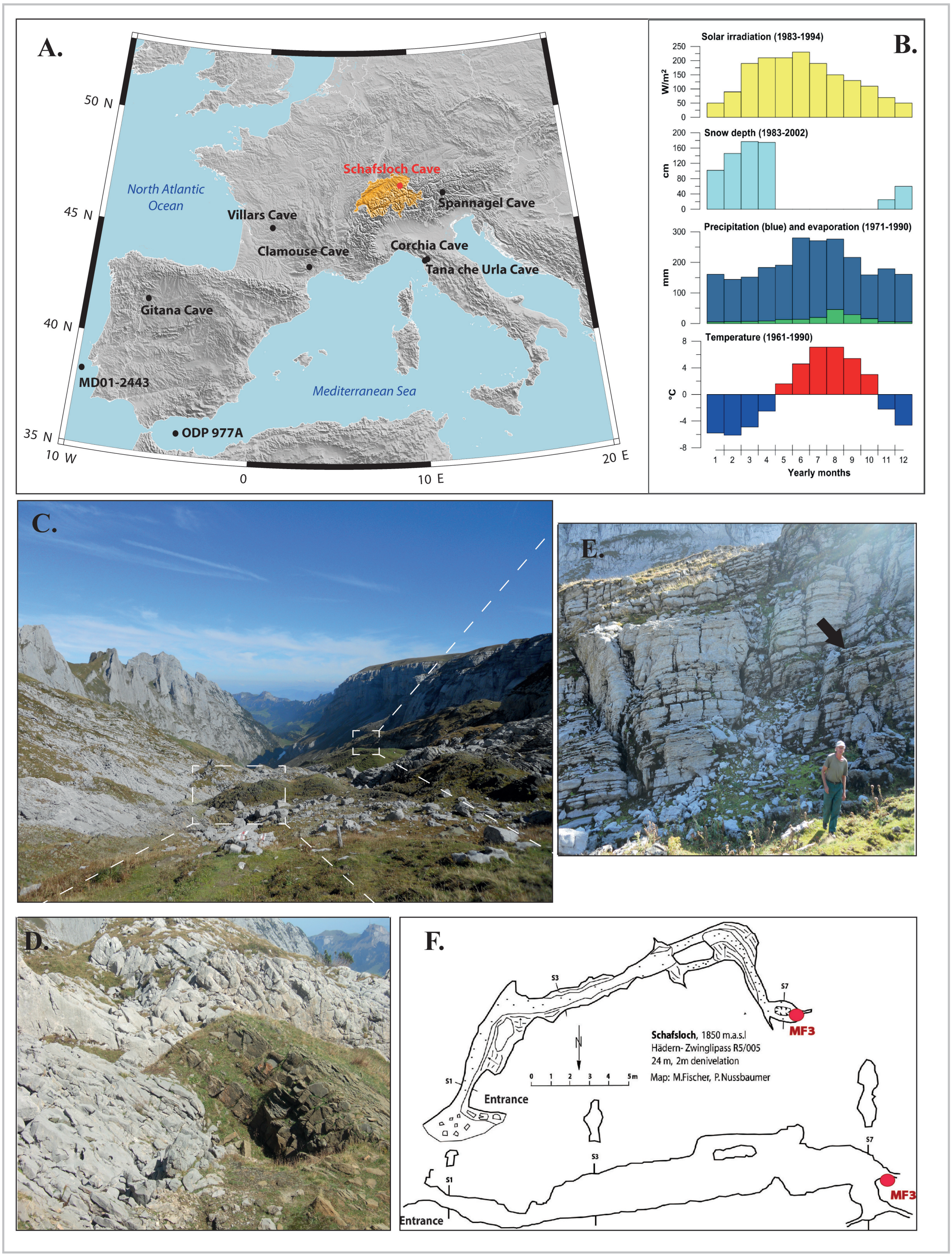

Figure 2.1. ***A.*** *Location of the Schafsloch Cave and the other sites mentioned in the text;* ***B.*** *Meteorological parameters measured at Säntis meteorological station (near Schafsloch Cave);* ***C.*** *View of the Alpstein Mountains and its surface geological formations;* ***D.*** *Garshella Formation outcropping close to the cave site;* ***E.*** *Seewerkalk profile at the entrance of Schafsloch Cave (indicated by the arrow)* ***F.*** *Map of Schafsloch Cave (plan and profile). Red dot indicates the location of the sediment pile where MF3 sample was found remobilized.*

Geologically the Alpstein is formed by a folded succession of Cretaceous sedimentary rocks. Schratten Kalk (Cenomanian-Santonian) is the dominating geological formation in Alpstein, a massive platform light-color carbonate, very rich in fossils. Seewer Kalk (early Barremian-early Aptian) is a well stratified pelagic limestone, with interbedded clay layers. Between Seewer Kalk and Schratten Kalk formations lies the glauconitic sandy-limestone formation of Garschella Formation (Geologischer Atlas der Schweiz, 1982). The steep carbonate relief was modeled and eroded during the last glacial cycle (Marine Isotope Stage 2, MIS 2), when ice reached an elevation of about 2000 m at the study site. Although MIS 6 is considered far more extensive compared to the Last Glaciation (Ehlers et al., 2011), the presence of a glacier during the penultimate glacial was not so far been documented at the site (Preusser et al., 2011).

The accessible part of Schafsloch Cave presently developed in the Seewer Kalk formation, and the bedrock above the cave is formed exclusively by this type of rock. Garschella Formation outcrops several tens of meters from the cave entrance (Fig. 2.1C-E). Schafsloch Cave developed 20 m below the surface, and the total length of the cave is not known, as after 25 m the access is blocked by a 2 m pile of sediments (Fig. 2.1F). Temperature measurement 25 m from the cave entrance was 6.5 °C in September 2011. This temperature is considerably higher than the temperature expected in the (unexplored) deeper galleries, as mean annual temperature at the site is 2.6°C and the temperature in Swiss caves located at similar altitudes ranges between 2.5 - 4.0 °C (Luetscher et al., 2011, 2015). Conditions in the cave are almost dry, and no actively growing speleothems are present. Similar conditions are reported in other caves of this area (M. Fisher, pers. comm.) although the large number of inactive speleothems (some of them older than 500 ka) indicates that deposition was more intensive in the past.

Sample MF3, subject of this study, was recovered from the upper part of the sediment pile, therefore remobilized from its original growth place. The transport distance was short, as proved by the small surface alteration of the sample. Transport direction of the sample, shown by the pebbles imbrication in the sediment pile and scallops on the cave wall, was toward the cave entrance. Stalagmite MF3 is 215 mm along the vertical growth axis, with a basal diameter of 80 mm (Fig. 2.2). It is composed of dense and translucent columnar-fibrous calcite. Localized dissolution porosity and recrystallization is observed between 79 - 100 mm depth in the sample. No macroscopic banding is observed.

2.3. Analitical Methodes

The stalagmite was cut longitudinally and polished. The top 80 mm of the sample were studied petrographically in thin sections by using an optical transmission microscope (standard transparent and UV light). The fabric of calcite and its organic matter content will help to better understand the environmental and cave conditions in which the sample formed. More importantly, an effort was made to document the presence and lateral extent of discontinuous petrographic boundaries (potential growth interruption) in the sample.

The stalagmite was dated using the ^{230}Th/^{234}U disequilibrium method. Age determination was performed on 70-100 mg calcite powder drilled along particular growth horizons in the sample. The chemical procedures of Edwards et al. (1987) were used for U/Th separation and isotopic analysis was performed on a multi-collector inductively coupled plasma mass spectrometer (MC-ICP-MS, Thermo-Finnigan-Neptune) at the Department of Earth Sciences, University of Minnesota. Details of the analytical procedure and U-series activity ratios are reported in Cheng et al. (2013). The U-series

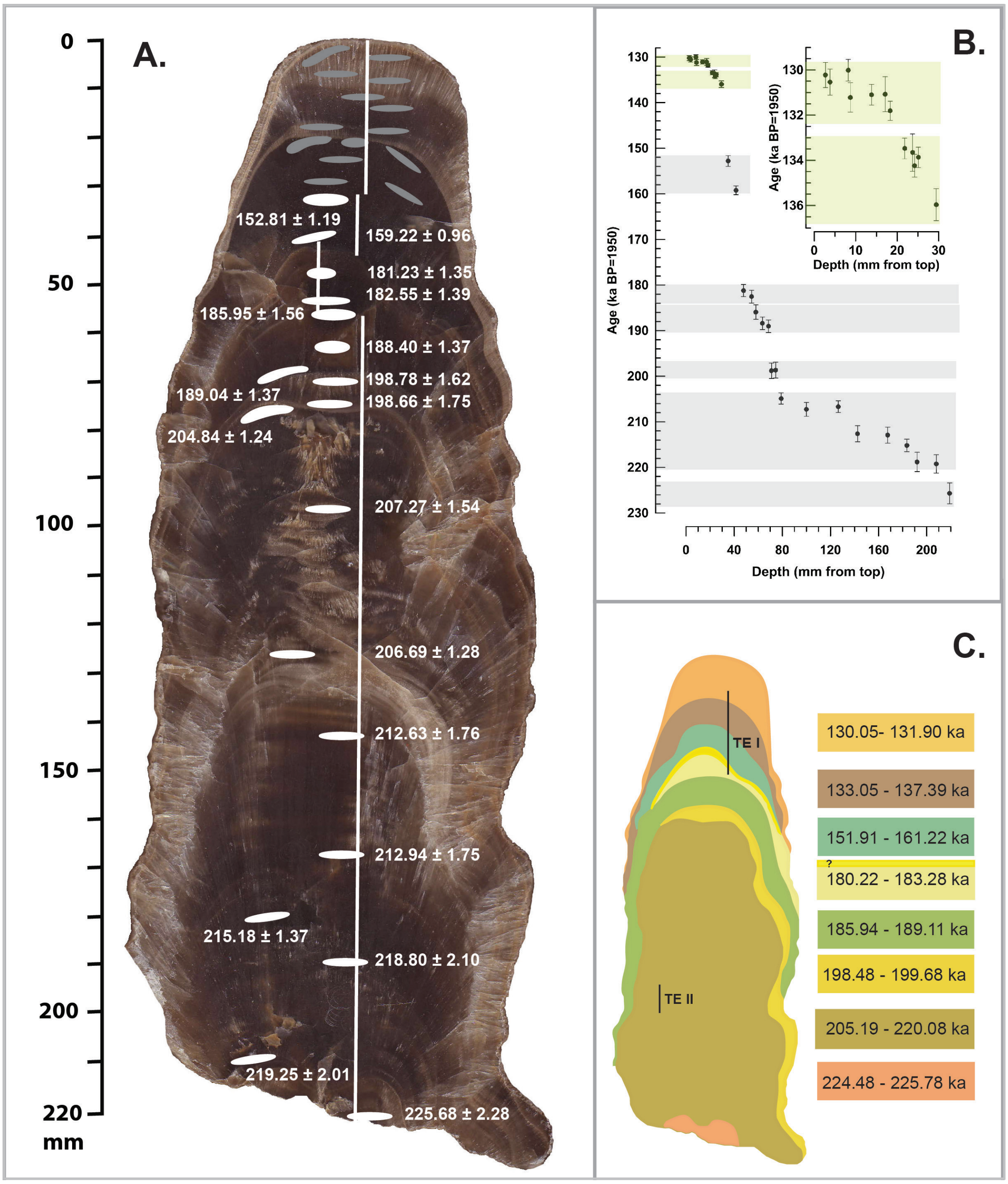

***Figure 2.2. A.** Polished section of MF3 showing micromilling paths (white lines) for isotopic analysis, sampling locations for U/Th calcite dating (white dots) and dating results; **B.** Age-depth plot of the sample MF3 (dating results as solid circles with errors); **C.** Growing intervals identified in sample MF3 and paths location for trace elements analysis (TE I and TE II).*

dating results are summarized in Table 2.1. Ages are reported as thousand years (ka) before AD1950. All ages are in chronological order within analytical errors. The analytical 2 σ error is in the range of 0.3 to 1.0 %, due to low detrital contamination and high ^{238}U content of the sample (783 to 9855 ppb).

For stable isotope analysis a total of 735 samples were micromilled continuously using a 0.8 mm diameter drill, following the growth axis of the sample (Fig. 2.2A). The sampling resolution varies between 0.1 and 0.5 mm. Modern calcite was sampled from the top of a stalactite, collected in the nearby Alpeel Cave (Alpstein Mts., 45 m length, 1774 m asl). Oxygen and carbon isotopic analysis ($\delta^{18}O$ and $\delta^{13}C$) were performed on a Finnigan Delta V Advantage mass spectrometer equipped with an automated carbonate preparation system (Gas Bench II) at the Institute of Geological Sciences, University of Bern, Switzerland. All $\delta^{18}O$ and $\delta^{13}C$ values are calibrated and reported relative to the Vienna Peedee Belemnite (VPDB) standard. Analytical errors for $\delta^{18}O$ and $\delta^{13}C$ are 0.07 ‰, respectively 0.06 ‰ VPDB (1 σ).

Trace element analyses were carried out continuously at a resolution of 13 μm between 17.0-58.3 mm and 151.0 – 152.0 mm from the top of the sample by using a 193 nm ArF excimer laser (GeoLas Pro, Lambda Physik) coupled to a quadrupole ICP-MS (ELAN 6100 DRC+, Perkin Elmer). A detailed description of the experimental setup has already been given in Kovacs et al. (2010) and optimized as described in Tabersky et al. (2013). Two cleaning line scans were applied to remove potential contaminations on the sample surface and only one third was used for quantification. NIST SRM 610 was used as external standard and values were normalized to 100% sum of oxides. Data evaluation was carried out in STALQUANT, an in-house Phyton-based software program to reduce large amounts of point-by-point quantification data (Fricker, 2012).

2.4. Results

2.4.1. Growth intervals in MF3 sample

It is common for high alpine stalagmites to present multiple growth-discontinuities, as their growth is very sensible to climatic and environmental changes above the cave (Spötl et al., 2007; Holzkämper et al, 2005).

Major discontinuities are associated with major environmental changes above the cave, although processes related to the cave environment and epikarst could account for minor discontinuities (rerouting of groundwater flow, blocking of the fissure feeding the stalagmite with drip water, temporarily submerging or burring of the sample (Spötl et al., 2007). Based on 30 ^{230}Th ages and petrographic observations, a robust age model was built for MF3 sample. Seven major hiatuses were identified in the sample, at 20.5, 33.75, 44.5, 49.0, 59.5, 71.0, 77.5, 214.5 mm depth. Macroscopic, under UV light, the hiatuses at 20.5, 77.5, and 214.5 cm depth show a distinctive intensity in photoluminescence.

Eight growth intervals were identified, and numbered from I to VIII in Fig. 2.3. The location of hiatuses is marked by gray lines, and other potential hiatuses at 49 and 137 mm depth (later discussed), are marked by gray dashed lines. Growth interval IV (GI_{IV}) was divided in two sub-intervals, noted GI_{IVa} and GI_{IVb}, as discussed later. Note that during GI_{IV} calcite precipitation was much more localized compared to the other GI, calcite built mainly laterally with respect to main the growth axis of the sample.

For each growth interval (GI) an age model was constructed. The StalAge algorithm (Scholz and Hoffmann, 2011) was used for GI_{I}, GI_{II} and GI_{VII}, and linear interpolation between central ages for G_{III}, G_{IV} and G_{V}. Special consideration must be given when referring to GI_{IVa}, GI_{VI} and GI_{VIII}. In GI_{VI}, please note that in the case of an age reversal between two similar ages, we used the most precise age and an average growth rate of 0.01 mm/year (averaging growth rates calculated for GI_{V} and GI_{VII}). This approach was also used for GI_{VIII}, where only one age was available. Although we observed the presence of a corrosive surface at 49.25 mm depth (just above G_{IV}), the temporal extension of a series of irregular detrital-rich laminae overlying this corrosive surface between 44.25 and 49.25 mm (just below G_{III}) could not be determined. This interval was integrated in the age model as part of the growth interval GI_{IV}, and referred to as GI_{IVa}.

The age-depth model for MF3 is shown in Fig. 2.3, and a summary for each growth interval is presented in Table 2.3. As expected for an alpine sample, average growth rate is very slow, around 6 mm/ka for the entire sample, with a minimal growth rate during GI_{III} (1.1 mm/ka) and a maximum during GI_{I} (6.3 mm/ka).

GI	Distance from top (mm)	Age interval (ka BP)	Mean error (ka)	Growth rate (mm/year)
I	0.00-20.50	130.05-131.90	0.43	0.0902
II	20.6-33.75	133.05-137.39	0.54	0.0032
III	34.00-44.50	151.91-161.22	1.05	0.0011
IVa	44.75-49.00	180.22-181.15	1.36	0.0048
IVb	49.25-59.5	181.20-183.28	1.37	0.0048
V	60.00-71.00	185.94-189.11	1.42	0.0050
VI	71.50-77.50	198.48-199.68	1.68	0.0050
VII	78.00-214.50	205.19-220.08	1.38	0.0163
VIII	215.00-221.5	224.48-225.78	2.28	0.0050

Table 2.3. *Summary of growth intervals (GI) identified in MF3.*

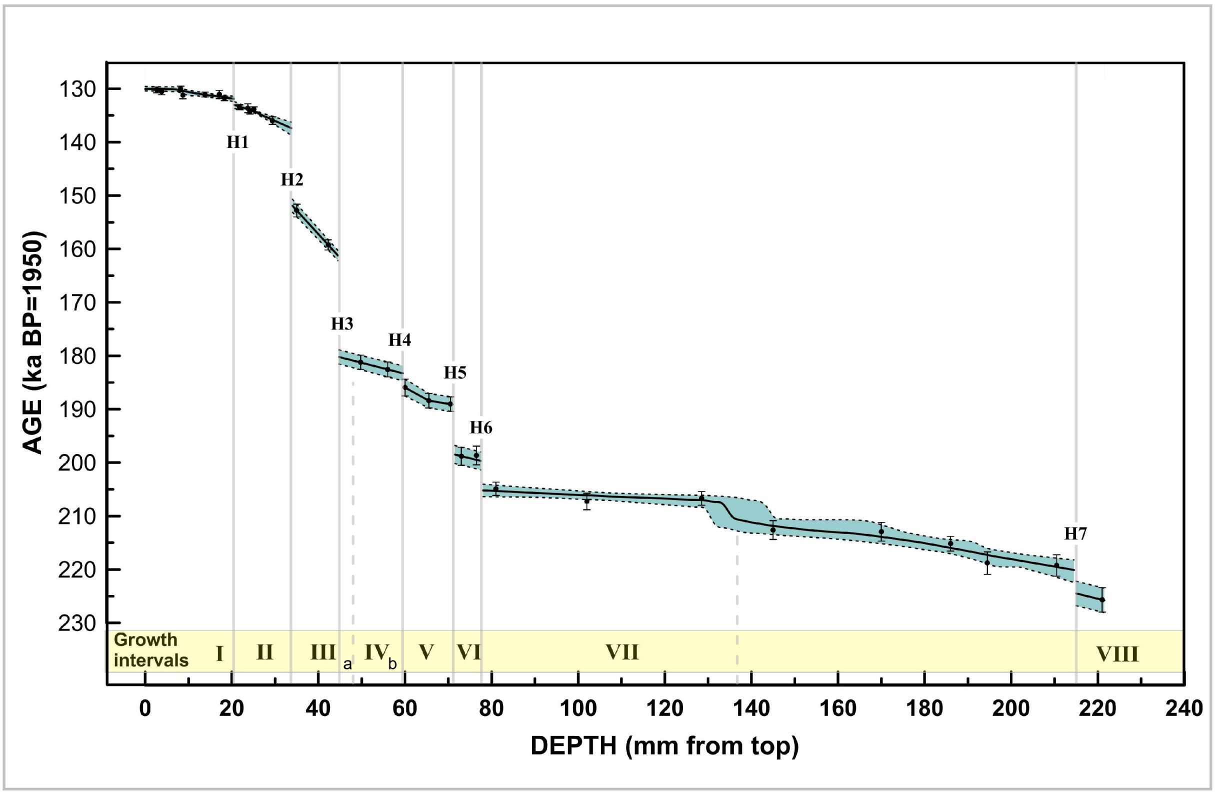

Figure 2.3. *Depth-age model of sample MF3. The outer shaded zones define the 95% uncertainties. Gray lines indicate hiatuses in the sample, and gray dotted lines represent possible hiatuses in the sample.*

Table 2.1. *^{230} Th age data for stalagmite MF3 (for ages from the top 35 mm of the sample, please refer to Table 3.1)*

Sample Number	**Depth (mm)**	**^{238}U (ppb)**		**^{232}Th (ppt)**		**^{230}Th / ^{232}Th (atomic x10^{-6})**		**δ ^{234}U* (measured)**		**^{230}Th / ^{238}U (activity)**		**^{230}Th Age (ka) (uncorrected)**		**δ ^{234}U$_{Initial}$** (corr.)**		**^{230}Th Age (ka BP)*** (corrected)**	
MF3-25	35	4950	±13	558	±11	124687	±2524	110.5	±1.7	0.8530	±0.0028	152.871	1.194	170	±3	**152.805**	**1.194**
MF3-13	41.5	3636.0	±5.1	2747	±55	18548	±374	89.3	±2.0	0.8500	±0.0014	159.305	0.958	140	±3	**159.224**	**0.958**
MF3-14	47.75	4814.5	±8.4	5452	±110	13212	±266	98.3	±2.1	0.9075	±0.0018	181.315	1.336	164	±3	**181.225**	**1.335**
MF3-15	54.5	5581.3	±9.7	901	±18	89704	±1835	66.0	±2.1	0.8781	±0.0017	182.617	1.393	111	±4	**182.552**	**1.393**
MF3-24	58	4288	±10	524	±11	120163	±2434	71.7	±1.4	0.8902	±0.0026	186.012	1.577	121	±2	**185.945**	**1.577**
MF3-16	63.5	5447.4	±8.6	3647	±73	21613	±434	54.6	±1.9	0.8775	±0.0015	188.482	1.367	93	±3	**188.403**	**1.367**
MF3-5	68.5	4444	±9	4193	±84	15568	±313	67	±1	0.8907	±0.0020	189.129	1.368	114	±2	**189.044**	**1.368**
MF3-17	71	891.2	±1.0	3831	±77	3688	±74	118.4	±2.4	0.9614	±0.0017	198.964	1.680	208	±4	**198.799**	**1.680**
MF3-18	74.5	783.0	±0.8	6584	±132	1907	±38	129.4	±2.4	0.9727	±0.0019	198.917	1.750	227	±4	**198.656**	**1.752**
MF3-6	79	1429	±2	4074	±82	5871	±118	159	±1	1.0151	±0.0017	205.019	1.242	284	±3	**204.893**	**1.242**
MF3-19	100	4135.0	±5.8	389	±9	172190	±3773	125.1	±1.9	0.9828	±0.0016	207.332	1.540	225	±4	**207.268**	**1.540**
MF3-9	126.5	2650	±4	2603	±52	16416	±329	121	±1	0.9777	±0.0017	206.775	1.283	217	±2	**206.691**	**1.283**
MF3-20	142.5	3841.3	±5.4	621	±14	99736	±2187	112.1	±2.1	0.9778	±0.0016	212.690	1.759	204	±4	**212.625**	**1.759**
MF3-21	167.5	4273.8	±6.5	580	±13	122260	±2638	138.3	±2.1	1.0063	±0.0018	213.002	1.752	252	±4	**212.937**	**1.752**
MF3-7	183.5	2676	±4	3019	±61	14747	±296	137	±1	1.0090	±0.0018	215.266	1.375	252	±2	**215.180**	**1.375**
MF3-22	192	1355.3	±1.8	565	±12	41336	±880	165.0	±2.7	1.0445	±0.0017	218.872	2.103	306	±7	**218.801**	**2.103**
MF3-8	208	3951	±10	5011	±101	13530	±272	161	±2	1.0407	±0.0027	219.337	2.007	298	±3	**219.248**	**2.007**
MF3-23	219	8755.5	±17.5	13314	±267	10378	±208	75.6	±2.0	0.9571	±0.0021	225.784	2.285	143	±4	**225.684**	**2.284**

U decay constants: λ_{238} = 1.55125x10^{-10} (Jaffey et al., 1971) and l$_{234}$ = 2.82206x10^{-6} (Cheng et al., 2013). Th decay constant: λ_{230} = 9.1705x10^{-6} (Cheng et al., 2013).

* δ^{234}U = ([^{234}U/^{238}U]$_{activity}$ – 1)x1000. ** δ ^{234}U$_{initial}$ was calculated based on ^{230}Th age (T), i.e., δ^{234}U$_{initial}$ = δ^{234}U$_{measured}$ x e^{l234xT}.

Corrected ^{230}Th ages assume the initial ^{230}Th/^{232}Th atomic ratio of 4.4 ±2.2 x10^{-6}. Those are the values for a material at secular equilibrium, with the bulk earth ^{232}Th/^{238}U value of 3.8. The errors are arbitrarily assumed to be 50%.

***B.P. stands for “Before Present” where the “Present” is defined as the year 1950 A.D.

Regarding the reliability of the ^{230}Th ages, large analytical errors can be ruled out, as age measurements were carried out over several dating campaigns, with consistent chrono-stratigraphic results. Furthermore, two overview samples were additionally prepared and measured in the laboratories of the Institute of Geological Sciences in Bern, with consistent results. That being said, based on the literature (e.g. Wainer et al., 2011 and references therein) most commonly reported possibilities for an "age alteration" are given by the U leaching from the sample (open-system behavior), and/or detrital contamination of the sample. Both possibilities will lead to an overestimation of the ^{230}Th ages. We observed no major variations within short intervals in the U concentration that could indicate leaching or contamination. Highest U concentration oscillations are observed during GI_{IVb} (5 to 15 mg/kg), and here no powder was sampled for age determination. Mean Th concentrations are consistent within all GI (between 0.28 and 0.33 mg/kg). Furthermore, in the areas of the stalagmite where calcite powder was collected for ^{230}Th dating analysis we observed no evidence of large (connected) pores to generate new percolation paths for water, to dissolve or even precipitate new calcite generation. Based on these observations, we conclude that no internal heterogeneities could support a potential "open-system" behavior with respect to U in our sample.

Speleothem deposition between 130.1 ± 0.4 to 131.9 ± 0.6 ka BP, 133.1 ± 0.7 to 137.4 ± 1.4 ka BP, 151.9 ± 1.2 to 161.2 ± 1.0 ka BP, 180.2 ± 1.3 to 183.3 ± 1.4 ka BP, 185.9 ± 1.6 to 189.1 ± 1.4 ka BP, 198.5 ± 1.7 to 199.7 ± 1.7 ka BP, 205.2 ± 1.2 to 220.1 ± 2.3 ka BP, 224.5 ± 2.3 to 225.8 ± 2.3 ka BP span intervals during the MIS 7, MIS 6 and transition into MIS 5 (known as Termination II, T-II). This provides a first-order indication of past climatic conditions, as minimum conditions for calcite to precipitate in caves are i) the presence of drip water and ii) a (seasonal) cave temperature above 0°C. In MF3 sample, calcite deposition after 137.4 ka BP (largely discussed in Chapter 3) and between 230-185 ka BP support evidences of calcite precipitation in European caves from high and low altitudes (Holzkämpfer et al., 2005 and references therein; Wainer et al., 2011). Between 185 -137.4 ka BP similar favorable conditions in caves from high altitudes are not reported in literature, largely as this time interval falls well within MIS 6 (based on SPECMAP timescale, Imbrie et al., 1984). It is difficult to reconcile with the idea of favorable conditions for calcite to precipitate (temperatures above freezing point, and therefore presence of liquid water) in this high altitude cave at a time of regional atmospheric cooling and glacier expansion. As most of the speleothems from low-altitude cave sites commonly show slow or no growth during cold climatic periods (Hodge et al, 2008), in the case of a high-altitude speleothem we could consider the presence of a glacier above Schafsloch Cave, allowing a (slow) calcite precipitation during glacial and severe cold climate conditions (stadials). The presence of a warm based glacier can maintain the cave temperature above freezing point and provide water, although climatic conditions above the cave are below the freezing point. Similar settings are extensively described for calcite precipitation in Spannagel and Castleguard Caves (Atkinson 1983, Spötl et al., 2007). A warm-based glacier of 30 m thickness will offer thermal protection and keep host rock, and therefore cave temperature, above freezing point, contrasting with atmospheric temperatures reaching down to -8°C (Spötl and Mangini, 2008). Following this line of evidences, rather than claiming ice-free conditions above the cave during MIS 6, we propose that calcite formed as a direct result of a warm-based glacier presence above our cave (Fig. 2.4). Its basal meltwater would feed the karst aquifer, and allow a slow formation of calcite in the cave. The lack of carbon derived from soil can be replaced by: i) very slow precipiattion as a result of warming of water after entering the cave or evaporation of drip water (Atkinson 1983 and references therein) , or ii) oxidation of pyrite (Spötl et al., 2007) present in the geological succession from Alpstein Mountains.

We emphasize that formation of a new calcite generation in the cave during the times of glacier presence at the surface is related to changes in the glacier state (from cold- to warm-based), as a direct result of positive shifts in the warm season temperature at the surface.

Isotopic and trace element composition of the sample, as discussed below, allows further constrains of the processes that governed the formation of MF3 during individual growth intervals.

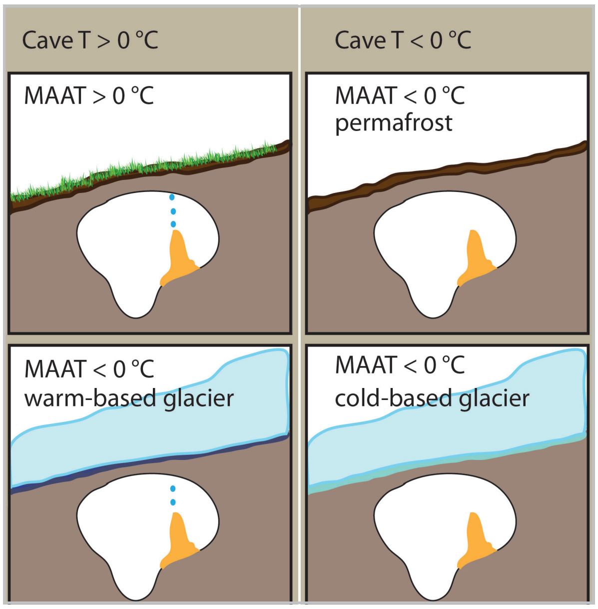

Figure 2.4. *Sketch presenting favorable and unfavorable conditions for calcite to precipitate in a high alpine environment*

2.4.2. OXYGEN AND CARBON ISOTOPE RECORDS

2.4.2.1. DISEQUILIBRIUM ISOTOPIC FRACTIONATION AND "SOURCE EFFECT" CORRECTION

The isotopic signals could be affected by disequilibrium isotopes fractionation. The main controlling mechanisms are linked to changes in i) prior-calcite precipitation in the epikarst (directly related with changes in the length of flow path, CO_2 degassing, low water availability (Spötl et al., 2005; Mattey et al., 2010; Wiedner et al., 2008; Polag et al., 2010; Scholtz et al., 2009) and ii) rapid CO_2 degassing and calcite precipitation at the stalagmite surface (Baker et al., 1997; Daeron et al., 2011, Mickler et al., 2004). As our sample lacks macroscopic lamination, this prevented a signal reliability test using the classical Hendy test method (Hendy, 1971). As a strong correlation between $\delta^{18}O$ and $\delta^{13}C$ could well indicate kinetic effects in the vadose zone and/or surface of the sample, r^2 was calculated for each GI, as presented in Fig. 2.5. Cross plotting of $\delta^{18}O$ and $\delta^{13}C$ values of stalagmite MF3 exhibit overall a medium correlation (r^2=0.39, with a slope of - 0.25). However, correlation of individual GI within the stalagmite vary from virtually absent (r^2=0.01) during GI_{IV} and GI_{VIII} to high (r^2=0.64) in the GI_{II} and GI_{III}. This could indicate a deterioration of the isotopic signal reliability in the latter ones. Nevertheless, if we compare the $\delta^{18}O$ from MF3, both during intervals of weak and strong kinetic control (e.g. GI_I, GI_{II}, GI_{VI} and GI_{VII}) with isotopic data from coeval samples collected from Spannagel and/or Corchia Cave (Spötl et al., 2007; Drysdale et al., 2009; Couchoud et al., 2011) we observe similar isotopic patterns, which give us confidence that the isotopic signal in MF3 is a reliable proxy.

$\delta^{18}O$ of alpine speleothems is primarily controlled by variations in $\delta^{18}O$ of drip water and therefore surface precipitation, whereas $\delta^{18}O$ of precipitation is related to source area of the moisture and local air temperature, global ice volume effect, seasonality of rainfall etc. In order to better compare the effect of

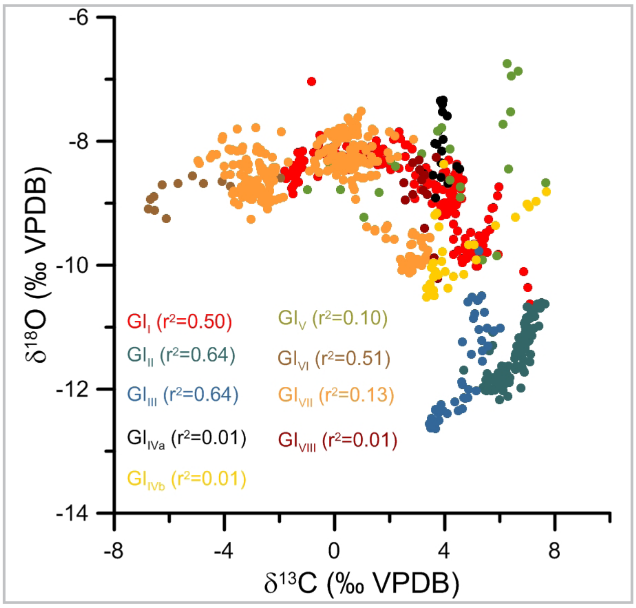

Figure 2.4. Correlation plot of δ^{18}O and δ^{13}C in sample MF3 during different growth intervals

local changes in the δ^{18}O signal (e.g. air temperature during individual growth episodes, changes in the water source) we corrected the measured δ^{18}O for isotopic variations in the moisture source area (North Atlantic Ocean at our cave site). Between 230 and 130 ka BP, episodes of ice cap growth and melt down accounted for changes in relative sea level (RSL) ranging from -99 m to +13 m (Rohling et al., 2009). Therefore, changes in δ^{18}O of North Atlantic Ocean seawater will alone justify 0.3 to 0.8 ‰ VPDB variation in the MF3 δ^{18}O signal (we considered a change of 0.008 ± 0.002 ‰ VPDB per meter of sea level drop, Duplessy et al., 2007). This first order approximation uses the assumption that there was no major shift of the Atlantic vapor source compared to present. A summary of the mean δ^{18}O measured (δ^{18}O), δ^{18}O correction applied and of the final corrected values ($\delta^{18}O_{corr}$) is presented in Table 2.4.

	MEAN			
GI	**δ^{18}O (‰VPDB)**	**RSL (m)**	**δ^{18}O correction**	**$\delta^{18}O_{corr}$ (‰VPDB)**
I	-8.63	3.29	0.03	-8.61
II	-11.41	-59.65	-0.48	-11.89
III	-11.72	-89.19	-0.71	-12.43
IVa	-9.19	-78.82	-0.63	-9.82
IVb	-9.87	-78.76	-0.63	-10.50
V	-8.33	-64.82	-0.52	-8.85
VI	-8.78	-23.97	-0.19	-8.97
VII	-8.60	-40.58	-0.32	-8.92
VIII	-8.87	-72.96	-0.58	-9.45

Table 2.4. *Mean isotopic correction applied to the original isotopic composition of sample MF3 in order to correct for glacial-interglacial changes (source effect) in the North Atlantic Ocean. For details please see text.*

2.4.2.2. Stable isotopic signal interpretation

The oxygen and carbon stable isotopic composition, as well as the average temporal resolution of micromilled subsamples for isotopic analysis varies substantially along and/or within the growth intervals of the sample (Table 2.5 and Fig. 2.6). Overall, the isotopic values in stalagmite MF3 vary between -13.41 ‰ to -6.96 ‰ VPDB for $\delta^{18}O_{corr}$ and from – 6.77 to 7.68 ‰ VPDB for δ^{13}C. For comparison, in recent deposited calcite (Alpeel Cave, Alpstein Mts.) -7.6 ‰ VPDB for δ^{18}O and - 0.4‰ VPDB for δ^{13}C were measured (dashed lines in Fig. 2.6).

	Age interval	**Temp. resolution**	δ^{13}C (‰VPDB)			$\delta^{18}O_{corr}$ (‰VPDB)		
GI	(ka BP)	(ka)	MEAN	MIN	MAX	MEAN	MIN	MAX
I	130.05-131.90	0.007	1.90	-1.81	7.32	-8.61	-10.76	-6.96
II	133.05-137.39	0.168	6.53	4.68	7.65	-11.89	-12.80	-10.73
III	151.91-161.22	0.222	4.57	3.44	6.02	-12.43	-13.41	-10.34
IVa	180.22-181.15	0.062	4.26	3.24	4.55	-9.82	-9.51	-8.03
IVb	181.20-183.28	0.070	4.51	3.33	7.68	-10.50	-11.09	-9.06
V	185.94-189.11	0.144	3.98	-0.99	7.68	-8.85	-10.48	-7.26
VI	198.48-199.68	0.097	-5.20	-6.77	-1.95	-8.97	-9.42	-8.47
VII	205.19-220.08	0.055	-0.43	-4.97	3.46	-8.92	-10.63	-7.90
VIII	224.48-225.78	0.100	3.16	2.52	3.73	-9.45	-10.82	-8.84

Table 2.5. *Temporal resolution of samples and overview of stable isotopic composition during each growth interval in MF3.*

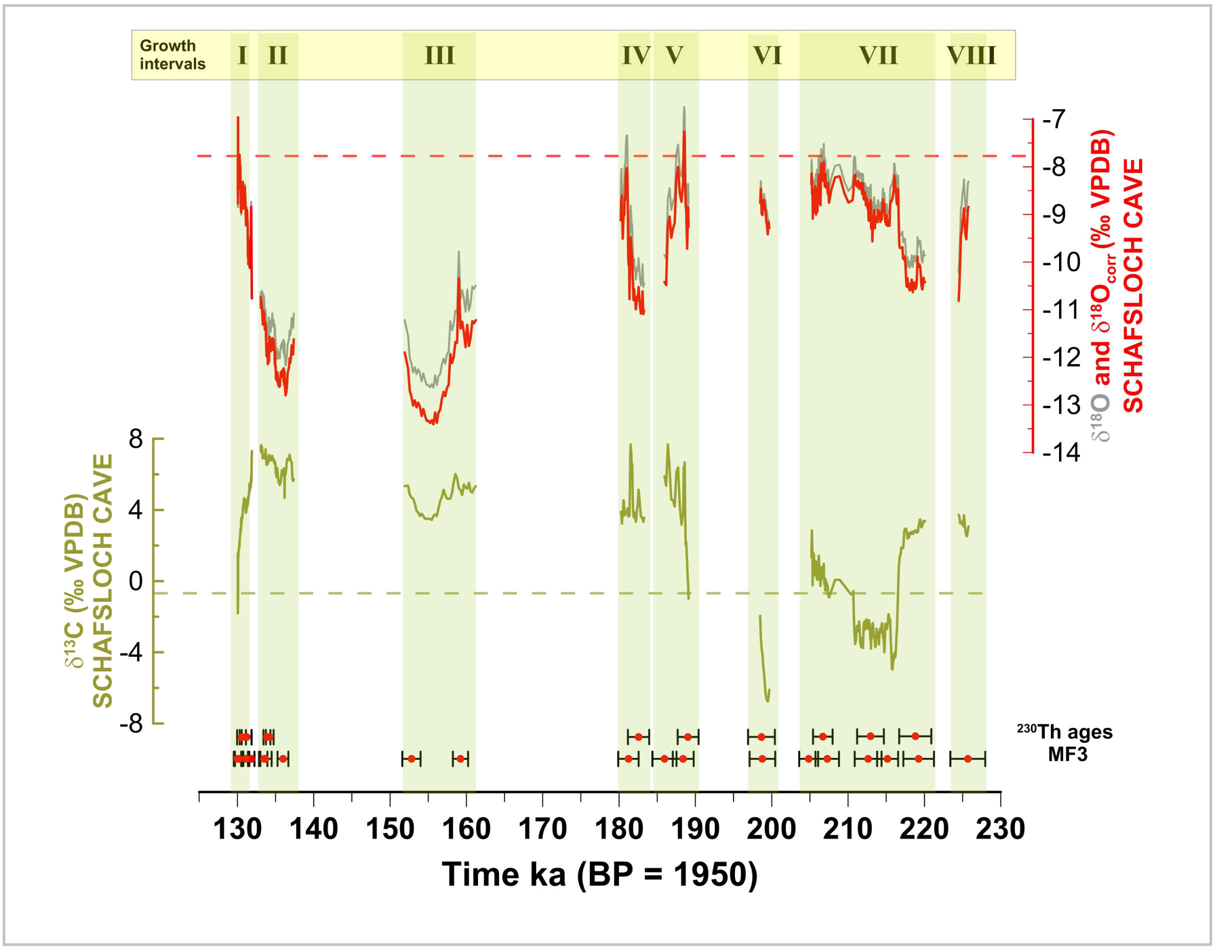

Figure 2.6. *δ^{18}O and δ^{13}C time series for MF3. Green bars indicate growth intervals in the sample.*

Warm (interglacial/interstadial) conditions will be reflected in positive $\delta^{18}O$ and cold (glacial/stadial) phases in negative $\delta^{18}O$, consistent with the relationship between isotopic composition of precipitation and temperature in temperate continental settings (McDermott 2004; Lachniet et al., 2009; Spötl and Mangini, 2007). At our cave site, the precipitation $\delta^{18}O$-temperature relation ($d\delta^{18}O/dT$) is around 0.7‰/°C (Schürch et al., 2003). Bearing in mind the temperature-dependent fraction of $\delta^{18}O$ during calcite precipitation (~ 0.17 ‰/°C; Tremaine et al., 2011), a positive temperature shift of 1°C will translate roughly into a 0.53 ‰ change in the $\delta^{18}O$ of MF3. Having these values as a guideline, the $d\delta^{18}O/dT$ relationship can be used to support the presence of a glacier above our cave during MIS 6. $\delta^{18}O_{corr}$ values from GI_{II} and GI_{III}, lower by 4.5‰ compared to modern $\delta^{18}O$ values, could therefore translate into changes of up to 8°C in the mean (seasonal) temperature at the cave surface. Present-day mean annual temperature above Schafsloch Cave is 2.6°C, and warm season temperature (April-September) is 5.8°C. Although a drop of 8°C in temperature is a first-order temperature approximation, under these conditions most probably permafrost formation will occur, and stop calcite formation in the cave. However, calcite precipitated in Schafsloch Cave, strongly supports the presence of a warm-based glacier body above our cave at least during the GI_{II} and GI_{III}.

Although not a direct temperature proxy, $\delta^{13}C$ values of speleothem calcite are primarily influenced by the type of vegetation and microbial processes in the soil zone. An increase in soil biogenic productivity (plant root respiration and microbial activity in the soil) will result in low $\delta^{13}C$ values. Dry and cold climatic conditions will have the opposite effect, and may be biased to a more bedrock and atmospheric CO_2 influence (McDermott, 2004; Spötl et al., 2005; Rudzka et al., 2011). In an alpine region, reduced soil thickness and nearly vegetation free conditions above the caves can be expected. This low, or even negligible, input of soil-derived organic carbon into the drip water, combined with increased kinetically controlled fractionation (degassing) could induce $\delta^{13}C$ as heavy as + 6‰ VPDB (Spötl et al., 2004). An overview of the $\delta^{13}C$ values recorded over the individual growth intervals in MF3 is presented in Table 2.5.

Mean $\delta^{13}C$ values range from to 6.5 ‰ (GI_{II}) to -5.2 ‰ (GI_{IV}), and indicate significant environmental changes above the cave during the individual GI periods. In the $\delta^{13}C$ composition of MF3, two major differences are observed between the calcite precipitated under warm-climate conditions and presumably subglacial conditions: the first show mean $\delta^{13}C$ values lighter than + 4‰ VPDB, while the latter group show mean $\delta^{13}C$ values heavier than + 4‰ VPDB. Positive $\delta^{13}C$ values are attributed to alpine vegetation and soil developing in the area as a direct result of favorable climate-induced conditions. High $\delta^{13}C$ are attributed to the lack of soil- derived C input into the subsurface (vegetation and soil free conditions), and locally, kinetically induced fractionation plays a significant role (as discussed in sub-chapter 4.2.1).

Based on the measured $\delta^{18}O$ and $\delta^{13}C$ values in MF3, and considering similar isotopic patterns described by Spötl et al. (2007) in speleothems from the high altitude Spannagel Cave (2200-2500 m a.s.l., Zillertal Alps, Austria), we identified the following climatic and environmental scenarios for the individual growth intervals:

- GI_{I}, GI_{VI}, and GI_{VII} show high $\delta^{18}O_{corr}$ (average ranging from -8.96 to -8.61 ‰) and low $\delta^{13}C$ (average ranging from -5.20 to 1.9 ‰), suggesting warm interglacial climate, with soil and alpine vegetation developing above the cave.
- GI_{IV}, GI_{V}, and GI_{VIII} show relatively high $\delta^{18}O_{corr}$ (average ranging from -10.5 to -9.45 ‰) and high $\delta^{13}C$ (average ranging from 3.16 to 4.51 ‰), and exhibit the lowest correlation coefficient (r^2=0.01), suggesting cool interglacial or interstadial climate, most probably without soil cover above the cave.

- GI_{II} and GI_{III} show low $\delta^{18}O_{corr}$ (average ranging from -11.89 to -12.43 ‰) and high $\delta^{13}C$ (average ranging from 4.57 to 6.53 ‰) and exhibit a highest correlation coefficient (r^2=0.64), characteristic of a cold stadial climate, a glacier above the cave and limited water availability.

One of the questions is if $\delta^{18}O$ represents a mean annual temperature proxy or is biased towards one of the seasons. For the interglacial and deglaciation intervals, we speculate a mixing between precipitation originating from both seasons. Using present day conditions as a reference, snow cover persists until late spring and its melting will feed the aquifer together with the warm season precipitation and snow meltwater (which will be enriched in $\delta^{18}O$ due to evaporation and sublimation). When the aquifer was fed by a glacier body (glacial and/or interstadial intervals), melting (if any) occurred during the warm season. The isotopic composition of the meltwater feeding the aquifer could depend on the i) degree of water mixing that originated from different parts of the glacier, ii) turnover time of the ice (could be several thousand years, Spötl et al., 2008), iii) dominant season of snowfall and glacier accumulation over different time intervals and iv) changes in the moisture source and moisture path. For the present study time of interest, we are not able to address these issues. Nevertheless, although it is more difficult to interpret these $\delta^{18}O$ depleted values in terms of absolute temperatures, a clear first-order structure of the isotopic profile gives valuable indications on the temperature evolution at the surface at a centennial time-scale, as well as the contribution of glacier or precipitation water into the karst aquifer (Fig. 2.6).

2.4.3. Organic matter and trace elements concentration

2.4.3.1. Organic matter concentration

At a time of ice-free conditions above Schafsloch cave, climate-controlled changes in soil type, vegetation and biological activity can be traced by changes in the organic matter (OM) in stalagmites (Baker et al., 1996; Baker and Genty, 1999; Perrette et al., 2005; Blyth et al., 2008 and references therein; Linge et al., 2009). From the overlying soils, organic matter is transported as colloids (Fairchild and Treble 2009) by percolating meteoric water from which the speleothems are precipitated. It is located between crystals or within small pores in the crystal structure (Ramseyer at al. 1997) and can be observed as photoluminescence when exposed to UV light (Shopov, 2004). The main organic matter molecules present in speleothems are humic and fulvic acids, with the humic acid (originating mostly from soil) displaying a higher intensity of photoluminescence (White, 2004; van Beynen et al., 2001). Over long time intervals, changes in intensity are therefore suggested to represent long term changes in the soil and vegetation (degree of organic matter degradation in the overlying soil), closely related to temperature and water excess (that controls the residence time of organic molecules in the soil (Backer and Genty, 1999). In subglacial waters one will expect the absence of humic substances, likely an outcome of i) low rates of production by microbial communities and ii) rapid flushing during periods of high flow (Foreman et al., 2013).

In the top 8 cm of MF3, changes in the luminescence intensity were observed under UV light. (Fig. 2.7) No absolute measurements of the intensity were performed. We used lower intensities (light color) as an indicator of low organic matter concentration, and high intensities (dark color) for high organic matter concentration (van Baynen et al, 2001). As presented in Fig. 2.7, changes in the organic matter content were observed between and within individual GI in the sample. The highest content of organic matter was observed during GI_{VII}. During GI_{VI}, $GI_{IVa,}$ and GI_{II} the intensity dropped and flat-topped fluorescent laminae are observed. During $GI_{V,}$ $GI_{VIb\ and}$ $GI_{III,}$ organic matter is exclusively present as irregular low-intensity fluorescent bands, and most of the calcite presents no color (white) under UV light.

There is a strong relation between the luminescence intensity and $\delta^{13}C$, implying that the two records are dominantly forced by closely related processes. We could not find any relation between the luminescence intensity and soil-derived trace elements (e.g P and Y), due to their strong bimodal source, as discussed later.

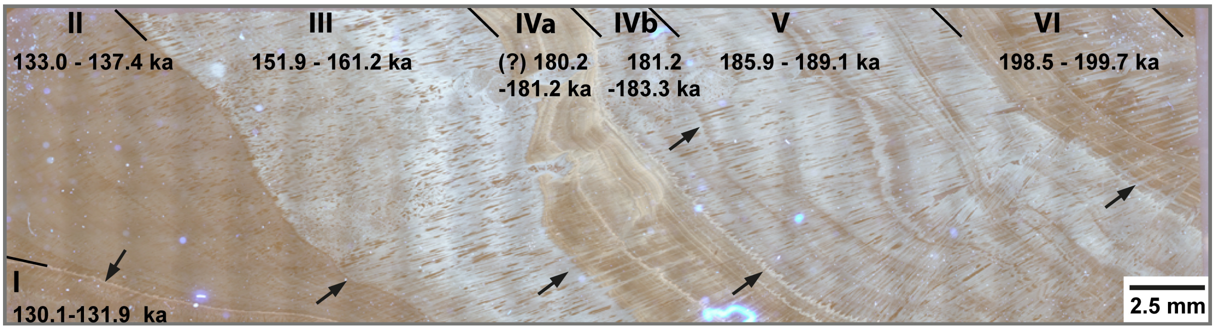

Figure 2.7. *Thin section of sample MF3, view under microscope and UV light. Arrows indicate location of discontinuity horizons (hiatuses)*

2.4.3.2. Trace elements concentration

Fairchild et al. (1998) demonstrated that trace element (TE) ratios available in the cave waters correspond to the reaction time between water and bedrocks. Although state-of-the-art laboratory techniques allow us to analyze a large suite of trace elements, processes that govern their incorporation on/within the calcite structure have been studied in detail and reported in literature. In the present study, we used Sr, U, Mg, Ba, P, Si, Fe, Y, and Al considered as reliable proxies for surface environmental changes that occurred above Schafsloch Cave.

To track changes in soil activity and vegetation productivity, we used P concentration. Nevertheless, variations in P could reflect also i) increase in colloidal transport from the soil and low or negligible prior calcite precipitation (PCP) following effective recharge of the aquifer, ii) a response to piston flow effects caused by effective recharge following dry intervals, iii) dissolution features and microbial processes, as a result of long dry phases (Treble et al., 2013; Fairchild et al., 2001; Treble et al. 2003; Borsato et al., 2007). The last ones are shown to have a negligible effect on the overall hydrologically-induced changes in P concentration (Frisia et al., 2013).

To track changes in the karst hydrology, we used the concentration of lithogenic trace elements (e.g. Ba, Mg, Sr, U), known to be dependent on dissolution and mobilization processes (e.g. effective rainfall and residence time in the rock body above the cave, Roberts et al., 1998; McDonald et al., 2004; Zhou et al., 2005; Fairchild and McMillan, 2007; Demarchelier et al., 2006). Treble et al. (2003, 2005) suggest that Sr concentration depends on stalagmite growth rate and soil processes. A high concentration of Ba, Mg, Sr, and U is caused by a longer residence time of water in the aquifer above the cave (Hellstrom et al., 2000; Baldini et al., 2002; McDonald et al., 2004; Johnson et al., 2006). The positive correlation between Sr and Mg can indicate PCP at times of low effective moisture (McDonald et al., 2007; Fairchild and McMillan, 2007).

Several other trace elements such as REE (e.g. Y) and metals (e.g. Ti, Al) are reported to be related with groundwater dynamics. These are common in so-called “impulse laminae” (Richter et al., 2004; Schimpf et al. 2011; Dasgupta, S., 2010; Borsato et al., 2007; Zhou et al., 2008), representing enrichments in colloid-transported events as a response to high infiltration events, or fracture fed flow. Ti for example is often used as a tracer for detritus, due to its extremely low solubility (Fairchild and Baker, 2012).

The references given above are mostly related to sites where drip water originates from rain and snow melting. As discussed in chapter 4.1, drip water at our site originated not only from these sources, but also from subglacial meltwater. Evolution of landscape (by erosion and weathering), highly influenced by glacial and periglacial processes, will have an influence on the concentration of elements in the (melt) water entering the karst aquifer. During prolonged cold periods, the solifluction (seasonal and diurnal freezing) intensifies and reduces soil thickness and vegetation. In this case, substantial amounts of fine-grained sediment is expected to increase in the waters feeding the karst aquifer (Meyer et al., 2012 and references therein). Ultimately, during the glacier formation the overriding source of trace elements may shift from soils and host rock towards a source which is highly influenced by the mineralogy of fragments derived from glacial abrasion and comminution. Water in the subglacial environment can be a powerful agent of chemical weathering as low temperatures facilitate enhanced solubility of CO_2 in water (Bögli, 1980; Ford and Williams, 2007), and an abundance of freshly ground rock powder provides a constantly renewing source of susceptible minerals. The processes that govern the incorporation of elements in the parent fluid are not extensively addressed in literature, and even fewer examples are given for limestone dominated accumulation areas (Felix and Hallet, 2002.). Nevertheless, several assumptions can be made. Generally, we expect that the meltwater will be rich in a range of solutes (depending on the geological setting) derived from i) precipitation or dry deposition from atmospheric sources, ii) interaction between water and material within the glacier or iii) interaction with soluble materials at the base of the glacier (where most of the solute load is located, Brown and Fuge, 1996). While coarser material can be filtered out in the vadose zone, the elements transported as colloids (e.g. Fe, Si, Al) will reach the stalagmite surface and be incorporated in the calcite structure (Meyer et al., 2012).

An overview of the mean concentration (9 points running average) for each growth interval is presented in Table 2.6. Mg concentration varies from 34 to 4775 mg/kg (min 9 and max 5757 mg/kg). Sr varies from 351 to 968 mg/kg (min 247 and max 1100 mg/kg). U varies from 5 to 12 mg/kg (min 2 and max 26 mg/kg). Ba varies from 16 to 27 mg/kg (min 6 and max 41 mg/kg). P varies from 158 to 527 mg/kg (min 79 and max 974 mg/kg). Y varies from 0.3 to 1.4 mg/kg (min 0.1 and max 7.5 mg/kg). Al varies from 5 to 1771 mg/kg (min 1 and max 4534 mg/kg). Ti varies from 4 to 16 mg/kg (min 2 and max 171 mg/kg). Si varies from 485 to 2893 mg/kg (min 311 and max 18681 mg/kg). Fe varies from 74 to 258 mg/kg (min 29 and max 3248 mg/kg). In the absence of studies regarding modern water chemistry in Schafsloch Cave, we used the values measured during GIVII as reference TE concentrations for an interglacial phase, the geomorphologic architecture and characteristics of karst aquifer above the cave during this time interval are not known. During GIVII barely any strong correlations between the analyzed trace elements are visible (Table 7, GIVII). We observed a positive correlation between Sr and U (r^2=0.31) and Sr and Ba (r^2=0.42), and K and Si (r^2=0.67) as detrital-related elements, although the calcite presents the lowest concentration of detrital and soil related trace elements, as well as in lithogenic ones (Table 2.7).

Concentrations of Sr, U, Mg, Ba, P, Si, Fe, Y, and Al are reported in Fig. 2.8 against a time scale based on linear interpolation between reference age analogues with the stable isotopes profile. Overall, we lack coherence between the MF3 trace element record (see Table 2.7 and Fig 2.8), suggesting very different processes and sources influencing TE concentration. Nevertheless, along individual GI there is an amount of structure, if one considers for example the co-variance among detrital-related (Si, K, Ti, Al) and alkaline-earth elements (U, Sr, Ba).

Several general observations were made based on the trace elements data:

- Sr, Ba and U have closely related signals (r^2 = 0.42 to 0.75, see Table 2.7 and Fig 2.8), implying similar processes influence their concentration change overall. There is no reason to doubt that their concentration in the sample originates mainly from dissolution processes that took place in the host rock. A small detrital (or similar source) contribution during GI_{III} and GI_{IVa} was observed based on positive correlations with Si, Al, Fe and P (r^2 from 0.33 to 0.72). It is likely that the last one took place when more host rock erosion occurred.
- Except the GI_{IVa} and GI_{IVb}, a negative correlation between Sr and P is observed (r^2 from -0.27 to -0.58). P is known to be a strong inhibitor of growth rate, and can change precipitation rate significantly (Meyer, 1984), inducing changes in the partition coefficients of other growth rate dependent elements (e.g, Sr, Tesoriero and Pankow, 1996).
- The Mg profile has a rather complex pattern, displaying no consistent positive or negative correlation throughout the overall dataset with any of the other lithogenic elements or detrital-related elements.
- Highest correlation between detrital trace elements (Fe, Ti, Al, K, Si) is observed during G_I (r^2 from 0.38 to 0.98), G_{III} (r^2 from 0.68 to 0.85) and GI $_{IVa}$ (r^2 from 0.72 to 0.97), and GI_{IVb} (r^2 from 0.32 to 0.77). Considering their absolute concentrations, most host rock erosion is indicated during $G_{I,}$ the second half of G_{III} and G_{IV} (no data are available for G_V and G_{VI}).
- The path and/or the origin of the percolating water changed during the second half of GI_{III} and GI_{IV} (we have no trace element data for GI_V) to a source area with higher contact to K, Fe and P rich mineral deposits. This is not peculiar, as phosphate minerals of the apatite group and glauconite (iron potassium phyllosilicate) are widely present in the rocks surrounding our cave site (Geologischer Atlas der Schweiz, 1982)

		Mg	Al	Si	P	K	Ti	Fe	Sr	Y	Ba	U
		mg/kg	mg/kg	mg/kg	mg/kg	mg/kg	mg/kg	mg/kg	mg/kg	mg/kg	mg/kg	mg/kg
GI I (131.46-131.89 ka BP)	Mean	2670.2	96.6	2893.8	318.4	82.1	15.6	187.5	466.3	0.5	22.2	5.2
	Max.	3366.4	1206.0	14880.3	558.1	585.3	170.8	1471.9	562.1	2.2	40.8	9.6
	Min.	2120.1	3.9	1689.8	187.0	26.6	4.8	51.2	393.0	0.2	14.8	2.1
GI II (133.05-137.39 ka BP)	Mean	4757.8	5.7	2463.9	158.0	38.1	6.7	107.6	968.6	0.3	19.2	12.2
	Max.	5757.6	265.3	6413.4	471.9	173.2	52.8	2453.0	1099.9	3.3	28.5	20.9
	Min.	3755.8	1.3	1374.3	79.5	25.8	3.8	40.6	746.3	0.1	12.5	5.4
GI III (151.91-161.22 ka BP)	Mean	2930.2	11.2	2158.1	417.7	59.8	5.2	115.2	779.4	1.4	17.0	7.6
	Max.	4983.0	166.3	16972.3	974.1	104.1	51.6	2356.5	967.5	7.5	26.6	26.1
	Min.	2257.7	2.4	1016.7	161.4	26.3	1.6	28.8	557.8	0.1	5.7	2.4
GI IV a (180.22-181.15 ka BP)	Mean	34.5	1771.5	485.1	280.4	77.5	8.4	257.6	351.5	1.0	19.0	4.7
	Max.	285.9	4534.0	773.6	389.5	306.3	87.5	3248.0	634.3	3.0	29.5	9.2
	Min.	9.5	1072.2	311.3	179.5	29.7	1.5	56.9	247.6	0.2	10.1	2.0
GI IV b (181.20-183.28 ka BP)	Mean	2417.7	41.1	2479.2	527.9	141.0	6.8	165.8	749.5	0.6	27.3	9.8
	Max.	2696.1	171.3	6605.0	778.2	396.5	21.9	798.7	919.2	1.2	38.4	16.6
	Min.	1906.6	11.2	1145.3	224.4	48.0	1.6	35.4	628.5	0.1	19.1	5.1
GI VII (213.2-213.3 ka BP)	Mean	1452.5	4.9	1712.8	176.3	29.2	3.6	73.6	457.4	0.4	15.7	6.5
	Max.	1874.2	98.8	18671.5	239.3	141.8	9.8	548.2	530.0	1.1	21.4	15.1
	Min.	1184.3	1.4	889.0	109.6	8.8	1.8	33.4	386.5	0.1	10.4	3.1

Table 2.6. *Statistics of trace element concentrations during several growth intervals in sample MF3. The exact temporal extension on which the measurements were made within each growth interval is listed.*

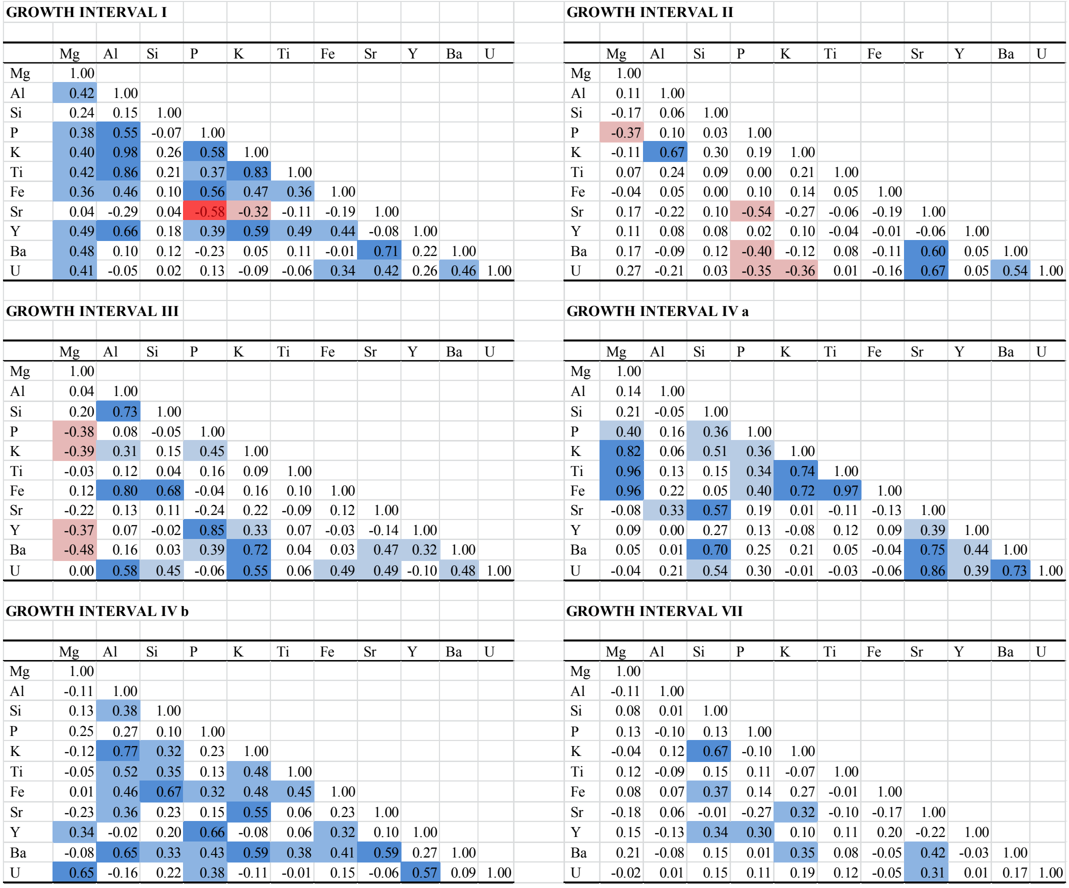

GROWTH INTERVAL I

	Mg	Al	Si	P	K	Ti	Fe	Sr	Y	Ba	U
Mg	1.00										
Al	0.42	1.00									
Si	0.24	0.15	1.00								
P	0.38	0.55	-0.07	1.00							
K	0.40	0.98	0.26	0.58	1.00						
Ti	0.42	0.86	0.21	0.37	0.83	1.00					
Fe	0.36	0.46	0.10	0.56	0.47	0.36	1.00				
Sr	0.04	-0.29	0.04	-0.58	-0.32	-0.11	-0.19	1.00			
Y	0.49	0.66	0.18	0.39	0.59	0.49	0.44	-0.08	1.00		
Ba	0.48	0.10	0.12	-0.23	0.05	0.11	-0.01	0.71	0.22	1.00	
U	0.41	-0.05	0.02	0.13	-0.09	-0.06	0.34	0.42	0.26	0.46	1.00

GROWTH INTERVAL II

	Mg	Al	Si	P	K	Ti	Fe	Sr	Y	Ba	U
Mg	1.00										
Al	0.11	1.00									
Si	-0.17	0.06	1.00								
P	-0.37	0.10	0.03	1.00							
K	-0.11	0.67	0.30	0.19	1.00						
Ti	0.07	0.24	0.09	0.00	0.21	1.00					
Fe	-0.04	0.05	0.00	0.10	0.14	0.05	1.00				
Sr	0.17	-0.22	0.10	-0.54	-0.27	-0.06	-0.19	1.00			
Y	0.11	0.08	0.08	0.02	0.10	-0.04	-0.01	-0.06	1.00		
Ba	0.17	-0.09	0.12	-0.40	-0.12	0.08	-0.11	0.60	0.05	1.00	
U	0.27	-0.21	0.03	-0.35	-0.36	0.01	-0.16	0.67	0.05	0.54	1.00

GROWTH INTERVAL III

	Mg	Al	Si	P	K	Ti	Fe	Sr	Y	Ba	U
Mg	1.00										
Al	0.04	1.00									
Si	0.20	0.73	1.00								
P	-0.38	0.08	-0.05	1.00							
K	-0.39	0.31	0.15	0.45	1.00						
Ti	-0.03	0.12	0.04	0.16	0.09	1.00					
Fe	0.12	0.80	0.68	-0.04	0.16	0.10	1.00				
Sr	-0.22	0.13	0.11	-0.24	0.22	-0.09	0.12	1.00			
Y	-0.37	0.07	-0.02	0.85	0.33	0.07	-0.03	-0.14	1.00		
Ba	-0.48	0.16	0.03	0.39	0.72	0.04	0.03	0.47	0.32	1.00	
U	0.00	0.58	0.45	-0.06	0.55	0.06	0.49	0.49	-0.10	0.48	1.00

GROWTH INTERVAL IV a

	Mg	Al	Si	P	K	Ti	Fe	Sr	Y	Ba	U
Mg	1.00										
Al	0.14	1.00									
Si	0.21	-0.05	1.00								
P	0.40	0.16	0.36	1.00							
K	0.82	0.06	0.51	0.36	1.00						
Ti	0.96	0.13	0.15	0.34	0.74	1.00					
Fe	0.96	0.22	0.05	0.40	0.72	0.97	1.00				
Sr	-0.08	0.33	0.57	0.19	0.01	-0.11	-0.13	1.00			
Y	0.09	0.00	0.27	0.13	-0.08	0.12	0.09	0.39	1.00		
Ba	0.05	0.01	0.70	0.25	0.21	0.05	-0.04	0.75	0.44	1.00	
U	-0.04	0.21	0.54	0.30	-0.01	-0.03	-0.06	0.86	0.39	0.73	1.00

GROWTH INTERVAL IV b

	Mg	Al	Si	P	K	Ti	Fe	Sr	Y	Ba	U
Mg	1.00										
Al	-0.11	1.00									
Si	0.13	0.38	1.00								
P	0.25	0.27	0.10	1.00							
K	-0.12	0.77	0.32	0.23	1.00						
Ti	-0.05	0.52	0.35	0.13	0.48	1.00					
Fe	0.01	0.46	0.67	0.32	0.48	0.45	1.00				
Sr	-0.23	0.36	0.23	0.15	0.55	0.06	0.23	1.00			
Y	0.34	-0.02	0.20	0.66	-0.08	0.06	0.32	0.10	1.00		
Ba	-0.08	0.65	0.33	0.43	0.59	0.38	0.41	0.59	0.27	1.00	
U	0.65	-0.16	0.22	0.38	-0.11	-0.01	0.15	-0.06	0.57	0.09	1.00

GROWTH INTERVAL VII

	Mg	Al	Si	P	K	Ti	Fe	Sr	Y	Ba	U
Mg	1.00										
Al	-0.11	1.00									
Si	0.08	0.01	1.00								
P	0.13	-0.10	0.13	1.00							
K	-0.04	0.12	0.67	-0.10	1.00						
Ti	0.12	-0.09	0.15	0.11	-0.07	1.00					
Fe	0.08	0.07	0.37	0.14	0.27	-0.01	1.00				
Sr	-0.18	0.06	-0.01	-0.27	0.32	-0.10	-0.17	1.00			
Y	0.15	-0.13	0.34	0.30	0.10	0.11	0.20	-0.22	1.00		
Ba	0.21	-0.08	0.15	0.01	0.35	0.08	-0.05	0.42	-0.03	1.00	
U	-0.02	0.01	0.15	0.11	0.19	0.12	-0.05	0.31	0.01	0.17	1.00

Table 2.7. *Trace elements correlation matrix for the growth intervals listed in Table 2.6. In light blue (red) positive (negative) correlation $r^2 < 0.5$ and dark blue (red) positive (negative) correlation $r^2 > 0.5$.*

During interglacial conditions (e.g. GI$_{\mathrm{VI}}$ and GI$_{\mathrm{VII}}$) high organic matter concentrations were observed and overall the smallest detrital contamination of the sample. P between 110 and 239 mg/kg (9 points r.a) characterize conditions of soil and vegetation presence above our cave. This is in agreement with indications of favorable temperatures (based on δ^{18}O values, Table 2.5) and low water retention in the bedrock (based on low Sr, Ba and U concentrations, Table 2.6). By contrast, high variability in organic matter content and trace element concentration is observed during G$_{\mathrm{II}}$ to GI$_{\mathrm{V}}$, reflecting a dynamic glacial and periglacial environment above the cave. Repeated changes of the glacier state from cold to warm-based (experienced as a result of "warm spells" at our cave site) are reflected in sporadic episodes of calcite regrowth. These episodes of calcite ceasing and regrowth during are indicated by a highly irregular development of fluorescent laminae (e.g. GI$_{\mathrm{IVb}}$, GI$_{\mathrm{V}}$) and a higher concentration of trace elements as K, P, Al after long intervals of accumulation in the bedrock as a result of limited (if any) water availability (high U, Ba, Sr concentration).

Contrary to GI$_{\mathrm{IVb}}$ and GI$_{\mathrm{V}}$, during G$_{\mathrm{III}}$ a continuous meltdown process is indicated by flat topped and homogeneous developed fluorescent laminae. With general conditions of atmospheric cooling, high glacial erosion at the surface of the cave (glacier advance) and low water availability in the epikarst are suggested in the older half of G$_{\mathrm{III}}$ (high P, Y, Sr, U concentration). Changes towards less erosion and dissolution processes occur in the youngest part of this interval (lower P, Y concentration). These conditions persisted during G$_{\mathrm{II,}}$ although more limited water availability in the aquifer is suggested.

Phases of fast meltdown of the glacier body, as a direct result of strong positive changes in temperature during GI$_{\mathrm{IVa}}$ and GI$_{\mathrm{I}}$ are clearly indicated by the drops in the concentration of U and Sr, along with an increase in metal concentration (Fe, Al) and organic matter composition (Table 2.6 and Fig. 2.8).

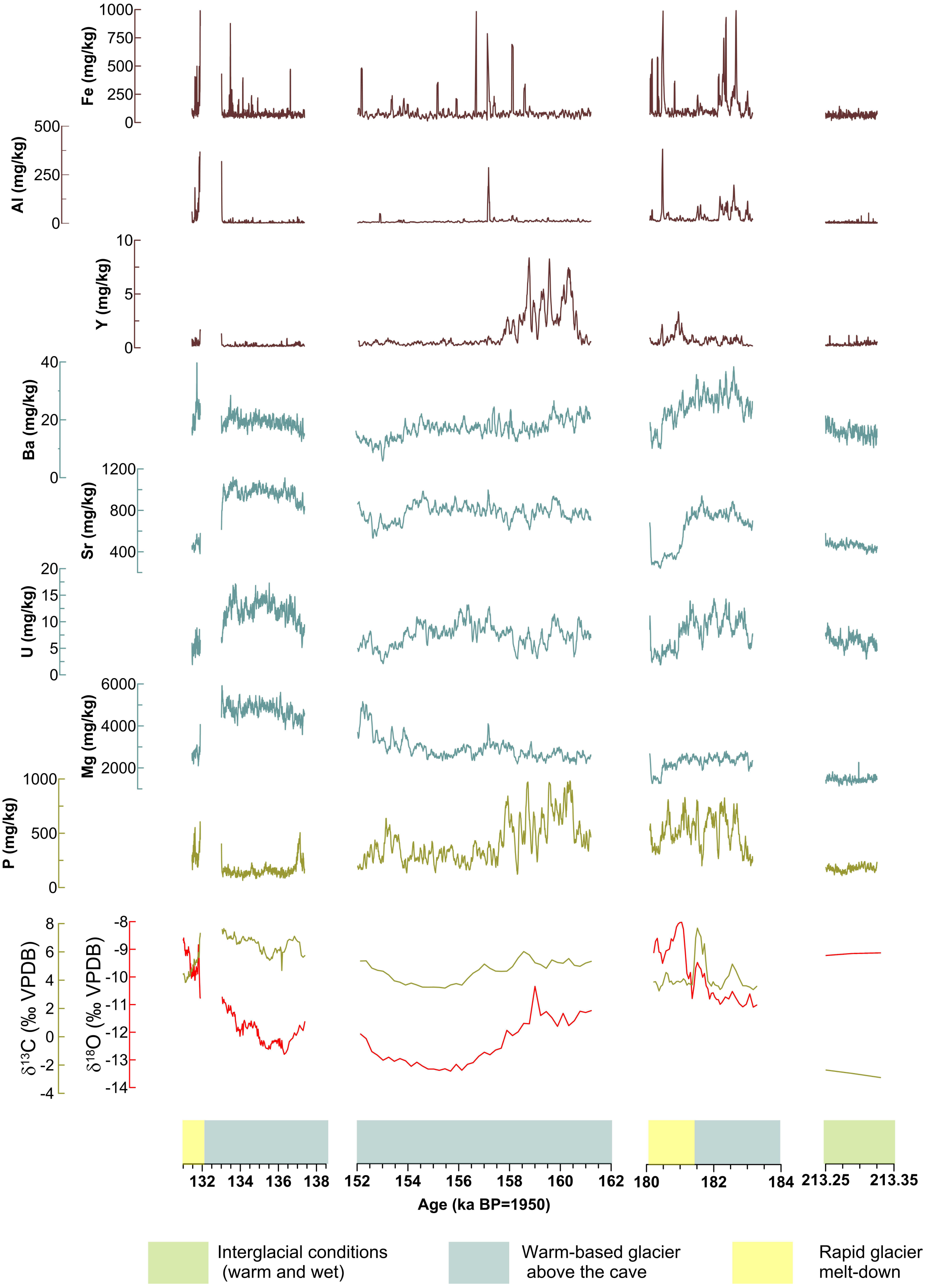

Figure 2.8. *Age model of trace element concentrations in MF3 together with stable isotopic composition of calcite, and environmental reconstruction above Schafsloch Cave*

2.5. DISCUSSION

2.5.1. LOCAL PALEO-HYDROLOGICAL AND ENVIRONMENTAL RECONSTRUCTION

Although highly discontinuous, our record allows the construction of a detailed chronology of climatic conditions in the Alpine region. Based on independent proxies and a precise chronological framework, the Schafsloch Cave record provides important clues regarding processes about the cave (e.g soil evolution, erosion history, favorable conditions of glaciers advance and retreat) of local and regional importance.

We stress that the timing of hiatuses in our sample can be related to either one of the following causes: i) specific site conditions above the cave and in the epikarst (high drip rate, drip water outside equilibrium, blockage of drip water pathways or lateral drift of the drip point), and ii) climate-induced changes in water availability (permafrost conditions or cold based glacier above the cave) and isotopic composition of local precipitation. As local site conditions can bias the growth of a single speleothem and mislead the interpretation of the proxies, caution is required when integrating records from multiple sites to distinguish regional climatic signatures from local variations. No coeval sample is available from surrounding area of the Alpstein Mts. Therefore, for a meaningful paleoclimate reconstruction we will refer here to well-documented isotopic records and growth intervals of speleothems from the Austrian Alps (Spannagel Cave; Spötl et al., 2008; Spötl and Mangini, 2010), and lower altitudes caves from Italy (Tan che Urla and Corchia Cave; Regattieri et al., 2014; Drysdale et al., 2009), France (Villars and Clamouse Cave; Planges et al., 2002; Wainer et al., 2011) and Spain (Gitana Cave; Hodge et al., 2008, Fig. 1). The temporal coverage of the MF3 isotopic record falls within the pollen-based sequences of Meikirch 1, 2 and 3 Interglacial (MIS 7), separated by Birchli, Chutzen and Hubel Stadials (Meikirch profile, Swiss lowlands, Preusser et al., 2005). However, based on the author's description, the Swiss record lacks any feasible pollen-based correlation with other European Middle Pleistocene vegetation records. For this reason, for quantitative climate indicators, we will refer to the well-characterized European pollen record of the Iberian Peninsula (Rocheaux et al., 2006), which is in broad agreement with similar records from France (Beaulieu et al., 2001), Italy (Follieri et al., 1988) and Greece (Tzedakis et al., 2004).

2.5.2. MIS 7

As mentioned before, MF3 was displaced from its original growth location and its base could not be analyzed. The oldest measurements in this sample were performed on a 1.3 ka long growth interval, between 225.8 - 224.5 (±2.3) ka BP. One could attribute the 2 ‰ drop in $\delta^{18}O$ at around 224.5 ka BP, to the end of MIS 7.5 (7e) warm interval and the transition into MIS 7.4 (7d) cold stadial. This timing is in disagreement with evidence from Spannagel Cave (Austria), that indicate a much earlier onset of stadial conditions in the region already around 240 ± 3 ka BP (Spötl et al., 2008, Fig. 2.9). Furthermore, regional climate was altered as a direct result of falling sea surface temperatures (SST) in the North Atlantic region and increasing global ice volume after an insolation minimum around 230 ka BP (Roucoux et al., 2006). For this reason, it is unlikely that interglacial conditions at Schafsloch Cave prevailed until around 225.8 ka BP. Therefore, we suggest that interstadial conditions in the region occurred between 225.8 - 224.5 (±2.3) ka BP, well supported by local evidence of (if any) sparse soil above the cave. Evidence of this warm spell are observed in a warm fluctuation recorded in the Iberian pollen profiles (MD47-7-5, Desprat et al., 2006) and SST fluctuations (Martrat et al., 2007).

After a 4.4 ka long hiatus in the sample, calcite started to form after 220.1 ± 1.4 ka BP. This coincides with the start of high precipitation rates over the Iberian Peninsula between 212-221 ka BP (Desprat et al., 2006). The isotopic profile of MF3 covers the last part of the MIS 7.4 (220.1 to 217.7 ± 1.4 ka BP) and the 800 year-long transition into MIS 7.3 (7c) in high detail. This transition towards the warm interglacial conditions of MIS 7.3 (7c) is marked by a 1.7 ‰ step-like shift in $\delta^{18}O$, between 216.5 - 217.7 ka BP (midpoint at 216.7 ± 1.4 ka BP), and an 6 ‰ negative shift in $\delta^{13}C$ due to rapid soil formation and vegetation development above the cave. Warm and wet interglacial conditions seem to prevail until 211.1 ± 1.4 ka BP. Between 211.1-207.5 ± 1.4 ka BP a drop in the growth rate, followed by positive shift of 3 ‰ in $\delta^{13}C$, mark the deterioration of environmental conditions above the cave. This vegetation decline, similar to the expansion of dry-grassland in the Iberian Peninsula between 208-212 ka BP (Desprat et al., 2006), suggest a water deficit (if not also temperature a drop) at our site, as proven by the slow growth rate of the sample. Between 205.2 - 207.5 ± 1.4 ka BP the growth rate of MF3 rises again, as a result of increased water availability (presence of filled macroscopic pores with microcrystalline calcite which suggest a faster drip rate). The 1‰ gradual negative trend in $\delta^{18}O$ indicates a temperature decline over this time interval, as soil and vegetation density remains low compared to the first part of MIS 7.3. A well-defined hiatus at 205.5 ± 1.4 ka BP marks the transition into MIS 7.2 (7b) cold stadial, although no significant drop in $\delta^{18}O$ is observed. Still, the age is again in good agreement with regional evidence. Both the onset and end of MIS 7.3 in MF3 (216.7 ± 1.6 ka BP and 205.5 ± 0.9 ka BP), agrees very well with the SPA record (215.0 ± 3.0 ka to 232.0 ± 3.0 ka BP, Spötl et al., 2008, Fig. 2.9) within errors.

Between 199.7 to 205.2 ka BP the sample growth ceased, influenced by the cold stadial conditions occurring during MIS 7.2 (7b). Calcite deposition restarted during MIS 7.1 (7a). This last warm phase of MIS 7 is represented by two growth intervals in MF3, between 198.5 - 199.7 ± 1.7 ka BP and 185.9 - 189.1 ± 1.4 ka BP. The timing of the 0.6 ‰ positive shift in $\delta^{18}O$, between 198.5 - 199.7 ± 1.7 ka BP, agrees well with the onset of interglacial conditions in the Austrian Alps (SPA 121 record) at 200 ± 3 ka BP. Negative $\delta^{13}C$ values (-6.7 to -1.2 ‰ VPDB) and high organic matter content in the calcite suggest a well-developed soil and vegetation above the cave during early MIS 7.1. The cessation of calcite growth between 189.1 ± 1.4 and 199.7 ± 1.9 ka BP is most likely related with changes in the local hydrological regime. None of the regional climatic reconstructions (e.g. Spannagel Cave record) suggest a major climatic reorganization at this time.

Between 185.9 - 189.1 ± 1.4 ka BP (late MIS 7.1) a 3.1 ‰ negative shift in $\delta^{18}O$, a gradual 7 ‰ increase in $\delta^{13}C$ and almost no organic matter content in the calcite, track temperature alteration and environmental changes above the cave, from warm interglacial towards cold glacial conditions (Fig. 2.6 and Fig. 2.7). The organic matter content and $\delta^{13}C$ values in this part of the sample suggest calcite precipitated in subglacial environment, in agreement with indications of cold and humid climate on the Iberian Peninsula (Desprat et al., 2006), and suggests a glacial advance above Schafsloch Cave at around 187.0 ka BP. In the absence of ice above our cave, we would expect a higher concentration of detrital-related particles in the calcite structure (see for example GI_{IVa}, discussed below). An intermittent growth of the sample is suggested by the irregular development of fluorescent laminae (Fig. 2.7), in good agreement with indications of repeated cold - warm fluctuations of relatively large amplitude during the MIS 7 / MIS 6 transition (Roucoux et al., 2006; Martrat et al., 2006).

Calcite growth ceased after 185.9 ± 1.6 ka BP is most probably related to a cold-based shift of the glacier or freezing of the cave. This marks the transition into the penultimate glaciation (MIS 6) at our site, well within age estimates reported from Spannagel Cave (SPA 52, 188.7 ± 2.8 ka BP, Spötl et al., 2008) and (Cla4 188.2 ± 1.5 ka BP, Planges et al., 2002, Fig. 2.9).

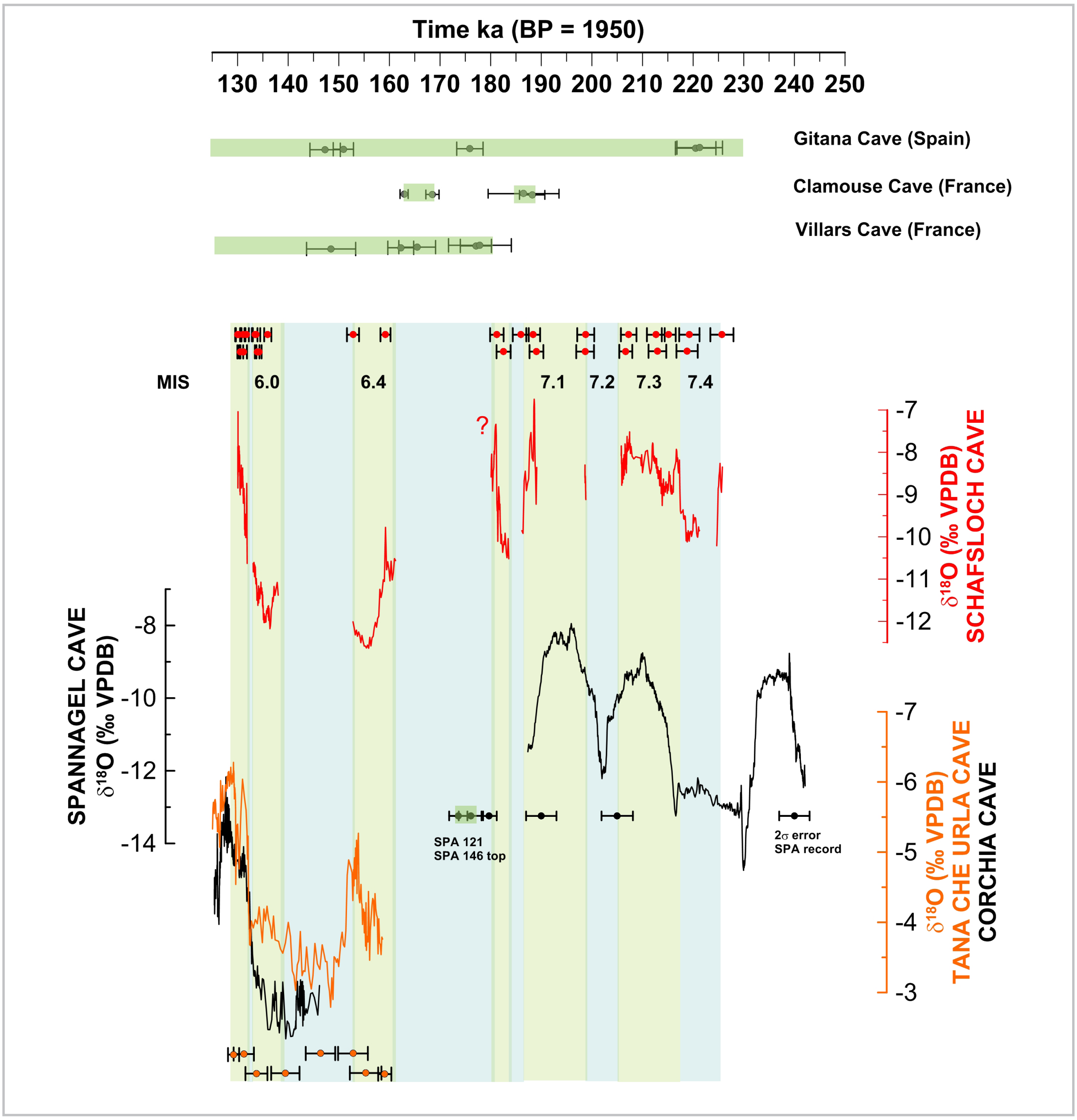

Figure 2.9. *Comparison between* $\delta^{18}O$ *of Schafsloch Cave (our study) and* $\delta^{18}O$ *of Spannagel Cave (Spötl et al., 2008), Tan ache Urla (Regattieri et al., 2014), Corchia Cave (Drysdale et al., 2009), together with growth intervals (horizontal green rectangles) of samples from Gitana Cave (Hodge et al., 2008,), Clamouse Cave (Planges et al., 2002), Villars Cave (Wainer et al., 2011) and Spannagel Cave (Spötl and Mangini., 2010, please note that for a clear comparison only the age of important isotopic shifts, together with their error are presented). Vertical light green boxes represent growth intervals in sample MF3.*

2.5.3. MIS 6

2.5.3.1. Local scale environmental changes

The presence of the glacier is recognized all across MIS 6 interval. Its dynamics (advance, erosion and/or retreat above the cave) is documented as chemical changes in the calcite of MF3 sample. During MIS 6, calcite formed in the cave between 181.1 - 183.3 ± 1.4 ka BP, 151.9 - 161.2 ± 1.0 ka BP, 137.4 - 133.0 ± 0.5 ka BP, and 131.9 - 130.1 ± 0.4 ka BP (respectively GI_{I} to GI_{IVb}). High chronological uncertainty is attributed to the 6 mm highly-corroded calcite attributed in our age model to the interval 180.2 - 181.15 ka BP.

The localized extension of calcite precipitated during 181.15 - 183.3 ka BP suggests extremely limited water availability at a time of cold climate conditions. Repeated changes in the thermal state of the glacier and water availability are indicated (similar with the 185.9 - 189.1 ka BP interval) by irregular fluorescent laminae and short-term high amplitude variation in the concentration of elements like P, Fe, Al and U (Fig. 2.8). During 180.2 - 181.15 ka BP interval conditions change drastically, as positive modifications in the hydrological regime (high water availability suggested by U, Sr, Ba low concentration), temperature (around 1.2 ‰ shift in $\delta^{18}O$) and a high detrital and organic matter concentration in calcite (Fig. 2.7) suggests the deglaciation of the area within 300 years. Without any indication of soil formation (high $\delta^{13}C$) and based on the presence of horizontal fluorescent bending in the calcite, we speculate an increased input of fine detrital material into the drip water, with its source in the erratic siliciclastic material overlying the cave after the glacier retreat. Three well-defined corrosion laminae suggest interruption of growth. Responsible processes could include the following: i) a rapid passage of water through the epikarst (allowing little dissolution of bedrock $CaCO_3$, drip water may not have reached equilibrium with respect to Ca, Railsback et al., 2013), ii) condensation-corrosion of the calcite during “dry”/”cold” intervals and calcite ceasing (Lauritzen 1995) or iii) flooding of the gallery and water-corrosion of calcite surface (Martin-Garcia et al., 2011).

Conditions at the surface change again between 151.9 – 161.2 ± 1.0 ka BP, with low isotopic values ($\delta^{18}O$ and $\delta^{13}C$) and lack of organic matter in calcite indicating a re- advance of the glacier between these two growth intervals. Very slow drip rates and intervals of strong degassing of CO_2 are suggested by the precipitation of calcite under disequilibrium conditions. Less complex layering of the fluorescent layers indicate a constant but slow drip rate and recharge of the aquifer above Schafsloch Cave, and no indication of a long absence of calcite deposition are observed during this time interval. Between 151.9 - 137.4 ka BP the glacier returned to its cold-based state.

Based on isotopic and TE evidences, we suggest a slow melt of the glacier starting with 137.4 ± 1.4 ka BP, followed by a return to cold-based conditions between 133.1 ± 0.7 to 131.9 ± 0.6 ka BP, followed by a rapid melting down of the glacier. Enhanced contribution of snow/rain water as a result of temperature increase is suggested by the abrupt change in $\delta^{18}O$, and pioneering soil and vegetation development are suggested at 131.7 ka BP. The columnar calcite, in combination with diffuse fluorescent properties of the calcite and absence of fluorescent banding suggest again a slow, but continuous feeding of the aquifer. The very low drip rates in combination with occasional high discharge events prevented seasonal karst water pulses to reach the drip point and rather facilitated mixing of seasonal surface signals (Meyer et al., 2012). Chemical changes in the calcite between 137.4 and 130.1 ka BP, local and regional environmental implications are discussed in detail in Chapter 3.

2.5.3.2. Integration on a regional and hemispheric scale during MIS 6

Indicators of climate amelioration during MIS 6 was already recognized in the region, based on calcite deposition in several European caves in France, England and Slovakia) (Plagnes et al., 2002 and citation therein). Speleothem growth is reported in France and England, starting at 177.7 ± 3.0 ka BP in Villars Cave (45°N, Wainer et al., 2011), between 162.3 ± 1.5 and 169.1 ± 1.5 ka BP in Clamouse Cave (43° N, Planges et al., 2002), and around 168 ± 3.4 ka BP in Stump Cross caverns (54°N, Baker et al., 1996). On the southern side of the Alps, detailed isotopic records from the Tana Che Urla and Corchia Cave (both 44°N, Regattieri et al., 2014; Drysdale et al., 2009) cover the time interval starting at around 159.1 ± 1.3 ka BP. The only record covering the entire MIS 6 interval is reported from Gitana Cave (37°N, Hodge et al., 2008). Spannagel Cave reports calcite growth between 173.6 ± 1.8 and 176.1 ± 2.4

ka BP (SPA 121, Spötl et al., 2008) and 179.7 ± 1.5 ka BP (top of SPA 146, Spötl and Mangini, 2010, Fig. 2.9).

At a local scale, glacial deposits of the Rhine paleoglacier in the Alpine foreland suggest at least two main glacial advances during MIS 6, separated by an interstadial phase (Graf, 2009; Preusser et al., 2011; Lowick et al., 2015). If one agrees with the robustness of our age model, changes in the thermal state of the glacier overlying Schafsloch Cave between 180.2 - 183.3 ± 1.4 ka BP and 151.9 -161.2 ± 1.0 ka BP brings therefore new insights in the regional climate during this interval.

Firstly, we will discuss the evidence that relates to a regional climatic amelioration between 180.2 - 183.3 ka BP, and propose an alternative age estimation for the younger calcite precipitated in Schafsloch Cave during this growth interval (GI_{IV}).

Around 180 ka a brief decrease in $\delta^{13}C$ of 3‰ VPDB marks a pulse to warmer and wetter conditions in southern Spain (Gitana Cave, Hodge et al., 2008). Other archives suggest increased moisture and warmth availability in S-W Europe (MD01-2443, Roucoux et al., 2006;Völker et al., 2011), coeval with a light excursion in planktonic $\delta^{18}O$ (SST warming) and a pause in the positive trend of benthic $\delta^{18}O$ (MD01-2443, Roucoux et al., 2006). These data can be corroborated with evidence of a sea level high stand lasting 5 to 10 ka after the 190 ka BP peak in MIS 7.1. Thompson and Goldstein (2005, 2006) and Henderson et al. (2006) suggest a MIS 6/7 mid-point at 184 ka BP, with a maximum extension of the warm interval to 180 ka BP (Roucoux et al., 2006; Henderson et al., 2006). This period of warmth in S-W Europe is consistent, within error, with the light isotopic excursion in our sample, between 181.15 - 183.3 ± 1.4 ka BP (GI_{IVb}).

Around 180.22 - 181.15 ± 1.4 ka BP (GI_{IVa}), evidence of strong local changes in temperature (and retreat of a glacier body) are difficult to reconcile with a decreasing trend in SST and land temperature as suggested by the archives listed above. Taking this into consideration, and emphasizing the lack of a direct ^{230}Th age control, we propose an alternative age for the 6 cm highly-corrosive and organic matter-rich calcite, around 175 ka BP. Precipitation of calcite in Schafsloch Cave is coeval with calcite precipitation in both low- and high- altitudes of western and Central Europe (Spannagel, Villars and Clamouse Cave; Plagnes et al., 2002; Spötl et al., 2008; Wainer et al., 2011, Fig. 2.9)

Calcite forming in Schafsloch Cave between 151.9 - 161.2 ka BP is in excellent agreement with evidence of climate amelioration and enhanced precipitation south of the Alps (Tana che Urla Cave, Regattieri et al., 2014) between 159.1 ± 1.3 ka BP and 152.1 ± 1.9 ka BP. This 9 ka long interval of glacier reorganization above our cave is in line with a significant retreat of the southern margin of Scandinavian ice sheet, and a large scale-scale melt-water event was recorded in deep-sediments from Bay of Biscay (NE Atlantic, Toucanne et al., 2009) between 150-160 ka BP. Alpine glacier meltwater input in the Pô River at around 150 ka was reported by Piva et al., 2008. Pollen evidence suggest interstadial conditions between 151-157 ka in Spain (Roucoux et al., 2006), and a short-lived increase in arboreal pollen in N Greece occurred around 150 ka (Tzedakis et al, 2003, SPACMAP tuned chronology).

Finally, one might assume that this interval (151.9 - 161.2 ka BP) of network break-down in the Alpstein glacier is coeval with a retreat of the main glaciers advancing towards the low-land regions north of the Alps, as suggested by previous studies. This retreat can also be related to precessional forcing which increased both summer insolation and seasonality (related to severe winters and warmer summers).

2.5.4. INTERNAL AND EXTERNAL FORCING ON ALPINE CLIMATE OVER MIS 6 AND MIS 7

We have shown that growth intervals in our sample are related to positive temperature changes in the Alpstein Mts. that induced either changes in the isotopic composition of the snow/rain during interglacial interval MIS 7 or changes in the thermal state of the glacier above Schafsloch Cave during glacial interval MIS 6. By using the temporal reconstructions of glacier dynamics and isotopic changes in the sample, we can evaluate the contribution of individual climate forcing (orbital and feedback of internal sea-ice-atmosphere system) over millennial-scale climate cycles.

Northern Alpine glaciers are sensitive to changes in warm season temperatures, which control the position of the equilibrium line and determine if the glacier has a positive or negative mass balance (Huss et al., 2008). Apart from the radiation budget received during the warm season (a function of precessional and obliquity cycles), the local climate is also influenced by changes occurring in the North Atlantic region and its atmosphere-ocean system, whereas climate variables in the North Atlantic region, such as the position of polar front, sea ice and formation of deep water (NADW) are influenced by the northern hemisphere ice sheet extent (Hodell et. al, 2013).

We compared our data with both variations in orbital parameters (Berger and Loutre, 1991) and reported evidence of oscillations in sea level (relative sea level, Rohling et al., 2009), formation of NADW (Völker et al., 2011), sea surface temperature (SST, Martrat et al., 2009) and atmospheric changes in greenhouse gas concentration (Loulerge et al., 2008).

The northern alpine climate during MIS 6 to MIS 7.3 appears to respond to both a rise in summer insolation and oceanic reorganization (Fig. 2.10). For the radiative budget, following the approach of Carlson and Winsor (2012), we have used mean boreal summer insolation from May to July (Fig. 2.10, red line, Berger and Loutre, 1991). The timing of these changes precedes changes in July insolation at 65°N (Fig 2.10, orange line, Berger and Loutre, 1991) by 2-3 ka. Overall, the MF3 $\delta^{18}O$ record does not display a consistent pattern with the variations in summer insolation, as observed for example in well-documented records from Asia or North America (Lachniet et al., 2014; Cheng et al., 2012 and references therein). During MIS 6 and T-II changes in the thermal state of the glacier follow positive changes in summer insolation shortly after minima in insolation (at 138 ka, 163 ka and 187 ka BP). Warming in the region follows the rising limb of insolation, with relatively weak precessional forcing strengthened by strong obliquity values (high seasonality).

During MIS 7 this relationship partly breaks down. Although low insolation around the minimum at 208 ka BP lead to a drop in calcite growth rate (and a possible hiatus occurs), during MIS 7.4 and 7.2 the region experiences cold stadial conditions at times of high summer insolation (500-520 W/m^2) and high obliquity. This suggests that other climatic mechanisms and interconnections should be considered.

If comparing the isotopic profile and growth intervals of MF3 sample with hemispheric evidence of internal forcing, our record confirms the relationship between processes over the North Atlantic Ocean (SST, state of NADW, meltdown contribution of ice caps) and alpine climate during 130 to 230 ka BP (Fig. 2.10). Hiatuses in our sample appear to correspond with intervals of slow NADW formation (see positive $\delta^{13}C$ in core MD01-2334, Völker et al., 2011), low North Atlantic SST (ODP 977a, Martrat et al., 2007) and a low relative sea level (Rohling et al., 2009; Grant et al., 2012). Calcite formation in the Schafsloch Cave occurs at times of change in greenhouse gas atmospheric concentration during MIS 7 and T-II (CH_4, Loulerge et al., 2008), as amplifier for warming.

For the MIS 6 interval, our data support the findings of Margari et al. (2010) who state that weak forcing (low insolation, obliquity, and green gasses concentration) could trigger major

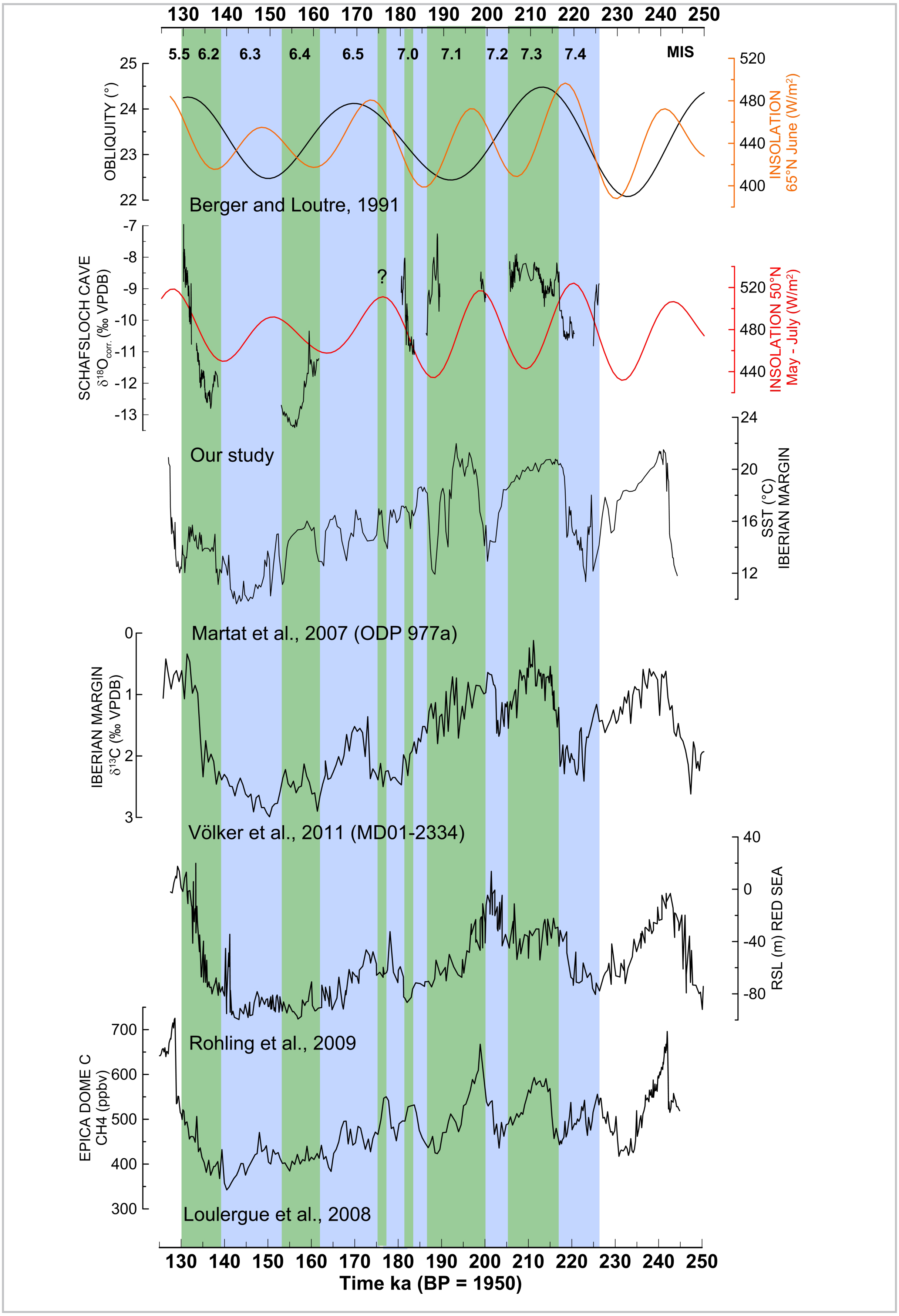

Figure 2.10. *Comparison between $\delta^{18}O$ of Schafsloch Cave (our study) and orbital parameters at 50°N and 65°N (Berger and Loutre, 1991), alkenone-based sea-surface temperatures from western Mediterranean core ODP-977A (Martrat et al., 2007), formation of NADW (Völker et al., 2011), oscillations in ice cap volume (relative sea level changes, Rohling et al., 2009), and atmospheric changes of the greenhouse gass concentrations (Loulerge et al., 2008)*

climate reorganization as a result of very low disruption thresholds in the NADW formation.

A slow resumption of NADW formation and changes in SST will favor increased air temperatures, evaporation and moisture advection across the Mediterranean region (Sanchez-Goni et al., 2012). Advection of warmer air masses (with a significant portion sourced from NAO) towards the north side of the Alps would have been possible via an enhanced southerly circulation (Florineth and Schlüchter, 2000) and/or at times of North Atlantic air masses penetrating towards the east Mediterranean regions (e.g, Plagnes et al., 2002). New records are required from both sides of the Alps in order to better understand these mechanisms. During MIS 6.4 and T-II, enhanced precipitation south of the Alps (Regattieri et al., 2013) match periods of positive temperature changes in the north of the Alps (our study, Fig. 2.9). This relationship breaks down, for example, between 162.3 - 169.1 ± 1.5 ka BP, when climatic amelioration is reported from Clamouse Cave data (Planges et al., 2002). Similarly, the beginning of the $\delta^{18}O$ plateau of MIS 7.3 in the isotopic profiles from Corchia Cave (Couchoud et al., 2011, around 224 ka BP) appears to lead by ca. 7 ka, the one recorded in northern alpine samples (Spötl et al., 2008 and this study). This could also suggest changes in the climate mechanisms influencing both sides of the Alps over glacial-interglacial cycles.

Moving from inter-regional to inter-hemispheric teleconnections, our data seem to agree with a southward displacement of the Intertropical Convergence Zone between 136.7 ± 1.2 ka to 134.5 ± 1.1 ka BP., 177.6 ± 1.7 ka to 182.2 ± 1.6 ka BP., around 205.8 ± 1.9 ka BP, and 207.0 ± 1.6 ka to 209.3 ± 1.8 ka BP (Wang et al., 2004). These intervals are suggested to be synchronous with cold periods in Greenland and Heinrich events in the North Atlantic, and correspond with slow growth intervals and hiatuses in our sample when regional climate experienced cold and glacial conditions.

2.6. Conclusions

The MF3 stalagmite provides a unique opportunity to investigate a regional expression of millennial-scale climate variability in Central Europe during MIS 6 and Late MIS 7. Based on our results, cave air temperatures above 0°C allowed the (slow) precipitation of calcite in the cave during eight individual growth phases coinciding with warm phases of MIS 7, interstadial conditions of MIS 6, and the transition into MIS 5 (penultimate deglaciation, T-II). Intervals of growth during MIS 6 and depleted oxygen values suggest the cave was thermally protected by a local mountain glacier body during this glacial stage. As no other evidence of its presence is preserved in the environmental archives at the surface, isotopic and trace elements evidence in this speleothem were used to document its dynamics above Schafsloch Cave. We suggest the Alpstein valley was ice-free during MIS 7 and in the second part of the penultimate deglaciation.

Taken together, growth intervals in MF3 provide a robust record of temperature-induced environmental changes in high alpine sites. The growth rate in the sample slows dramatically (or comes to a halt) at times of relatively large ice-sheet volume and low boreal summer insolation. At times when a glacier body covered the cave, small changes in summer insolation sustained by increased seasonality (high obliquity) triggered changes in the ice body. Nevertheless, the direct relationship between alpine temperature change and insolation values break down partially during MIS 7, suggesting additional triggers and/or mechanisms that should be considered. Generally, similar to present day conditions, we observed a strong influence of sea surface temperature and moisture advection over the continent, at times of enhanced NADW formation. Furthermore, we suggest coupling of climate at the north and south sides of the Alps during late MIS 6 and T-II (Drysdale et al., 2009; Häuselmann et al., in review), which was broke for example during MIS 7 (Couchoud et al., 2011).

BIBLIOGRAPHY

Atkinson, T.C., 1983. Growth Mechanisms of Speleothems in Castleguard Cave, Columbia Icefields, Alberta, Canada. Arctic and Alpine Research 15, 523-536.

Baker, A., Barnes, W.L. and Smart, P.L., 1996. Speleothem luminescence intensity and spectral characteristics: Signal calibration and a record of palaeovegetation change. Chem Geol 130, 65-76.

Baker, A., Caseldine, C.J., Gilmour, M.A., Charman, D., Proctor, C.J., Hawkesworth, C.J. and Phillips, N., 1999. Stalagmite luminescence and peat humification records of palaeomoisture for the last 2500 years. Earth Planet Sc Lett 165, 157-162.

Baker, A., Ito, E., Smart, P.L., McEwan, R.F., 1997. Elevated and variable values of C-13 in speleothems in a British cave system. Chem Geol 136, 263-270.

Baker, A., Smart, P.L., Edwards, R.L., 1996. Mass spectrometric dating of flowstones from Stump Cross Caverns and Lancaster Hole, Yorkshire: palaeoclimate implications. Journal of Quaternary Science 11, 107-114.

Baldini, J.U., McDermott, F., Fairchild, I.J., 2002. Speleothem trace elements as palaeohydrological proxies during the ‘8,200 year’ cold/dry event. Geochim Cosmochim Ac 66, A46-A46.

Baldini, J.U.L., McDermott, F., Fairchild, I.J., 2006. Spatial variability in cave drip water hydrochemistry: Implications for stalagmite paleoclimate records. Chem Geol 235, 390-404.

Berger, A., Loutre, M.F., 1991. Insolation values for the climate of the last 10 million years. Quaternary Sci Rev 10, 297-317.

Blyth, A.J., Baker, A., Collins, M.J., Penkman, K.E.H., Gilmour, M.A., Moss, J.S., Genty, D., Drysdale, R.N., 2008. Molecular organic matter in speleothems and its potential as an environmental proxy. Quaternary Sci Rev 27, 905-921.

Borsato, A., Frisia, S., Fairchild, I.J., Somogyi, A., Susini, J., 2007. Trace element distribution in annual stalagmite laminae mapped by micrometer-resolution X-ray fluorescence: Implications for incorporation of environmentally significant species. Geochim Cosmochim Ac 71, 1494-1512.

Brown, G.H., Tranter, M., Sharp, M.J., 1996. Experimental investigation of the weathering of suspended sediment by alpine glacial meltwater. Hydrological Processes 10, 579-597.

Bögli, A. 1978. Karsthydrologie und physische Speläologie, Springer Vorlag Berlin, 291 p.

Cheng, H., Lawrence Edwards, R., Shen, C.-C., Polyak, V.J., Asmerom, Y., Woodhead, J., Hellstrom, J., Wang, Y., Kong, X., Spötl, C., Wang, X., Calvin Alexander Jr, E., 2013. Improvements in 230Th dating, 230Th and 234U half-life values, and U–Th isotopic measurements by multi-collector inductively coupled plasma mass spectrometry. Earth Planet Sc Lett 371–372, 82-91.

Cheng, H., Zhang, P.Z., Spötl, C., Edwards, R.L., Cai, Y.J., Zhang, D.Z., Sang, W.C., Tan, M., An, Z.S., 2012. The climatic cyclicity in semiarid-arid central Asia over the past 500,000 years. Geophys Res Lett 39.

Couchoud, I., Drysdale, R., Hellstrom, J., Zanchetta, G., Regattieri, E., and Isola, I., 2011. A precisely dated speleothem record of Termination III and Marine Isotope Stage 7 from Corchia Cave, Italy, Proceedings of the 6th International Conference Climate Change -The Karst Record, Birmingham

Daeron, M., Guo, W., Eiler, J., Genty, D., Blamart, D., Boch, R., Drysdale, R., Maire, R., Wainer, K., Zanchetta, G., 2011. (CO)-C-13-O-18 clumping in speleothems: Observations from natural caves and precipitation experiments. Geochim Cosmochim Ac 75, 3303-3317.

Dasgupta, S., Saar, M.O., Edwards, R.L., Shen, C.-C., Cheng, H., Alexander Jr, E.C., 2010. Three thousand years of extreme rainfall events recorded in stalagmites from Spring Valley Caverns, Minnesota. Earth Planet Sc Lett 300, 46-54.

de Beaulieu, J.-L., Andrieu-Ponel, V., Reille, M., Grüger, E., Tzedakis, C., Svobodova, H., 2001. An attempt at correlation between the Velay pollen sequence and the Middle Pleistocene stratigraphy from central Europe. Quaternary Sci Rev 20, 1593-1602.

Desprat, S., Sánchez Goñi, M.F., Turon, J.-L., Duprat, J., Malaizé, B., Peypouquet, J.-P., 2006. Climatic variability of Marine Isotope Stage 7: direct land–sea–ice correlation from a multiproxy analysis of a north-western Iberian margin deep-sea core. Quaternary Sci Rev 25, 1010-1026.

Drysdale, R.N., Hellstrom, J.C., Zanchetta, G., Fallick, A.E., Goni, M.F.S., Couchoud, I., McDonald, J., Maas, R., Lohmann, G., Isola, I., 2009. Evidence for Obliquity Forcing of Glacial Termination II. Science 325, 1527-1531.

Duplessy, J.C., Roche, D.M., Kageyama, M., 2007. The Deep Ocean During the Last Interglacial Period. Science 316, 89-91.

E., C.B., B., W.W., 2012. Measurement of luminescent banding in speleothems: some techniques and limitations. Int J Speleol.

Edwards, R.L., Chen, J.H., Wasserburg, G.J., 1987. U-238, U-234, Th-230, TH-232 systematics and the precise measurement of time over the past 500 000 years. Earth Planet Sc Lett 81, 175-192.

Fairchild, I.J., Baker, A., 2012. Speleothem Science: From Process to Past Environments. Wiley-Blackwell.

Fairchild, I.J., Baker, A., Borsato, A., Frisia, S., Hinton, R.W., McDermott, F., Tooth, A.F., 2001. Annual to sub-annual resolution of multiple trace-element trends in speleothems. J Geol Soc London 158, 831-841.

Fairchild, I.J., McMillan, E.A., 2007. Speleothems as indicators of wet and dry periods. Int J Speleol 36, 69-74.

Fairchild, I.J., Treble, P.C., 2009. Trace elements in speleothems as recorders of environmental change. Quaternary Science Reviews 28, 449-468.

Felix, N.G., Hallet, B., 2002. Patterning mechanisms in subglacial carbonate dissolution and deposition. Journal of Glaciology 48, 386-400.

Florineth, D., Schluchter, C., 2000. Alpine evidence for atmospheric circulation patterns in Europe during the last glacial maximum. Quaternary Research 54, 295-308.

Fricker, M.B., 2012. Design of ablation cells for LA-ICP-MS: from modeling to high spatial resolutionanalysis applications. ETH Zürich.

Funk, H., Habicht, K., Hantke, R., Pfiffner, A., 2000. Blat 1115 Säntis, In: 1:25000, G.A.d.S. (Ed.). Bundesamt für Wasser und Geologie, Bern.

Graf, R., 2009. Stratigraphie und Morphogenese von frühpleistozänen Ablagerungen zwischen Bodensee und Klettgau. Eiszeitalter und Gegenwart Quaternary Science Journal 58/1, 12-53.

Grant, K.M., Rohling, E.J., Bar-Matthews, M., Ayalon, A., Medina-Elizalde, M., Ramsey, C.B., Satow, C., Roberts, A.P., 2012. Rapid coupling between ice volume and polar temperature over the past 150,000 years. Nature 491, 744-747.

Hellstrom, J.C., McCulloch, M.T., 2000. Multi-proxy constraints on the climatic significance of trace element records from a New Zealand speleothem. Earth Planet Sc Lett 179, 287-297.

Henderson, G.M., Robinson, L.F., Cox, K., Thomas, A.L., 2006. Recognition of non-Milankovitch sea-level highstands at 185 and 343 thousand years ago from U-Th dating of Bahamas sediment. Quaternary Sci Rev 25, 3346-3358.

Hendy, C.H., 1971. The isotopic geochemistry of speleothems: The calculations of the effects of different modes of Formation on the isotopic composition of speleothems and their applicability as palaeclimate indicators. Geochim Cosmochim Ac 35, 801-824.

Hodell, D., Crowhurst, S., Skinner, L., Tzedakis, P.C., Margari, V., Channell, J.E.T., Kamenov, G., Maclachlan, S., Rothwell, G., 2013. Response of Iberian Margin sediments to orbital and suborbital forcing over the past 420 ka. Paleoceanography 28, 185-199.

Hodge, E.J., Richards, D.A., Smart, P.L., Andreo, B., Hoffmann, D.L., Mattey, D.P., González-Ramón, A., 2008. Effective precipitation in southern Spain (~ 266 to 46 ka) based on a speleothem stable carbon isotope record. Quaternary Res 69, 447-457.

Holzkamper, S., Spotl, C., Mangini, A., 2005. High-precision constraints on timing of Alpine warm periods during the middle to late Pleistocene using speleothem growth periods. Earth Planet Sc Lett 236, 751-764.

Huss, M., Farinotti, D., Bauder, A., Funk, M., 2008. Modelling runoff from highly glacierized alpine drainage basins in a changing climate. Hydrological Processes 22, 3888-3902.

Imbrie, J.e.a., 1984. The orbital theory of Pleistocene climate: Support from revised chronology of the marine del18O record, In: (eds.), A.L.B.e.a. (Ed.). D. Reidel Publishing Company.

Johnson, K.R., Lynn Ingram, B., Sharp, W.D., Zhang, P., 2006. East Asian summer monsoon variability during Marine Isotope Stage 5 based on speleothem δ18O records from Wanxiang Cave, central China. Palaeogeography, Palaeoclimatology, Palaeoecology 236, 5-19.

Kovacs, R., Nishiguchi, K., Utani, K., Gunther, D., 2010. Development of direct atmospheric sampling for laser ablation-inductively coupled plasma-mass spectrometry. J Anal Atom Spectrom 25, 142-147.

Lachniet, M.S., 2009. Climatic and environmental controls on speleothem oxygen-isotope values. Quaternary Sci Rev 28, 412-432.

Lachniet, M.S., Denniston, R.F., Asmerom, Y., Polyak, V.J., 2014. Orbital control of western North America atmospheric circulation and climate over two glacial cycles. Nature Communications 5.

Lauritzen, S.-E., 1995. High-Resolution Paleotemperature Proxy Record for the Last Interglaciation Based on Norwegian Speleothems. Quaternary Research 43, 133-146.

Loulergue, L., Schilt, A., Spahni, R., Masson-Delmotte, V., Blunier, T., Lemieux, B., Barnola, J.-M., Raynaud, D., Stocker, T.F., Chappellaz, J., 2008. Orbital and millennial-scale features of atmospheric CH4 over the past 800,000[thinsp]years. Nature 453, 383-386.

Lowick, S.E., Buechi, M.W., Gaar, D., Graf, H.R., Preusser, F., 2015. Luminescence dating of Middle Pleistocene proglacial deposits from northern Switzerland: methodological aspects and stratigraphical conclusions. Boreas

Luetscher, M., Hoffmann, D.L., Frisia, S., Spotl, C., 2011. Holocene glacier history from alpine speleothems, Milchbach cave, Switzerland. Earth and Planetary Science Letters 302, 95-106.

Luetscher, M., Boch, R., Sodemann, H., Spötl, C., Cheng, H., Edwards, R.L., Frisia, S., Hof, F., Müller, W., 2015. North Atlantic storm track changes during the Last Glacial Maximum recorded by Alpine speleothems. Nature Communications 6.

Margari, V., Skinner, L.C., Tzedakis, P.C., Ganopolski, A., Vautravers, M., Shackleton, N.J., 2010. The nature of millennial-scale climate variability during the past two glacial periods. Nature Geoscience 3, 127-131.

María Fernanda Sánchez, G., Edouard, B., Amaelle, L., Linda, R., Francesco, d.E., 2013. Air-sea temperature decoupling in western Europe during the last interglacial-glacial transition. Nature Geoscience 6, 837-841.

Martín-García, R., Martín-Pérez, A., Alonso-Zarza, A., 2011. Weathering of host rock and corrosion over speleothems in Castañar cave, Spain: an example of a complex meteoric environment. Carbonates Evaporites 26, 83-94.

Martrat, B., Grimalt, J.O., Shackleton, N.J., Abreu, L.d., Hutterli, M.A., Stocker, T.F., 2007. Four Climate Cycles of Recurring Deep and Surface Water Destabilizations on the Iberian Margin. Science 317, 502-507.

Mattey, D., Lowry, D., Duffet, J., Fisher, R., Hodge, E., Frisia, S., 2008. A 53 year seasonally resolved oxygen and carbon isotope record from a modem Gibraltar speleothem: Reconstructed drip water and relationship to local precipitation. Earth Planet Sc Lett 269, 80-95.

Mattey, D.P., Fairchild, I.J., Atkinson, T.C., Latin, J.-P., Ainsworth, M., Durell, R., 2010. Seasonal microclimate control of calcite fabrics, stable isotopes and trace elements in modern speleothem from St Michaels Cave, Gibraltar. Geological Society, London, Special Publications 336, 323-344.

McDermott, F., 2004. Palaeo-climate reconstruction from stable isotope variations in speleothems: a review. Quaternary Science Reviews 23, 901-918.

McDonald, J., Drysdale, R., 2007. Hydrology of cave drip waters at varying bedrock depths from a karst system in southeastern Australia. Hydrological Processes 21, 1737-1748.

McDonald, J., Drysdale, R., Hill, D., 2004. The 2002-2003 El Nino recorded in Australian cave drip waters: Implications for reconstructing rainfall histories using stalagmites. Geophys Res Lett 31.

Meyer, M.C., Spötl, C., Mangini, A., Tessadri, R., 2012. Speleothem deposition at the glaciation threshold — An attempt to constrain the age and paleoenvironmental significance of a detrital-rich flowstone sequence from Entrische Kirche Cave (Austria). Palaeogeography, Palaeoclimatology, Palaeoecology 319–320, 93-106.

Mickler, P.J., Banner, J.L., Stern, L., Asmerom, Y., Edwards, R.L., Ito, E., 2004. Stable isotope variations in modern tropical speleothems: Evaluating equilibrium vs. kinetic isotope effects. Geochim Cosmochim Ac 68, 4381-4393.

Plagnes, V., Causse, C., Genty, D., Paterne, M., Blamart, D., 2002. A discontinuous climatic record from 187 to 74 ka from a speleothem of the Clamouse Cave (south of France). Earth Planet Sc Lett 201, 87-103.

Polag, D., Scholz, D., Muhlinghaus, C., Spotl, C., Schroder-Ritzrau, A., Segl, M., Mangini, A., 2010a. Stable isotope fractionation in speleothems: Laboratory experiments. Chem Geol 279, 31-39.

Polag, D., Scholz, D., Mühlinghaus, C., Spötl, C., Schröder-Ritzrau, A., Segl, M., Mangini, A., 2010b. Stable isotope fractionation in speleothems: Laboratory experiments. Chem Geol 279, 31-39.

Preusser, F., Drescher-Schneider, R., Fiebig, M., Schlüchter, C., 2005. Re-interpretation of the Meikirch pollen record, Swiss Alpine Foreland, and implications for Middle Pleistocene chronostratigraphy. Journal of Quaternary Science 20, 607-620.

Preusser, F., Graf, H., Keller, G., Krayss, E., Schluchter, C., 2011. Quaternary glaciation history of northern Switzerland. Quaternary Science Journal 60, 282-305.

Ramseyer, K., Miano, T.M., D'Orazio, V., Wildberger, A., Wagner, T. and Geister, J., 1997. Nature and origin of organic matter in carbonates from speleothems, marine cements and coaral skeletons. Organic Geochemistry 26, 361-378.

Regattieri, E., Zanchetta, G., Drysdale, R.N., Isola, I., Hellstrom, J.C., Roncioni, A., A continuous stable isotope record from the penultimate glacial maximum to the Last Interglacial (159–121 ka) from Tana Che Urla Cave (Apuan Alps, central Italy). Quaternary Research.

Richter, D.K., Gotte, T., Niggemann, S., Wurth, G., 2004. REE3+ and Mn2+ activated cathodoluminescence in lateglacial and Holocene stalagmites of central Europe: evidence for climatic processes? Holocene 14, 759-767.

Riechelmann, D.F.C., Schroder-Ritzrau, A., Scholz, D., Fohlmeister, J., Spotl, C., Richter, D.K., Mangini, A., 2011. Monitoring Bunker Cave (NW Germany): A prerequisite to interpret geochemical proxy data of speleothems from this site. J Hydrol 409, 682-695.

Roberts, N., Jones, M.D., Benkaddour, A., Eastwood, W.J., Filippi, M.L., Frogley, M.R., Lamb, H.F., Leng, M.J., Reed, J.M., Stein, M., Stevens, L., Valero-Garcés, B., Zanchetta, G., 2008. Stable isotope records of Late Quaternary climate and hydrology from Mediterranean lakes: the ISOMED synthesis. Quaternary Sci Rev 27, 2426-2441.

Rohling, E.J., Grant, K., Bolshaw, M., Roberts, A.P., Siddall, M., Hemleben, C., Kucera, M., 2009. Antarctic temperature and global sea level closely coupled over the past five glacial cycles. Nature Geosci 2, 500-504.

Roucoux, K.H., Tzedakis, P.C., de Abreu, L., Shackleton, N.J., 2006. Climate and vegetation changes 180,000 to 345,000 years ago recorded in a deep-sea core off Portugal. Earth Planet Sc Lett 249, 307-325.

Rudzka, D., McDermott, F., Baldini, L.M., Fleitmann, D., Moreno, A., Stoll, H., 2011. The coupled delta C-13-radiocarbon systematics of three Lateglacial/early Holocene speleothems; insights into soil and cave processes at climatic transitions. Geochim Cosmochim Ac 75, 4321-4339.

Schimpf, D., Kilian, R., Kronz, A., Simon, K., Spötl, C., Wörner, G., Deininger, M., Mangini, A., 2011. The significance of chemical, isotopic, and detrital components in three coeval stalagmites from the superhumid southernmost Andes (53°S) as high-resolution palaeo-climate proxies. Quaternary Sci Rev 30, 443-459.

Scholz, D., Hoffmann, D.L., 2011. StalAge – An algorithm designed for construction of speleothem age models. Quaternary Geochronology 6, 369-382.

Scholz, D., Mühlinghaus, C., Mangini, A., 2009. Modelling δ^{13}C and δ^{18}O in the solution layer on stalagmite surfaces. Geochim Cosmochim Ac 73, 2592-2602.

Schürch, M., Kozel, R., Schotterer, U., Tripet, J.-P., 2003. Observation of isotopes in the water cycle—the Swiss National Network (NISOT). Env Geol 45, 1-11.

Sodemann, H., Zubler, E., 2010. Seasonal and inter-annual variability of the moisture sources for Alpine precipitation during 1995-2002. Int J Climatol 30, 947-961.

Spötl, C., Fairchild, I.J., Tooth, A.F., 2005. Cave air control on dripwater geochemistry, Obir Caves (Austria): Implications for speleothem deposition in dynamically ventilated caves. Geochim Cosmochim Ac 69, 2451-2468.

Spötl, C., Holzkamper, S., Mangini, A., 2007. The Last and the Penultimate Interglacial as Recorded by

Speleothems from a Climatically Sensitive High-Elevation Cave Site in the Alps, In: Sirocko, F., Claussen, M., Litt, T., Sánchez Goñi, M.F. (Eds.), The Climate of Past Interglacials. Developments in Quaternary Science Series. Elsevier, pp. 441-491.

Spotl, C., Mangini, A., 2007. Speleothems and paleoglaciers. Earth Planet Sc Lett 254, 323-331.

Spotl, C., Mangini, A., 2010. Paleohydrology of a High-Elevation, Glacier-Influenced Karst System in the Central Alps (Austria). Austrian J Earth Sci 103, 92-105.

Spötl, C., Mangini, A., Bums, S., Frank, N., Pavuza, R., 2004. Speleothems from the High-Alpine Spannagel Cave, Zillertal Alps (Austria), In: Sasowsky, I., Mylroie, J. (Eds.), Studies of Cave Sediments. Springer US, pp. 243-256.

Spotl, C., Scholz, D., Mangini, A., 2008. A terrestrial U/Th-dated stable isotope record of the Penultimate Interglacial. Earth Planet Sc Lett 276, 283-292.

Tabersky, D., Nishiguchi, K., Utani, K., Ohata, M., Dietiker, R., Fricker, M.B., de Maddalena, I.M., Koch, J., Gunther, D., 2013. Aerosol entrainment and a large-capacity gas exchange device (Q-GED) for laser ablation inductively coupled plasma mass spectrometry in atmospheric pressure air. J Anal Atom Spectrom 28, 831-842.

Thompson, W.G., Goldstein, S.L., 2005. Open-system coral ages reveal persistent suborbital sea-level cycles. Science 308, 401-404.

Toucanne, S., Zaragosi, S., Bourillet, J.-F., Cremer, M., Eynaud, F., Van Vliet-Lanoë, B., Penaud, A., Fontanier, C., Turon, J., Cortijo, E., 2009. Timing of massive ‘Fleuve Manche’discharges over the last 350kyr: insights into the European ice-sheet oscillations and the European drainage network from MIS 10 to 2. Quaternary Sci Rev 28, 1238-1256.

Treble, P., Shelley, J.M.G., Chappell, J., 2003. Comparison of high resolution sub-annual records of trace elements in a modern (1911-1992) speleothem with instrumental climate data from southwest Australia. Earth Planet Sc Lett 216, 141-153.

Treble, P.C., Bradley, C., Wood, A., Baker, A., Jex, C.N., Fairchild, I.J., Gagan, M.K., Cowley, J., Azcurra, C., 2013. An isotopic and modelling study of flow paths and storage in Quaternary calcarenite, SW Australia; implications for speleothem paleoclimate records. Quaternary Sci Rev 64, 90-103.

Treble, P.C., Chappell, J., Shelley, J.M.G., 2005. Complex speleothem growth processes revealed by trace element mapping and scanning electron microscopy of annual layers. Geochim Cosmochim Ac 69, 4855-4863.

Tremaine, D.M., Froelich, P.N., Wang, Y., 2011. Speleothem calcite farmed in situ: Modern calibration of δ18O and δ13C paleoclimate proxies in a continuously-monitored natural cave system. Geochim Cosmochim Ac 75, 4929-4950.

Tzedakis, P.C., McManus, J.F., Hooghiemstra, H., Oppo, D.W., Wijmstra, T.A., 2003. Comparison of changes in vegetation in northeast Greece with records of climate variability on orbital and suborbital frequencies over the last 450 000 years. Earth Planet Sc Lett 212, 197-212.

Tzedakis, P.C., Roucoux, K.H., de Abreu, L., Shackleton, N.J., 2004. The duration of forest stages in southern Europe and interglacial climate variability. Science 306, 2231-2235.

van Beynen, P., Bourbonniere, R., Ford, D., Schwarcz, H., 2001. Causes of colour and fluorescence in speleothems. Chem Geol 175, 319-341.

Voelker, A.H.L., de Abreu, L., 2013. A Review of Abrupt Climate Change Events in the Northeastern Atlantic Ocean (Iberian Margin): Latitudinal, Longitudinal, and Vertical Gradients, Abrupt Climate Change: Mechanisms, Patterns, and Impacts. American Geophysical Union, pp. 15-37.

Wainer, K., Genty, D., Blamart, D., Daeron, M., Bar-Matthews, M., Vonhof, H., Dublyansky, Y., Pons-Branchu, E., Thomas, L., van Calsteren, P., Quinif, Y., Caillon, N., 2011. Speleothem record of the last 180 ka in Villars cave (SW France): Investigation of a large delta O-18 shift between MIS6 and MIS5. Quaternary Science Reviews 30, 130-146.

Wang, X.F., Auler, A.S., Edwards, R.L., Cheng, H., Cristalli, P.S., Smart, P.L., Richards, D.A., Shen, C.C., 2004. Wet periods in northeastern Brazil over the past 210 kyr linked to distant climate anomalies. Nature 432, 740-743.

Wanner, H., Rickli, R., Salvisberg, E., Schmutz, C., Schuepp, M., 1997. Global climate change and variability and its influence on Alpine climate - Concepts and observations. Theor Appl Climatol 58, 221-243.

White, W., 2004. Paleoclimate Records from Speleothems in Limestone Caves, In: Sasowsky, I., Mylroie, J. (Eds.), Studies of Cave Sediments. Springer US, pp. 135-175.

Wiedner, E., Scholz, D., Mangini, A., Polag, D., Mühlinghaus, C., Segl, M., 2008. Investigation of the stable isotope fractionation in speleothems with laboratory experiments. Quaternary International 187, 15-24.

Zhou, H.Y., Chi, B.Q., Lawrence, M., Zhao, J.X., Yan, J., Greig, A., Feng, Y.X., 2008. High-resolution and precisely dated record of weathering and hydrological dynamics recorded by manganese and rare-earth elements in a stalagmite from Central China. Quaternary Res 69, 438-446.

Zhou, J.Z., Lundstrom, C.C., Fouke, B., Panno, S., Hackley, K., Curry, B., 2005. Geochemistry of speleothem records from southern Illinois: Development of (U-234)/(U-238) as a proxy for paleoprecipitation. Chem Geol 221, 1-20.

CHAPTER 3.

TIMING AND NATURE OF THE PENULTIMATE DEGLACIATION IN A HIGH ALPINE STALAGMITE FROM SWITZERLAND

In collaboration with Dominik Fleitmann [1,2], Hai Cheng[3,4], R. Lawrence Edwards[3], Daniel Tabersky[5], Detlef Günther[5]

[1] *Institute of Geological Sciences and Oeschger Centre for Climate Change Research, University of Bern, Switzerland*

[2] *Department of Archaeology and Center for Past Climate Change, School of Archaeology, Geography and Environmental Science, University of Reading, UK.*

[3] *Department of Geology and Geophysics, University of Minnesota, USA*

[4] *Institute of Global Environmental Change, Xi'an Jiaotong University, Xi'an 710049, China*

[5] *Department of Chemistry and Applied Biosciences, Laboratory of Inorganic Chemistry, ETH Zürich, Vladimir-Prelog-Weg 1, CH-8093 Zürich*

3.1. INTRODUCTION

Knowledge about the timing and nature of glacial/interglacial transitions (termed "Terminations"; T hereinafter) is crucial for a better understanding of the complex relationship between external (e.g., insolation) and internal (e.g., ice sheets, greenhouse gases, ocean circulation) climate forcing mechanisms (e.g., Tzedakis et al., 2009; Waelbroeck et al., 2008; Cheng et al., 2009; Drysdale et al., 2009). Dating of terminations prior to the last deglaciation (Termination I), however, remains challenging due to the lack of precise and absolute dating techniques for marine and terrestrial sediment sequences and ice cores covering. As a result, chronologies of almost all palaeoclimate records are based on orbital-tuning, which makes it difficult to reveal the leads and lags between insolation and climatic changes during deglaciations. Independently derived absolute and precise chronologies covering terminations are thus in high demand.

Well-constrained ages for the timing of terminations can be obtained by Uranium-series dated (^{230}Th hereinafter) speleothems and corals. The latter, however, are more prone to diagentic alteration and remobilization of Uranium ('open system conditions') (e.g., Thompson and Goldstein, 2005), and both effects can lead to inaccurate ages. Among all palaeoclimate archives, speleothems have currently the highest potential to deliver absolute and accurate age estimates for the timing of terminations, including the intensively studied T-II at around 130 ka BP. This glacial/interglacial transition is currently covered either in full or in part by several ^{230}Th-dated speleothem records from caves located in different climatic zones. However, the dating accuracy of most of these records is rarely below ±1.5 ka (2σ-errors) and ^{230}Th-ages are not always in stratigraphic order, making it still challenging to provide precise estimates of leads and lags between these records.

To date, the most precisely-dated record covering T-II is the Sanbao Cave δ^{18}O record from China (Cheng et al., 2009), which suggests an age of 129.0 ± 0.1 ka BP for the midpoint of T-II in the Asian monsoon domain. This age estimate is in good agreement with less-precisely-dated stalagmites from Dongge Cave, China, (Kelly et al., 2006), and appears to be broadly consistent with speleothem records from Soreq Cave (Israel) and Sofular Cave (Turkey) (Badertscher et al., 2011; Grant et al., 2012). However, speleothem records from Corchia and TUC Caves (Italy), Nevada Caves (N. America), suggest significantly older ages of 132.6 ± 1.8 and 132.0 ± 0.6 ka BP for the midpoint of T-II (Drysdale et al., 2009; Shakun et al., 2011; Regatierri et al., 2014; Lachniet et al., 2014). Additional speleothem records covering T-II were obtained from Hoti Cave (Oman; Fleitmann et al. 2003), Mukallah Cave (Yemen; Fleitmann et al., 2011), Spannagel Cave (Austria; Holzkämper et al., 2005), Oregon Caves National Monument (USA; Esrek et al. 2009), several caves in the Negev (Israel; Vaks et al. 2010) and Villars Cave (France; Wainer et al., 2011), but their chronologies suffer from considerable age uncertainties and/or reversals, and are thus not well-suited to shed further light on the timing of T-II. Nevertheless, they provide valuable information on the magnitude and nature of regional climatic changes during the penultimate deglaciation.

Additional well-dated speleothem records are therefore needed to reduce the current uncertainties surrounding the timing of T-II and to account for possible site-specific response times of local and regional climate during the penultimate deglaciation. To add further evidence regarding the nature of T-II in central Europe, we present a precisely dated high alpine speleothem δ^{18}O record from Schafsloch Cave in Switzerland. High Uranium concentrations of several mg/kg and negligible detrital contamination permit the determination of very precise ^{230}Th-ages with age uncertainties of generally less than ± 0.6

ka. In addition, highly-resolved stable isotope and trace element profiles provide detailed information on changes in temperature, precipitation and ecosystem across T-II at this high alpine cave site. The stalagmite MF3 record covers much of T II in an area that is very sensitive to changes in North Atlantic climate, allowing us to refine our knowledge of the nature of T II in central Europe and the North Atlantic realm.

3.2. Site and sample description

Stalagmite MF3 was collected from Schafsloch Cave located in the Appenzell Alps (47°14'N, 9°23'E, 1890 m above sea level (a.s.l.; Fig. 3.1). Climate in this area is strongly influenced by the North Atlantic region, which is the main source of moisture (Sodemann and Zubler, 2010; Wanner et al., 1997). Lapse-rate corrected (0.54°C/100 m) mean annual air temperature (MAAT) at Schafsloch Cave derived from meteorological station data (1961-2010) from the Säntis (47°24'N, 9°34'E, 2500 m a.s.l.; Fig. 3.1) are around 2.6°C, with winter and summer temperatures averaging -2.5°C and 8.5°C respectively. Precipitation at the cave site is around 2200 mm yr^{-1}. Soil depth above Schafsloch Cave ranges between a few centimeters to decimeters, whereas vegetation is sparse.

Schafsloch Cave is situated in the pure planktonic limestone of Seewerkalk Formation, and is covered by ~20 m thick epikarst (bedrock above the cave). Today, only the first 25 m of the cave are accessible, as the inner part is blocked by sediments in which the 215 mm long stalagmite MF3 (Fig. 3.2A) was found. Its original position within the cave is therefore unknown. Stalagmite MF3 is composed by dense and translucent columnar-fibrous calcite. For this study, only the uppermost 33.75 mm of the sample were studied in detail.

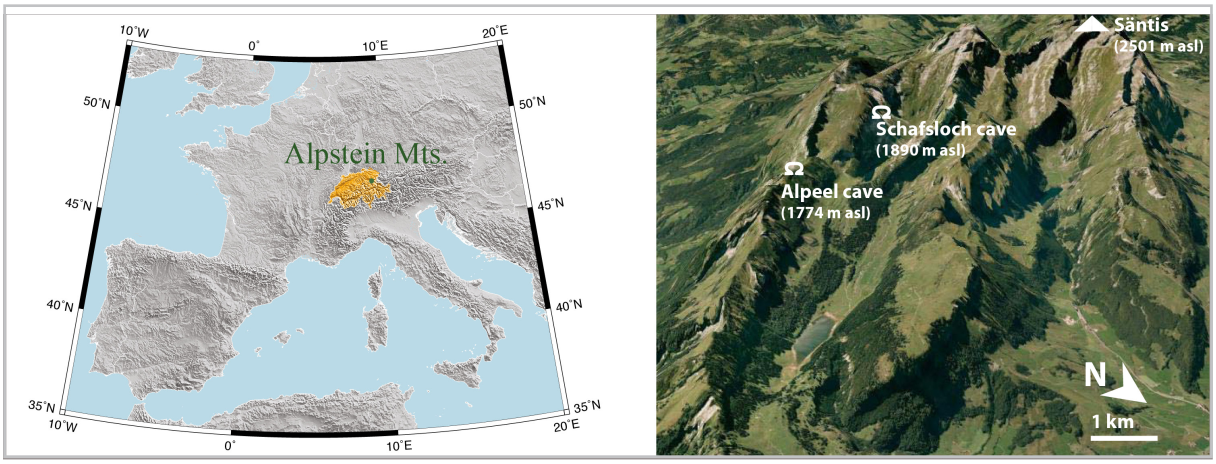

Fig. 3.1. *Location maps of Schafsloch and Alpeel Caves (view: Google Earth Maps)*

3.3. Methods

Petrographic observations were carried out using an optical transmission microscope at the Institute of Geological Sciences, Bern, Switzerland.

^{230}Th-ages were determined on a multi-collector inductively coupled plasma mass spectrometer (MC-ICP-MS, Thermo-Finnigan Neptune) at the Department of Geology and Geophysics, University of Minnesota. Details of the methods, including standards used for mass fractionation and yield correction can be found in Cheng et al. (2013). For analysis, between 70 and 100 mg of powder was drilled along discrete growth horizons (Fig. 3.2B).

For stable carbon and oxygen isotope analysis, a total of 321 samples were micromilled continuously at 0.1 mm and 0.25 mm increments from 0 to 31 mm and 31 to 34.5 mm, respectively. Powdered samples were measured using a Finnigan Delta V Advantage mass spectrometer equipped with an automated carbonate preparation system (Gas Bench II) at the Institute of Geological Sciences, University of Bern, Switzerland. Results are reported relative to the international Vienna Peedee Belemnite (VPDB) standard. Analytical errors for $\delta^{18}O$ and $\delta^{13}C$ are 0.07 and 0.06 ‰ VPDB (1σ), respectively (Fleitmann et al., 2009).

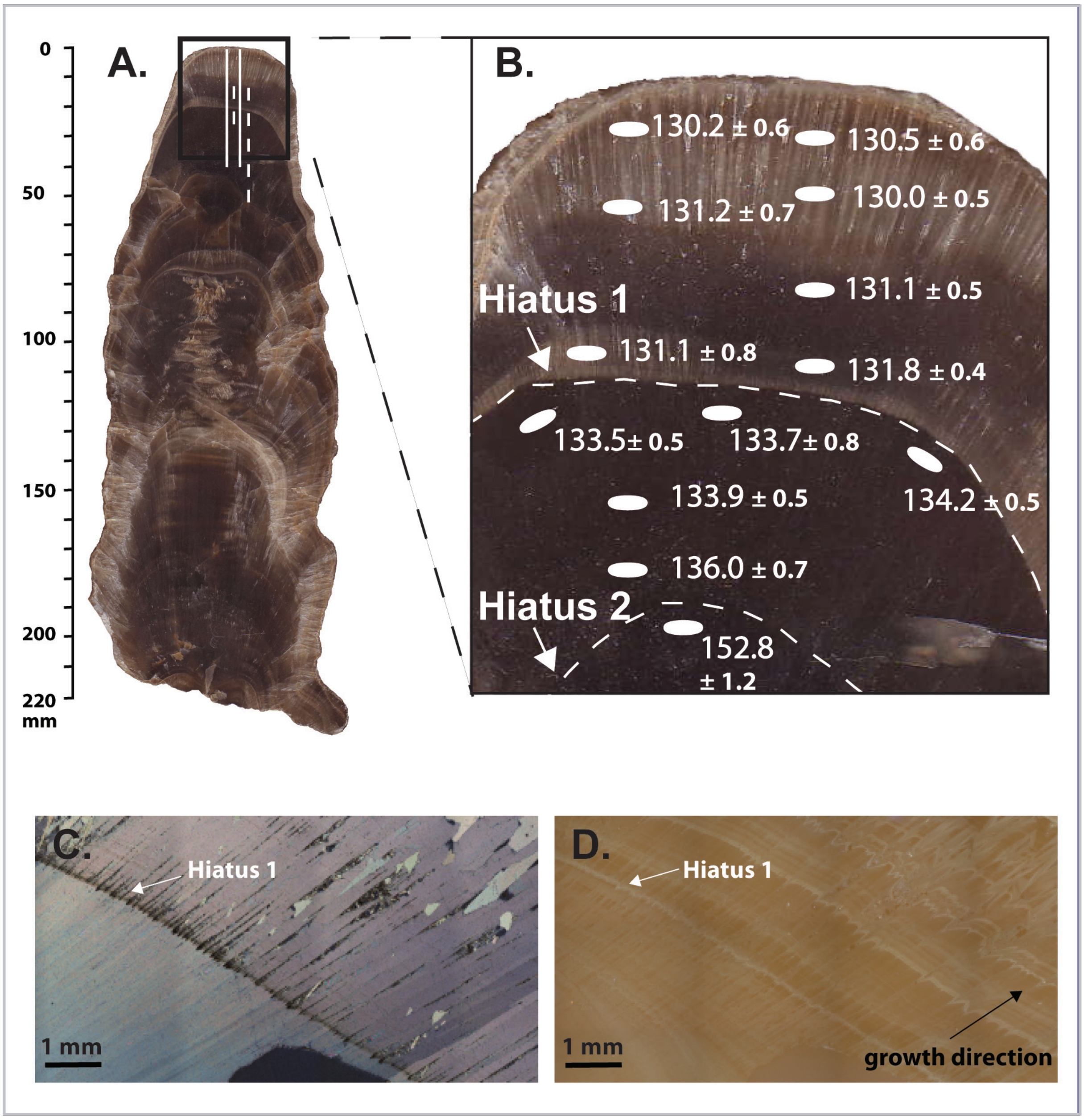

Fig. 3.2. ***A*** *Macroscopic view of stalagmite MF3, white lines denote the isotopic (solid line) and trace element (dashed lines) tracks.* ***B*** *Macroscopic view of the upper 40 mm of MF3. White dots denote 230Th sampling locations. Discontinuities in the sample are indicated by dashed lines and arrows.* ***C*** *Optical microscope image (cross- polarized light) of the top of MF3. Typical calcite fabric in the sample: closed columnar fabric under the discontinuity layer (Hiatus 1, indicated by the white arrow in both images) and opened columnar fabric above it.* ***D*** *Optical microscope image under UV light. Fluorescent laminae are observed in the entire section. Above hiatus 1 (H1), at the growth interference of crystals irregular organic matter enriched zones are present. Growth direction of the sample is indicated by the black arrow.*

Trace element analyses were carried out using a 193 nm ArF excimer laser (GeoLas Pro, Lambda Physik) coupled to a quadrupole ICP-MS (ELAN 6100 DRC+, Perkin Elmer). Operating conditions are listed in Chapter 2, Table 2.2. A detailed description of the experimental setup has already been given in Kovacs et al. (2010) and was subsequently further optimized as described in Tabersky et al. (2013). In brief, laser ablation was performed in atmospheric ambient air without further sample size reduction. The laser-generated aerosol was pumped into a gas exchange device (J-Science, Japan) by a membrane pump (DSA-2-12BL, Denso Sangyo, Japan) via an in-house built plume entrainment device at a suction flow of 0.8 L/min and afterwards transported into the ICP-MS in an Argon atmosphere. Element concentrations were measured using line scans parallel to the growth axis and isotope sampling tracks. Two cleaning line scans were applied to remove potential contaminations on the sample surface and only the third was used for quantification, which was carried out by non-matrix-matched calibration using NIST SRM 610 as external standard. Additionally, $^{42}Ca^+$ was used for internal standardization, using the stoichiometry of Ca in carbonates (400 000 mg/kg pure calcite) and values were normalized to 100% sum of oxides, whereas the calcium concentration was normalized to $CaCO_3$. Data evaluation was carried out in STALQUANT, an in-house Phyton-based software program to reduce large amounts of point-by-point quantification data (Fricker, 2012).

Wavelength	193 nm
Crater size	60 µm (aquistion); 120 µm (cleaning)
Scan speed	20 µm/s
Repetition rate	10 Hz
Fluence	21 J/cm^2
GED	Q-GED
Sweep Gas	10 L/min (Ar)
Overpressure (Sweep Gas)	500 Pa
Ablation plume entrainment	Manta (Taberska et al.2013)
Carrier gas	0.8 L/min (Air)
Type of Pump	Denso Sangyo DSA-2-12BL
Nebulizer Gas Flow	0.57 L/min
ICP	ELAN 6100 DRC+
Dwell time	10 ms
Auxiliary gas flow	0.75 L/min
Plasma gas flow	17.5 L/min
RF Power	1380 W
Isotopes measured	$^{13}C^+$,$^{18}O^+$, $^{23}Na^+$, $^{24}Mg^+$, $^{25}Mg^+$, $^{26}Mg^+$, $^{27}Al^+$, $^{29}Si^+$, $^{31}P^+$, $^{32}S^+$, $^{33}S^+$; $^{34}S^+$, $^{35}Cl^+$, $^{39}K^+$, $^{42}Ca^+$, $^{43}Ca^+$, $^{45}Sc^+$,$^{46}Ca^+$, $^{49}Ti^+$, $^{51}V^+$, $^{52}Cr^+$, $^{53}Cr^+$, $^{55}Mn^+$, $^{57}Fe^+$, $^{59}Co^+$, $^{60}Ni^+$, $^{63}Cu^+$, $^{65}Cu^+$, $^{66}Zn^+$, $^{75}As^+$, $^{85}Rb^+$, $^{88}Sr^+$, $^{89}Y^+$, $^{92}Mo^+$, $^{95}Mo^+$, $^{111}Cd^+$, $^{137}Ba^+$, $^{140}Ce^+$, $^{159}Tb^+$, $^{165}Ho^+$, $^{182}W^+$, $^{184}W^+$, $^{207}Pb^+$, $^{208}Pb^+$, $^{209}Bi^+$, $^{232}Th^+$, $^{238}U^+$, $^{248}ThO^+$

Table 2.2. *Operating conditions for the LA-GED-ICPMS measurement (Tabersky et al., 2013).*

Table 3.1. *^{230}Th age data for top 35 mm of stalagmite MF3*

Sample Number	Depth (mm)	^{238}U (ppb)		^{232}Th (ppt)		^{230}Th / ^{232}Th (atomic x10^{-6})		δ^{234}U* (measured)		^{230}Th / ^{238}U (activity)		^{230}Th Age (ka) (uncorrected)		δ^{234}U$_{Initial}$** (corrected)		**^{230}Th Age (ka BP)*** (corrected)**	
MF3-3	2.7	1079	±1	14902	±298	1048	±21	222	±2	0.8785	±0.0014	130.285	±0.553	320	±2	**130.225**	**±0.553**
MF3-G	3.8	1307	±1	29908	±599	633	±13	218.6	±1.5	0.8779	±0.0011	130.603	±0.577	316	±2	**130.540**	**±0.577**
MF3-F	8.2	1950	±2	8835	±177	3197	±64	223.3	±1.6	0.8783	±0.0012	130.078	±0.480	322	±2	**130.015**	**±0.480**
MF3-10	8.7	1729.7	±2.1	9502	±190	2638	±53	218.4	±2.3	0.8788	±0.0014	131.279	±0.651	316	±3	**131.218**	**±0.651**
MF3-E	13.8	2274	±2	467	±11	69983	±1601	210.1	±1.4	0.8712	±0.0012	131.160	±0.457	304	±2	**131.097**	**±0.457**
MF3-11	17.1	2942.3	±4.3	61335	±1229	692	±14	212.2	±2.5	0.8744	±0.0015	131.133	±0.773	307	±4	**131.072**	**±0.773**
MF3-D	18.3	2981	±3	8377	±168	5126	±103	209.7	±1.4	0.8736	±0.0010	131.871	±0.426	304	±2	**131.808**	**±0.426**
MF3-C	21.8	8007	±8	1148	±24	98733	±2069	184.7	±1.2	0.8587	±0.0012	133.537	±0.456	269	±2	**133.474**	**±0.456**
MF3-4	23.7	7535	±20	7265	±146	14609	±294	179	±2	0.8543	±0.0025	133.716	±0.828	261	±2	**133.656**	**±0.828**
MF3-B	24.2	9855	±12	575	±12	241755	±5233	178.2	±1.4	0.8559	±0.0013	134.301	±0.507	260	±2	**134.238**	**±0.507**
MF3-A	25.1	7333	±7	150	±6	692787	±26699	183.5	±1.3	0.8590	±0.0011	133.932	±0.453	268	±2	**133.869**	**±0.453**
MF3-12	29.4	6716.0	±12.0	6819	±137	14033	±282	181.0	±2.0	0.8641	±0.0017	136.031	±0.708	266	±3	**135.970**	**±0.708**
MF3-25	35	4950	±13	558	±11	124687	±2524	110.5	±1.7	0.8530	±0.0028	152.868	±1.194	170	±3	**152.805**	**±1.194**

U decay constants: λ_{238} = 1.55125x10^{-10} (Jaffey et al., 1971) and l_{234} = 2.82206x10^{-6} (Cheng et al., 2013). Th decay constant: λ_{230} = 9.1705x10^{-6} (Cheng et al., 2013).

* δ^{234}U = ([^{234}U/^{238}U]$_{activity}$ – 1)x1000. ** δ ^{234}U$_{initial}$ was calculated based on ^{230}Th age (T), i.e., δ^{234}U$_{initial}$ = δ^{234}U$_{measured}$ x e^{l234xT}.

Corrected ^{230}Th ages assume the initial ^{230}Th/^{232}Th atomic ratio of 4.4 ±2.2 x10^{-6}. Those are the values for a material at secular equilibrium, with the bulk earth ^{232}Th/^{238}U value of 3.8. The errors are arbitrarily assumed to be 50%.

***B.P. stands for “Before Present” where the “Present” is defined as the year 1950 A.D.

3.4. RESULTS

3.4.1. CHRONOLOGY OF STALAGMITE MF3

The age model for the uppermost 33.75 mm of stalagmite MF3 is constrained by thirteen ^{230}Th-dates, all of them are in stratigraphic order within their 2 σ dating uncertainties, and based on the StalAge algorithm (Scholz and Hoffmann, 2011; Fig. 3.3). High U content (1.7 to 7.5 mg/kg) and negligible detrital contamination result in very precise ages with age uncertainties of between 0.4 and 0.6 ka (Table 1). Stalagmite MF3 growth started at 137.4 ± 1.4 ka BP (growth phase II), ceased (hiatus H1; for further details see discussion below) between 133.1 ± 0.7 and 131.9 ± 0.6 ka BP, and then continued until 130.1 ± 0.5 ka BP (growth phase I). As expected for a stalagmite from a high alpine region with low mean annual air temperatures, growth rates vary between 0.003 and 0.1 mm yr^{-1} during growth phases II and I respectively.

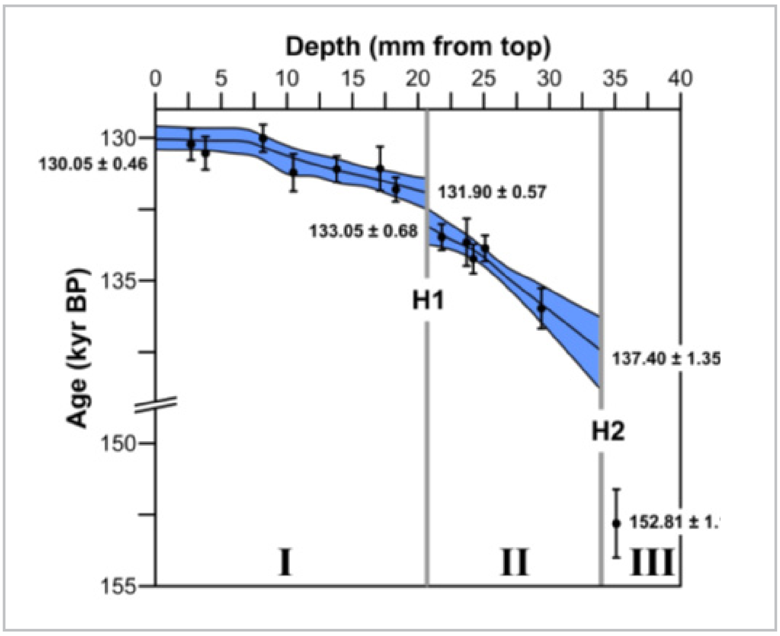

Fig. 3.3. Age-depth plot for stalagmite MF3. The blue shaded area shows the 95% confidence intervals of the MF3 age model as determined with STALAGE (Scholz and Hoffmann, 2011). Grey vertical bars denote discontinuities, labelled H1 and H2. Roman numbers denote growth phases of stalagmite MF3.

Stalagmite MF3 is composed by columnar calcite. The hiatus at 20.6 mm is characterized by sudden changes in calcite fabric, abundance of fluid inclusions and content of organic matter (Fig. 3.2A). Under UV light this discontinuity is marked by a thin layer of calcite enriched in detrital material and also by a change from a compact columnar (growth phase II) to an inclusion-rich columnar calcite fabric (growth phase I). The top layer of stalagmite MF3 shows no signs of corrosion as the crystal terminations have a regular shape.

Towards the top of the sample, the fabric changes from microcrystalline subtype of columnar fabric to an open columnar inclusion-rich calcite. Under UV light banding is observed in both fabrics, but the content of organic matter (lighter color in Fig 3.2) is considerable higher above hiatus H1. The dense close columnar fabric in growth phase II precipitated at low supersaturation conditions, regular flow and negligible presence of impurities (Frisia et al., 2000). These conditions changed with the beginning of growth phase I, directly related with changes in the growth rates, high supersaturation conditions, presence of impurities and higher drip rate (Frisia and Borsato, 2010, Boch et al., 2011). Fluorescent laminae are observed in both growth phases, they are flat-topped (on less developed crystal terminations) during growth phase II, and enriched fluorescent bands can be observed at the surface of more irregular crystals terminations in growth phase I. This may be the result of a thick film of water on the surface of the growing stalagmite, together with a higher input of organic matter and detrital material in the sample.

3.4.2. Stable isotopes

The temporal resolution of the oxygen and carbon isotope profiles varies between 6 and 40 years (Fig. 3.4). Both isotope profiles show distinct trends, with $\delta^{18}O$ values increasing by 3.2 ‰ and $\delta^{13}C$ values decreasing by 9.3‰ across the penultimate deglaciation. Isotope values for growth phase II vary between -11.9 to -10.8 ‰ for $\delta^{18}O$ and +6.1 and +7.5 ‰ for $\delta^{13}C$. In contrast, growth phase I is characterized by a steep rise in $\delta^{18}O$ from -10.3 to -8.2 ‰, whereas $\delta^{13}C$ values show an opposite shift, from +6.9 to -1.5‰ VPDB. Second order variations of around 0.5‰ are apparent in both isotope profiles.

3.4.3. Trace elements

A total of 32 elements were analyzed across H1 between 17.0 and 27 mm at a resolution of 13 µm (Fig. 3.4). Trace element profiles cover the time intervals from 134.9 ± 0.4 to 133.1 ± 0.7 (growth phase II) and 131.9 ± 0.6 to 131.5 ± 0.5 ka BP (growth phase I). Of these elements, only Mg, Sr, P, Al, Y, Ti and U were considered as their paleoclimatic and environmental significance is well characterized by numerous studies (Fairchild and Treble, 2009). The MF3 trace element profiles show pronounced changes in trace element concentrations between growth phases I and II (Fig. 3.4). Between 27.0 to 20.6 mm (growth phase II), Mg concentrations vary from 3538 to 10110 mg/kg, around a mean of 4907 mg/kg. Between 20.6 and 17.0 mm (growth phase I) Mg concentrations are lower and vary between 1946 and 3725 mg/kg around a mean of 2755 mg/kg. Sr concentration for growth interval I vary from 543 to 1208 mg/kg (mean 948 mg/kg), and from 333 to 818 mg/kg (mean 458 mg/kg) for growth interval. U concentrations vary from 6 to 30 mg/kg (mean 12 mg/kg) below, and from 2 to 11 mg/kg (mean 5 mg/kg) above H1. P concentrations vary from 29 to 598 mg/kg (mean 140 mg/kg) below, and from 110 to 717 mg/kg (mean 322 mg/kg) above H1. After H1, at 20.6 mm depth in the sample, concentration peaks in trace elements such as Al (from 0.5 to 1285 mg/kg), Ti (from 1 to 104 mg/kg) and Y (0.1 to 3.5 mg/kg) were determined. Moreover, the peaks in Al, Y and Ti above H1 correlate with a distinct positive shift in the $\delta^{18}O$ profile between 20.3 and 19.7 mm.

3.5. Discussion

3.5.1. Growth phases

Growth phases of stalagmite MF3can provide first information on the climatic conditions at the cave site since stalagmite growth is dependent on the availability of drip water. The inception of stalagmite growth in Schafsloch Cave at 137.4 ± 1.4 ka BP indicates the presence of drip water and cave air temperatures above 0°C (Fig. 3.3). This timing is in good agreement with the onset of speleothem deposition at 136.7 ± 2.8 ka BP in Spannagel Cave (2200-2500 m a.s.l) in Austria (Holzkämper et al., 2005). Such an early inception of speleothem growth in both alpine caves is most likely related to climate-induced switches from a cold- to a warm-based glacier above both caves (Holzkämper et al., 2005; Spötl et al., 2006; Spötl and Mangini, 2007; Fig. 3.5A, B) as a warm-based glacier can keep the cave temperature above 0°C and provide a drip water supply even if mean annual air temperatures at the surface are below the freezing point (Atkinson, 1983, Spötl et al., 2006). Though there is currently no direct geological evidence for the presence of a glacier above Schafsloch Cave as pre-Eemian glacial deposits in this area were eroded by subsequent glaciations, positive $\delta^{13}C$ values of around 6.5‰ are very similar to those values measured in contemporaneously deposited stalagmites from the slightly

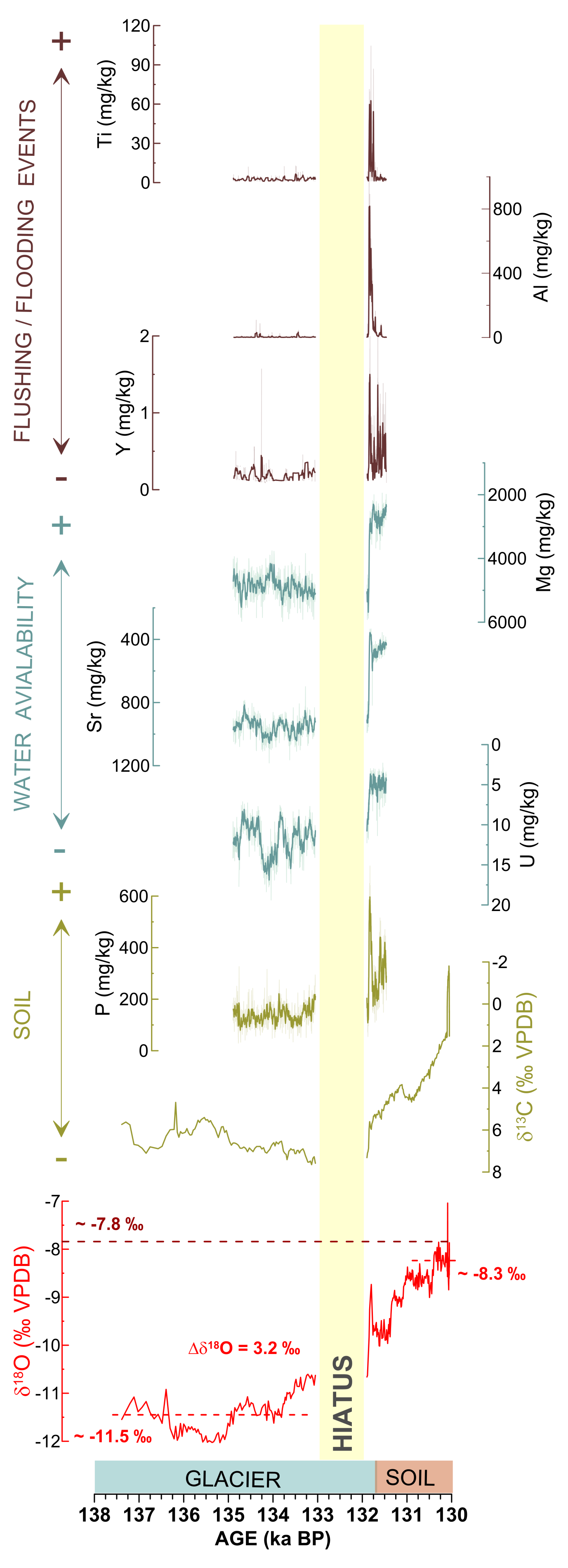

Fig. 3.4. *Trace element and stable isotope profiles for stalagmite MF3. Dashed red line denotes $\delta^{18}O$ values of actively growing stalagmites in Alpeel Cave. Dashed red lines with values denote mean δ18O for growth phases II and I (see also Fig. 3 for further details). The vertical yellow bar denotes the hiatus 1.*

higher elevated Spannagel Cave, which was also covered by a glacier at the beginning of the penultimate deglaciation (Spötl and Mangini, 2007).

The cessation of stalagmite growth between 133.1 ± 0.7 and 131.9 ± 0.6 ka BP is more difficult to explain and could be related to at least three factors: (1) a climate-induced change from a warm- to a cold-based glacier and subsequent cessation of water supply, (2) drop in cave air temperatures below 0 °C due to ice free conditions and lack of an insulating effect of the ice above the cave, and (3) a temporary blocking of the fissure feeding stalagmite MF3 with water (Fig. 3.5C). The latter hypothesis appears to be rather unlikely considering the evidence from Spannagel Cave where the growth of several stalagmites also ceased at 133.0 ± 0.9 ka BP due to a cold spell and glacier re-advance (Spötl et al., 2006; Spötl and Mangini, 2007). Considering the elevation of Schafsloch Cave (1890 a.s.l.) makes it rather unlikely that the area was ice-free at around 133.1 ± 0.7 ka BP. Rather, we suggest that the glacier above the Schafsloch Cave changed its thermal state again from a cold- to a warm-based glacier (Fig. 3.5D). It is therefore more likely that the 1.2 ka-long hiatus (H1) in stalagmite MF3 is related to a return to colder and drier climatic conditions and decrease in seasonality (colder summers) (Spötl et al., 2006).

Growth of stalagmite MF3 resumed at 131.9 ± 0.6 ka BP and indicates a change from cold- to warm-based glacier and its subsequent retreat and an increase in MAAT above 0°C. The final cessation of MF3 stalagmite growth occurs at 130.1 ± 0.5 ka BP, whereas the ultimate cause for final cessation remains enigmatic.

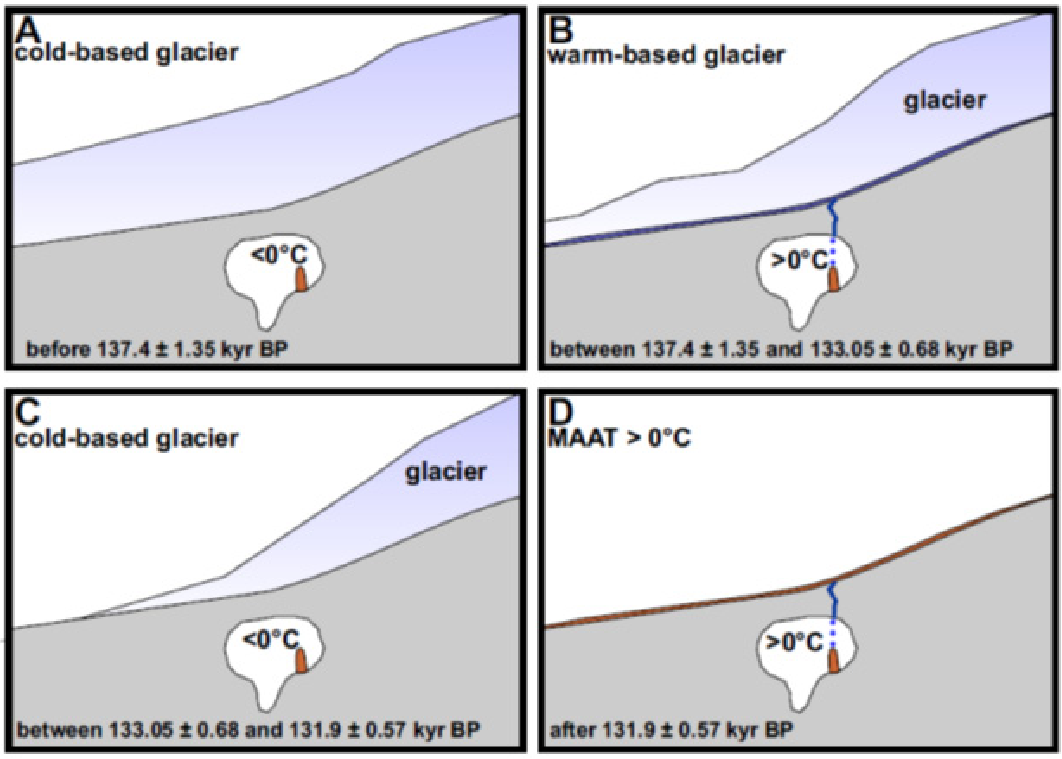

Fig. 3.5. A-D *Schematic model of the environmental conditions above Schafsloch Cave during the penultimate deglaciation.*

3.5.2. PALAEOCLIMATIC SIGNIFICANCE OF OXYGEN AND CARBON ISOTOPES

The oxygen isotopic composition of speleothems is primarily controlled by variations in $\delta^{18}O$ of the seepage water and precipitation above the cave, whereas fluctuations in $\delta^{18}O$ of precipitation are closely related to climatic changes (Lachniet, 2009).

A key-question is whether stalagmite MF3 covers T-II in full, as its growth stops already at 130.1 ± 0.5 ka BP (Fig. 3.3). At least two observations suggest that T-II is indeed captured by the MF3 record. First, $\delta^{18}O$ values (Fig. 3.4) of around -7.9 ‰ at around 130.1± 0.5 ka BP are close to modern calcite values of around -7.6 ‰ (-7.8 ‰ when the altitude effect of around 0.2 ‰ per 100 meters (Schürch et al., 2003) is taken into account) in the nearby Alpeel Cave (Alpstein Mts. , 1774 m a.s.l.; Fig. 3.1), and also very close to Eemian $\delta^{18}O$ values of around –9 ‰ in stalagmites from Spannagel Cave (Holzkämper et al., 2004, 2005). Secondly, the increase of ~3.5 ‰ in the MF3 $\delta^{18}O$ record across the penultimate deglaciation is almost identical to the positive isotopic shift of around 3.0 ‰ in contemporaneously deposited speleothems from Spannagel Cave (Holzkämper et al., 2005; Spötl and Mangini, 2007). We therefore assume that T-II is almost fully covered by stalagmite MF3.

The positive shift of 3.5 ‰ in the MF3 $\delta^{18}O$ record (Fig. 3.4) can be related to several effects such as changes in (1) $\delta^{18}O$ of North Atlantic surface water ("ice volume effect"), (2) air mass trajectories ("moisture source effect"), (3) air temperature ("temperature effect"), (4) the seasonality of precipitation and (5) cave air temperature.

The 3.2 ‰ positive shift in $\delta^{18}O$ cannot be explained alone by a change in $\delta^{18}O$ of North Atlantic surface water. Assuming that seawater $\delta^{18}O$ decreases by 0.08 ± 0.02‰ per 10 meters of global sea level rise, the increase of ~120 m in global sea level (Fig. 3.6A) across T-II accounts for only a 1 ‰ negative shift in $\delta^{18}O$ seawater (Duplessy et al., 2007). The "ice volume effect" is therefore not responsible for the positive shift of around 3.2 ‰ in calcite $\delta^{18}O$. A significant change in the moisture source cannot be ruled out completely, but it is reasonable to assume that the Atlantic was the main vapor source throughout the penultimate deglaciation. Because $\delta^{18}O$ of modern precipitation in Switzerland is strongly governed by air temperature (Schürch et al., 2003; Kern et al., 2013), the distinct positive shift in the MF3 $\delta^{18}O$ profile is most likely related to an increase in air temperature above Schafsloch Cave. At present, the $\delta^{18}O$-temperature relation ($d\delta^{18}O/dT$) at high alpine sites in Switzerland is around 0.7‰/°C, a value that is only slightly higher compared to 0.6‰/°C at lower elevated sites in Switzerland and central Europe (Rozanski et al., 1997; Schürch et al., 2003). This $\delta^{18}O/dT$ relationship could vary over time, which limits the use of MF3 $\delta^{18}O$ values for precise quantitative temperature reconstruction across T-II. A rough estimation, however, is possible. Taking the modern $d\delta^{18}O/dT$ relationship of 0.7‰, the temperature-dependent fraction of $\delta^{18}O$ during calcite precipitation ranging between 0.17 - 0.22 ‰/°C; Kim and O`Neil, 1997; Tremaine et al., 2011) and the positive shift of ~1‰ in $\delta^{18}O$ of Atlantic surface water into account, the net isotopic shift of around 4.2‰ translates to an increase in mean annual air temperature of around 8.0 °C above Schafsloch Cave during the penultimate deglaciation. This glacial/interglacial temperature shift compares with other marine and terrestrial archives covering T-II, which provide evidence for a rapid increase of between 8° and 14.0 ± 2.7 °C in mean annual air temperature across T-II (Wainer et al., 2011; Brewer et al., 2008; Sanchez-Goni et al., 2012; Martrat et al., 2014). The small mismatch could indicate an additional influence of seasonal changes in precipitation and/or infiltration on $\delta^{18}O$ of cave drip water, an effect that has been also observed in a contemporaneously deposited stalagmite from Villars Cave (Wainer et al., 2011).

Speleothem calcite $\delta^{13}C$ values are sometimes difficult to interpret in terms of climatic and environmental changes as they can be influenced by multiple factors acting within the soil zone, the karst aquifer and the cave system. The most decisive factors include changes in (1) the density and type of vegetation (proportion of C3 and C4 plants), (2) microbial processes in the soil zone, (3) recharge conditions (closed versus open system dissolution) and (4) CO_2 degassing. In general, $\delta^{13}C$ calcite values of -14 to -6‰ and -6 to +2‰ can be indicative of C3 and C4 vegetation respectively (McDermott, 2004; Frisia and Borsato, 2010). Soil microbial activity will be enhanced at higher temperatures and soil moisture, which would lead to lower $\delta^{13}C$ values in the stalagmite (McDermott, 2004; Spötl et al., 2005; Fleitmann et al., 2009; Rudzka et al., 2011). However, recharge conditions and equilibration of infiltrating water with soil CO_2 are additional parameters influencing $\delta^{13}C$ values in speleothems, particularly when soils are thin or absent above the cave. Finally, low drip rates and ventilation of the cave can lead to enhanced CO_2 degassing and thus elevated calcite $\delta^{13}C$ values (Baker et al., 1997; Mühlinghaus et al., 2009; Deininger et al., 2012). In high alpine caves, speleothems derived from pure atmospheric CO_2 source can be as heavy as + 6 ‰ VPDB, with higher values indicating kinetic isotope fractionation (Spötl et al., 2004).

Stalagmite MF3 $\delta^{13}C$ values of around 6.5‰ between 137.4 ±1.4 and 133.1 ± 0.7 ka BP indicate both a lack of soil-derived CO_2 in seepage water due to ice above Schafsloch Cave (Fig. 3.4). Thus, $\delta^{13}C$ values are primarily influenced by bedrock $\delta^{13}C$ of the Seewerkalk Formation (approx. +2‰; Wissler et al., 2003) and degassing effects due to very slow drip rates within Schafsloch Cave. MF3 $\delta^{13}C$ values decrease rapidly after 131.9 ± 0.6 ka BP until values of around -2‰ are reached at around 131.3 ± 0.8 ka BP, reflecting an increasing contribution of biogenic carbon as a result of soil and vegetation development above Schafsloch Cave. This assumption is also supported by our observations of growth phase I under UV-light, where content of organic matter appears to be generally higher compared to growth phase II (Fig. 3.2). It is also noteworthy that these $\delta^{13}C$ values are even more negative than those obtained from a present-day stalactite (-0.4‰ VPDB) from the nearby Alpeel Cave (Alpstein Mts., 45 m length, 1774 m alt., Fig. 3.1).

3.5.3. TRACE ELEMENTS

Trace elements can provide additional climatic and environmental information and, thus, complement stable isotope records. They are transported as particles, solutes or adsorbed onto colloids and incorporated in calcite according to their concentration in the drip water (Fairchild and Treble, 2009). For this study, Mg, Al, P, Ti, Sr, Y and U were used as they are well-established indicators for effective rainfall, groundwater residence time, soil processes, erosion and growth rate (Fairchild and McMillan, 2007; McDonald et al., 2004; Roberts et al., 1998; Zhou et al., 2005).

Higher concentrations of Mg and U are commonly interpreted to reflect longer residence times of water in the aquifer above the cave at times of lower effective recharge and precipitation respectively (Baldini et al., 2002; Hellstrom and McCulloch, 2000; McDonald et al., 2004). In addition, Mg and U contents are also related to prior calcite precipitation at times of low effective moisture (Fairchild and McMillan, 2007; Drysdale et al., 2009). Treble et al., (2003) suggest that fluctuations in Sr are related to changes in stalagmite growth rate and soil processes, whereas P is often used as an indicator for soil and vegetation productivity linked to both temperature and precipitation changes (Borsato et al., 2007; Fairchild et al., 2001; Treble et al., 2003). Rare earth elements, such as Y and Ti, are not frequently used, but they are considered to be indicators for enhanced weathering of the overlying soil and host rock during wetter climatic conditions (Richter et al., 2004; Zhou et al., 2008). Y can be used as a tracer for detrital (including colloidal) transport and rainfall proxy (Schimpf et al., 2011, whereas concentrations of Ti can vary in concert with detritus content due to its extremely low solubility (Fairchild and Baker, 2012). Another element that is typically incorporated in the fine-grained detrital layers deposited on speleothems during flooding events is Al (Borsato et al., 2007). Ti, Y and Al are thus common in so-called "impulse laminae", which are formed during high infiltration events and associated enhanced mobilization of colloids and particles from soils and debris above Schafsloch Cave (Fairchild and Treble, 2009; Fairchild and Baker, 2012).

Varying trace element concentrations in stalagmite MF3 are therefore additional proxies for changes in precipitation and groundwater residence time (Mg, U), growth rate (Sr), soil processes (P) and input of detrital material (Ti, Y, Al) (Fig. 3.4). The abrupt decrease in U and Mg concentrations immediately after 131.9 ± 0.6 ka BP and their low contents (compared to growth phase II between 137.4 ± 1.4 and 133.1 ± 0.7 ka BP) is strong evidence for higher precipitation and shorter groundwater residence times. The inverse correlation between the U and P profiles supports our interpretation that U concentrations are related to bedrock dissolution processes. The distinct and short-lived peaks in Ti, Y and Al at the beginning of growth phase I (Fig. 3.4) clearly exceeding background variability and are most likely related to erosion of glacial debris and high infiltration of water (lower Mg and U concentrations), supporting our assumption that the glacier covered Schafsloch Cave until 133.1 ± 0.5 ka BP. The higher P content during growth phase I (131.9 ± 0.6 – 130.1 ± 0.5 ka BP) is related to climatic amelioration and development of soil and vegetation above the cave. Overall, the observed trace element pattern supports our interpretation of a rapid disintegration of the glacier above Schafsloch Cave and a significant increase in temperature and precipitation immediately after 131.9 ± 0.6 ka BP.

3.5.4. Timing of the penultimate deglaciation

The precise chronology and high temporal resolution of the stalagmite MF3 isotope (~20 yr resolution) and trace element (< 1 yr resolution) records allows us to study the inception and progression of the penultimate deglaciation in the Swiss Alps, and to compare the timing of the midpoint of T-II in the Swiss Alps with other absolutely dated stalagmite records.

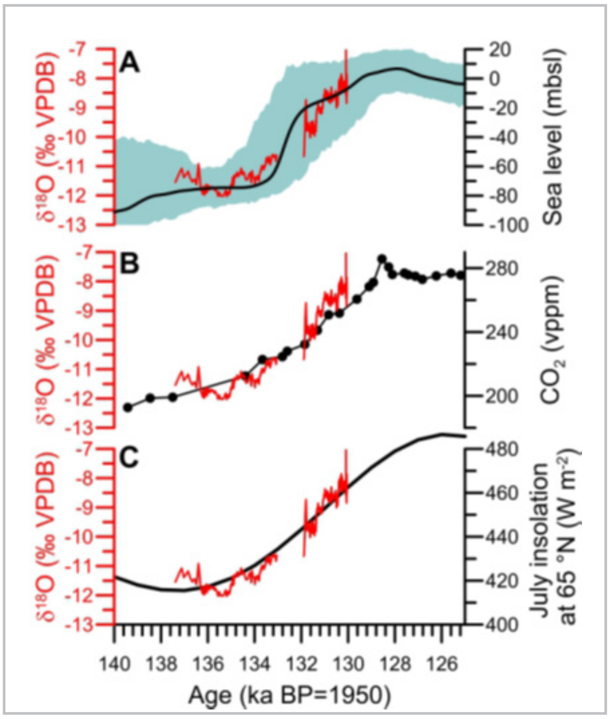

Fig. 3.6. *Comparison of the Schafsloch $\delta^{18}O$ profile (red curves in A-C) with (**A**) smoothed global sea level (Grant et al., 2012; blue shaded area denotes the 95% confidence intervals), (**B**) carbon dioxide concentration in ice cores from Antarctic (Schneider et al., 2012), and (**C**) summer insolation (July) at 65 °N (Berger and Loutre, 1992).*

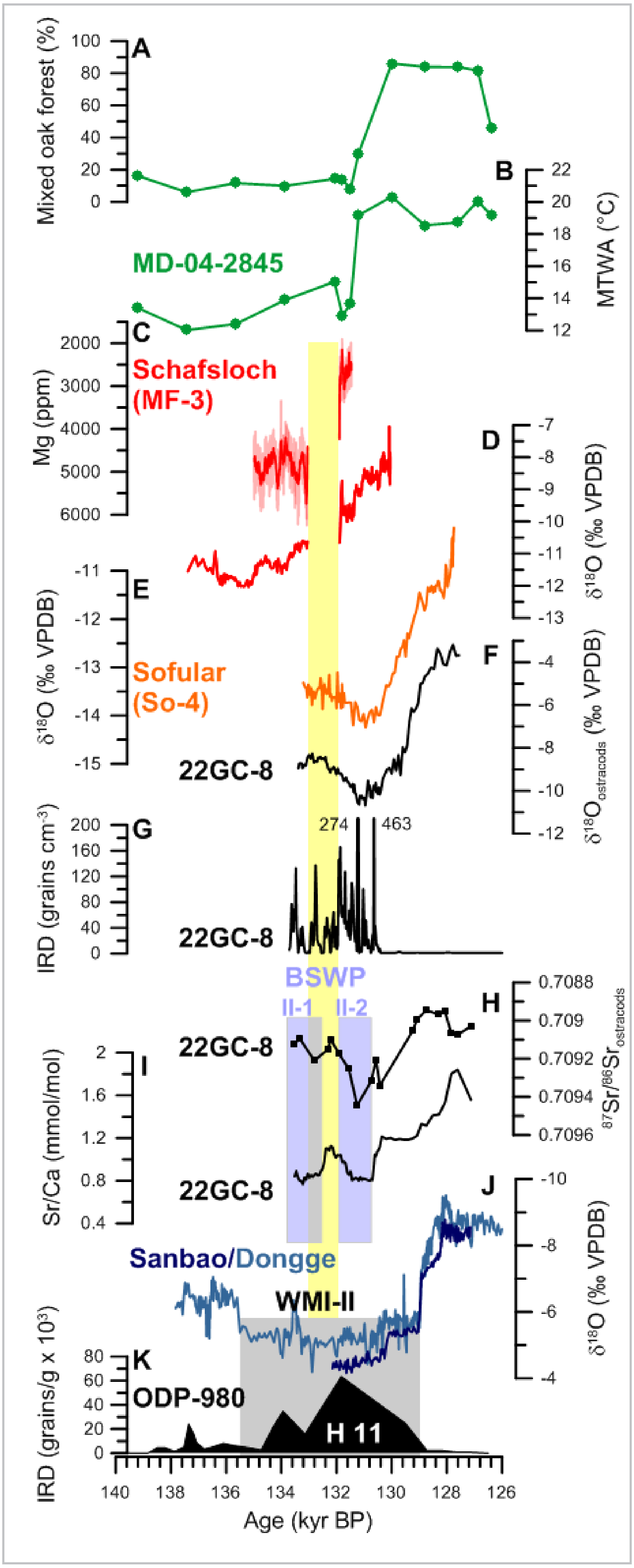

Fig. 3.7. Comparison of palaeoclimate records covering the penultimate deglaciation. ***A*** *Mixed oak forest and* ***B*** *pollen-based summer temperature reconstructions in core MD-04-2845 (Goni et al., 2012).* ***C*** *Schafsloch Cave Mg record and* ***D*** *$\delta^{18}O$ record. The yellow vertical bar denotes the hiatus 1 in the stalagmite MF3.* ***E*** *$\delta^{18}O$ record from Sofular Cave (Badertscher et al., 2011).* ***F*** *$\delta^{18}O$ostracod record from the Black Sea (22GC-8; Wegwerth et al., 2014).* ***G*** *Record of ice rafted debris (IRD) in core 22GC-8.* ***H*** *Strontium isotope record derived from the Black Sea. The blue bars denote Black Sea water pulses (BSWP) as identified by Wegwerth et al., 2014.* ***I*** *Core 22GC-8 Sr/Ca record.* ***J*** *Sanbao and Dongge Cave $\delta^{18}O$ record from China (Kelly et al., 2006; Cheng et al., 2009), WMI-II denotes the weak monsoon interval.* ***K*** *The North Atlantic record of ice rafted debris (IRD) (McManus et al., 1999). The age model is based on tuning the IRD record to the Sanbao Cave record, further details are provided by Cheng et al., 2009.*

At Schafsloch Cave the penultimate deglaciation started at 137.4 ± 1.4 ka BP with a change from a cold- to warm-based glacier when summer temperatures rose above 0 °C (modern mean summer temperature at Schafsloch Cave is 8.5°C). This change occurs at a time of low but rising northern hemisphere summer insolation (Fig. 3.6C), and is within age uncertainties also in phase with increasing atmospheric carbon dioxide concentrations in ice cores from East Antarctica (EDC and Talos dome ice cores; Schneider et al., 2013; Fig. 3.6B) and rising global sea level (Grant et al., 2012; Fig. 3.6A). Furthermore, the start of the penultimate deglaciation in the Alps at around 137.4 ± 1.4 ka BP is concurrent with the onset of stalagmite growth in Spannagel Cave at 136.7 ± 2.8 ka BP and in southwestern Oregon (Oregon Caves National Monument; Ersek et al., 2009) at 135.0 ± 1.2 ka BP, and also the beginning retreat of the Laurentide and Scandinavian ice sheets at around ~140 ± 3 ka BP (Wood et al., 2010; Larsen et al., 2009).

The growth cessation of stalagmite MF3 between 133.1 ± 0.7 and 131.9 ± 0.6 ka BP was most likely triggered by a cold spell and an associated change in the thermal state of the glacier (from warm- to cold-based) above Schafsloch Cave (Fig. 3.5C). The timing of this cold episode is in good agreement with the cessation of speleothem growth in Spannagel Cave at around 133 ka BP (Spötl et al., 2006), and appears to be also a feature of stalagmite records from Norway, Spain and France (Lauritzen, 1995; Spötl et al., 2006, Hodge et al., 2008; Genty et al., 2013), albeit chronologies of these records suffer from large (>2 ka BP) chronological uncertainties and age reversals. This cold-spell in the Alps could be related to the “T-II pause” (Gouzy et al., 2004) or a Younger Dryas-type event. Interestingly, a cold anomaly, centered at 131.4 ± 2 ka BP, is also evident in the pollen-derived temperature reconstruction in sediment core MD04-2845 (Goni et al., 2012; Fig. 3.7A, B). Furthermore, this cold spell occurs at a time of rapidly rising sea level (Fig. 3.6A), very weak East Asian Monsoon (EAM) intensity (Fig. 3.7J) and coincides also with Heinrich event 11, suggesting that the cold spell in the Alps might have been triggered by a weakening of the Atlantic Meridional Ocean Circulation (AMOC) due to an increased influx of meltwater and icebergs into the North Atlantic (e.g., Cheng et al., 2009). However, we must emphasize that evidence for a comparable cold event is missing in numerous other records, including in the stalagmite records from Corchia and Nevada Caves (Fig. 3.8D-F). Clearly, further research is required to fully explore the amplitude and spatial extent of this cold anomaly in closer detail.

The recommencement of stalagmite deposition at 131.9 ± 0.6 ka BP coincides with the disintegration of the glacier above Schafsloch Cave within several decades or centuries, as evidenced by a sudden positive shift in $\delta^{18}O$, rapidly decreasing $\delta^{13}C$ values due to an rising contribution of organic carbon, and very distinct spikes in Ti, Al and Y as a result of enhanced inflow of debris by the melting ice (Fig. 3.4). Furthermore, increased precipitation, higher infiltration and shorter groundwater residence times are indicated by a rapid decrease in Mg and U concentrations. The rapid disintegration of the glacier covering Schafsloch Cave is concurrent with a stepwise increase in pollen-derived summer temperatures and mixed oak forest in sediment core MD04-2845 from the European margin at (Goni et al., 2012; Fig. 3.7A, B). This is not surprising since summer temperatures are the key factor for the mass balance of glaciers in the Alps (e.g., Huss et al., 2010). It is noteworthy that stalagmite growth started later in Spannagel Cave at around 129.9 ± 0.9 ka BP, which is probably related to the higher elevation of Spannagel Cave (2250-2500 m asl) compared to Schafsloch Cave (1890 m asl). Almost full interglacial conditions were reached at around 130.3 ± 0.3 ka BP, when MF3 $\delta^{18}O$ calcite values are almost identical to those recorded in modern stalagmites in the nearby Alpeel Cave, and very similar to $\delta^{18}O$ values of -9 ‰ in Eemian speleothems from Spannagel Cave (Holzkämper et al., 2004).Taking the half-height

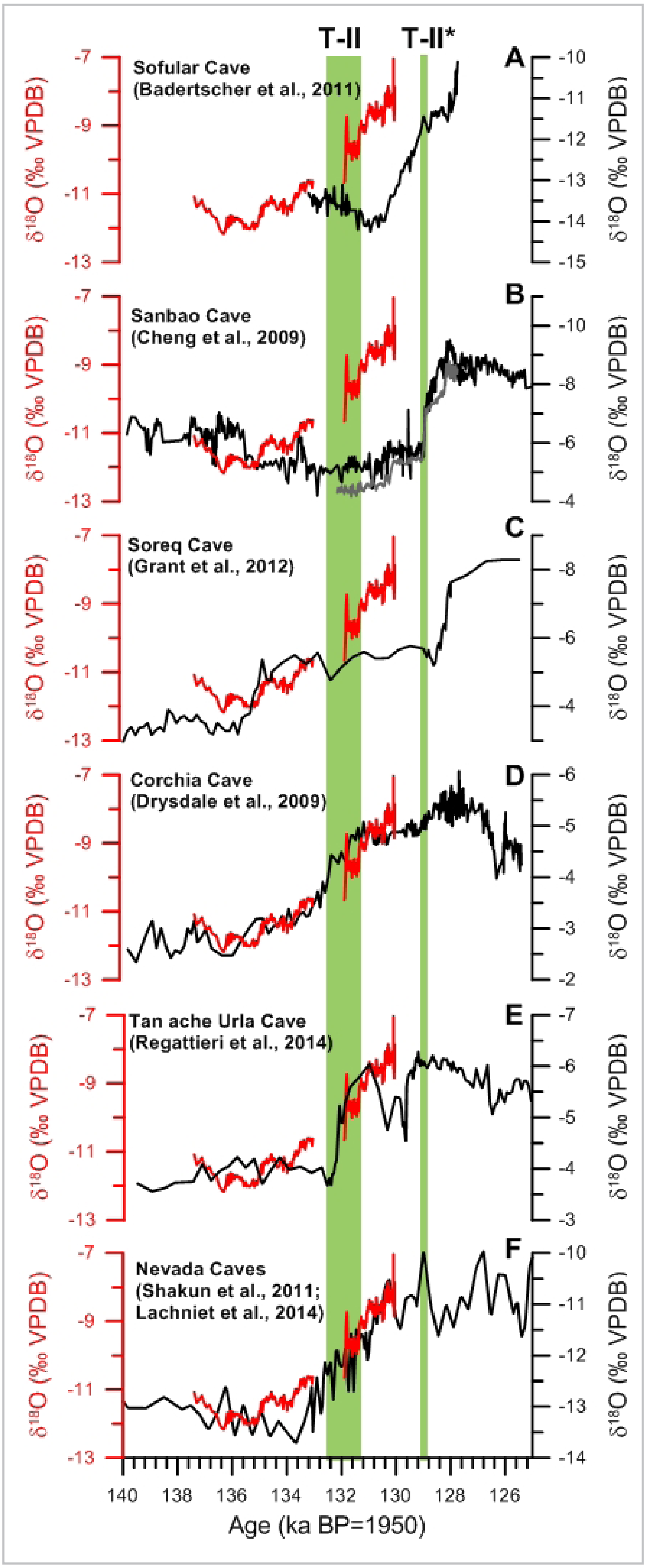

Fig. 3.9. Comparison of the stalagmite MF3 δ18O-profile (A-F) with other ^{230}Th-dated stalagmite records covering the penultimate deglaciation. A Sofular Cave (Badertscher et al., 2011), B Dongge and Sanbao Cave (Kelly et al, 2006; Cheng et al., 2009), C Soreq Cave (Grant et al., 2012), D Corchia Cave (Drysdale et al., 2009), E Tan ache Urla Cave (Regattieri et al., 2014), F Nevada Caves (Shakun et al., 2011; Lachniet et al., 2014). The green vertical bars denote the timing of the midpoint of T-II in stalagmites from Schafsloch, Corchia, Tan ache Urla and Nevada Caves (T-II) and Sanbao Cave (T-II)*

increase of MF3 $\delta^{18}O$ values of around -9.9 ‰ (Fig. 3.4), the timing of the mid-point of T-II should be placed at around 131.8 ± 0.6 ka BP. This date is in excellent agreement with independently derived age estimates for the midpoint of T-II of 131.8 ± 0.6 ka BP in precisely-dated stalagmites from Nevada (Shakun et al., 2011; Lachniet et al., 2014; Fig. 3.8F) and 132.1 ± 1.8 ka BP in stalagmites from Corchia Cave and Tan ache Urla Cave, Italy (Drysdale et al., 2009; Regattieri et al., 2014; Fig. 3.8D, E). Furthermore, the $\delta^{18}O$ profiles of all stalagmites are remarkably similar during the entire penultimate deglaciation, whereas the Nevada Cave composite $\delta^{18}O$ record is also governed by temperature changes in the Great Basin (Shakun et al., 2011; Lachniet et al., 2014). In contrast to Schafsloch and Nevada Caves, variations in $\delta^{18}O$ in the Corchia and Tan ache Urla Cave records are primarily driven by fluctuations in the amount of precipitation (the so-called "amount effect") driven by changes in sea surface temperatures (SST) in the Atlantic and Mediterranean. Because temperatures in the Swiss Alps are strongly influenced by SSTs in the Atlantic (e.g., Huss et al., 2010), a close relationship between the Corchia, Tan ache Urla and Schafsloch $\delta^{18}O$ records can be expected. Taken these evidences together, the temperature-controlled $\delta^{18}O$ stalagmite records from Nevada, Switzerland and Italy place the midpoint of T-II close to132 ka BP. This age, however, is not concurrent with the one in precisely-dated stalagmite $\delta^{18}O$ records from Sanbao Cave (Cheng et al., 2009), Dongge Cave (Kelly et al., 2005), Soreq Cave (Grant et al., 2012) and Sofular Cave (Badertscher et al., 2011). All of these records suggest a much younger age for the midpoint of T-II. The most precise age estimate is provided by the Sanbao Cave record from China, which places the midpoint of T-II at 129.1 ± 0.1 ka BP, and thus 2.8 ± 0.7 ka later compared to the precisely-dated Schafsloch and the Nevada, Tan ache Urla and Corchia cave records. Given the integrity of the ^{230}Th-dating of the Sanbao, Sofular and Schafsloch Cave stalagmites (and all other stalagmites shown in Fig. 3.8), both samples were dated in the same laboratory at the University Minnesota, the age offset cannot be explained by methodological or analytical artefacts. The phase lag between Sanbao Cave (and also Sofular and Soreq Caves) and Schafsloch Cave (and also Corchia and Nevada Caves) is indeed real.

Two further records, Soreq and Sofular Cave (Fig. 3.8A, C), are of limited use for determining the timing of the midpoint of T-II as their $\delta^{18}O$ calcite values are primarily influenced by changes in $\delta^{18}O$ of sea surface waters in the Mediterranean and Black Sea (the so-called "source effect"; Bar-Matthews et al., 2003; Fleitmann et al., 2009; Badertscher et al., 2011). Because seawater $\delta^{18}O$ values of both seas are strongly driven by riverine influx from the Nile and from the Danube/Dniester/Dnieper into the Eastern Mediterranean basin and the Black Sea respectively (particularly when the Black Sea was landlocked; Badertscher et al., 2011), both the Soreq and Sofular $\delta^{18}O$ records are not direct recorders of precipitation and temperature. However, the Soreq Cave $\delta^{18}O$ record holds some information on the strength African monsoonal rainfall in the highlands of Ethiopia, the headwaters of the Blue Nile. The abrupt negative shift shortly after 129 ka BP in the Soreq Cave $\delta^{18}O$ profile reveals a stepwise intensification of the African monsoon and is herefore in very good agreement with the abrupt increase in EAM intensity at 129.1 ± 0.1 ka BP in China.

The different ages between the mid-points of T-II between absolutely-dated stalagmite records appear to be puzzling and there is an apparent systematic age offset between mid-latitudinal and low-latitudinal stalagmite records. However, we propose that this offset can be best explained by the competing effects of insolation forcing and glacial boundary forcing on the intensity of the EAM (and also African monsoon) during the penultimate deglaciation. A detailed comparison between the Schafsloch, Sofular, Sanbao Cave $\delta^{18}O$ records and a Black Sea sediment trace element, Sr isotope and IRD record (core 22GC-8; Wegwerth et al., 2014) helps to shed further light on the mechanisms leading to the delayed and very abrupt response of the EAM. Figure 8 clearly reveals that the transition towards warmer /wetter conditions in Europe and North America occurs during a weak (dry) phase of the EAM, as indicated by high $\delta^{18}O$ values between 135.5 ± 1.0 to 129.1 ± 0.1 ka BP (the so-called "weak monsoon interval" WMI II; Fig. 3.7J) in the Sanbao $\delta^{18}O$ profile (Cheng et al., 2009; Cheng et al., 2006). An abrupt shift of 4‰ in $\delta^{18}O$ at 129.0 ± 0.1 ka BP marks the fast transition into full interglacial conditions and a strong EAM in China (Cheng et al., 2009). The lagged and abrupt response of the EAM has been attributed to cold winter temperature anomalies in the North Atlantic during the WMI II (Cheng et al., 2009), which were probably caused by a weakening of the Atlantic meriodional overturning circulation (AMOC) and reduced surface-ocean heat flux to the North Atlantic as a result of a high influx of meltwater and icebergs (as evidenced by ice rafted debris during Heinrich event 11; Fig. 3.7K) from the rapidly disintegrating ice-sheets. This cold anomaly would have been even amplified by a greater extent of sea-ice, causing longer and more severe winters between 135.5 ± 1.0 to 128.9 ± 0.1 ka BP (Cheng et al., 2009), and also greater snow cover extent in Eurasia. Evidence for extremely cold winters in Eurasia is provided by a record (core 22GC-8) of ice rafted debris (IRD) from the Black Sea (Nowaczyk et al., 2013; Shumilovskikh et al., 2013; Wegwerth et al., 2014; Fig. 3.7G), whereas the uncertainties of this record are around 0.7 ka as its chronology is based on the correlation between the 22GC-8 $\delta^{18}O_{ostracod}$ and the precisely dated Sofular So-6 $\delta^{18}O_{calcite}$ records (see Shumilovskikh et al., 2013 for further details on the chronology of core 22GC-8). The presence of IRD in the 22GC-8 IRD shows that strong winters in Eurasia with extended sea ice in the Black persisted at least until 129.9 ± 0.7 ka BP (Wegwerth et al., 2014), a timing that is in almost perfect agreement with the abrupt increase of EAM intensity at around 129.0 ± 0.1 ka BP in the Sanbao Cave record. Furthermore, both the Sofular and the 22GC IRD records reveal at least two prolonged pulses of meltwater discharge from the disintegrating ice sheets in Eurasia between 133.5 and 132.5 (BSWP-II-1) and 131.5 and 130.5 ka BP (BSWP-II-2) into the Black Sea (Badertscher et al., 2011; Wegwerth et al., 2014; Fig. 3.7E, H, J). Based on Sr-isotope signatures in ostracod shells, Wegwerth et al. (2014) suggest that BSWP-II-2 originated partly from the western Himalaya and entered the Black Sea from the Caspian Sea through the Manych depression (see also Badertscher et al., 2011 for detailed discussion on meltwater routing), providing direct evidence that larger ice sheets persisted at least until 130.5 ± 0.7 ka in Eurasia. Considering these evidences, the persistence of IRD in the Black Sea until 129.9 ± 0.7 ka BP and occurrence of BSWP-II-2 between 131.5 ± 0.7 and 130.5 ± 0.7 ka BP (Fig. 3.7G-I), supports the assumption that cold winters, enhanced snow cover as well as the remaining ice sheets in Eurasia suppressed Asian monsoon intensity until at least 129.9 ± 0.7 ka BP. We thus support the notion that the Asian monsoon and ITCZ responds largely to wintertime cold anomalies in the North Atlantic and Eurasia (e.g., Barnett et al., 1988; Denton et al., 2005; Cheng et al., 2009; Fleitmann et al., 2008), as suggested by Denton et al. (2005): "winter is the common link between Greenland-European temperatures, the Atlantic ITCZ and Asian Monsoons". This is not in contradiction to rising temperatures documented by the Schafsloch, Corchia and Nevada Cave $\delta^{18}O$ records, which can be attributed to insolation-driven increases in summer temperatures. While rising summer temperatures since around 137 ka BP triggered the melting of the glaciers during the penultimate deglaciation, the resultant increased influx of meltwater weakened the AMOC caused colder winter temperatures until at least 129.9 ± 0.7 ka BP. The resultant greater extent of Eurasian snow cover outweighed rising summer insolation and locked the EAM in a weak mode as shown by the Sanbao Cave $\delta^{18}O$ record.

3.6. CONCLUSIONS

High-precision ^{230}Th – dating reveals that stalagmite MF3 was deposited between 137.4 ± 1.4 ka BP and 133.1 ± 0.7 ka BP, and 131.9 ± 0.6 ka BP and 130.1 ± 0.5 ka BP. The onset of the stalagmite growth at 137.4 ± 1.4 ka BP was triggered by a switch in the thermal state of the glacier (from cold- to warm-based) overlying the cave, as a result of increasing summer insolation and temperatures, respectively. The change from warm to cold-based led to a rise in cave air temperature above 0°C and allowed the water to enter the cave. However, δ^{13}C values of around 6.5 ‰ until 131.9 ± 0.6 ka BP indicate a lack of soil-derived CO_2, as the cave was still covered by a glacier. It is therefore most likely that the cessation of stalagmite growth between 133.1 ± 0.7 and 131.9 ± 0.6 ka BP was caused by a distinct temperature drop and associated change from warm to cold-based glacier during Heinrich event 11. Rapidly increasing δ^{18}O values after 131.9 ± 0.6 ka BP indicate a rapid warming and a melting of the glacier within a few decades, an observation that is also supported by rapidly decreasing δ^{13}C values and distinct peaks in Y, Ti and Al. Almost full interglacial conditions were reached at around 130.3 ± 0.3 ka BP when calcite δ^{18}O values of around -8.3 ‰ are comparable with those measured in modern calcite precipitated in the nearby Alpeel Cave. Based on the MF3 δ^{18}O profile we place the timing of the mid-point of T-II at around 131.8 ± 0.6 ka BP, which is in good agreement with precisely-dated records from North America and Europe. Such as early timing of T-II, however, is 2.8 ± 0.7 ka earlier than that recorded in the Sanbao Cave monsoon record from China, which places T-II in the Asian monsoon region at 129.0 ± 0.1 ka BP. The delayed response of the Sanbao Cave monsoon record is related to colder winter temperature anomalies and greater extent of Euroasian snow cover, which is confirmed by high ice drifted debris in the Black Sea sediments until 129.9 ± 0.7 ka BP. This confirms that the Asian monsoon and latitudinal position of the ICTZ during the penultimate deglaciation were strongly influenced by wintertime cold anomalies in the North Atlantic and Euroasia.

BIBLIOGRAPHY

Atkinson, T.C., 1983. Growth Mechanisms of Speleothems in Castleguard Cave, Columbia Icefields, Alberta, Canada. Arctic and Alpine Research 15, 523-536.

Badertscher, S., Fleitmann, D., Cheng, H., Edwards, R.L., Göktürk, O.M., Zumbühl, A., Leuenberg, M., Tüysüz, O., 2011. Pleistocene water intrusions from the Mediterranean and Caspian seas into the Black Sea. Nature Geoscience.

Baker, A., Ito, E., Smart, P.L., McEwan, R.F., 1997. Elevated and variable values of C-13 in speleothems in a British cave system. Chemical Geology 136, 263-270.

Baldini, J.U., McDermott, F., Fairchild, I.J., 2002. Speleothem trace elements as palaeohydrological proxies during the '8,200 year' cold/dry event. Geochim Cosmochim Ac 66, A46-A46.

Bar-Matthews, M., Ayalon, A., Kaufman, A., 2000. Timing and hydrological conditions of Sapropel events in the Eastern Mediterranean, as evident from speleothems, Soreq cave, Israel. Chem Geol 169, 145-156.

Barnett, T.P., Dümenil, L., Schlese, U., Roeckner, E., 1988. The effect of Eurasion snow cover on global climate. Science 239, 504-507.

Barker, S., Diz, P., Vautravers, M.J., Pike, J., Knorr, G., Hall, I.R., Broecker, W.S., 2009. Interhemispheric Atlantic seesaw response during the last deglaciation. Nature 457, 1097-1102.

Bauch, H.A., 2013. Interglacial climates and the Atlantic meridional overturning circulation: is there an Arctic controversy? Quaternary Science Reviews 63, 1-22.

Berger, A.a.L., M.F., 1992. Astronomical solutions for paleoclimate studies over the last 3 million years. Earth and Planetary Science Letters 111, 369-382.

Boch, R., Spotl, C., Frisia, S., 2011. Origin and palaeoenvironmental significance of lamination in stalagmites from Katerloch Cave, Austria. Sedimentology 58, 508-531.

Borsato, A., Frisia, S., Fairchild, I.J., Somogyi, A., Susini, J., 2007. Trace element distribution in annual stalagmite laminae mapped by micrometer-resolution X-ray fluorescence: Implications for incorporation of environmentally significant species. Geochim Cosmochim Ac 71, 1494-1512.

Brewer, S., Guiot, J., Sanchez-Goni, M.F., Klotz, S., 2008. The climate in Europe during the Eemian: a multi-method approach using pollen data. Quaternary Science Reviews 27, 2303-2315.

Broecker, W.S., 2013. What drives glacial cycles? Eldigio Press.

Broecker, W.S., Henderson, G.M., 1998. The sequence of events surrounding Termination II and their implications for the cause of glacial-interglacial CO2 changes. Paleoceanography 13, 352-364.

Carlson, A.E., Winsor, K., 2012. Northern Hemisphere ice-sheet responses to past climate warming. Nature Geosci 5, 607-613

Cheng, H., Edwards, R.L., Broecker, W.S., Denton, G.H., Kong, X., Wang, Y., Zhang, R., Wang, X., 2009. Ice Age Terminations. Science 326, 248-252.

Cheng, H., Edwards, R.L., Shen, C.C., Polyak, V.J., Asmerom, Y., Woodhead, J., Hellstrom, J., Wang, Y.J., Kong, X.G., Spotl, C., Wang, X.F., Alexander, E.C., 2013. Improvements in Th-230 dating, Th-230 and U-234 half-life values, and U-Th isotopic measurements by multi-collector inductively coupled plasma mass spectrometry. Earth and Planetary Science Letters 371, 82-91.

Clemens, S.C., Prell, W.L., 2003. A 350,000 year summer-monsoon multi-proxy stack from the Owen ridge, Northern Arabian sea. Mar Geol 201, 35-51.

Clemens, S.C., Prell, W.L., 2007. The timing of orbital-scale Indian monsoon changes. Quaternary Science Reviews 26, 275-278.

Deininger, M., Fohlmeister, J., Scholz, D., Mangini, A., 2012. Isotope disequilibrium effects: The influence of evaporation and ventilation effects on the carbon and oxygen isotope composition of speleothems - A model approach. Geochim Cosmochim Ac 96, 57-79.

Denton, G.H., Alley, R.B., Comer, G.C., Broecker, W.S., 2005. The role of seasonality in abrupt climate change. Quaternary Science Reviews 24, 1159-1182.

Drysdale, R.N., Hellstrom, J.C., Zanchetta, G., Fallick, A.E., Goni, M.F.S., Couchoud, I., McDonald, J., Maas, R., Lohmann, G., Isola, I., 2009. Evidence for Obliquity Forcing of Glacial Termination II. Science 325, 1527-1531.

Duplessy, J.C., Roche, D.M., Kageyama, M., 2007. The Deep Ocean During the Last Interglacial Period. Science 316, 89-91.

Ersek, V., Hostetler, S.W., Cheng, H., Clark, P.U., Anslow, F.S., Mix, A.C., Edwards, R.L., 2009. Environmental influences on speleothem growth in southwestern Oregon during the last 380 000 years. Earth Planet Sc Lett 279, 316-325.

Fairchild, I.J., Baker, A., 2012. Speleothem Science: From Process to Past Environments. Wiley-Blackwell.

Fairchild, I.J., Baker, A., Borsato, A., Frisia, S., Hinton, R.W., McDermott, F., Tooth, A.F., 2001. Annual to sub-annual resolution of multiple trace-element trends in speleothems. J Geol Soc London 158, 831-841.

Fairchild, I.J., McMillan, E.A., 2007. Speleothems as indicators of wet and dry periods. Int J Speleol 36, 69-74.

Fairchild, I.J., Treble, P.C., 2009. Trace elements in speleothems as recorders of environmental change. Quaternary Science Reviews 28, 449-468.

Fleitmann, D., Burns, S.J., Neff, U., Mangini, A., Matter, A., 2003. Changing moisture sources over the last 330,000 years in Northern Oman from fluid-inclusion evidence in speleothems. Quaternary Res 60, 223-232.

Fleitmann, D., Cheng, H., Badertscher, S., Edwards, R.L., Mudelsee, M., Göktürk, O.M., Fankhauser, A., Pickering, R., Raible, C.C., Matter, A., Kramers, J., Tüysüz, O., 2009. Timing and climatic impact of Greenland interstadials recorded in stalagmites from northern Turkey. Geophys Res Lett 36.

Fleitmann, D., Burns, S.J., Pekala, M., Mangini, A., Al-Subbary, A., Al-Aowah, M., Kramers, J., Matter, A., 2011. Holocene and Pleistocene pluvial periods in Yemen, southern Arabia. Quaternary Science Reviews 30, 783-787.

Florineth, D., Schlüchter, C., 2000. Alpine Evidence for Atmospheric Circulation Patterns in Europe during the Last Glacial Maximum. Quaternary Res 54, 295-308.

Fricker, M.B., 2012. Design of ablation cells for LA-ICP-MS: from modeling to high spatial resolutionanalysis applications. ETH Zürich.

Frisia, S., Borsato, A., Fairchild, I.J., McDermott, F., 2000. Calcite fabrics, growth mechanisms, and environments of formation in speleothems from the Italian Alps and southwestern Ireland. J Sediment Res 70, 1183-1196.

Frisia, S., Borsato, A., 2010. Karst, In: Alonso-Zarza, A.M., Tanner, L.H. (Eds.), Carbonates in Continental Settings: Facies, Environments, and Processes. Elsever, Amsterdam, pp. 269-318.

Genty, D., Verheyden, S., Wainer, K., 2013. Speleothe records over the last interglacial PAGES news 21, 24-25.

Gouzy, A., Malaize, B., Pujol, C., Charlier, K., 2004. Climatic «pause» during Termination II identified in shallow and intermediate waters off the Iberian margin. Quaternary Science Reviews 23, 1523-1528.

Grant, K.M., Rohling, E.J., Bar-Matthews, M., Ayalon, A., Medina-Elizalde, M., Ramsey, C.B., Satow, C., Roberts, A.P., 2012. Rapid coupling between ice volume and polar temperature over the past 150,000 years. Nature 491, 744-747.

Gruber, S., Haeberli, W., 2009. Mountain Permafrost, In: Margesin, R. (Ed.), Permafrost Soils. Springer Berlin Heidelberg, pp. 33-44.

Hai, C., Edwards, R.L., Chuan-Chou, S., Victor, J.P., Yemane, A., Jon, W., John, H., Yongjin, W., Xinggong, K., Christoph, S., Xianfeng, W., Alexander, E.C., 2013. Improvements in 230 Th dating, 230 Th and 234 U half-life values, and U-Th isotopic measurements by multi-collector inductively coupled plasma mass spectrometry. Earth Planet Sc Lett 371-372, 82-91.

Hellstrom, J.C., McCulloch, M.T., 2000. Multi-proxy constraints on the climatic significance of trace element records from a New Zealand speleothem. Earth Planet Sc Lett 179, 287-297.

Henderson, G.M., Slowey, N.C., 2000. Evidence from U-Th Dating against Northern Hemisphere forcing of the penultimate deglaciation. Nature 404, 61-66.

Hodge, E.J., Richards, D.A., Smart, P.L., Andreo, B., Hoffmann, D.L., Mattey, D.P., González-Ramón, A., 2008. Effective precipitation in southern Spain (266 to 46 ka) based on a speleothem stable carbon isotope record. Quaternary Res 69, 447-457.

Holzkämper, S., Mangini, A., Spotl, C., Mudelsee, M., 2004. Timing and progression of the Last Interglacial derived from a high alpine stalagmite. Geophysical Research Letters 31.

Holzkämper, S., Spotl, C., Mangini, A., 2005. High-precision constraints on timing of Alpine warm periods during the middle to late Pleistocene using speleothem growth periods. Earth Planet Sc Lett 236, 751-764.

Huss, M., Hock, R., Bauder, A., Funk, M., 2010. 100-year mass changes in the Swiss Alps linked to the Atlantic Multidecadal Oscillation. Geophysical Research Letters 37.

Huybers, P., Wunsch, C., 2004. A depth-derived Pleistocene age model: Uncertainty estimates, sedimentation variability, and nonlinear climate change. Paleoceanography 19.

Johnston, V.E., Borsato, A., Spotl, C., Frisia, S., Miorandi, R., 2013. Stable isotopes in caves over altitudinal gradients: fractionation behaviour and inferences for speleothem sensitivity to climate change. Clim Past 9, 99-118.

Kelly, M.J., Edwards, R.L., Cheng, H., Yuan, D.X., Cai, Y.J., Zhang, M.L., Lin, Y.S., An, Z.S., 2006. High resolution characterization of the Asian Monsoon between 146,000 and 99,000 years BP from Dongge Cave, China and global correlation of events surrounding Termination II. Palaeogeogr Palaeocl 236, 20-38.

Kern, Z., Kohán, B., Leuenberger, M., 2013. Monthly resolved biannual precipitation oxygen isoscape for Switzerland. Atmos. Chem. Phys. Discuss. 13, 9895-9916.

Kim, S.T., ONeil, J.R., 1997. Equilibrium and nonequilibrium oxygen isotope effects in synthetic carbonates. Geochim Cosmochim Ac 61, 3461-3475.

Kovacs, R., Nishiguchi, K., Utani, K., Gunther, D., 2010. Development of direct atmospheric sampling for laser ablation-inductively coupled plasma-mass spectrometry. J Anal Atom Spectrom 25, 142-147.

Lachniet, M.S., 2009. Climatic and environmental controls on speleothem oxygen-isotope values. Quaternary Science Reviews 28, 412-432.

Lachniet, M.S., Denniston, R.F., Asmerom, Y., Polyak, V.J., 2014. Orbital control of western North America atmospheric circulation and climate over two glacial cycles. Nat Commun 5.

Landais, A., Dreyfus, G., Capron, E., Jouzel, J., Masson-Delmotte, V., Roche, D.M., Prie, F., Caillon, N., Chappellaz, J., Leuenberger, M., Lourantou, A., Parrenin, F., Raynaud, D., Teste, G., 2013. Two-phase change in CO2, Antarctic temperature and global climate during Termination II. Nature Geosci 6, 1062-1065.

Lane, C.S., Brauer, A., Blockley, S.P.E., Dulski, P., 2013. Volcanic ash reveals time-transgressive abrupt climate change during the Younger Dryas. Geology.

Larsen, N.K., Knudsen, K.L., Krohn, C.F., Kronborg, C., Murray, A.S., Nielsen, O.L.E.B., 2009. Late Quaternary ice sheet, lake and sea history of southwest Scandinavia – a synthesis. Boreas 38, 732-761.

Lauritzen, S.E., 1995. High-Resolution Paleotemperature Proxy Record for the Last Interglaciation Based on Norwegian Speleothems. Quaternary Res 43, 133-146.

Linge, H., Baker, A., Andersson, C., Lauritzen, S.E., 2009. Variability in luminescent lamination and initial Th-230/Th-212 activity ratios in a late Holocene stalagmite from northern Norway. Quaternary Geochronology 4, 181-192.

Masson-Delmotte, V., Stenni, B., Blunier, T., Cattani, O., Chappellaz, J., Cheng, H., Dreyfus, G., Edwards, R.L., Falourd, S., Govin, A., Kawamura, K., Johnsen, S.J., Jouzel, J., Landais, A., Lemieux-Dudon, B., Lourantou, A., Marshall, G., Minster, B., Mudelsee, M., Pol, K., Rothlisberger, R., Selmo, E., Waelbroeck, C., 2010. Abrupt change of Antarctic moisture origin at the end of Termination II. P Natl Acad Sci USA 107, 12091-12094.

McDermott, F., 2004. Palaeo-climate reconstruction from stable isotope variations in speleothems: a review. Quaternary Science Reviews 23, 901-918.

McDonald, J., Drysdale, R., Hill, D., 2004. The 2002-2003 El Nino recorded in Australian cave drip waters: Implications for reconstructing rainfall histories using stalagmites. Geophys Res Lett 31.

Meckler, A.N., Sigman, D.M., Gibson, K.A., Francois, R., Martinez-Garcia, A., Jaccard, S.L., Rohl, U., Peterson, L.C., Tiedemann, R., Haug, G.H., 2013. Deglacial pulses of deep-ocean silicate into the subtropical North Atlantic Ocean. Nature 495, 495-498.

Mühlinghaus, C., Scholz, D., Mangini, A., 2009. Modelling fractionation of stable isotopes in stalagmites. Geochim

Cosmochim Ac 73, 7275-7289.

Nowaczyk, N.R., Arz, H.W., Frank, U., Kind, J., Plessen, B., 2012. Dynamics of the Laschamp geomagnetic excursion from Black Sea sediments. Earth Planet. Sci. Lett. 351–352, 54–69.

Preusser, F., Graf, H., Keller, G., Krayss, E., Schluchter, C., 2011. Quaternary glaciation history of northern Switzerland. Quaternary Science Journal 60, 282-305.

Proctor, C.J., Baker, A., Barnes, W.L., Gilmour, R.A., 2000. A thousand year speleothem proxy record of North Atlantic climate from Scotland. Climate Dynamics 16, 815-820.

Railsback, L.B., Akers, P.D., Wang, L.N., Holdridge, G.A., Riavo Voarintsoa, N., 2013. Layer-bounding surfaces in stalagmites as keys to better paleoclimatological histories and chronologies. Int J Speleol 42, 167-180.

Ramseyer, K., Miano, T.M., D›Orazio, V., Wildberger, A., Wagner, T. and Geister, J., 1997. Nature and origin of organic matter in carbonates from speleothems, marine cements and coaral skeletons. Organic Geochemistry 26, 361-378.

Regattieri, E., Zanchetta, G., Drysdale, R.N., Isola, I., Hellstrom, J.C., Roncioni, A., 2014. A continuous stable isotope record from the penultimate glacial maximum to the Last Interglacial (159-121 ka) from Tana Che Urla Cave (Apuan Alps, central Italy). Quaternary Research 82, 450-461.

Richter, D.K., Gotte, T., Niggemann, S., Wurth, G., 2004. REE3+ and Mn2+ activated cathodoluminescence in lateglacial and Holocene stalagmites of central Europe: evidence for climatic processes? Holocene 14, 759-767.

Roberts, M.S., Smart, P.L., Baker, A., 1998. Annual trace element variations in a Holocene speleothem. Earth Planet Sc Lett 154, 237-246.

Rozanski, K., Johnsen, S.J., Schotterer, U., Thompson, L.G., 1997. Reconstruction of past climates from stable isotope records of palaeo-precipitation preserved in continental archives. Hydrolog Sci J 42, 725-745.

Rudzka, D., McDermott, F., Baldini, L.M., Fleitmann, D., Moreno, A., Stoll, H., 2011. The coupled delta C-13-radiocarbon systematics of three Late Glacial/early Holocene speleothems; insights into soil and cave processes at climatic transitions. Geochim Cosmochim Ac 75, 4321-4339.

Sánchez Goñi, M.F., Bakker, P., Desprat, S., Carlson, A.E., Van Meerbeeck, C.J., Peyron, O., Naughton, F., Fletcher, W.J., Eynaud, F., Rossignol, L., Renssen, H., 2012. European climate optimum and enhanced Greenland melt during the Last Interglacial. Geology 40, 627-630.

Scholz, D., Hoffmann, D.L., 2011. StalAge – An algorithm designed for construction of speleothem age models. Quaternary Geochronology 6, 369-382.

Schürch, M., Kozel, R., Schotterer, U., Tripet, J.-P., 2003. Observation of isotopes in the water cycle—the Swiss National Network (NISOT). Env Geol 45, 1-11.

Severinghaus, J.P., 2009. CLIMATE CHANGE Southern see-saw seen. Nature 457, 1093-1094.

Shakun, J.D., Burns, S.J., Clark, P.U., Cheng, H., Edwards, R.L., 2011. Milankovitch-paced Termination II in a Nevada speleothem? Geophys Res Lett 38.

Sodemann, H., Zubler, E., 2010. Seasonal and inter-annual variability of the moisture sources for Alpine precipitation during 1995-2002. Int J Climatol 30, 947-961.

Spötl, C., Fairchild, I.J., Tooth, A.F., 2005. Cave air control on dripwater geochemistry, Obir Caves (Austria): Implications for speleothem deposition in dynamically ventilated caves. Geochim Cosmochim Ac 69, 2451-2468.

Spötl, C., Holzkamper, S., Mangini, A., 2007. The Last and the Penultimate Interglacial as Recorded by Speleothems from a Climatically Sensitive High-Elevation Cave Site in the Alps, In: Sirocko, F., Claussen, M., Litt, T., Sánchez Goñi, M.F. (Eds.), The Climate of Past Interglacials. Developments in Quaternary Science Series. Elsevier, pp. 441-491.

Spötl, C., Mangini, A., 2007. Speleothems and paleoglaciers. Earth Planet Sc Lett 254, 323-331.

Spötl, C., Mangini, A., Bums, S., Frank, N., Pavuza, R., 2004. Speleothems from the High-Alpine Spannagel Cave, Zillertal Alps (Austria), In: Sasowsky, I., Mylroie, J. (Eds.), Studies of Cave Sediments. Springer US, pp. 243-256.

Tabersky, D., Nishiguchi, K., Utani, K., Ohata, M., Dietiker, R., Fricker, M.B., de Maddalena, I.M., Koch, J., Gunther, D., 2013. Aerosol entrainment and a large-capacity gas exchange device (Q-GED) for laser ablation inductively coupled plasma mass spectrometry in atmospheric pressure air. J Anal Atom Spectrom 28, 831-842.

Tan, M., Hou, J.Z., Liu, T.S., 2004. Sun-coupled climate connection between eastern Asia and northern Atlantic. Geophys Res Lett 31, -

Thomas, A.L., 2009. Penultimate Deglacial Sea-Level timing from Uranium/Thorium Dating of corals. Science.

Thompson, W.G., Goldstein, S.L., 2005. Open-system coral ages reveal persistent suborbital sea-level cycles. Science 308, 401-404.

Thompson, W.G., Goldstein, S.L., 2006. A radiometric calibration of the SPECMAP timescale. Quaternary Science Reviews 25, 3207-3215.

Timmermann, A., Menviel, L., 2009. What Drives Climate Flip-Flops? Science 325, 273-274.

Treble, P., Shelley, J.M.G., Chappell, J., 2003. Comparison of high resolution sub-annual records of trace elements in a modern (1911-1992) speleothem with instrumental climate data from southwest Australia. Earth Planet Sc Lett 216, 141-153.

Tremaine, D.M., Froelich, P.N., Wang, Y., 2011. Speleothem calcite farmed in situ: Modern calibration of delta(18) O and delta(13)C paleoclimate proxies in a continuously-monitored natural cave system. Geochimica et Cosmochimica Acta 75, 4929-4950.

Tzedakis, P.C., Palike, H., Roucoux, K.H., de Abreu, L., 2009. Atmospheric methane, southern European vegetation and low-mid latitude links on orbital and millennial timescales. Earth Planet Sc Lett 277, 307-317.

Vaks, A., Bar-Matthews, M., Matthews, A., Ayalon, A., Frumkin, A., 2010. Middle-Late Quaternary paleoclimate of northern margins of the Saharan-Arabian Desert: reconstruction from speleothems of Negev Desert, Israel. Quaternary Science Reviews 29, 2647-2662.

Vaks, A., Woodhead, J., Bar-Matthews, M., Ayalon, A., Cliff, R.A., Zilberman, T., Matthews, A., Frumkin, A., 2013. Pliocene-Pleistocene climate of the northern margin of Saharan-Arabian Desert recorded in speleothems from the Negev Desert, Israel. Earth Planet Sc Lett 368, 88-100.

Waelbroeck, C., Frank, N., Jouzel, J., Parrenin, F., Masson-Delmotte, V., Genty, D., 2008. Transferring radiometric dating of the last interglacial sea level high stand to marine and ice core records. Earth Planet Sc Lett 265, 183-194.

Wainer, K., Genty, D., Blamart, D., Daeron, M., Bar-Matthews, M., Vonhof, H., Dublyansky, Y., Pons-Branchu, E., Thomas, L., van Calsteren, P., Quinif, Y., Caillon, N., 2011. Speleothem record of the last 180 ka in Villars cave (SW France): Investigation of a large delta O-18 shift between MIS6 and MIS5. Quaternary Science Reviews 30, 130-146.

Wanner, H., Rickli, R., Salvisberg, E., Schmutz, C., Schuepp, M., 1997. Global climate change and variability and its influence on Alpine climate - Concepts and observations. Theor Appl Climatol 58, 221-243.

Wegwerth, A., Dellwig, O., Kaiser, J., Menot, G., Bard, E., Shumilovskikh, L., Schnetger, B., Kleinhanns, I.C., Wille, M., Arz, H.W., 2014. Meltwater events and the Mediterranean reconnection at the Saalian-Eemian transition in the Black Sea. Earth and Planetary Science Letters 404, 124-135.

Winograd, I.J., Coplen, T.B., Landwehr, J.M., Riggs, A.C., Ludwig, K.R., Szabo, B.J., Kolesar, P.T., Revesz, K.M., 1992. Continuous 500,000-Year Climate Record from Vein Calcite in Devils-Hole, Nevada. Science 258, 255-260.

Wolff, E.W., Fischer, H., Rothlisberger, R., 2009. Glacial terminations as southern warmings without northern control. Nature Geosci 2, 206-209.

Zhou, H.Y., Chi, B.Q., Lawrence, M., Zhao, J.X., Yan, J., Greig, A., Feng, Y.X., 2008. High-resolution and precisely dated record of weathering and hydrological dynamics recorded by manganese and rare-earth elements in a stalagmite from Central China. Quaternary Res 69, 438-446.

Zhou, J.Z., Lundstrom, C.C., Fouke, B., Panno, S., Hackley, K., Curry, B., 2005. Geochemistry of speleothem records from southern Illinois: Development of (U-234)/(U-238) as a proxy for paleoprecipitation. Chem Geol 221, 1-20.

CHAPTER 4

LATE GLACIAL ENVIRONMENTAL AND TEMPERATURE RECONSTRUCTION IN CENTRAL EUROPE: A MULTI-PROXY AND MULTI-TECHNIQUES APPROACH ON SPELEOTHEMS FROM MILANDRE CAVE (SWISS JURA MOUNTAINS)

In collaboration with Stéphane Affolter[1], Daniel Tabersky[2], Silvia Schmassmann[3], Sebastian Breitenbach[4], Nadia Vogel[5], Hai Cheng[6,7], Detlef Günther[3], Rolf Kiefer [5], Markus Leuenberger[1], Gerald Haug[4], Lawrence R. Edwards[6], Pierre-Yves Jeannin[3], Dominik Fleitmann [8,9]

[1] Climate and Environmental Physics and Oeschger Centre for Climate Change Research, Physics Institute, University of Bern, CH-3012 Bern

[2] Department of Chemistry and Applied Biosciences, Laboratory of Inorganic Chemistry, ETH Zürich, Wolfgang-Pauli-Strasse 10, CH-8093 Zürich

[3] Swiss Institute for Speleology and Karst Studies, P.O. Box 818, CH-2301 La-Chaux-de-Fonds

[4] Geological Institute, ETH Zürich, Sonneggstrasse 5, CH-8092 Zürich

[5] Eawag, Swiss Federal Institute of Aquatic Science and Technology, Department of Water Resources and Drinking Water, Überlandstrasse, Dübendorf, and ETH Zurich, Department of Earth Sciences, Institute of Geochemistry and Petrology, Clausiusstrasse, Zurich, Switzerland

[6] Institute of Global Environmental Change, Xi'an Jiaotong University, Xi'an 710049, China

[7] Department of Geology and Geophysics, University of Minnesota, Minneapolis, Minnesota 55455, USA

[8] Department of Archaeology, School of Human and Environmental Sciences, University of Reading, Whiteknights, PO Box 227, Reading

[9] Institute of Geological Sciences and Oeschger Centre for Climate Change Research, Baltzerstrasse 1+3, CH-3012 Bern

4.1. Introduction

Despite the last deglaciation being one of the most studied climatic intervals, numerous questions still remain with respect to its timing across the North Atlantic region, as regional impact and amplitude of the recorded proxy signals.

The present study focuses on the ultra-high resolution regional fluctuations during the Bölling-Allerød (B/A) and Younger Dryas (YD) in three coeval stalagmites from Milandre Cave in Switzerland. By replication of the isotopic time series in coeval stalagmites from the same cave we achieved the best confidence for this new data-set (Lachniet, 2009, Fohlmeister, 2012). Previous studies confirmed that stable isotopes in speleothems from Milandre Cave capture local and regional climatic fluctuations (Schmassmann, 2010, Hasenfratz, 2012, Affolter et al, 2015). A good understanding of the factors controlling the isotopic composition in the speleothems from Milandre Cave was achieved through monitoring studies in the cave (Affolter et al., submitted in revised form) and a strong correlation between calcite oxygen isotope ($\delta^{18}O$) values and surface temperature between 1700 and 1950 AD (Hasenfratz et al., in prep.). Calcite $\delta^{18}O$ values of speleothems in Milandre Cave therefore reflect long-term evolution (millennial-scale) of mean annual temperature with a bias toward the cold season, conditions similar to the ones described for Bunker Cave site, Germany (Fohlmeister, 2012).

The purpose of this study is three-fold: i) to reconstruct regional climate-induced environmental changes during the B/A and YD, independently dated and at a high-resolution scale, ii) to confirm the $\delta^{18}O$/°C transfer function calculated by Hasenfratz et al. (in prep.) by using different independent approaches (calcite $\delta^{18}O$, $\delta^{18}O$ and δD in fluid inclusions, and noble gasses in fluid inclusions), and iii) to obtain absolute annual-decadal temperature changes at the surface of the cave using the calculated transfer function.

4.2. Site and sample description

Milandre Cave, is located in the Ajoie region of the Swiss Jura Mountains (47°49’N/ 7°02’E, 400 masl, Fig. 4.1), which represent the first significant orographic boundary for the moist and mild maritime air originating from the North Atlantic Ocean. Precipitation is therefore strongly controlled by westerly propagated air masses. The Eastern part of the Jura Mountains is almost completely shielded from a Mediterranean influence, with the Swiss Alps acting as a weather divide (MeteoSchweiz; Veit, 2002). The Alpine barrier is most efficient during winter, while during summer the Mediterranean moisture sources shift their position with about 14° northerly latitude and are able to contribute to the total local moisture budget by up to about 17.3 ± 5.7 % (Sodemann and Zauber, 2011). Precipitation and temperature is measured at the nearby Fahy meteorological station (47°42’N/ 6°94’E, 596 masl, 200 m higher than our cave site) which is operated by the Swiss Federal Office of Meteorology and Climatology (MeteoSchweiz). For the interval 1961-1990 mean annual precipitation rate is 1037 mm/year and mean annual air temperature (MAAT) 8.1 °C. The values changed for the 1990-2012 interval, with increased values of 1077 mm/year, and MAAT 9.2 °C (Fig. 4.1). Of importance for our study is mean autumn to spring temperature (October-May) of 5.7°C, and the mean summer temperature (JJA) of 17.1°C. Precipitation is relatively equal over the year; with precipitation averaging 292 mm in summer and 224 mm in winter. Snowfall may occur from November to March, although this region exhibits a mild climate during winter (mean temperature above 0°C, MeteoSchweiz).

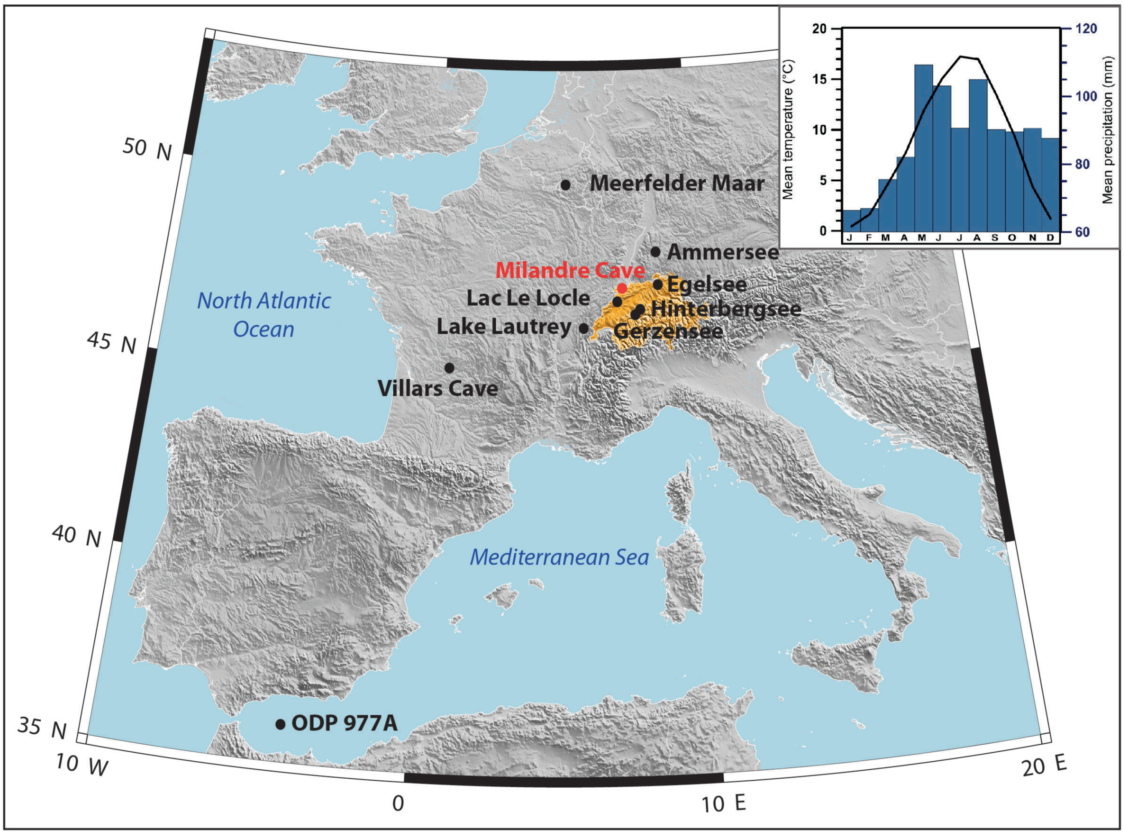

Figure 4.1. Location of the Milandre Cave and the other sites mentioned in the text. Right corner: Monthly averages of temperature and precipitation measured at Fahy meteorological station (near Milandre Cave).

Milandre Cave was developed in the limestone of the St.-Ursanne Formation, only 30-80 m below the surface. Nowadays, the bedrock is covered by less than 60 cm of soil, and a cardamine beech forest has developed above the cave. The cave is on two levels, with the lower level developing around 30 m below a fossil gallery. The lower level is active and used by the underground Milandrine River. Three stalagmites (M2, M6, M8) were collected from the Galerie des Fistuleuses, the upper level of the cave, about 450-500 m from the natural entrance. The temperature in this gallery is 9.8 ± 0.2°C (Affolter et al., submitted in revised form), with < 100 l/s air flow, humidity 100% and pCO_2 from 0.3 to 1.41 % (continuous and punctual measurements from 2008 to 2014). Occasionally, the pCO_2 concentration in the gallery can rise up to values around 4%, especially during late autumn and early spring, and the cause of this remains under investigation (pers.comm. Ph. Häuselmann, SISKA).

The sample locations in the gallery are shown by Fig. 4.2. The stalagmites M6 and M8 grew only several centimeters distance from each other, and in a distance of around 50 m from M2.Their growing location is less exposed to changes in ventilation and water flooding, due to a rather lateral and elevated position within the gallery compared to stalagmite M2.

All samples are composed of compact columnar calcite, and annual laminations are visible macroscopically and/or microscopically on the entire length of the samples. M2 was active when collected in 2008, and it was fed by a soda straw dripping at 5`10``- 6`20`` time intervals (Schmassmann, 2010). The sample grew on the top of a clay deposit, in an area of the gallery exposed to changes in atmosphere and hydrology in the cave. M2 is a 25.6 cm long stalagmite, with a fairly constant diameter of 6-7 cm. Several clay layers in the upper 14 cm of the sample indicate flooding events in the cave. In this paper we will refer only to the basal 15.1 – 25.6 cm of the sample (Fig. 4.3), where no flood layers are visible. Alternations of irregular laminae of white - porous and darker-compact calcite are present at 16 - 22 cm depth in sample. M6 and M8 grew on the same calcite base (Marine Isotope Stage 5 calcite, author pers. data), and a well-defined corrosion laminae marks the hiatus between the two calcite generations. Sample M6 is a 145.2 cm long stalagmite, and was active when collected in autumn 2011. The sample was fed by a soda straw dripping at 0`15``- 6`00`` time intervals (Affolter et al., submitted in revised form). In this paper we will refer only to the basal 118 –145.2 cm of the M6 sample (Fig. 4.3). Axial pores are observed in this section of the samples, with laminations observed between the rims of the pores. Sample M8 is a 13.25 cm long stalagmite, with a diameter of 8-10 cm. The sample was not active when collected in 2012. In this paper we will refer only at the basal 6.4–13.25 cm of the sample. The presence of white porous calcite between 7 to 8.2 cm depth and a change in the growth axis at 8.5 cm were observed (Fig. 4.3)

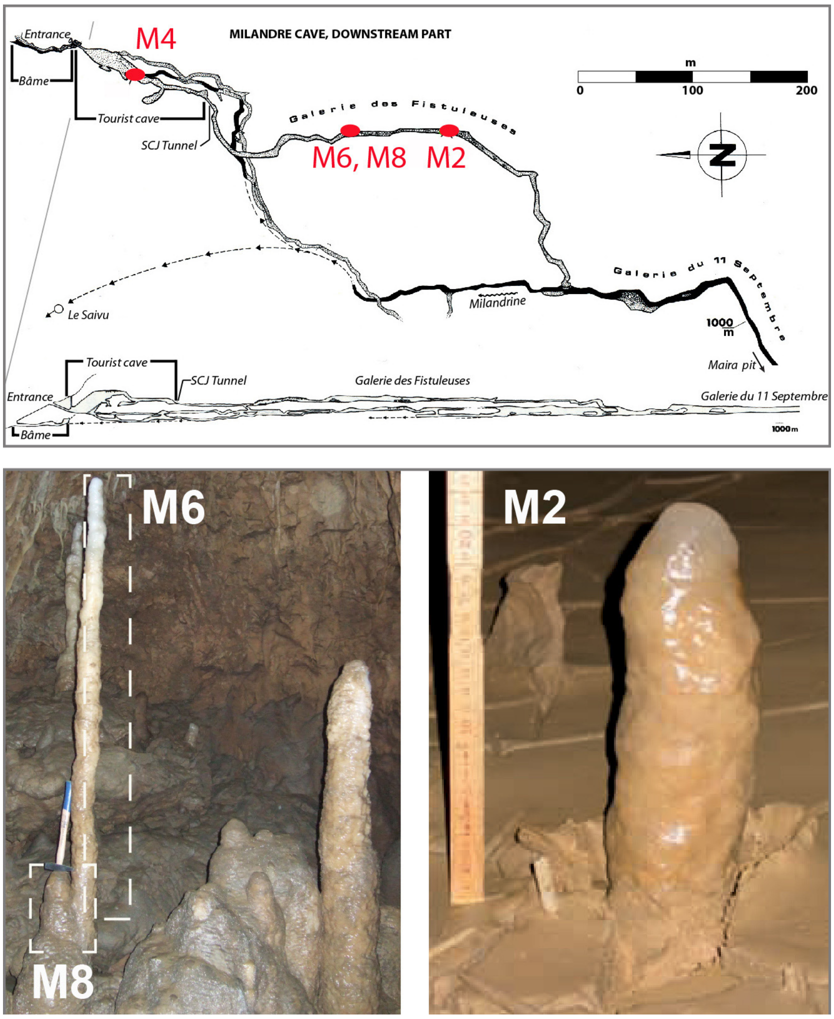

Figure 4.2. Map of Milandre cave (modified from Gigon and Wenger, 1986) and location of the samples in the cave (red dots). Bottom: Samples M6 and M8 and M2 before sampling. (photos: S.Schmassmann and A.D. Häuselmann)

4.3. METHODS

For Uranium-series dating (^{230Th} hereinafter), approximately 200 mg of powder was drilled along discrete growth horizons (Fig. 4.3). The ^{230}Th ages were determined on a multi-collector inductively coupled plasma mass spectrometer (MC-ICP-MS, Thermo-Finnigan Neptune) at the Department of Earth Sciences, University of Minnesota. Details of the methods, including standards used for mass fractionation and yield correction can be found in Cheng et al. (2013). The ^{230}Th dates of all samples are listed in the Table 4.1. An additional age for sample M2 is reported by Schmassmann (2010), 14 304 ±

343 y BP at 24.5 cm depth in the sample, respectively. The samples ^{230}Th/^{232}Th ratio ranges between 89 -1092 atomic * 10^{-6} and have a U concentration of 63-430 ppb. All ages are quoted as years before 1950 (BP=1950).

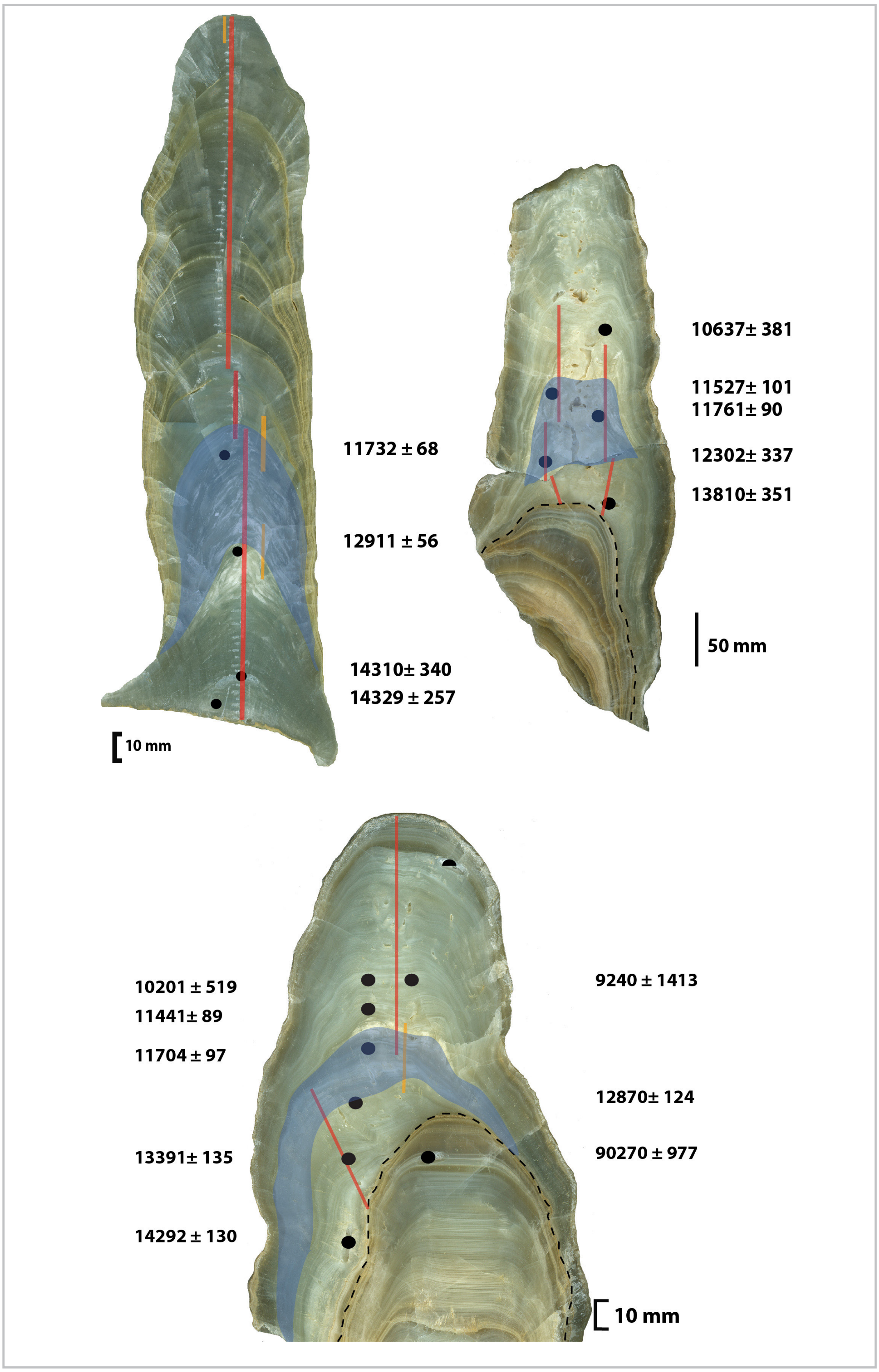

Figure 4.3. *Polished sections of M2 (upper left), M6 (upper right) and M8 showing micromilling paths for isotopic analysis (red lines), paths of trace elements analysis (orange lines), sampling locations for* ^{230}*Th calcite dating (black dots) and dating results. Blue sections approximate the location in samples of calcite precipitated during the Younger Dryas event.*

A total of 930 samples were micromilled continuously at 0.2 mm and 0.5 mm increments. About 150-200 µg of powdered sample was placed in 12 ml vacutainers, flushed with He, and reacted with 5 drops of 99 % P_5O_5 at 70°C for 80 minutes. The samples were measured using a Finnigan Delta V Advantage mass spectrometer equipped with an automated carbonate preparation system (Gas Bench II) at the Institute of Geological Sciences, University of Bern, Switzerland. Results are reported relative to the international Vienna Peedee Belemnite (VPDB) standard. The analytical reproducibility based on repeated measurement of the internal standard for $\delta^{18}O$ and $\delta^{13}C$ is lower than 0.07 and 0.06 ‰ VPDB (1σ).

Laser ablation analyses were carried out in the Department of Chemistry and Applied Biosciences, Laboratory of Inorganic Chemistry, ETH Zürich. We used a 193 nm ArF excimer laser (GeoLas Pro, Lambda Physik) coupled to a quadrupole ICP-MS (ELAN 6100 DRC+, Perkin Elmer). A detailed description of the experimental setup is given in Kovacs et al. (2010) and optimized as described in Tabersky et al. (2013).

Noble gases in fluid inclusions (NG) were measured at the Department of Water Resources and Drinking Water, Eawag, using a recently developed combined vacuum crushing and sieving (CVCS) system'. The setup and operation conditions are described in Vogel et al. (2013). Absolute cave air temperature estimtes are reconstructed using Ar, Kr, and Xe concentration extracted from the calcite water inclusions, with an uncertainty of up to ±2°C.

$\delta^{18}O$ and δD of speleothem fluid inclusions were measured using a wavelength scanned cavity ring down spectroscopy (WS-CRDS) instrument, following the set up and procedure described in Affolter et al., 2014. For water released by the stalagmite calcite samples 0.5 µl, the standard deviation of isotope measurements is smaller than 1.5 ‰ for δD over a range of 0 and −210 ‰ at least and 0.4 ‰ for $\delta^{18}O$ over a range of 0 and − 27 ‰. Temperature estimates were obtained using the formula of Tremaine et al. 2011 (these compare most closely with modern conditions in the cave), and the uncertainty of the temperature reconstructions related to analytical error is around 0.9°C (Affolter et al., 2014).

4.4. Results and discussion

4.4.1. Chronology

Age models were built for each sample using the COPRA algorithm (Breitenbach et al., 2012). Figure 4.4 shows the individual age-depth models for all three stalagmites and indicates that the samples were deposited between 11 000 and 14 560 years BP (BP=1950). The isotopic profiles for the samples are presented in Fig. 4.5 (upper part) and Fig. 4.6. Based on the assumption that climatic changes above the cave should be recorded simultaneously by each sample, we align distinct shifts in $\delta^{18}O$ (Fig. 4.5) to the most reliable dated record (in terms of dated subsamples and dating precision), which is sample M8. A new chronology for samples M2 and M6 was therefore established by applying an eye-fit "event stratigraphy" in order to correlate the isotopic records (both $\delta^{18}O$ and $\delta^{13}C$) to the M8 isotopic chronology (Fig. 4.4, 4.5 and 4.6), while the tuning was done within the error intervals of each record. Detailed information regarding the position of the fix points in each speleothem, age and error of the individual fix points (based on M8 chronology) are listed in Table 4.2.

To each fix point we attributed its corresponding 2 σ error given by the M8 COPRA chronology. This approach will account both for the error within M8 chronology and for the one introduced by the temporal resolution of our records (14 years for M2, and 7 years for M6, 25 years for M8). Fig. 4.4 shows the new calculated age-models for the samples M2 and M6.

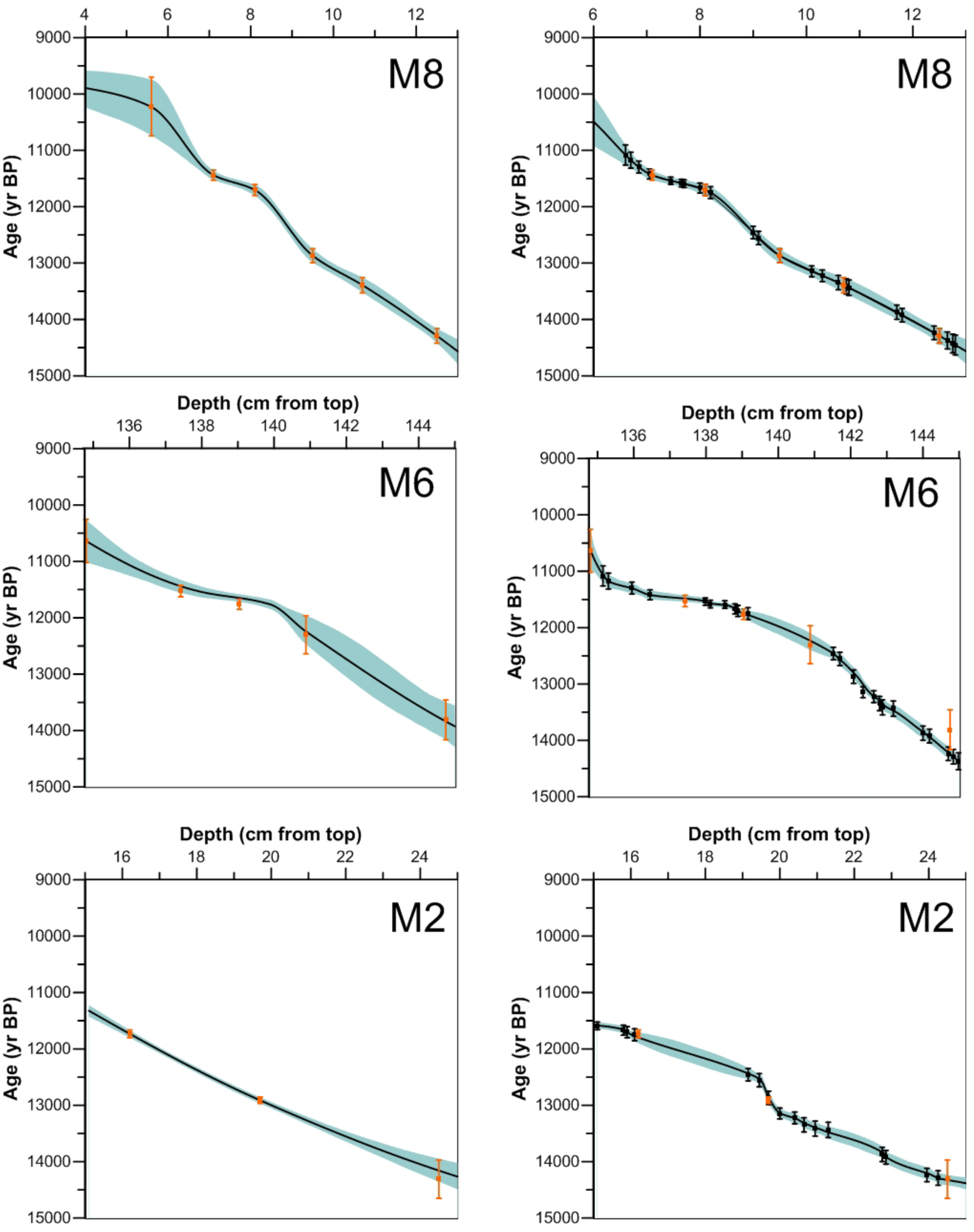

__Figure 4.4.__ Depth-age models of samples M2, M6 and M8 (Milandre Cave). Left side: individual depth-age models. Right side: depth-age models after the tuning. The outer shaded zones define the 95% uncertainties. In orange color are represented the measured ages and in black color the tuned ages. Please note the different depth scale for sample M8.

Table. 4.1. *^{230}Th age of samples M2, M6 and M8*

Sample number	Depth (cm)	^{238}U (ppb)		^{232}Th (ppt)		^{230}Th / ^{232}Th (atomic x10^{-6})		δ ^{234}U* (measured)		^{230}Th / ^{238}U (activity)		^{230}Th Age (y) (uncorrected)		^{230}Th Age (y) (corrected)		δ ^{234}U$_{\text{Initial}}$** (corrected)		^{230}Th Age (y BP)*** (corrected)	
M2-C	16.2	72.5	±0.1	194	±4	792	±16	248	±2	0.1289	±0.0005	11854	±52	11792	±68	256	±2	**11732**	**±68**
M2-D	19.7	112.3	±0.1	235	±5	1092	±22	225	±2	0.1384	±0.0004	13020	±43	12971	±56	234	±2	**12911**	**±56**
M2-E	25.3	145.4	±0.1	2525	±51	169	±3	398	±2	0.1779	±0.0005	14747	±45	14389	±257	414	±2	**14329**	**±257**
M8-9	5.6	111.2	±0.1	3414	±68	63	±1	221.8	±1.7	0.1177	±0.0006	11014	±57	10284	±519	228	±2	**10221**	**±519**
M8-5	7.1	123.3	±0.2	547	±11	457	±9	216.2	±1.8	0.1232	±0.0005	11610	±48	11504	±89	223	±2	**11441**	**±89**
M8-7	8.1	125.4	±0.2	629	±13	413	±8	211.6	±1.6	0.1255	±0.0004	11886	±48	11767	±97	219	±2	**11704**	**±97**
M8-6	9.5	164.5	±0.2	1127	±23	335	±7	224.5	±1.7	0.1390	±0.0004	13095	±47	12933	±124	233	±2	**12870**	**±124**
M8-8	10.7	173.7	±0.3	1316	±26	315	±6	229.1	±1.8	0.1450	±0.0004	13632	±48	13454	±135	238	±2	**13391**	**±135**
M8_2	12.5	430.0	±0.9	3244	±65	359	±7	312.5	±2.0	0.1644	±0.0006	14521	±57	14355	±130	325	±2	**14292**	**±130**
M8_3	13	63.5	±0.1	3237	±65	216	±4	158.4	±1.5	0.6690	±0.0019	91571	±438	90333	±977	204	±2	**90270**	**±977**
M6-47	134.8	103.2	±0.2	2279	±46	89	±2	210.6	±2.9	0.1188	±0.0007	11230	±72	10701	±381	217	±3	**10637**	**±381**
M6-48	137.9	120.6	±0.3	569	±11	429	±9	203.8	±2.8	0.1229	±0.0005	11704	±61	11591	±101	211	±3	**11527**	**±101**
M6-50	139.9	121.8	±0.2	499	±10	500	±10	196.1	±1.8	0.1242	±0.0005	11924	±57	11825	±90	203	±2	**11761**	**±90**
M6-49	140.9	105.2	±0.2	2027	±41	114	±2	199.9	±2.4	0.1336	±0.0006	12832	±71	12366	±337	207	±3	**12302**	**±337**
M6_31	144.7	225.4	±0.3	4698	±94	120	±2	228.8	±1.5	0.1522	±0.0004	14364	±48	13873	±351	238	±2	**13810**	**±351**

U decay constants: λ_{238} = 1.55125x10^{-10} (Jaffey et al., 1971) and λ_{234} = 2.82206x10^{-6} (Cheng et al., 2013). Th decay constant: λ_{230} = 9.1705x10^{-6} (Cheng et al., 2013).

*$\delta^{234}U = ([^{234}U/^{238}U]_{activity} - 1)x1000$. ** $\delta^{234}U_{initial}$ was calculated based on ^{230}Th age (T), i.e., $\delta^{234}U_{initial} = \delta^{234}U_{measured}$ x $e^{\lambda 234xT}$.

Corrected ^{230}Th ages assume the initial ^{230}Th/^{232}Th atomic ratio of 4.4 ±2.2 x10^{-6}. Those are the values for a material at secular equilibrium, with the bulk earth ^{232}Th/^{238}U value of 3.8. The errors are arbitrarily assumed to be 50%.

After tuning, the record of stalagmites from Milandre Cave show continuous growth of the samples as it follows: i) sample M2 (15.1 to 26.6 cm depth) over 11586 ± 63 to 14570 ± 166 y BP interval, ii) sample M6 (135.05 to 145.18 cm depth) over 10963 ± 187 to 14546 ± 140 y BP interval and iii) sample M8 (6.5 to 13.25 cm depth) over 10985 ± 223 to 14705 ± 285 y BP interval (Fig. 4.5 B). Growth rates range from 0.006 to 0.222 mm/y (overall mean 0.047 mm/y) in sample M2, from 0.007 to 0.192 mm/y (overall mean 0.053) mm/y in sample M6, and from 0.004 to 0.073 mm/y (overall mean 0.028 mm/y) in sample M8.

Fix point	M8 Depth	M6 (cm)	M2	Fix point Age (BP)	2σ
1	12.80	145.16	25.35	14453	176
2	12.75	145.08	25.10	14426	166
3	12.65	144.98		14371	150
4	12.50	144.84	24.25	14290	129
5	12.40	144.70	23.95	14236	119
6	11.80	144.18	22.85	13922	121
7	11.70	144.00	22.75	13872	125
8	10.80	143.18	21.30	13436	136
9	10.75	142.88	20.95	13413	134
10	10.60	142.80	20.65	13346	126
11	10.30	142.64	20.40	13224	104
12	10.10	142.34	20.00	13145	96
13	9.50	142.08	19.70	12869	119
14	9.10	141.70	19.45	12555	117
15	9.00	141.52	19.15	12457	110
16	8.20	139.16	16.10	11749	105
17	8.10	138.88	15.90	11703	97
18	8.00	138.80	15.80	11668	88
19	7.70	138.52	15.10	11590	68
20	7.65	138.12		11580	67
21	7.45	137.98		11538	65
22	7.05	136.45		11418	88
23	6.85	135.95		11296	105
24	6.70	135.30		11174	141
25	6.60	135.15		11082	178

Table 4.2. *List of fix points (isotopic events) used for age model tuning in the Milandre samples, the corresponding depth in each sample (cm from top) for each event, together with the age and error assigned to each fix point (based on the M8 age model).*

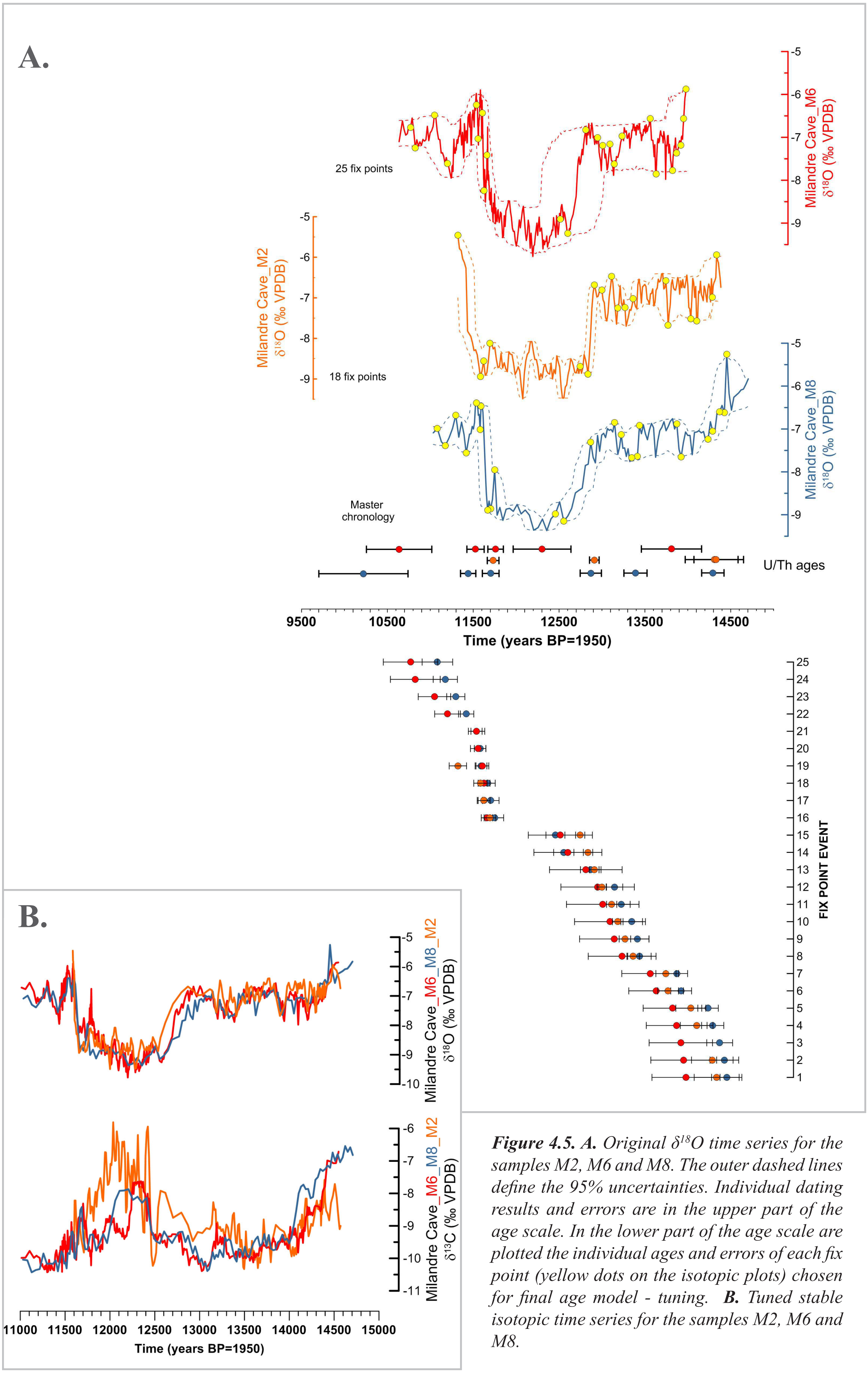

Figure 4.5. A. *Original $\delta^{18}O$ time series for the samples M2, M6 and M8. The outer dashed lines define the 95% uncertainties. Individual dating results and errors are in the upper part of the age scale. In the lower part of the age scale are plotted the individual ages and errors of each fix point (yellow dots on the isotopic plots) chosen for final age model - tuning.* ***B.*** *Tuned stable isotopic time series for the samples M2, M6 and M8.*

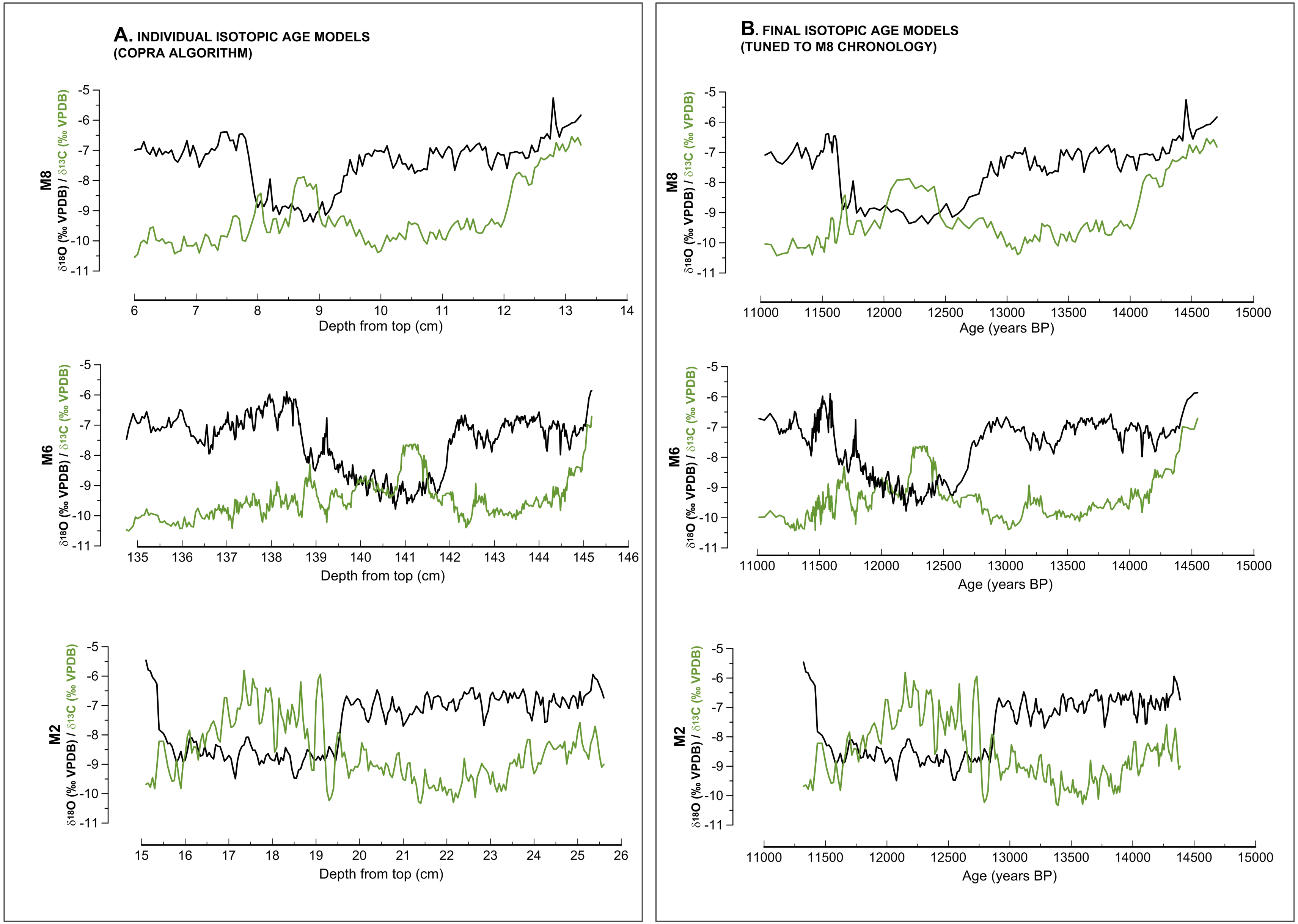

Figure 4.6. A. Depth-scale stable isotopic time series for the samples M2, M6 and M8. B. Tuned stable isotopic time series for the samples M2, M6 and M8.

4.4.2. STABLE ISOTOPES ($\delta^{18}O$ AND $\delta^{13}C$) RESULTS

As the three stalagmites were precipitated in the same passage of the cave within a distance of 50 m, we assume that all grew under very similar environmental conditions. Calcite $\delta^{18}O$ values are influenced by (i) $\delta^{18}O$ of the drip water, (ii) temperature in the cave (mean annual temperature at the surface of the cave), and (iii) kinetic effects during calcite precipitation, leading to simultaneous enrichments of heavier isotopes in the calcite and a positive correlation between $\delta^{18}O$ and $\delta^{13}C$ (Fairchild and Baker, 2012 and citations therein). For $\delta^{18}O$ we consider kinetic effects as negligible in our samples, as proven by the good replication between the isotopic signal of the three samples and also by parallel track replicates in the same sample (e.g. M6 and M8). The samples are located in a part of the cave not affected by seasonal changes in temperature, and we assume that long term changes in the cave temperature will affect their isotopic composition simultaneously. Finally, differences between $\delta^{18}O$ values of coeval samples may be given by slight differences in $\delta^{18}O$ of the drip water. At our site this can be related mostly to the mixing of seasonal precipitation water and its retention time in different epikarst reservoirs, and may differ at the individual dripping sites. A significant influence of these factors was observed mainly in the $\delta^{13}C$ composition of sample M2, where higher mean values compared to the other samples was observed (Fig. 4.5). Otherwise, changes in $\delta^{13}C$ of Milandre samples are mainly related to changes in soil microbial activity and vegetation type above the cave (Schmassmann, 2010).

The amplitude of the $\delta^{18}O$ signal in all three samples is remarkably similar and highlights the proxy quality of their $\delta^{18}O$ signal. In further discussion we will refer to the sample with the highest sampling temporal resolution, namely M6.

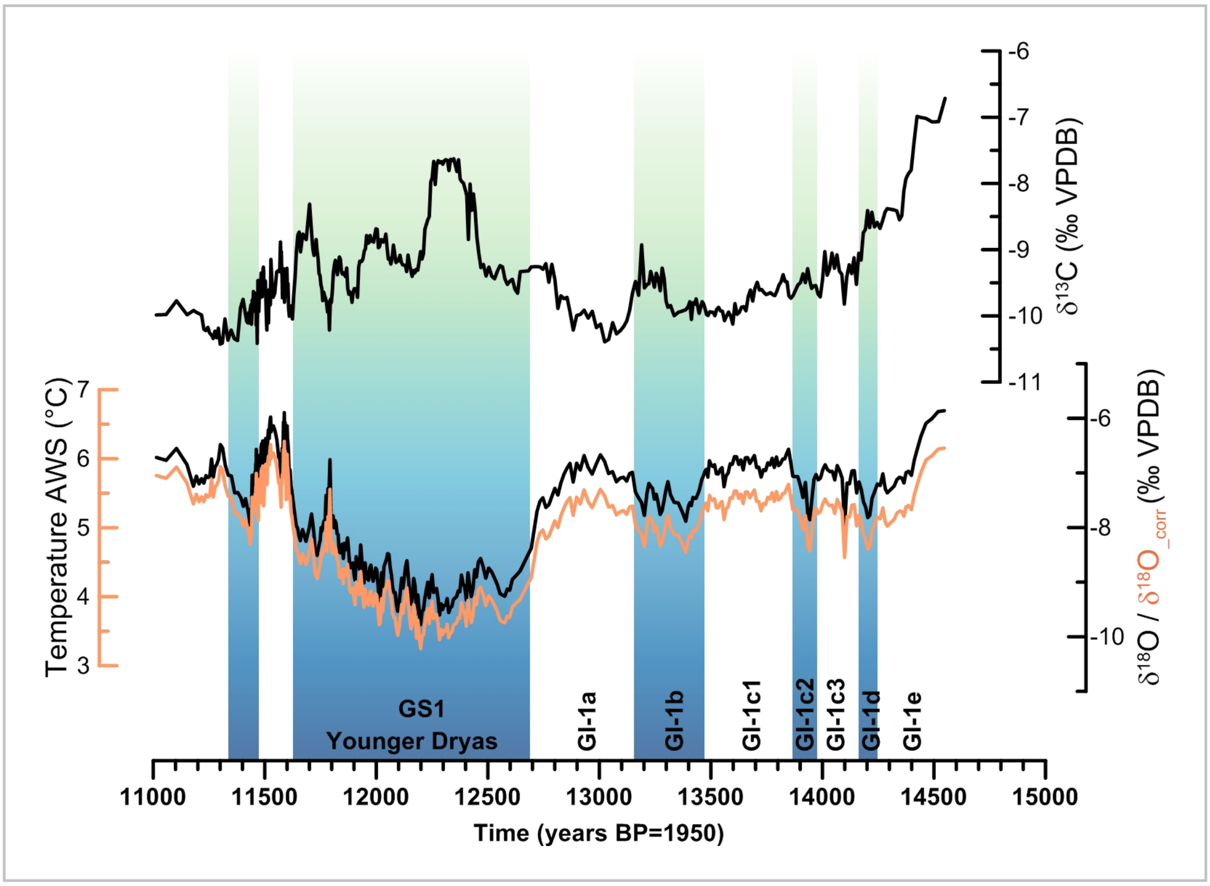

Figure 4.7. *$\delta^{18}O$ and $\delta^{13}C$ time series (black lines) of speleothem M6, source-effect corrected $\delta^{18}O$ ($\delta^{18}O$_corr, orange line), and autumn to spring temperature reconstruction (AWS T) based on $\delta^{18}O$_corr and 0.69 ‰/°C transfer function (orange line).*

$\delta^{18}O$ calcite values from Milandre Cave are closely related to surface temperatures, with low $\delta^{18}O$ values corresponding to low surface temperatures and high $\delta^{18}O$ values to warmer temperatures (Schmassmann, 2010, Hasenfratz et al., in prep).

Figure 4.7 presents the high resolution isotopic record of sample M6. For chronozone nomenclature we used the GICC05 (Lowe et al., 2008) and the modified GICC05 terminology, as published by von Raden et al. (2012) based on the Gerzensee isotopic stack. Table 4.3 summarizes the chronozones, the depth in M6 sample covered by each chronozone, age onset of each chronozone, average temporal resolution and the isotopic composition.

A pattern of short-term variation in $\delta^{18}O$ is overprinted by the long-term trend between GI-1a and GI-1e (Bølling-Allerød interval, B/A). There, distinct variations with a negative isotopic shift of 0.6 - 0.7 ‰ VPDB were identified, representing transition phases in GI-1d, GI-1c2, respectively GI-1b. During interstadial intervals, such as GI-1a, GI-1c1 and GI-1c3, the amplitude of secondary-variation is only 0.2 -0.3 ‰ around the mean isotopic value of the intervals. In $\delta^{13}C$, a 3 ‰ VPDB negative trend is observed over GI-1e to GI-1c. A 0.6 ‰ positive shift is observed during the last 200 y of GI-1b (Fig. 4.7). Overall, these isotopic fluctuations during GI-1d to GI-1b did not influence the growth rate of the sample, which shows a relatively constant rate of 0.018-0.023 mm/y. A slower growth rate is observed during GI-1a and GI-1d, with an average of 0.012 mm/y.

Isotopic	Depth (cm from top)		Age (y BP)				Average isotopic data		
event	from	to	from	to	error	Duration	Res. (y)	$\delta^{18}O$	$\delta^{13}C$
GI-1e*	144.76	145.18	14246.2	14546.2	139.6	300.0	10	-7.5	-7.9
GI-1d	144.58	144.76	14153.3	14246.2	85.3	92.9	10	-7.4	-8.9
GI-1c3	144.22	144.58	13961.8	14153.3	104.3	191.5	11	-7.1	-9.4
GI-1c2	144.04	144.22	13867.3	13961.8	100.7	94.5	11	-7.3	-9.5
GI-1c1	143.14	144.04	13459.9	13867.3	109.1	407.4	9	-6.9	-9.8
GI-1b	142.54	143.14	13147.8	13459.9	89.8	312.1	10	-7.5	-9.7
GI-1a	142.12	142.54	12827.5	13147.8	83.3	320.3	16	-7.0	-10.0
Tranzition	141.72	142.12	12576.1	12827.5	107.8	251.5	14	-8.2	-9.4
GS1	138.8	141.72	11659.3	12576.1	99.9	916.7	6	-8.8	-8.9
Tranzition	138.54	138.8	11600.2	11659.3	46.3	59.1	4	-7.3	-9.5
E. Holocene	138.26	138.54	11598.7	11600.2	43.0	1.5	1	-6.2	-9.5

Table 4.3. *List of isotopic events (nomenclature based on Gerzensee defined chronozones, van Raden et al., 2012), their location in the M6 sample depth, time interval covered and their mean duration based on the modified M6 chronology. For each chronozone mean temporal resolution of isotopic sampling and mean stable isotopic composition is given. * Full extension of GI-1e is not recorded in sample M6.*

A 1.8 ‰ VPDB negative shift in $\delta^{18}O$ marks the transition into GS1 (Younger Dryas interval, YD). The first half of the YD (between 12 025 - 12 565 y BP) shows a 0.4 ‰ more negative mean isotopic composition (-9.1 ‰) compared to the second half (between 11 650 -12 025 y BP, -8.7 ‰ VPDB). Secondary $\delta^{18}O$ oscillations of around 0.6 ‰ are observed in the first half of the YD, and a 1.2 ‰ event is superimposed on the gradual positive transition during the second half. The overall positive trend during YD is also reflected by an increase in the growth rate of the sample from 0.028 to 0.037mm/year. In $\delta^{13}C$ a + 1 ‰ VPDB change is observed just before the YD transition (between 12 717 -13 020 y BP), and a second positive shift of 1.6 ‰ is observed between 12 325 - 12 495 y BP. A minimum in $\delta^{13}C$ (average -7.7 ‰) is observed between 12 375 to 12 245 y BP. Between 11 600 to 12 130 y BP, the $\delta^{13}C$ shows second-order oscillations of around 0.6 ‰ varying around a mean of -9.2 ‰. Positive shifts of 2.2 ‰ in $\delta^{18}O$ and of -1.2 ‰ in $\delta^{13}C$ mark the transition into the Early Holocene.

During the early Holocene, the isotope profiles of $\delta^{18}O$ and $\delta^{13}C$ present short isotopic events of high amplitude (around 0.6 ‰ amplitude in $\delta^{18}O$ and 1‰ in $\delta^{13}C$) that overprinted the negative trend in both isotopes. A minimum of -7.95 ‰ in $\delta^{18}O$ was measured during early Holocene (between 11 350 - 11 450 y BP).

For comparison, fresh calcite precipitated between 2012 and 2014 in the sampling location of sample M6 shows isotopic values of around -6.7 ‰ for $\delta^{18}O$ and -12.1‰ for $\delta^{13}C$. This suggests temperatures comparable with present during the Early Holocene in the Jura Mountains, with less developed vegetation and soil cover above the cave.

The timing and amplitude of the successive cold and warm events are generally in agreement with other evidence from this region and Central Europe. Changes of 2.1 ‰ in $\delta^{18}O$ during GI-1a / GS1 and 1.9 ‰ VPDB during GS1/Holocene, as recoded in speleothem M6 calcite, are very similar to changes in the isotopic composition of lake carbonates from the region. Shifts of 2.5 ‰ during GI-1a / GS1and 2.2 ‰ VPDB during GS1/Holocene, are reported from Ammersee Lake (von Grafenstein et al., 1999), of around 2.2 ‰ VPDB for both transitions from Gerzensee Lake (Lotter et al, 2012, Fig. 4.8). The small differences may be related with the fact that $\delta^{18}O$ values of the lake carbonates represent annual air temperature changes in the region (von Grafenstein et al., 2012, von Raden et al., 2012), whereas our record is biased towards cold season air temperatures. The positive isotopic trend within the Younger Dryas event is observed in most of the records (e.g., Milandre Cave, Chauvet Cave, Ammersee, NGRIP) confirming the suitability of the isotopic signal of speleothems from Milandre Cave to capture regional and super-regional climatic fluctuations.

Isotope event	GICC05		GERZENSEE		MILANDRE		GICC05-MIL	GRZ-MIL
	age, y BP	error	age, y BP	error	age, y BP	error	years	years
Transition**	11653	99			11615	43	35	
GS1			12710	138	12576	100		143
Transition**	12846	138	12877	143	12715	142	136	167
GI-1a	13049	143	12989	148	13147	83	-98	-158
GI-1b	13261	148	13274	148	13453	90	-192	-179
GI-1c1			13522	158	13857	109		-335
GI-1c2			13624	158	13952	101		-328
GI-1c3	13904	165	13908	158	14143	104	-239	-235
GI-1d	14025	169	14044	159	14234	85	-209	-190
GI-1e*	14642	186	14590	196	14546	140	-	-

Table 4.4. *Comparison between the onset of major isotopic events as recorded in Greenland ice core chronology (GICC05, Rasmussen et al., 2006, Lowe et al., 2006), Gerzensee Lake (GRZ, van Raden et al., 2012) and Milandre record (our study).*

Timing of $\delta^{18}O$ shifts shows a very good agreement (within errors) with other regional terrestrial $\delta^{18}O$ records from Chauvet Cave (Genty et al., 2006), Gerzensee Lake (van Raden et al., 2012, Lotter et al., 2012), Ammersee Lake sediments (von Grafenstein et al., 1999), and from the Greenland ice core chronology (GICC05, Rasmussen et al., 2006, Lowe et al., 2000, Fig. 4.8). Before the YD event, the Milandre isotopic profile display consistently older ages for warm and cold interval transitions if compared with GICC05 and Gerzensee stack, and younger for the YD transitions (Table 4.4). Nevertheless, the disagreement falls within the age model errors of the records. An exception is observed between Milandre and Gerzensee records for the onset into GI-1c2 and GI-1c1 chronozones, which is most probably related to a bias in the age model construction of both records.

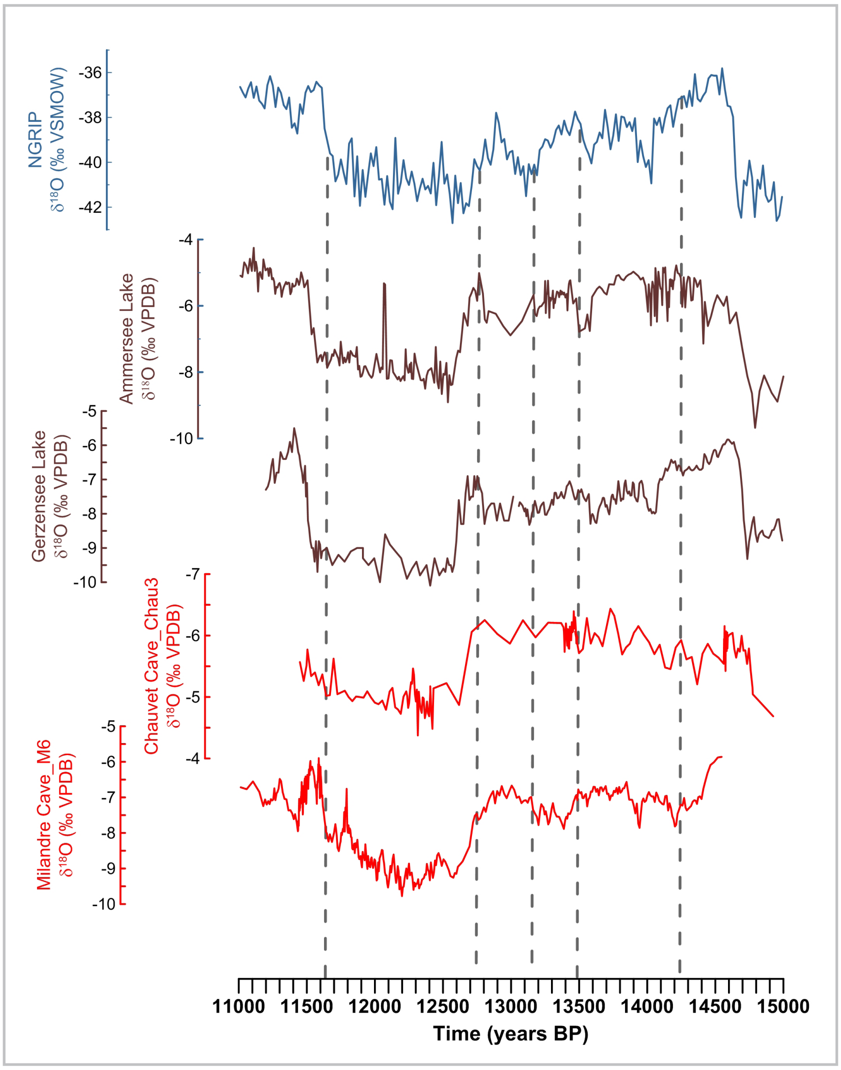

Figure 4.8. *Comparison between δ18O record from Milandre Cave and δ18O records from Chauvet Cave (Genty et al., 2006), Gerzensee Lake (van Raden et al., 2012, Lotter et al., 2012), and Ammersee Lake (von Grafenstein et al., 1999), and from the Greenland ice core (GICC05, Rasmussen et al., 2006, Lowe et al., 2006). Dashed lines indicate the boundaries of important chronozones in M6 time series.*

4.4.3. TRACE ELEMENT RESULTS

Trace element concentrations were measured in samples M2 and M8. Here we consider the results obtained from sample M8, due to a better age model control. On the same time interval, sample M2 shows excellent agreement with the observed trends and values in M8 sample. Based on our age model, the trace element profiles cover the 11 502 to 13 263 y BP time interval (GI-1b to Early Holocene), with a temporal resolution of 0.6-2.2 years. In this study we consider Mg and Sr as well-established indicators of effective rainfall and groundwater residence time in the karst aquifer above the cave (Fairchild and Baker, 2012). Higher concentrations of Mg and Sr are interpreted to reflect longer groundwater residence times at times of lower precipitation and effective recharge, respectively (Baldini et al., 2002; Hellstrom and McCulloch, 2000; McDonald et al., 2004). The positive correlation between the two elements could indicate prior calcite precipitation in the bedrock during these low effective moisture time intervals (Fairchild and McMillan, 2007). Al is common in the “impulse laminae” (Fairchild and Baker, 2012 and references therein), representing enrichment of drip water in colloid-transported material in response to high infiltration events, or fracture fed flow. Concentration of Si in calcite was suggested to be related is the rate of wind-blown silicate supply and weathering rates above the caves (Hu et al., 2005).

Both Mg and Sr show a general decreasing trend in their concentration over the Younger Dryas (Fig. 4.9). Concentration from the onset to the end of the YD decreases from around 688 mg/kg to 377 mg/kg for Mg and from 87 mg/kg to 54 mg/kg for Sr. Around 12 450 y BP we observe a drop of 23 mg/kg in the concentration of Sr and in the concentration of Mg, most probably related to climate-induced hydrologic changes (increase in precipitation) at the surface, at a time of reduced vegetation cover at the cave surface (indicated by more positive $\delta^{13}C$).

Al concentration in the sample varies between 1 - 227 mg/kg around a mean 14.5 mg/kg. After 12 350 y BP a frequent occurrence of impulse laminae rich in Al is observed. Si concentration varies between 230 - 12 780 mg/kg, with a pronounced increase in concentration between 12 740 – 12 900 y BP (peak around 12 800 y BP).

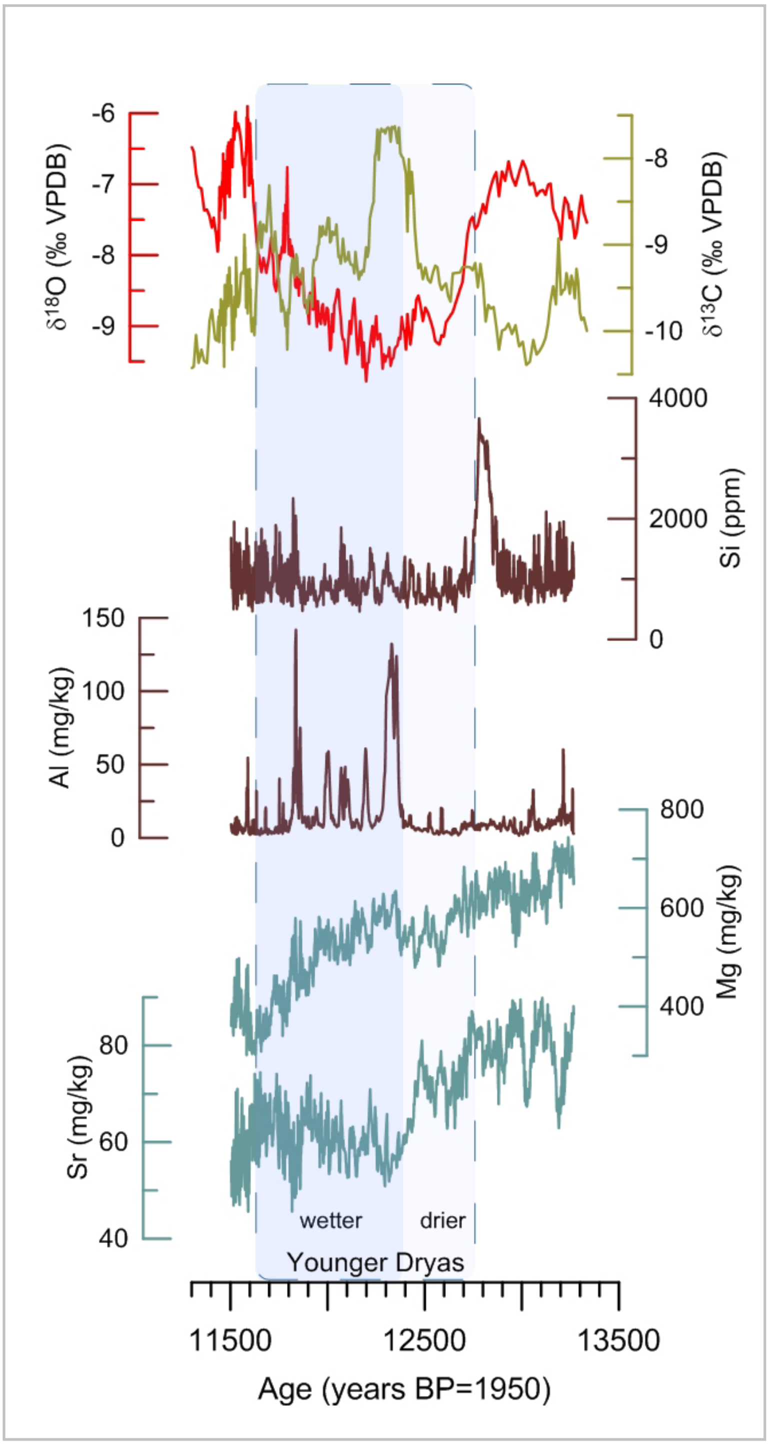

Figure 4.9. *Time series of trace element concentration (Si, Al, Sr and Mg) and stable isotopes ($\delta^{18}O$ and $\delta^{13}C$) during the Younger Dryas interval*

4.4.4. TEMPERATURE RECONSTRUCTIONS BASED ON SPELEOTHEM PROXIES

4.4.4.1. PREVIOUS RESULTS

Samples for water inclusion analysis were obtained from sample M2 (noble gas based reconstructions, NG) and M8 (water $\delta^{18}O$ and δD) in order to reconstruct absolute temperatures in the cave/at the cave surface at the time of calcite formation. Protocols and results are presented and discussed in detail in Vogel et al. (in prep.) and Affolter et al. (in prep.). The ages of the fluid inclusion samples (mean age of their sampling interval) are based on the M2 and M8 chronologies presented in sub-chapter 3. Table 4.5 presents a summary of the results (water concentration in calcite and absolute temperature reconstructions). To account for a +1.2°C temperature offset observed between modern calcite temperature reconstructions and modern cave temperature, Affolter et al. (in prep.) applied an identical correction to the reconstructed temperatures. Based on several replicates, the authors propose a mean temperature of 6.2 ± 0.9°C during Allerød, 4.2 ± 0.9°C for YD and 7.3 ± 0.9°C for Early Holocene. For NG-based reconstruction (Vogel et al., in prep.) temperatures of around 3.7 ± 2.3°C were calculated for Allerød, 1.2 ± 2.0°C for YD, and 6.3 ± 2.6°C for Early Holocene. Reconstructions for the Allerød and early Holocene agree well within errors with the ones obtained by Affolter et al. (in prep.), while YD reconstructions shown a stronger cooling (Fig. 4.10), at times with cave temperatures just above the freezing point.

Sample	Age	Water content	Temperature	
	years BP	mg/g	°C	2σ
M2-162	11607	8.9	6.3	2.6
M2-179	12339	7.2	0	3
M2-192	12762	11.1	1.2	2
M2-199	12969	14.4	3.7	2.3
M2-214	13391	20	2.2	1.5

Sample	Age	Water content	Temperature	
	years BP	μl/g	°C	2σ
M8-6	10974	0.37	6.6	0.9
M8-7	11366	1.33	4.7	0.9
M8-7a	11600	1.54	6.8	0.9
M8-8	11765	0.65	5.8	0.9
M8-9	11976	0.37	3.4	0.9
M8-10	12354	0.36	5.8	0.9
M8-11	12799	1.36	3.4	0.9
M8-12	13111	1.38	4.9	0.9
M8-13	13389	0.55	5.2	0.9
M8-14	13700	0.6	6.1	0.9

Table 4.5. *Overview of absolute temperature reconstruction results based on fluid inclusion analysis in sample M2 (NGT, Vogel et al., in prep.) and M8 (Affolter et al., in prep.). Ages represents mean ages of the sampled interval based on the tuned age models of each sample.*

Finding an explanation for the temperature offset between the two methods is difficult but may be related to one, or a combination, of the following factors: i) analytical errors, and a series of replicated samples is recommended for sample M2 (using both methods), ii) methodological errors (Meckler et al, submitted), iii) a climate-induced difference between mean annual temperature at the surface (reflected in the cave temperature and NG concentration of fluid inclusions) and the autumn to spring season temperature (as reflected by the isotopic composition of fluid inclusions), or iv) in the cave and/or in the sample specific conditions that could alter the geochemical signal and concentrations. The results obtained from the isotopic composition of the fluid inclusions in Milandre speleothems are considered more robust due to i) replicated analysis, and ii) reliable analogy with modern conditions (Affolter et al., submitted in revised form).

4.4.4.2. $\delta^{18}O$ / TEMPERATURE TRANSFER FUNCTION

Climatic changes at the surface are transmitted to the cave through chemical and physical properties of the drip water. If the calcite is deposited in or close to isotopic equilibrium, $\delta^{18}O$ of speleothems is dominated by the $\delta^{18}O$ ratio of surface precipitation (Fairchild and Baker, 2012 and citations therein). Several studies show that, if excluding eventual changes in the moisture source area and moisture path, temperature exhibits the strongest influence over changes in $\delta^{18}O$ of precipitation at the cave site, typical for sites in the mid-latitudes (Dansgaard, 1964; Rozanski et al., 1997; Kern et al., 2014). For the period between 1994-2001, $\delta^{18}O$ in Swiss precipitation is significantly related to air temperature, having a gradient 0.56 ‰/ °C at 500 m alt., and no relation between $\delta^{18}O$ and the amount of precipitation was found (Schürch et al., 2003). Effective infiltration and residence time in the epikarst control the $\delta^{18}O$ of drip water and in the speleothems calcite, respectively.

Above Milandre Cave, as a result of evapotranspiration, the effective infiltration during the warm season (April to September) is limited. This is confirmed not only by calculations (Häsenfratz, 2012), but also by monitoring (underground river discharge, vadose flow and drip rate counts in several cave locations, Perrin and Kopp, 2005; Hasenfratz, 2012; Affolter et al, submitted in revised form). All confirm that the karstic aquifer is recharged mainly between October to April and is drained in summer. An open question for Milandre site is if the drip water $\delta^{18}O$ signal i) is biased towards the season with highest effective infiltration (in this case October-March, as suggested by Hasenfratz et al. in prep.), or ii) this cold season signal is buffered towards a mean annual $\delta^{18}O$ signal as a result of a long residence time of the water in epikarst of up to several years, as suggested by Affolter et al.(in review).

In order to isolate in the speleothem $\delta^{18}O$ signal the influence of the local surface temperature, we have corrected the $\delta^{18}O$ in M6 and M8 samples for isotopic changes that occurred in the source area of the moisture, i.e. the North Atlantic Ocean. Between 14 700 and 10 500 y BP the relative sea level (RSL) rose from - 77 to - 35 m (Bard et al., 2010). Therefore, considering a change of -0.008 ± 0.002 ‰ VPDB per meter of sea level rise (Duplessy et al., 2007), we corrected the Milandre isotope data for the so-called “ice volume effect”, as presented in Figure 4.7 (orange line). This correction is based on the assumption that there was no major shift of the Atlantic vapor source compared to present. We will refer to the correct isotopic data as $\delta^{18}O_{corr}$.

To calculate a $\delta^{18}O$/temperature transfer function for the YD transitions, and to quantify atmospheric temperature reconstructions over long time intervals (Late glacial to present) we used several lines of evidence obtained from research on Milandre Cave speleothems. The aim was also to test the long-term reliability (across the Holocene) of the 0.69 ‰/°C transfer function developed for the past 300 years by

Hasenfratz et al. (in prep.), by adopting an independent approach. We compiled recent results from three analytical techniques, applied independently to our three samples, that deliver temperature variations in the cave and at the cave surface: i) $\delta^{18}O$ and δD measurements of fluid inclusions in stalagmite M8 ($\delta^{18}O$ was calculated based on δD and $\delta^{18}O_{calc}$ values in Fig. 4.10, Affolter et al., in prep.), ii) based on noble gas concentrations in the gas inclusions of M2 sample (Vogel et al., in prep), and iii) using a $\delta^{18}O$/temperature transfer function calculated for the last 300 years in stalagmite M6 (Hasenfratz et al., in prep, see also Appendix).

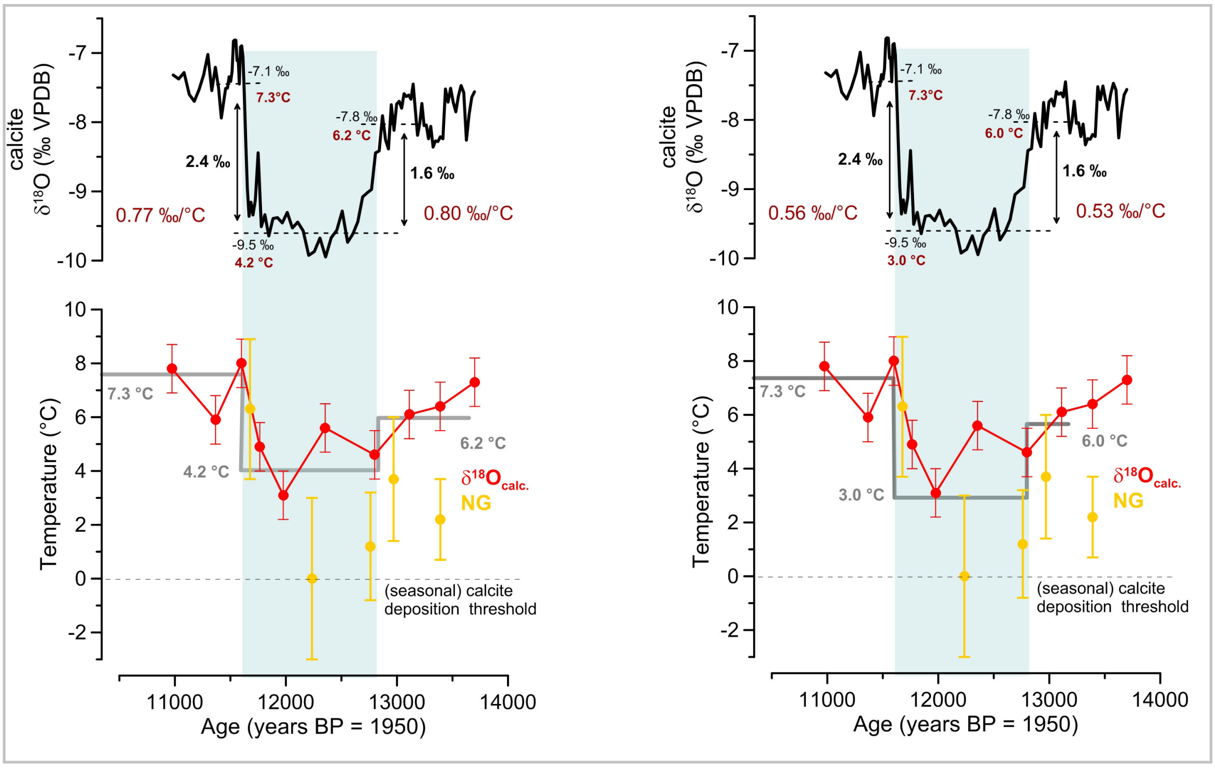

Figure 4.10. *Transfer function calculation based on calcite powder isotopic composition in sample M8 and absolute temperature reconstructions based on fluid inclusion analysis (M8 sample, red dots with errors, Affolter et al., in prep.) and noble gas temperatures (M2 sample, yellow dots with errors, Vogel et al., in prep.). Black numbers represent mean isotopic composition of calcite for the time intervals represented by the dotted black lines. Gary lines and numbers represent average values for the absolute temperature reconstructions, as used in the calculation for transfer functions. Please refer to the text for details.*

For the YD we compared the calcite powder $\delta^{18}O_{corr}$ values of stalagmite M8 and the absolute temperature reconstruction based on the fluid inclusion method listed above. Mean calcite powder $\delta^{18}O_{corr}$ values are presented in Fig. 4.10. A $\delta^{18}O_{corr}$ depletion of 1.6 ‰ was measured during the Allerød /Younger Dryas transition (GI-1a/GS1), and an enrichment of 2.4 ‰ during Younger Dryas/Holocene transition (GS1/Holocene). To compare the isotopic shift with absolute temperature changes based on fluid inclusion analysis was not a straightforward calculation. The data obtained from water inclusion analysis do not fully agree over the YD interval. This situation presented two possibilities to determine a mean temperature shift over the intervals of interest: i) to consider only the Affolter et al., (in prep.) results, which have the advantage of the most replicates and a calibration with modern calcite in the cave (Fig. 4.10, left side, gray line and values), or ii) choose a mean temperature value between both methods (which fall within error limits, Fig. 4.10, right side, gray line and values). Using the first approach, temperature shifts of 2°C, respectively 3.1°C, result in simple transfer function of 0.80 ‰/°C for Allerød/Younger Dryas and 0.77 ‰/°C for Younger Dryas/Holocene (Fig. 4.9). Using the second approach, a temperature shift of 3°C, respectively 4.3°C, result in simple transfer function of 0.53 ‰/°C for Allerød /Younger Dryas and 0.56 ‰/°C for Younger Dryas/Holocene. Nevertheless, the $\delta^{18}O$-temperature coefficient calculated for Late Holocene (0.69 ‰/°C, Hasenfratz et al., in prep) falls well within the range of values estimated for this Late Glacial interval (0.53 - 0.80 ‰/°C) using both approaches. This i) offers strong evidence regarding the validity of the 0.69 ‰/°C transfer function over millennial-scale intervals in samples from Milandre Cave, and ii) implies that the temperature dependency of the isotopic composition of regional precipitation has remained relatively constant (or was affected by minor changes) over Late Glacial and present-day period. Supporting evidence for this assumption is presented by Würth et al. (2004), who report a constant $\delta^{18}O$-temperature coefficient of 0.9-1.1 ‰/°C during Late Glacial interval and across the Holocene at a higher elevation European cave (Germany, Hölloch Cave, 1440 m alt). The 0.2 ‰/°C difference within the two transfer functions can be attributed to the difference in altitude between the two cave sites and/or different methods used to calibrate the data.

4.4.4.3. COLD SEASON TEMPERATURE RECONSTRUCTION AT MILANDRE SITE

Temperature changes at the surface are calculated using the $\delta^{18}O_{corr}$ values (Fig. 4.7) and a 0.69 ‰/°C transfer function. Temporal resolution of the reconstruction varies between 2 to 16 years (Table 4.3). Mean AWS surface temperatures for each chronozone are summarized in Table 4.6. Mean temperatures fluctuate between 5.0-5.5°C during GI-1e and GI-1a, with the highest temperatures just after the penultimate deglaciation. Lowest temperatures (around 5.0°C) are observed during the cold stages GI-1d and GI-1b. Our data suggest small changes in temperature (around 0.5 °C) for the GI-1d and GI-1c intervals, and point towards a gradual cooling of around 1.2° C (from 5.4 to 4.2° C) during the GI-1a/GS-1 (Allerød/Younger Dryas, AL/YD) transition, respectively a rapid 1.4 °C warming (from 4.6 to 6.0° C) during the Younger Dryas-Holocene (YD/HO) transition. During the YD event a gradual positive trend is observed, from mean values of 3.5 to 4.6°C. For comparison, autumn to spring temperatures (October to May, AWS T) measured for the interval 1960-2010 at Fahy meteo station (600 m alt, MeteoSchweitz) average 5.7 °C.

Isotopic event	Age (y BP)	AWS T (°C)		
		Mean	Min	Max
GI-1e*	14546	5.50	5.10	6.15
GI-1d	14234	5.03	4.79	5.18
GI-1c3	14143	5.30	4.68	5.46
GI-1c2	13952	5.11	4.77	5.31
GI-1c1	13857	5.45	5.19	5.66
GI-1b	13453	5.04	4.75	5.28
GI-1a	13147	5.38	5.12	5.59
GS1	12576	4.18	3.47	5.59
Early Holocene	11598	6.02	5.45	6.23

Table 4.6. *Overview of mean AWS T as reconstructed based on the isotopic composition of calcite from sample M6. Age represents the onset of each isotopic event. * Full extension of GI-1e is not recorded in sample M6.*

4.4.5. Temperature evolution and environmental changes in Jura Mts. based on Milandre Cave speleothem proxies

4.4.5.1. Comparism of Milandre-derived temperature and regional reconstructions

A comprehensive comparison of quantitative temperature reconstructions in the region, using various approaches, is given in Mangy et al. (2006). Most of the studies report temperature changes during the warm season (JJA) and the warmest month of the year (July, Fig. 4.11). Winter temperature reconstruction from Lake Le Locle (47°N/ 7°E, 915 m alt, Magny et al., 2001) suggest stable YD temperatures, both during the coldest month (from -2 to -3 °C) and mean annual temperatures (from 5 to 5.5 °C). The same study indicates high lake levels and slightly drier (lower precipitation) during the YD.

Calcite-based reconstructions from Milandre Cave add new evidences of regional absolute temperature changes during the cold season (autumn to spring, AWS T, Fig. 4.11). Based on this new evidence, a 0.3 to 0.5 °C decrease in temperature takes place during the cold oscillations over Bølling and Allerød (GI-1d to GI-1a). A slightly larger cooling during the warm season of around 0.5-2°C is suggested by both the pollen and chironomid-based reconstructions from Lake Lautrey (Peyron et al., 2005) and Gerzensee pollen and cladoceran records (Lotter et al., 2000). When comparing the reconstruction during larger temperature shift events, during GI-1a /GS1 transition (Allerød/YD) the 1.2°C shift is similar to the temperature shift of 1.5-2°C inferred from chironomide-based reconstructions from the Swiss lakes of Hinterbergsee (Heiri et al., 2003) and Egelsee (Larocque-Toble et al., 2010). However, this temperature decrease is smaller when compared to estimates in the order of 3°C (July temperatures) from Lac Lautrey (Heiri and Millet, 2005) and 5°C summer (JJA) temperature estimates from Gerzensee Lake (von Grafenstein et al., 2000).

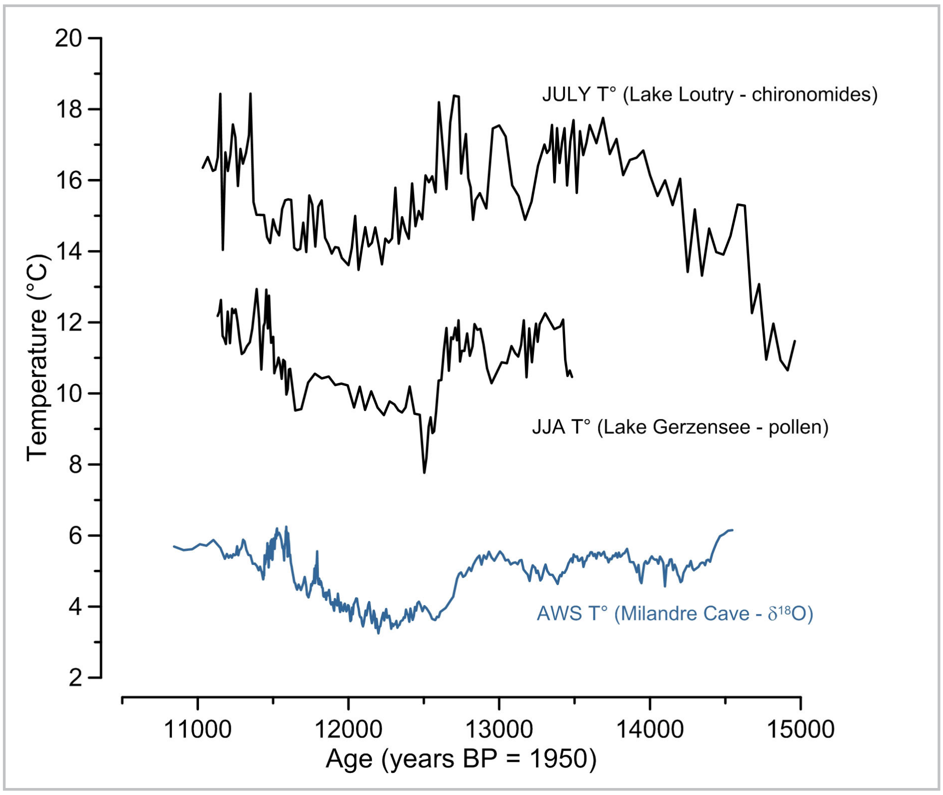

Figure 4.11. *Comparison between AWS T at Milandre site and regional temperature reconstruction from Lake Gerzensee (von Grafenstein et al., 2000).and Lake Lautrey (Heiri and Millet, 2005)*

The record from Milandre Cave shows that the first part of the YD (12 750 -12 030 y BP) was colder than the second part (12 030 – 11 653 y BP). The inferred AWS T averages 3.9 °C in the first part of the YD, and 4.6 °C in the latter. This pattern, including a high-internal variability during the YD, is apparent in a number of European temperature reconstructions in Central and NW Europe (e.g. von Grafenstein et al., 1999, Brooks and Birks, 2000, Peyron et al., 2005).

The centennial 1.3°C warming before the YD/Ho transition (centered at around 11780 y BP) has not been reported before. Replication of the event in two samples from Milandre (original chronologies) can be considered strong evidence for its existence. The short 40-year long mid-YD isotopic event observed in regional lake proxies from Ammersee and Lake Lautrey (von Grafenstein et al., 1999; Magny et al., 2006) is not present in the Milandre records.

The 1.8 °C YD/Ho shift in regional AWS T is lower compared to other regional temperature reconstructions. Regional low-land warm season paleotemperature records show a range of 1.5 - 3°C (Peyron et al., 2005; Magny et al., 2006; Lotter et al., 2000; Larocque-Toble et al., 2010), 3.9° C from the Central Alps (chironomid, Samartin et al., 2012), or even 6°C from tree rings (Tinner and Theurillat, 2003) and coleopteran records in northern France (Ponel et al., 2007). Mean annual temperatures around the Alps during the transition are reported to have increased by an order of 3-6°C (Eicher, 1994; Schwander et al, 2000).

During the early Holocene, temperature reconstruction above Milandre Cave suggests AWS T of around 0.4 °C above present values. The cooling event dated between 11 350 -11 450 y BP agrees well with the Preboreal Oscillation (PBO, e.g. Lotter et al., 1992). This short cooling event is described as a drop of 2°C in July T in the Central Alps (Maloja Riegel, Switzerland, Ilyashuk et al, 2009), 0.5–3.5 °C in the Lake Lautrey pollen and chironomid records (Peyron et al., 2005; Magny, 2006) and of 2°C in the Le Locle pollen record (Magny et al., 2001).

4.4.5.2. Late Glacial environmental changes at Milandre site

The Milandre data set shows a detailed sequence of climatic and environmental changes in the Jura Mountains. during the last deglaciation. After the last glacial maximum, calcite starts to form in Milandre Cave speleothems around 14 546 ± 140 y BP, indicating temperatures in the cave (= mean annual air temperature at the surface) above 0°C. The cave environment reacted shortly after the onset of warm conditions in the Swiss lowlands (14 590 ± 196 y BP, Gerzensee record, von Raden et al., 2012) and high alpine regions (14 708 ± 40 y BP, Siebenhengste record, Luetscher et al., 2015). Previous research provided evidence of changes in the hydrological cycle, with an increase in precipitation and moisture availability at the onset of GI-1d and the Holocene (Cupillard et al., 2014 and references therein). Temperatures at the site at the transition into GI-1d (Bølling) were around 6.6°C, approximately 1.0°C higher compared to modern conditions. A decrease of 0.9 °C in temperature occurred over a time span of 146 y during the first part of the GI-1d. Between GI-1e and GI-1a the highest and lowest temperatures are around 5.7 °C and 4.8°C respectively. The amplitude of cold minor oscillations in temperature is generally similar to the ones of decadal variations recorded in the first part of the YD event, and a third of the amplitude of the big shift that occur at the onset of the YD. The isotopic oscillations GI-1d and GI-1c2 have a duration of around 80 y, while GI-1b extends over 305 y (Table 4.4), longer than the timing calculated from Gerzensee data (258 y, von Raden et al., 2012), and GICC05 (212 y, Rasmussen et al., 2006).

During GI-1e, forests gradually form in the north of the Alps under rather continental conditions (Theuerkauf and Joosten, 2012). These forests were composed mainly of pine and birch, and where the

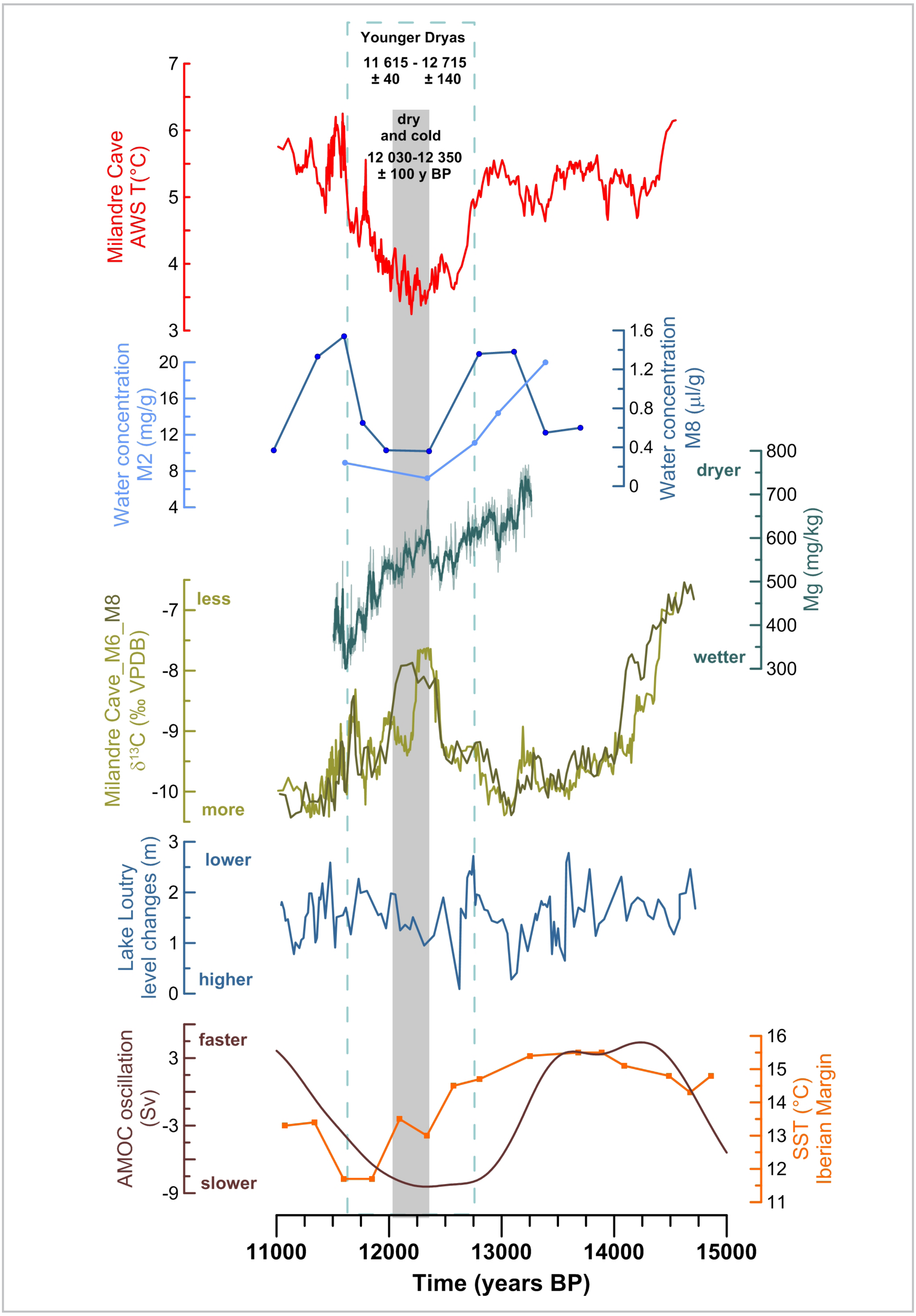

Figure 4.12. *Comparison between AWS T at Milandre site (red line, our study), variations in the water content of calcite in Milandre Cave (Vogel et al., in prep, Affolter et al., in prep), hydrological-driven changes in Mg concentration of sample M8 (our study), vegetation and soil evolution above the cave (*δ^{13}*C of sample M2 and M8), changes in the Lake Lautrey relative level (Peyron et al., 2005), variations in AMOC strainght (relative to 16 000 y BP, Ritz et al., 2013) and alkenone-based sea-surface temperatures from western Mediterranean core ODP-977A (Martrat et al., 2007).*

dominant forest composition until the early Holocene. Pronounced negative shifts in $\delta^{13}C$, until around 14 150 y BP (Fig. 4.12), likely represent shifts in the relative abundance of vegetation and soil development based both on increased temperature and moisture availability at our site. The cooling events centered at 14 210 and 13 950 y BP (GI-1d and GI-1c2) do not seem to affect vegetation development in the area, probably due to their short extent and rather small amplitude.

After the onset of GI-1b we observe a 140 y delay of the vegetation response, with a decline between 13 145-13 310 (± 85) y BP. Changes in temperature and water availability (drier periods) induce a degradation of the forest, with low soil productivity. Nevertheless, the vegetation generally has an immediate positive response (within 10 y) at the transition into warmer conditions (e.g. into GI-1a).

Around 12 880 y BP begins a decline in both temperature and vegetation development. An abrupt 1.3°C decrease in temperature between 12 565 - 12 746 (± 100) y BP marks the transition into the YD, followed by a series of low-frequency warmer/colder oscillations, until around 12 030 (± 134) y BP. Based on multiple proxy data sets (isotopic composition, trace elements concentration, water content in calcite) this first part of YD (12 750 -12 030 y BP) was colder and drier compared to the second part (12 030 – 11 653 y BP). The second part exhibit also low-amplitude high-frequency oscillations in temperature overprinted on the general increasing trend. Compared to the 1°C increase in AWS T during the YD, regional summer T reconstructions show a 3°C decrease (from 18.4 to 15.5°C, Magny et al., 2006). Although significant cooling is associated with the YD event, generally we observe an increased effective infiltration in the epikarst (wetter conditions) across this interval. A hydrological partition of YD is observed based on Mg and Sr concentration (Fig. 4.9), with hydrological conditions changing around 12 350 – 12 450 y BP. Increased water availability in the second part of the YD is also suggested by higher frequency of flushing/flooding events in the cave environment (Al concentration peaks, Fig. 4.9) between 12 350 (± 119) y BP and 11 800 (± 90) y BP. This bi-partite structure of the YD was already discussed in previous studies of terrestrial records (Bakke et al., 2009 and references therein). Magny et al., (2001, 2006) and references therein suggest a lowering of lake levels in the Jura Mountains in the first part of the YD (until around 11 934 y BP) due to dry summers and wet winters, followed in the second part by a different seasonal pattern, characterized by dry winters and wet summers. At Milandre, the coldest and driest conditions within YD occurred between 12 350 - 12 030 y BP, in agreement with the progressive lowering of regional lakes (Fig. 4.12) and with the age of the maximum Younger Dryas (Egesen) glacier advance in the Central and Eastern Alps, at 12 200 - 12 300 (± 1500) years BP (Ivy-Ochs et al., 1999; Ivy-Ochs et al., 2006). The vegetation also responded to the changes in temperature and water availability. Following the important temperature transition in the YD, an accentuated vegetation decline is recorded between 12 465 - 12 365 (± 100) y BP. Vegetation recovery starts around 12 210 y BP, and returns to pre-YD conditions only around 11 900 (± 123) y BP (Fig. 4.12, $\delta^{13}C$). Drier conditions have been inferred for the Younger Dryas in Middle Europe (Walker, 1995; Zolitschka et al., 1992), with a reduction of 25% of precipitation compared to modern conditions in Switzerland (Wohlfarth et al., 1994). In addition, changes in the amount of precipitation within the Younger Dryas are reported from different regions of Europe. In the first part of the YD, drier conditions are observed in Poland and western Germany, whereas in the Netherlands, Switzerland and the Jura Mountains a trend from wetter, towards drier conditions, has been found for the second part (Lücke and Brauer, 2004 and citations therein). Interestingly, our data support an increase in moisture availability (effective infiltration) towards the second part of the YD. No permafrost conditions developed at our cave site during the YD, as proven both by the continuous growth of calcite in the cave, and by the temperature reconstructions.

The GS-1/Holocene transition is characterized by an abrupt 1.4 °C change in temperature over approximately 60 y (11 600 - 11 660 y BP), with an almost immediate response of the vegetation. Temperature reconstructions based on fluid inclusions from Milandre speleothems suggest the onset of climatic warming already around 11 765 y BP, before the beginning of the major increase in calcite δ^{18}O. A similar observation was made in pollen-based reconstructions from Gerzensee Lake sediment, where the JJA temperature rise preceded the oxygen-isotope signal by several decades (Lotter et al., 2000), although these observations were not supported by cladoceran-inferred July temperatures reconstructions at the same site. A high amplitude centennial-scale event (11 748-11 843 y BP, peak at 11 785 y BP) ended 100 y before the transition to the Holocene (Fig, 4.12). For the speleothem-based reconstruction, the low resolution of water inclusion analysis allows a mixing of calcite precipitated during the last 200 y of the YD (during which the warm spell occurred) and the results are therefore biased. Higher resolution reconstructions and replicates in other samples could bring more answers regarding this issue.

After the transition into the Holocene, a water deficit at the Milandre site is indicated (decreased water content of the calcite) by a negative trend in temperature (Fig. 4.12). A 30 y long cold spell, centered at 11 573 (± 42) y BP occurred 20 y after the transition, while a new minimum in temperature was reached at 11 434 (± 79) y BP, 175 y after the transition to the Holocene. Pollen and cladoceran-inferred summer temperatures suggest changes that occurred over 190 – 260 y (Lotter et al., 2000). At the Milandre site, vegetation was little affected by the negative trend in temperature during this 175 yearlong period, and the maximum development of soil/vegetation for the studied interval (and close to present day conditions) reached around 11 380 (± 67) y BP.

4.4.6. Local influences of the variation in North Atlantic atmospheric circulation

The sea-ice-atmosphere system of the North Atlantic Ocean plays a major role for the climate of north-western and central Europe, by cooling surface air temperatures and influencing the position of the storm tracks (Wanner et al., 2001). After the onset of the last deglaciation, episodic discharges of fresh-water into the North Atlantic caused a weakening of the Atlantic Meridional Overturning Circulation (AMOC) sufficient to affect the European climate (Grafenstein et al., 1999 and references therein). Our new data show the close relationship between the changes in AMOC state and temperature/ moisture availability at the Milandre site (Fig. 4.12). The onset of YD occurred at a slow state of AMOC, and mid-YD hydrologic changes at the site occurred shortly after its resumption (Fig. 4.12, Ritz et al., 2013). Interestingly, across the YD we did not observe a close association between temperature and moisture availability at the Milandre site and changes in the North Atlantic Sea surface temperature, as observed for example in previous deglaciation intervals in other regions of Switzerland (see Chapter 2).

Regarding the YD event, previous studies suggest a strong similarity between several European climate proxies in terrestrial and marine records, with Late glacial climate shifts almost synchronous over wide regions (van Raden et al., 2014 and references therein). Differences in the regional responses are attributed to the gradual repositioning of the polar air masses and storm tracks from central to north Europe (Bakke et al., 2009; Lane et al., 2013). Southward expansion of Atlantic sea ice (as far as 52°N, Broecker, 2006) at the onset of YD induced abrupt changes in westerly circulation towards a stronger and more zonal jet over central Europe. Milandre Cave was situated at the southern limit of the polar front during the YD (Lane et al., 2013) and recorded its dynamics over this particular cold event. Around 12 680 y BP the vegetation decline starts at the site, and a coeval increase in Si concentration in Milandre calcite indicates an increase in storminess during the autumn to spring seasons (when maximum water infiltration occurs in the cave), broadly coincident with regional reduction of vegetation cover and wind intensity changes (Bakke et al., 2009; Theuerkauf and Joosten, 2012; Magny et al., 2006). Nevertheless, during the YD warmer and moisture masses prevailed at the latitude of our cave site compared to the north of Europe (latitudes north of the sea-ice limit) where cold and dry masses enabled, for example, the formation of permafrost (Theuerkauf and Joosten, 2012). Throughout the YD, the climate system in the North Atlantic region was generally unstable (e.g. Bakke et al. 2009; Brauer et al. 2008, our study). At the Milandre site we observe a more stable first part of the YD compared with its second part, with an increasing trend in temperature and moisture availability across the YD, similar to conditions described in North Europe in proxy and model reconstructions (Bakke et al., 2009 and references therein). The establishment of wetter conditions at our cave site (46°N) after 12 100 ± 100 y BP follow most probably the gradual northward retreat of the polar front and subsequent increased moisture delivery into Western Europe (around 12 240 ± 40 y BP, Lane et al., 2013) as a result of retreat of sea ice in the North Sea around 12 150 y BP (Bakke et al., 2009). The latter study suggest that the last 400 years of YD were characterized by a regime "repeatedly 'flickered' towards interstadial conditions", similar to the high isotopic variability reflected in the isotopic profile of our samples in the second part of the YD before the rapid transition to the Holocene.

The good preservation conditions of climate-induced environmental changes (vegetation, temperature, moisture availability) in the stalagmites from Milandre site are indicative of the very high sensitivity of this cave speleothems, not only at regional scale, but equally on hemispheric temperature and hydrologic changes.

4.5. Conclusions

A multi-proxy approach was used to reconstruct in high detail cold-season temperature changes and environment evolution over the Late Glacial-Holocene interval at Milandre Cave site (Swiss Jura Mountains). Timing of chronozones show very good agreement with regional terrestrial δ^{18}O records (e.g. von Grafenstein et al., 1999, Genty et al., 2006, van Raden et al., 2012, Lotter et al., 2012, Luetscher et al., 2015).

A new high resolution cold-season temperature reconstruction of the region is provided. Coeval samples from Milandre Cave started to grow shortly after the last deglaciation, around 14 546 ± 140 y BP, as mean AWS temperatures around 5.5 °C prevailed at the cave site. Over Bølling and Allerød intervals mean AWT fluctuate between 5.0-5.5°C. A 1.2° C gradual cooling makes the transition into YD, and a 1.4 °C warming marks the transition into Holocene. The first part of YD, between 12 750 -12 030 y BP, was colder and drier compared to the second part, between 12 030 – 11 653 y BP. Vegetation responded almost immediate to major changes in temperature.

Our paleo hydrologic reconstructions are consistent with interpretations based on climate archives from central and northern Europe. The establishment of wetter conditions at our cave site (46°N) after 12 100 ± 100 y BP follow most probably the gradual northward retreat of the polar front and subsequent increased moisture delivery into Western Europe (around 12 240 ± 40 y BP, Lane et al., 2013) as a result of retreat of sea ice in the North Sea around 12 150 y BP (Bakke et al., 2009).

Furthermore, as the δ^{18}O-temperature coefficient calculated for Late Holocene falls well within the range of values estimated for this Late Glacial interval, brings evidences that the source of the moisture in Swiss Jura Mountains did not overcome major changes over the last 14 550 y BP.

BIBLIOGRAPHY

Affolter, S., 2015. Innovative isotope ratio measurements of speleothem fluid inclusions, Physics Institute. Bern University, p. 163.

Affolter, S., Fleitmann, D., Leuenberger, M., 2014. New online method for water isotope analysis of speleothem fluid inclusions using laser absorption spectroscopy (WS-CRDS). Clim. Past 10, 1291-1304.

Affolter, S., Häuselmann, A.D., Fleitmann, D., Leuenberger, M., Breecker, D., submitted in revised form. Triple isotope (δD, δ18O, δ17O) study on precipitation, drip water and speleothem fluid inclusions for a central European cave (NW Switzerland). Quaternary Science Reviews.

Bakke, J., Lie, O., Heegaard, E., Dokken, T., Haug, G.H., Birks, H.H., Dulski, P., Nilsen, T., 2009. Rapid oceanic and atmospheric changes during the Younger Dryas cold period. Nature Geosci 2, 202-205.

Baldini, J.U., McDermott, F., Fairchild, I.J., 2002. Speleothem trace elements as palaeohydrological proxies during the '8,200 year' cold/dry event. Geochim Cosmochim Ac 66, A46-A46.

Bard, E., Hamelin, B., Delanghe-Sabatier, D., 2010. Deglacial Meltwater Pulse 1B and Younger Dryas Sea Levels Revisited with Boreholes at Tahiti. Science 327, 1235-1237.

Brauer, A., Haug, G.H., Dulski, P., Sigman, D.M., Negendank, J.F.W., 2008. An abrupt wind shift in western Europe at the onset of the Younger Dryas cold period. Nature Geoscience 1, 520-523.

Breitenbach, S.F.M., Rehfeld, K., Goswami, B., Baldini, J.U.L., Ridley, H.E., Kennett, D.J., Prufer, K.M., Aquino, V.V., Asmerom, Y., Polyak, V.J., Cheng, H., Kurths, J., Marwan, N., 2012. COnstructing Proxy Records from Age models (COPRA). Clim. Past 8, 1765-1779.

Broecker, W.S., 2006. Was the Younger Dryas Triggered by a Flood? Science 312, 1146-1148.

Brooks, S.J., Birks, H.J.B., 2000. Chironomid-inferred late-glacial and early-Holocene mean July air temperatures for Krakenes Lake, western Norway. J Paleolimnol 23, 77-89.

Cheng, H., Lawrence Edwards, R., Shen, C.-C., Polyak, V.J., Asmerom, Y., Woodhead, J., Hellstrom, J., Wang, Y., Kong, X., Spötl, C., Wang, X., Calvin Alexander Jr, E., 2013. Improvements in 230Th dating, 230Th and 234U half-life values, and U–Th isotopic measurements by multi-collector inductively coupled plasma mass spectrometry. Earth and Planetary Science Letters 371–372, 82-91.

Cupillard, C., Magny, M., Bocherens, H., Bridault, A., Bégeot, C., Bichet, V., Bossuet, G., Drucker, D.G., Gauthier, E., Jouannic, G., Millet, L., Richard, H., Rius, D., Ruffaldi, P., Walter-Simonnet, A.-V., 2014. Changes in ecosystems, climate and societies in the Jura Mountains between 40 and 8 ka cal BP. Quaternary International.

Dansgaard, W., 1964. Stable Isotopes in Precipitation. Tellus 16, 436-468.

Duplessy, J.C., Roche, D.M., Kageyama, M., 2007. The Deep Ocean During the Last Interglacial Period. Science 316, 89-91.

Eicher, U., 1994. Sauerstoffisotopenanalysen durchgeführt an spät- sowie frühpostglazialen Seekreiden, Dissertationes Botanicae, p. 277.

Fairchild, I.J., Baker, A., 2012. Speleothem Science: From Process to Past Environments. Wiley-Blackwell.

Fairchild, I.J., McMillan, E.A., 2007. Speleothems as indicators of wet and dry periods. Int J Speleol 36, 69-74.

Fohlmeister, J., Vollweiler, N., Spötl, C., Mangini, A., 2012. COMNISPA II: Update of a mid-European isotope climate record, 11 ka to present. The Holocene.

Genty, D., Blamart, D., Ghaleb, B., Plagnes, V., Causse, C., Bakalowicz, M., Zouari, K., Chkir, N., Hellstrom, J., Wainer, K., Bourges, F., 2006. Timing and dynamics of the last deglaciation from European and North African delta C-13 stalagmite profiles - comparison with Chinese and South Hemisphere stalagmites. Quaternary Science Reviews 25, 2118-2142.

Gigon, R. and Wegner; R. 1986.Inventaire spéléologique de la Suisse, tome II, canton du Jura, Schweizerische Akademeie des Naturwissenschaften, Porrontruy.

Veit, H., 2002. Die Alpen. Geoökologie und Landschaftsentwicklung. Ulmer, Stuttgard, 352 p.

Hasenfratz, A., 2012. Temperature reconstruction over the past two millenia based on stalagmite δ18O record from the Jura Swiss Mountains, Institute of Geological Sciences. Bern University, p. 79.

Hasenfratz, A., Fleitmann, D., Häuselmann, A.D., Lehner, F., Cheng, H., Edwards, R.L., Leuenberger, M., Affolter, S., Raible, C.C., Breitenbach, S.F.M., Luterbacher, J., in prep. Central European temperature variations over the past two millennia based on a stalagmite oxygen isotope record from the Swiss Jura Mountains.

Heiri, O., Millet, L., 2005. Reconstruction of Late Glacial summer temperatures from chironomid assemblages in Lac Lautrey (Jura, France). J Quaternary Sci 20, 33-44.

Hellstrom, J.C., McCulloch, M.T., 2000. Multi-proxy constraints on the climatic significance of trace element records from a New Zealand speleothem. Earth Planet Sc Lett 179, 287-297.

Hu, C., Huang, J., Fang, N., Xie, S., Henderson, G.M., Cai, Y., 2005. Adsorbed silica in stalagmite carbonate and its relationship to past rainfall. Geochimica Et Cosmochimica Acta 69, 2285-2292.

Ilyashuk, B., Gobet, E., Heiri, O., Lotter, A.F., van Leeuwen, J.F.N., van der Knaap, W.O., Ilyashuk, E., Oberli, F., Ammann, B., 2009. Late Glacial environmental and climatic changes at the Maloja Pass, Central Swiss Alps, as recorded by chironomids and pollen. Quaternary Science Reviews 28, 1340-1353.

Ivy-Ochs, S., Kerschner, H., Kubik, P.W., Schlüchter, C., 2006. Glacier response in the European Alps to Heinrich Event 1 cooling: the Gschnitz stadial. J Quaternary Sci 21, 115-130.

Ivy-Ochs, S., Schlüchter, C., Kubik, P.W., Denton, G.H., 1999. Moraine Exposure Dates Imply Synchronous Younger Dryas Glacier Advances in the European Alps and in the Southern Alps of New Zealand. Geografiska Annaler: Series A, Physical Geography 81, 313-323.

Kern, Z., Kohán, B., Leuenberger, M., 2014. Precipitation isoscape of high reliefs: interpolation scheme designed and tested for monthly resolved precipitation oxygen isotope records of an Alpine domain. Atmos. Chem. Phys. 14, 1897-1907.

Kovacs, R., Nishiguchi, K., Utani, K., Gunther, D., 2010. Development of direct atmospheric sampling for laser ablation-inductively coupled plasma-mass spectrometry. J Anal Atom Spectrom 25, 142-147.

Lachniet, M.S., Denniston, R.F., Asmerom, Y., Polyak, V.J., 2014. Orbital control of western North America atmospheric circulation and climate over two glacial cycles. Nature Communications 5.

Lane, C.S., Brauer, A., Blockley, S.P.E., Dulski, P., 2013. Volcanic ash reveals time-transgressive abrupt climate change during the Younger Dryas. Geology.

Larocque-Tobler, I., Heiri, O., Wehrli, M., 2010. Late Glacial and Holocene temperature changes at Egelsee, Switzerland, reconstructed using subfossil chironomids. J Paleolimnol 43, 649-666.

Lotter, A.F., Birks, H.J.B., Eicher, U., Hofmann, W., Schwander, J., Wick, L., 2000. Younger Dryas and Allerød summer temperatures at Gerzensee (Switzerland) inferred from fossil pollen and cladoceran assemblages. Palaeogeography, Palaeoclimatology, Palaeoecology 159, 349-361.

Lotter, A.F., Heiri, O., Brooks, S., van Leeuwen, J.F.N., Eicher, U., Ammann, B., 2012. Rapid summer temperature changes during Termination 1a: high-resolution multi-proxy climate reconstructions from Gerzensee (Switzerland). Quaternary Science Reviews 36, 103-113.

Lowe, J.J., Rasmussen, S.O., Bjorck, S., Hoek, W.Z., Steffensen, J.P., Walker, M.J.C., Yu, Z.C., Grp, I., 2008. Synchronisation of palaeoenvironmental events in the North Atlantic region during the Last Termination: a revised protocol recommended by the INTIMATE group. Quaternary Science Reviews 27, 6-17.

Lücke, A., Brauer, A., 2004. Biogeochemical and micro-facial fingerprints of ecosystem response to rapid Late Glacial climatic changes in varved sediments of Meerfelder Maar (Germany). Palaeogeography, Palaeoclimatology, Palaeoecology 211, 139-155.

Luetscher, M., Boch, R., Sodemann, H., Spötl, C., Cheng, H., Edwards, R.L., Frisia, S., Hof, F., Müller, W., 2015. North Atlantic storm track changes during the Last Glacial Maximum recorded by Alpine speleothems. Nature Communications 6.

Magny, M., Aalbersberg, G., Bégeot, C., Benoit-Ruffaldi, P., Bossuet, G., Disnar, J.-R., Heiri, O., Laggoun-Defarge, F., Mazier, F., Millet, L., Peyron, O., Vannière, B., Walter-Simonnet, A.-V., 2006. Environmental and climatic changes in the Jura mountains (eastern France) during the Late Glacial–Holocene transition: a multi-proxy record from Lake Lautrey. Quaternary Science Reviews 25, 414-445.

Magny, M., Guiot, J., Schoellammer, P., 2001. Quantitative Reconstruction of Younger Dryas to Mid-Holocene Paleoclimates at Le Locle, Swiss Jura, Using Pollen and Lake-Level Data. Quaternary Res 56, 170-180.

McDermott, F., 2004. Palaeo-climate reconstruction from stable isotope variations in speleothems: a review. Quaternary Science Reviews 23, 901-918.

Perrin, J., Koop, L., 2005. Hétérogénité des écoulements dans la zone non saturöe dùn aquifère karstique (site de Milandre, Jura suisse). Bulletin du centre d`hydrogöologie de l`université de Neuchatel, No. 21.

Peyron, O., Begeot, C., Brewer, S., Heiri, O., Magny, M., Millet, L., Ruffaldi, P., Van Campo, E., Yu, G., 2005. Late-Glacial climatic changes in Eastern France (Lake Lautrey) from pollen, lake-levels, and chironomids. Quaternary Res 64, 197-211.

Rasmussen, S.O., Andersen, K.K., Svensson, A.M., Steffensen, J.P., Vinther, B.M., Clausen, H.B., Siggaard-Andersen, M.L., Johnsen, S.J., Larsen, L.B., Dahl-Jensen, D., Bigler, M., Röthlisberger, R., Fischer, H., Goto-Azuma, K., Hansson, M.E., Ruth, U., 2006. A new Greenland ice core chronology for the last glacial termination. Journal of Geophysical Research: Atmospheres 111, D06102.

Ritz, S.P., Stocker, T.F., Grimalt, J.O., Menviel, L., Timmermann, A., 2013. Estimated strength of the Atlantic overturning circulation during the last deglaciation. Nature Geosci 6, 208-212.

Rozanski, K., Johnsen, S.J., Schotterer, U., Thompson, L.G., 1997. Reconstruction of past climates from stable isotope records of palaeo-precipitation preserved in continental archives. Hydrolog Sci J 42, 725-745.

Samartin, S., Heiri, O., Vescovi, E., Brooks, S.J., Tinner, W., 2012. Late Glacial and early Holocene summer temperatures in the southern Swiss Alps reconstructed using fossil chironomids. J Quaternary Sci 27, 279-289.

Schmassmann, S., 2010. Speleothem-based climate and environmental reconstruction: A pilot study in the Swiss Jura Mountains, Institute for Geological Sciences. University of Bern, p. 149.

Schürch, M., Kozel, R., Schotterer, U., Tripet, J.-P., 2003. Observation of isotopes in the water cycle—the Swiss National Network (NISOT). Env Geol 45, 1-11.

Schwander, J., Eicher, U., Ammann, B., 2000. Oxygen isotopes of lake marl at Gerzensee and Leysin (Switzerland), covering the Younger Dryas and two minor oscillations, and their correlation to the GRIP ice core. Palaeogeography, Palaeoclimatology, Palaeoecology 159, 203-214.

Sodemann, H., Zubler, E., 2010. Seasonal and inter-annual variability of the moisture sources for Alpine precipitation during 1995-2002. Int J Climatol 30, 947-961.

Tabersky, D., Nishiguchi, K., Utani, K., Ohata, M., Dietiker, R., Fricker, M.B., de Maddalena, I.M., Koch, J., Gunther, D., 2013. Aerosol entrainment and a large-capacity gas exchange device (Q-GED) for laser ablation inductively coupled plasma mass spectrometry in atmospheric pressure air. J Anal Atom Spectrom 28, 831-842.

Theuerkauf, M., Joosten, H., 2012. Younger Dryas cold stage vegetation patterns of central Europe – climate, soil and relief controls. Boreas 41, 391-407.

Tinner, W., Theurillat, J.-P., 2003. Uppermost Limit, Extent, and Fluctuations of the Timberline and Treeline Ecocline in the Swiss Central Alps during the past 11,500 Years. Arctic, Antarctic, and Alpine Research 35, 158-169.

Tremaine, D.M., Froelich, P.N., Wang, Y., 2011. Speleothem calcite farmed in situ: Modern calibration of δ18O and δ13C paleoclimate proxies in a continuously-monitored natural cave system. Geochimica Et Cosmochimica Acta 75, 4929-4950.

van Raden, U.J., Colombaroli, D., Gilli, A., Schwander, J., Bernasconi, S.M., van Leeuwen, J., Leuenberger, M., Eicher, U., 2013. High-resolution late-glacial chronology for the Gerzensee lake record (Switzerland): δ18O correlation between a Gerzensee-stack and NGRIP. Palaeogeography, Palaeoclimatology, Palaeoecology 391, Part B, 13-24.

Vogel, N., Scheidegger, Y., Brennwald, M.S., Fleitmann, D., Figura, S., Wieler, R., Kipfer, R., 2013. Stalagmite water content as a proxy for drip water supply in tropical and subtropical areas. Clim. Past 9, 1-12.

Vogel, N., Brennwald, M.S., Figura, S., Häuselmann, A.D., Fleitmann, F., Maden, C., Kipfer, R., in prep., Temperature reconstruction by noble gas thermometry on a stalagmite grown in the Swiss Jura Mountains during the last glacial-interglacial transition.

von Grafenstein, U., Belmecheri, S., Eicher, U., van Raden, U.J., Erlenkeuser, H., Andersen, N., Ammann, B., 2013. The oxygen and carbon isotopic signatures of biogenic carbonates in Gerzensee, Switzerland, during the rapid warming around 14,685 years BP and the following interstadial. Palaeogeography, Palaeoclimatology, Palaeoecology 391, Part B, 25-32.

von Grafenstein, U., Eicher, U., Erlenkeuser, H., Ruch, P., Schwander, J., Ammann, B., 2000. Isotope signature of the Younger Dryas and two minor oscillations at Gerzensee (Switzerland): palaeoclimatic and palaeolimnologic interpretation based on bulk and biogenic carbonates. Palaeogeography, Palaeoclimatology, Palaeoecology 159, 215-229.

von Grafenstein, U., Erlenkeuser, H., Brauer, A., Jouzel, J., Johnsen, S.J., 1999. A mid-European decadal isotope-climate record from 15,500 to 5000 years BP. Science 284, 1654-1657.

Walker, M.J.C., 1995. Climatic changes in Europe during the last glacial/interglacial transition. Quaternary International 28, 63-76.

Wohlfarth, B., Gaillard, M.-J., Haeberli, W., Kelts, K., 1994. Environment and climate in southwestern Switzerland during the last termination, 15-10 ka BP. Quaternary Science Reviews 13, 361-394.

Wurth, G., Niggemann, S., Richter, D.K., Mangini, A., 2004. The younger dryas and holocene climate record of a stalagmite from Holloch cave (Bavarian Alps, Germany). J Quaternary Sci 19, 291-298.

Zolitschka, B., Haverkamp, B., Negendank, J.F.W., 1992. Younger Dryas Oscillation - Varve dated, microstratigraphic, palynological and paleomagnetic records from Lake Holzmaar, Germany., In: Bard;e., Broecker, W.S. (Eds.), The last deglaciation: Absolute and radiocarbon chronologies Springer-Verlag, pp. 80-101.

CHAPTER 5.

PRELIMINARY RESULTS ON HOLOCENE COLD TEMPERATURE RECONSTRUCTIONS, AS RECORDED IN SPELEOTHEM M6 FROM MILANDRE CAVE (SWISS JURA MOUNTAINS)

In collaboration with Adam Hasenfratz[1], Hai Cheng[2,3], Lawrence R. Edwards[3], Dominik Fleitmann [4,5]

[1]Geological Institute, ETH Zürich, Sonneggstrasse 5, CH-8092 Zürich

[2]Institute of Global Environmental Change, Xi'an Jiaotong University, Xi'an 710049, China

[3]Department of of Geology and Geophysics, University of Minnesota, Minneapolis, Minnesota 55455, USA

[4]Department of Archaeology, School of Human and Environmental Sciences, University of Reading, Whiteknights, PO Box 227, Reading

[5]Institute of Geological Sciences and Oeschger Centre for Climate Change Research, Baltzerstrasse 1+3, CH-3012 Bern

5.1. Introduction

Although the warm climate of the Holocene, which is considered as an interglacial, there is increasing interest in studying the climate variability during this period (e.g. Allen et al., 2007; Wanner et al., 2011 and references therein; Wirth et al., 2013). Detailed and well- dated paleoclimate archives show that significant temperature variation occurred in Europe during most of the Holocene (Litt et al., 2009; Büntger et al, 2011; Esper et al., 2014). Although their amplitudes cannot be compared with the large millennial-scale temperatures of glacial climates (e.g. Dansgaard/Oeschger cycles), the social-economic impact was considerable (Wanner et al., 2011 and references therein; Schennan et al., 2013)

As there is much to be learned about the mechanisms that could be responsible for the observed climate variability during the Holocene, high-resolution and precisely-dated archives are needed. Natural proxies such as tree rings, lake sediments, ice cores, cave deposits, peat, and corals allow us to evaluate climate variability and forcing mechanisms in time. Each of these proxies presents its own weaknesses and strengths in terms of temporal resolution, spatial coverage, age model construction and target season (e.g. Jones and Mann, 2004 and references therein). Furthermore, all proxy records are an indirect measurement of climate change and need some kind of transfer function to translate their signature into climate parameters (e.g. water availability, temperature).

One of the main goals of the SINERGIA project was to construct a complete and highly-resolved Holocene record of the air temperature from Switzerland. Milandre cave was chosen as a sampling site for several reasons. First, during the last decades, Milandre Cave was the subject of multiple scientific studies, addressing its hydrology and physical parameters in the cave aquifer (e.g., Jeannin, 1996; Perrin et al., 2003a, 2003b; Perrin, 2003) which allow a good understanding of this spelaean environment. Second, Schmassmann (2010) has already shown the suitability of the cave stalagmites from Milandre Cave to host reliable proxies of climate and environmental changes from annual to millennial scales.

The difficulty to determine any transfer function over long time intervals (e.g. Holocene) is given by the fact that several climate parameters influence the proxies, and/or the parameters will not remain constant over time. In order to overcome this issue, we adopted the following strategy: test the reliability of the transfer function independently, based on multiple paleothermometer proxies in speleothems from Milandre Cave. This calculation was done both for Late Holocene and Late Glacial intervals.

5.2. Site and sample description

Milandre Cave is located in the Ajoie region of the Swiss Jura Mountains (47°49’N / 7°02’E, 400 m asl, Fig. 4.1). Surface meteoric parameters in the region are measured at the nearby Fahy weather station (47°42’N / 6°94’E, 596 m asl, 200 m higher than our cave site) which is operated by the Swiss Federal Office of Meteorology and Climatology (MeteoSchweiz). The mean annual average of surface air temperature for the interval 1960-2010 is 8.6°C, with mean winter and summer temperatures of 1.1°C and 16.4°C, respectively. A high seasonality is present in the outside air temperature, with maximum mean temperatures in August with 17.2°C, and minimum in January with 0.4°C. Precipitation is relatively equal over the year; with precipitation averaging 292 mm in summer and 224 mm in winter. Snowfall may occur from November to March, although this region exhibits a mild climate during winter (mean temperature above 0°C, MeteoSchweiz).

Milandre Cave formed in the limestone of the St.-Ursanne Formation (Tabular Jura unit). The cave has a total length of 10.5 km and develops on two levels. The upper level is fossil and covered by only

30-80 m of host rock. The lower level is 30 m lower below the upper level and used by the 4.6 km long underground Milandrine River. Our sampling campaign focused on a fossil gallery of the cave, named Galerie des Fistuleuses (see Fig. 4.2). This part of the cave can be accessed by a 15 m long tunnel, which was enlarged by mining in 1967. Cave air temperature is 9.8°C and constant throughout the year (±0.2 °C; monitored between 2012 and 2014). Air flow circulation in this part of the gallery was under detection limit (< 100 l/s air flow), and relative humidity is 100 %. Values of pCO_2 between 0.3 to 1.41 % were measured (2008 - 2014, measuring campaigns) although pCO_2 in the gallery can rise up to values around 4 %, especially during late autumn and early winter (pers.comm. Ph. Häuselmann).

Sample M6 is a 145.2 cm long candlestick stalagmite and was active (precipitated calcite on its top) when collected in autumn 2011. The sampling location, from a slightly elevated lateral side of the Galerie des Fistuleuses, 200 m south of the northern entrance of the cave, assured a minimal influence of in-cave processes, such as high ventilation and flooding events. The sample was fed by a soda straw dripping at 0`15`` to 6`00`` time intervals. The sample has no visible hiatus, is composed by columnar fabric crystals, and well defined macroscopic laminae are observed on the top 20 cm of the sample (Fig. 5.1). Axial holes (aligned along the axis of the sample) are a common feature in M6. They are possibly related with the action of the falling drop, which reduces the deposition rate of the calcite at the apex of sample (Shtober-Zisu et al., 2014). Laminations were observed between the pores, a clear indication that the calcite deposition continued at a normal rate. The focus of the present study is the top 135.9 cm of the M6 sample, for data obtained in the lower part of the sample please refer to Chapter 3 of this thesis.

5.3. Methods and results

^{230}Th-ages were determined on a multi-collector inductively coupled plasma mass spectrometer (MC-ICP-MS, Thermo-Finnigan Neptune) at the Department of Geology and Geophysics, University of Minnesota. Details of the methods, including standards used for mass fractionation and yield correction can be found in Edwards et al. (1987) and Cheng et al. (2013). For analysis, between 170 and 200 mg of powder was drilled along discrete growth horizons (Fig. 5.1). The ^{230}Th-dating results for the top 135.9 cm of stalagmite M6 are provided in Table 5.1. The low U content, averaging 70 ppb (min. 37.7 and max. 225.5 ppb) and presence of detrital Th resulted in high chronological uncertainties. Ages are in chronostratigraphic order, except a reversal (sample M6_32) at 56.75 cm depth in the sample. This reversal could not be resolved by the statistical program used to construct our age model (COPRA algorithm, Breitenbach et al., 2012) and therefore was excluded. Therefore, the final age model of sample M6 is constrained by using 36 ^{230}Th ages, all in stratigraphic order within their 2 σ dating uncertainties. The resulting median of the 1000 Monte Carlo simulations and its 95% confidence interval (blue colour) are presented in Fig. 5.2. Growth rate of the sample varies between 0.018 and 0.698 mm/year, around a mean of 0.195 mm/year.

For stable carbon and oxygen isotope analysis, a total of 3170 samples were micromilled continuously at 0.1 mm (top 4.4 cm) and 0.5 mm increments from 0 to 4.4 cm and from 4.4 to 135.9 cm, respectively. Powdered samples were measured using a Finnigan Delta V Advantage mass spectrometer equipped with an automated carbonate preparation system (Gas Bench II) at the Institute of Geological Sciences, University of Bern, Switzerland. Results are reported relative to the international Vienna Peedee Belemnite (VPDB) standard. Analytical errors for $\delta^{18}O$ and $\delta^{13}C$ are 0.07 and 0.06 ‰ VPDB (1σ), respectively (Fleitmann et al., 2009). The temporal resolution of the oxygen and carbon isotope profiles varies between subannual and 92 years, with an average of 4 years. $\delta^{18}O$ values vary between -5.15 and -8.36 ‰ around a mean of -6.82 ‰ VPDB. Superimposed on the long-term trends distinct short-term

Table 5.1.

^{230} Th ages of sample M6

Sample	Depth (cm)	^{238}U (ppb)		^{232}Th (ppt)		^{230}Th / ^{232}Th (atomic x10^{-6})		^{230}Th / ^{238}U (activity)		^{230}Th Age (y) (uncorrected)		**^{230}Th Age (y BP) (corrected)**	
M6_18	1.2	50.7	±0.1	223	±5	9	±3	0.0023	±0.0007	208	±63	**41**	**±97**
M6_25	7.3	46.1	±0.1	809	±16	8	±1	0.0081	±0.0004	724	±39	**243**	**±298**
M6_19	12.1	48.3	±0.1	290	±6	14	±2	0.0051	±0.0007	451	±66	**246**	**±120**
M6_24	17	48.9	±0.1	365	±7	15	±1	0.0070	±0.0004	620	±40	**381**	**±131**
M6_12	19.85	58.8	±0.1	429	±9	17	±1	0.0075	±0.0006	669	±58	**433**	**±135**
M6_20	22.4	51.8	±0.1	139	±3	47	±4	0.0076	±0.0007	679	±59	**553**	**±74**
M6_26	22.5	47.0	±0.1	402	±8	16	±1	0.0081	±0.0004	723	±38	**458**	**±148**
M6_29	27.5	37.7	±0.1	308	±6	24	±1	0.0120	±0.0005	1079	±47	**820**	**±146**
M6_21	29.5	47.0	±0.1	298	±6	30	±2	0.0115	±0.0008	1036	±73	**822**	**±130**
M6_27	34.7	45.1	±0.1	340	±7	33	±1	0.0153	±0.0005	1374	±42	**1131**	**±134**
M6_10	40.35	41.6	±0.1	426	±9	30	±2	0.0187	±0.0009	1669	±83	**1365**	**±191**
M6_17	47	60.8	±0.1	233	±5	93	±3	0.0215	±0.0007	1935	±62	**1782**	**±89**
M6_28	52	46.1	±0.1	233	±5	82	±2	0.0249	±0.0005	2260	±42	**2076**	**±95**
M6-35	55.6	64.7	±0.1	825	±17	37	±1	0.0287	±0.0004	2617	±35	**2246**	**±220**
M6_32	56.75	50.2	±0.1	662	±13	47	±1	0.0377	±0.0007	3424	±66	**3046**	**±232**
M6-36	60.8	58.5	±0.1	655	±13	50	±1	0.0341	±0.0007	3109	±61	**2776**	**±200**
M6_16	62.2	62.6	±0.1	687	±14	53	±2	0.0355	±0.0008	3234	±71	**2909**	**±199**
M6_9	68.45	65.3	±0.1	447	±9	95	±2	0.0395	±0.0007	3620	±63	**3393**	**±132**
M6-37	70.3	60.5	±0.1	811	±16	52	±1	0.0426	±0.0006	3914	±60	**3527**	**±236**
M6-38	77.2	51.8	±0.1	1484	±30	30	±1	0.0517	±0.0007	4770	±64	**4014**	**±494**
M6_22	80.35	62.4	±0.1	522	±10	98	±2	0.0500	±0.0007	4577	±65	**4314**	**±156**
M6-39	83.54	68.8	±0.1	1196	±24	52	±1	0.0543	±0.0006	5033	±58	**4549**	**±303**
M6-40	87.1	62.3	±0.1	1419	±28	42	±1	0.0573	±0.0006	5299	±59	**4686**	**±393**
M6_15	91.6	62.8	±0.1	800	±16	77	±2	0.0596	±0.0008	5506	±75	**5138**	**±229**
M6-41	94.8	64.1	±0.1	575	±12	112	±2	0.0613	±0.0004	5689	±41	**5409**	**±159**
M6_33	98	57.0	±0.1	484	±10	129	±3	0.0664	±0.0006	6158	±61	**5890**	**±157**
M6-42	102.3	78.0	±0.1	3316	±67	29	±1	0.0743	±0.0006	6915	±60	**5824**	**±729**
M6_14	105.1	84.1	±0.2	842	±17	114	±3	0.0692	±0.0006	6400	±64	**6098**	**±181**
M6-43	109.1	70.1	±0.1	1891	±38	48	±1	0.0781	±0.0006	7269	±57	**6556**	**±462**
M6_13	111.05	74.8	±0.1	395	±8	235	±5	0.0750	±0.0007	6964	±67	**6776**	**±111**
M6-44	113.6	80.9	±0.1	796	±16	134	±3	0.0802	±0.0006	7468	±57	**7168**	**±176**
M6_34	116	66.5	±0.1	897	±18	105	±2	0.0859	±0.0007	7989	±70	**7603**	**±239**
M6-45	118.8	100.8	±0.2	3047	±61	51	±1	0.0930	±0.0006	8690	±61	**7901**	**±516**
M6_11	121.6	85.5	±0.2	277	±6	474	±10	0.0930	±0.0008	8615	±85	**8476**	**±100**
M6_23	126.3	80.0	±0.1	541	±11	237	±5	0.0974	±0.0006	9126	±62	**8902**	**±130**
M6-46	127.6	82.9	±0.1	5028	±101	31	±1	0.1147	±0.0007	10877	±74	**9347**	**±1040**
M6_30	133.2	82.1	±0.1	3723	±75	42	±1	0.1162	±0.0007	11017	±70	**9860**	**±778**
M6-47	134.8	103.2	±0.2	2279	±46	89	±2	0.1188	±0.0007	11230	±72	**10637**	**±381**
M6-48	137.9	120.6	±0.3	569	±11	429	±9	0.1229	±0.0005	11704	±61	**11527**	**±101**

U decay constants: λ_{238} = 1.55125x10^{-10} (Jaffey et al., 1971) and λ_{234} = 2.82206x10^{-6} (Cheng et al., 2013).

Th decay constant: l230 = 9.1705x10-6 (Cheng et al., 2013).

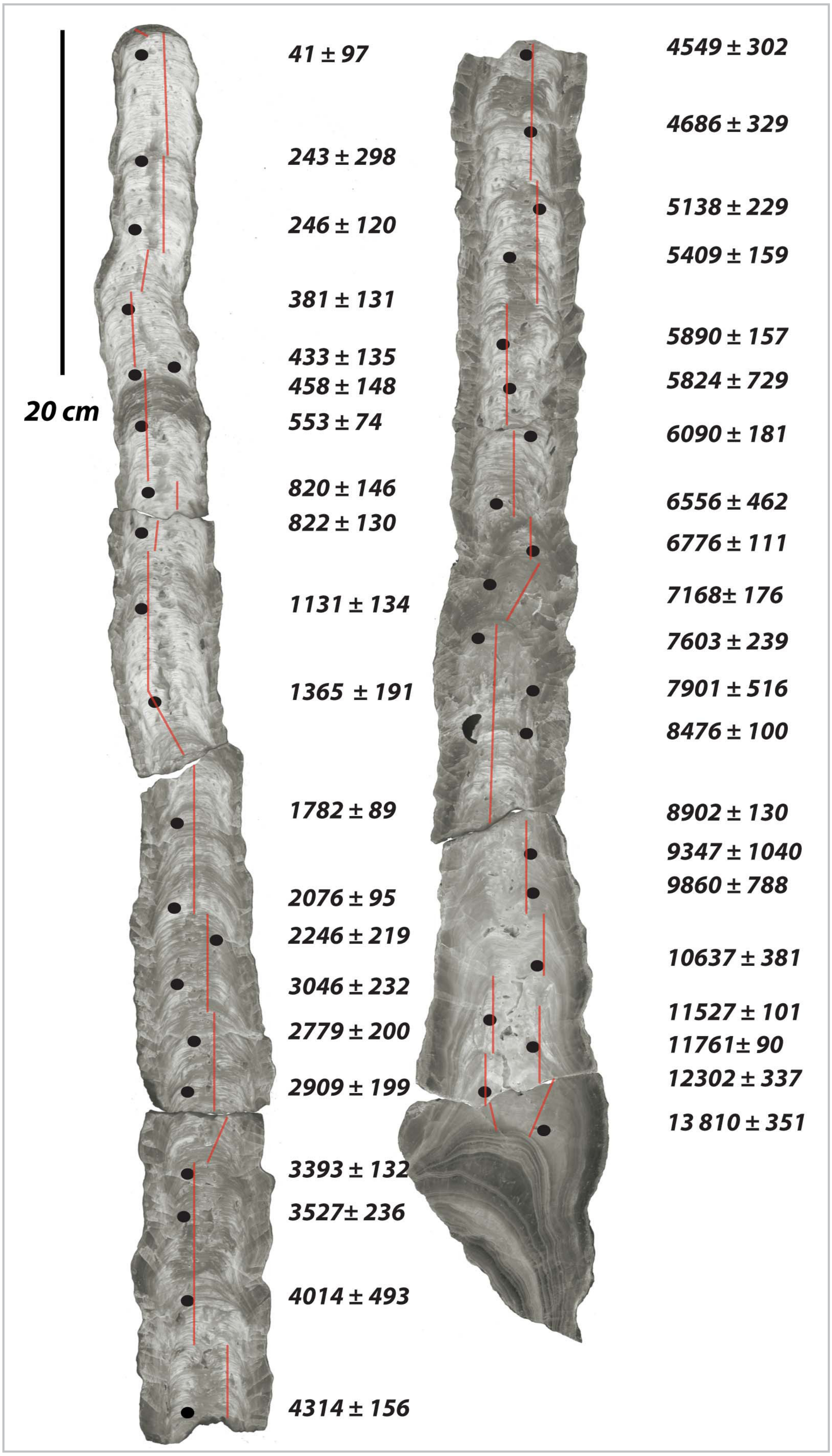

Figure 5.1. *Polished section of stalagmite M6 (Milandre Cave) showing micromilling paths for isotopic analysis, sampling locations for* ^{230}*Th calcite dating (black dots) and dating results.*

variations of 1 to 1.5 ‰ are observed. $\delta^{13}C$ values vary between -8.63 and -11.68 ‰, around a mean of -10.31 ‰ VPDB. To compare, mean isotopic values of calcite precipitated between June 2012 and July 2014 are -6.68 ‰ VPDB for $\delta^{18}O$ and -12.10 ‰ VPDB for $\delta^{13}C$.

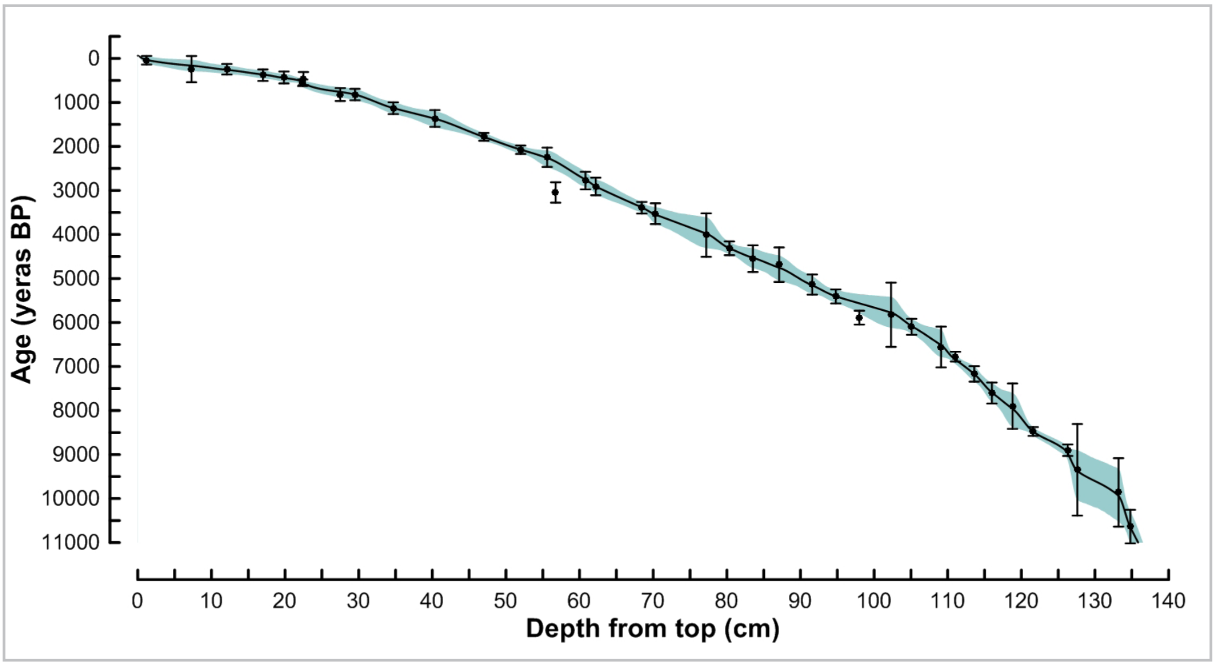

Figure 5.2. *Depth-age models of sample M6. Error bars represent 2 σ errors and the blue shaded zones define the 95% uncertainties of the age model.*

5.4. PALEOCLIMATIC SIGNIFICANCE OF STALAGMITE $\delta^{18}O$ VALUES

$\delta^{18}O$ of precipitation at Milandre site is dominated by three main drivers, i) the source of precipitation (North Atlantic Ocean for our region), ii) changes in the moisture trajectory, and iii) the temperature at the site (Schürch et al., 2003). The North Atlantic Ocean is considered to be the main source of moisture at our study site, with contributions of around 17.3 ± 5.7 % from Mediterranean moisture sources could occur mainly during the summer months (Sodemann and Zauber, 2011). During the Holocene, only minor changes occurred in $\delta^{18}O$ of the ocean. For example, as a result of ice caps melt between 7 000 and 11 000 y BP, the 24 m rise in the relative sea level could induced changes of - 0.10 to - 0.28 ‰ in the isotopic signal (Dupplesy et al., 2007, Grant et al., 2012). No major trajectory reorganization of westerlies air masses was reported in literature. The $\delta^{18}O$ of modern precipitation in Switzerland, and therefore at our cave site, is strongly governed by the air temperature (Schürch et al., 2003; Kern et al., 2014). At present, the $\delta^{18}O$-temperature relation is 0.56 ‰/°C at 500 m asl. (Schürch et al. 2003), comparable with values calculated for other regions of central Europe (0.60 ‰/°C; Rozanski et al., 1992; 1997).

If deposited close to equilibrium conditions, the calcite $\delta^{18}O$ of stalagmites from Milandre should capture a direct temperature signal transmitted through the $\delta^{18}O$ of the drip water. If we consider a constant annual temperature in the cave, shifts in the M6 $\delta^{18}O$ record (Fig. 5.3) should be related with changes in the $\delta^{18}O$ of local precipitation and its seasonality. Thus, the timing and amount of recharge to the karst aquifer above Milandre Cave is an important control on drip water $\delta^{18}O$ values. Results of the stable isotope monitoring of the drip water and the precipitation at Milandre site indicates that the dripping water feeding the stalagmite is very close with the weighted average of the precipitation $\delta^{18}O$ over the interval June 2012 to July 2014. Comparing $\delta^{18}O$ of drip water from different locations in the cave, a well mixing of waters in soil, epikarst and the vadose zone above the cave before being transferred to the cave drip sites is suggested (Affolter et al., submitted in revised form). Monitoring of drip rates at M6 sampling site (between June 2012 to July 2014, Affolter et al., submitted in revised form) also supported earlier observations that the Milandre karst aquifer is generally recharged during the cold season and drained in the summer (Jeannin and Grasso, 1995a, 1995b; Jeannin, 1996; Perrin et al., 2003; Perrin and Kopp, 2005). Water excess is positive from November to April, as summer evapotranspiration controls the water balance that recharges the karst aquifer between the months of May and October. Seasonal variability was observed both in the δ^{18}O values of precipitation (ranging from 3.4 ‰ to -21.8 ‰ SMOW) and δ^{18}O of drip water, with two observations: the δ^{18}O signal of drip water is delayed by 8 to 10 months and its amplitude is smoothed (Affolter et al., submitted in revised form).

Several methods were used to test whether the M6 calcite was deposited close to isotopic equilibrium. Hasenfratz (2012) successfully used the "Hendy test" (Hendy, 1971) for calcite precipitated during the last 2000 y. For longer time intervals, Häuselmann et al. (in prep., Chapter 4 of this thesis) has shown the striking similarity between the M6 isotopic signal and other coeval stalagmites from Milandre Cave, proving the reliability of M6 in preserving the climate signal.

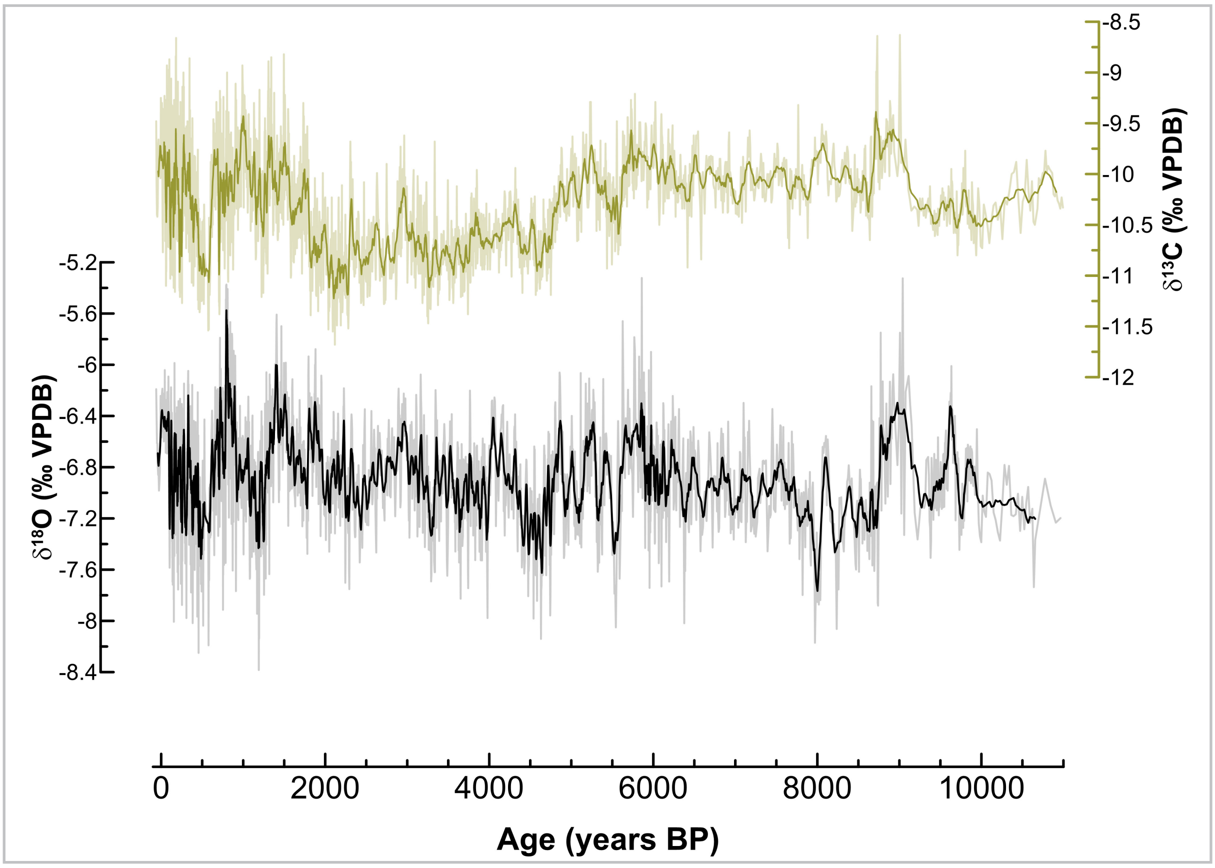

Figure 5.3. *Stable isotopes profile of stalagmite M6. Thick lines represent the 11 points running average data-set*

In summary, we argue that changes in the calcite δ^{18}O are closely related to changes in drip water δ^{18}O, which in turn is strongly influenced by temperature-controlled variations in the δ^{18}O of precipitation. As infiltration takes place mainly in the cold season, stalagmite M6 it is very well suited to capture variations in autumn to spring (AWS) temperature at the cave site. A strong argument to support this hypothesis was brought by Hasenfratz (2012) and Hasenfratz et al. (in prep.). Hasenfratz et al. (in prep.) developed a temperature transfer function by correlating the M6 calcite δ^{18}O to regional historical and instrumental temperature reconstructions for the last 300 y (Luterbacher et al., 2004; Xoplaki et al. 2005). A variation of 0.69 ‰ corresponds to an increase of 1°C during the cold season (October to May) surface air temperature. Häuselmann et al. (in prep., Chapter 4 of this thesis) tested the long-term validity of this transfer function, and observed the calcite $\delta^{18}O$ shows the same bias towards cold season temperature also during the Late Glacial-Early Holocene interval.

5.5. TEMPERATURE VARIABILITY AND VEGETATION EVOLUTION OVER THE LAST 11 000 YEARS BP

We have shown that there are strong indications that the relation between precipitation $\delta^{18}O$ and temperature has remained relatively constant (or was affected by minor changes) over Late Glacial and Late Holocene (Häsenfratz et al., in prep., Häuselmann et al., in prep.). Thus, we applied the calculated transfer function (0.69 ‰/°C) to the Holocene M6 $\delta^{18}O$ data and extended the autumn to spring temperature reconstruction (AWS T) until 11 000 y BP. For the AWS T reconstruction for the interval between 11 000 to 14 550 y BP please refer to Chapter 4 of this thesis (Fig.4, upper side).

Figure 5.4 presents the AWS T variability over the last 11 000 ka BP as recorded in the calcite $\delta^{18}O$ of M6 stalagmite. The variations are reported to the average temperature of the interval, which is 5.87 °C. The 5.87 °C value is also similar with the mean autumn to spring temperatures measured between 1960 and 2010 at Fahy meteorological station, which is 5.8 °C.

Overall, AWS T varies between 4.8 to 6.9 °C, around a mean of 5.9°C. High frequency and high amplitude variability is observed in the dataset. We filtered the dataset by applying an 11 points running average. Several peaks in temperature (warm and cold) were observed. Temperature below 5.5°C are centred around 478 ± 83, 1 175 ± 119, 4 619 ± 206, 7 965 ± 399 y BP, while temperatures above 6.2°C peak around 325 ± 93, 718 ± 103, 790 ±125, 1 390 ± 174, 1 490 ± 152, 1 798 ± 75, 1 856 ± 72, 5 826 ± 142, 8 924 ± 124 and 9 600 ± 554 y BP. Around 19 colder and 11 warm centennial and multi-centennial intervals were observed. Figure 5.4 presents their distribution and temporal extension, with positive (negative) intervals as red (blue) boxes. Please note that currently no statistical program was used to delimitate the temporal boundaries for these intervals.

Variations in the vegetation density, as recorded in the $\delta^{13}C$ profile, suggest that changes in temperature alone do not seem to affect the development of vegetation at the site. A lower frequency and amplitude variation is observed compare with temperature evolution. An increase in vegetation density and soil formation are observed between 4 700 – 5 717 y BP and 498 - 975 y BP. The highest vegetation density is recorded between 2 080 – 4 700 y BP, followed by a decrease between 975 – 2 080 y BP, and from 498 y BP until today.

Fig. 5.4. (next page) *Autumn to spring temperature reconstruction (AWS T, October to May) based on from calcite $\delta^{18}O$ from Milandre cave (Swiss Jura Mountains). Temperature variability is reported to the mean vale of the Holocene interval. Red and blue boxes represent warmer and colder centennial intervals in the reconstruction. Yellow boxes represent intervals of minima in total solar irradiance (Renssen et al., 2006) and blue arrow maxima in ice-rafted debris (IRD) in North Atlantic Ocean (Bond et al., 2001)*

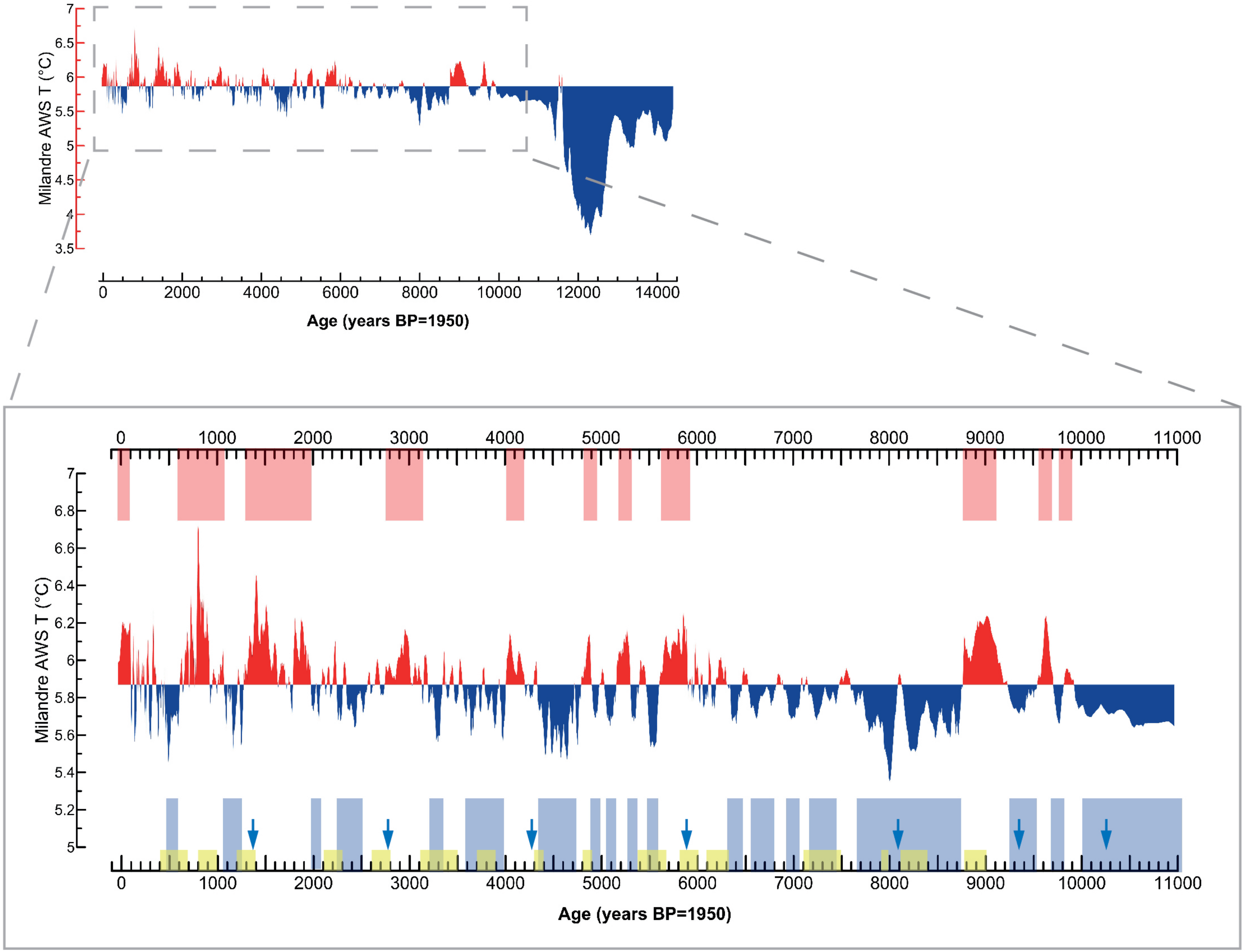
Milandre AWS T (°C)
7
6.5
6
5.5
5
4.5
4
3.5
0
2000
4000
6000
8000
10000
12000
14000
Age (years BP=1950)
0
1000
2000
3000
4000
5000
6000
7000
8000
9000
10000
11000
Milandre AWS T (°C)
7
6.8
6.6
6.4
6.2
6
5.8
5.6
5.4
5.2
5
0
1000
2000
3000
4000
5000
6000
7000
8000
9000
10000
11000
Age (years BP=1950)

5.6. DISCUSSIONS AND OUTLOOK

Recently it has been shown that the calcite $\delta^{18}O$ in samples from Milandre Cave represent reliable qualitative proxy for $\delta^{18}O$ in precipitation and linked temperature, as well as $\delta^{18}O$ in the moisture source (Häuselmann et al., in prep., Affolter et al., submitted in revised form). The new M6 $\delta^{18}O$ record represents one of the few continuous highly-resolved and precisely-dated Holocene records from Europe, and provides both quantitative and qualitative climate reconstructions of regional and hemispheric relevance. Nevertheless, represents one of the very few high-resolution cold-season temperature reconstructions in Central Europe. The features of reconstructed climate variability at our cave site are in excellent agreement with previous paleoclimate reconstructions over the North Atlantic region, from a regional to a hemispheric scale (later discussed). Nevertheless, its high resolution and accuracy will make possible robust regional intercomparison and bring support in decoupling and understanding the impact of external and internal climate forgings in Central Europe and North Atlantic region.

Our record underlines the teleconnections between the climate in Switzerland and the sea-ice-atmosphere system of the North Atlantic Ocean. We confirm the synchronicity between intervals of colder temperatures (and more negative calcite $\delta^{18}O$) occurring around intervals of maxima in ice-rafted debris (IRD) in North Atlantic Ocean (Bond et al., 2001; blue arrows in Fig. 5.4). A similar synchronicity was suggested for northern Europe by Niggemann et al. (2003), who investigated speleothem $\delta^{18}O$ from B7 Cave (Germany). Bond events (Bond et al., 2001) are usually correlated with minima in total solar irradiance (TSI, yellow boxes in Fig. 4, Renssen et al., 2006). Most of the TSI minima intervals have a corresponding cold intervals recorded in Milandre $\delta^{18}O$ record (and consequently in the AWS T, Fig. 5.4). The role of orbital forcing in driving changes in this mid-latitude region was already observed in other natural archives (e.g. Ivy-Ochs et al., 2012; Wanner et al., 2007; Mangini et al., 2007; Nicolussi and Schlüchter, 2012; Solomina et al., 2015 and references therein). Nevertheless, there are cold events that do not follow any of the patterns earlier discussed, and therefore our record has the potential to deepen our understanding of the regional climate variability (magnitude, duration and frequency of temperature changes) and the nature of its forcing mechanisms.

Despite recent efforts of several research groups in reconstructing climate variability based on speleothem proxies from Central Europe the results do not seem to validate each other (Fohlmeister et al., 2012 and 2014, our study Fig. 5.5). This is probably related with climatic parameter influencing the oxygen isotopic composition of the samples at different cave sites. In detail, $\delta^{18}O$ variations in stalagmites from Spannagel Cave (Austrian Alps) are suggested to reflect variations in the moisture source region (North Atlantic Ocean vs. the Mediterranean Sea) and/or variations in the seasonality of precipitation (Mangini et al., 2005; Fohlmeister et al., 2013), with a reverse $\delta^{18}O$ /temperature relation if compared to Milandre Cave. The calcite $\delta^{18}O$ of speleothems from Bunker Cave (Germany) is expected to be primarily driven by seasonal infiltration of rainfall in the epikarst, similar to Milandre site (Fohlmeister et al., 2012). Nevertheless, these special different relations between temperature, seasonality of precipitation and atmospheric processes (changes in the main source of moisture) could provide important insights in the regional teleconnections (e.g., Casty et al., 2005).

Teleconnection could be observed also with other Northern Hemisphere regions influenced by the North Atlantic climate variability (e.g. North America and Asia). Similar with our dataset, four events punctuating the high Asian monsoon intensity centred at 11 200, 10 900, 9 200, 8 300 and 8 100 y BP are recorded in the stalagmite stable isotope series from China (Dykoski et al., 2005), suggesting that M6 $\delta^{18}O$ record provides a good base in testing special and temporal teleconnections at a large hemispheric scale.

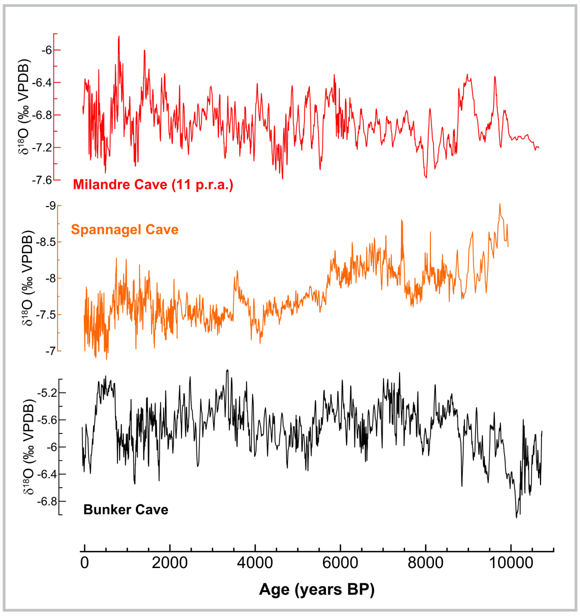

Figure 5.5. *Comparison between $\delta^{18}O$ record from Milandre Cave and $\delta^{18}O$ records from Spannagel Cave (COMNISPA II, Fohlmeister et al., 2013) and Bunker Cave (Fohlmeister et al., 2012)*

Not only $\delta^{18}O$, but also in depth investigation of $\delta^{13}C$ variation can provide further hydrological and environmental information. For example, several studies (e.g. Wanner et al, 2011; Fohlmeister et al., 2013 and references therein) report changes in the climatic proxies around 6 000 y BP related with enhanced rainout during the Holocene and orbital-induced changes in temperatures seasonality (Fig. 5.6). This trend is not evident in our $\delta^{18}O$ profile, but it exists in the $\delta^{13}C$ profile. After 5 717 y BP, a general negative trend is observed in $\delta^{13}C$ and marks the increase in vegetation density and microbial activity as a result of increase water availability and milder winters.

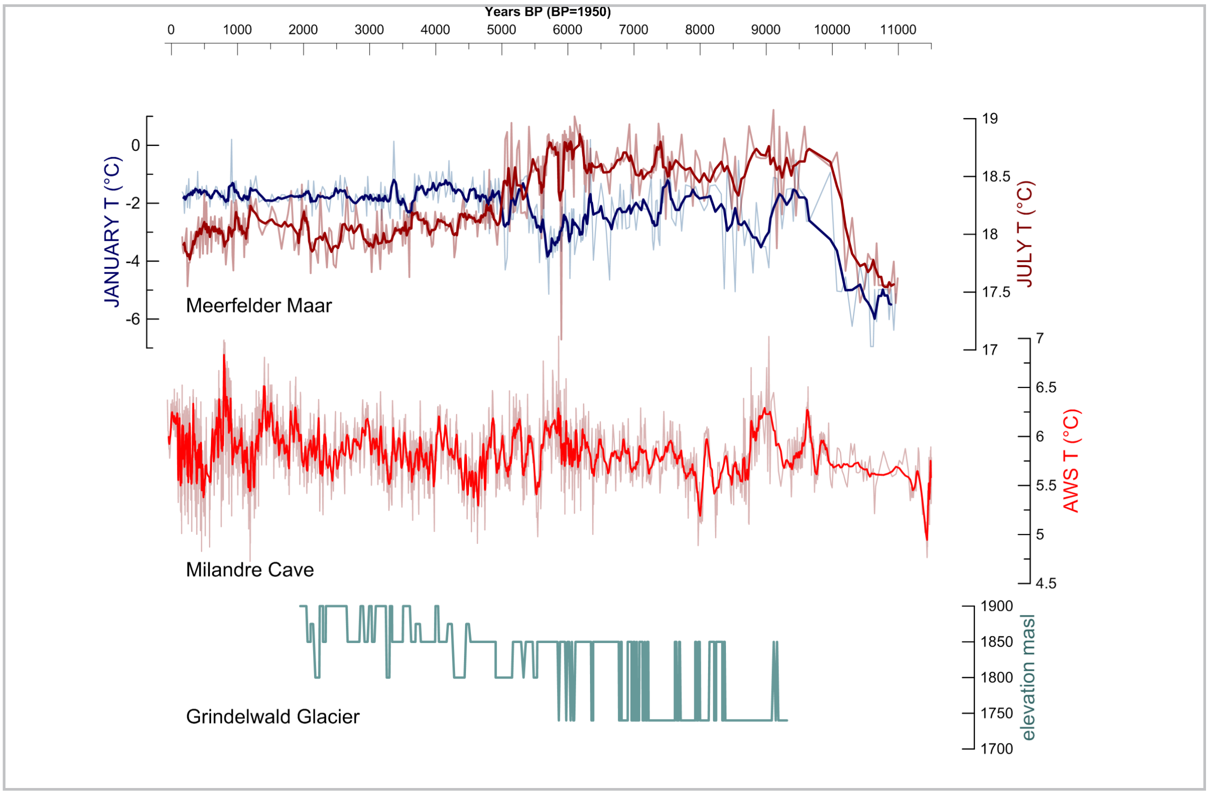

Figure 5.6. *Comparison between AWS T at Milandre site and regional temperature reconstruction of January and July months (Meerfeld Maar, Germany; Litt et al., 2009) and phases of glacier advance and retreats in Swiss Alps (Grindelwald Glacier, Luetscher et al., 2011)*

The new Milandre dataset provides a robust base for large areas of research. In the near future, spectral analysis are to be performed on the M6 $\delta^{18}O$ time series and AWS T record (e.g. Frisia et al, 2003, Niggemann et al., 2003). Furthermore, absolute temperature reconstructions based on the $\delta^{18}O$ and δH in the fluid inclusions of M6 calcite are now performed at the Institute of Physic (Bern University) using the Affolter et al., (2013) method. These new fluid inclusion data could add further evidences for the reliability of the transfer function used for the last 11 000 years, and in the same time provide novel information regarding any changes in the moisture source of the moisture.

The new gained knowledge of long-term climate variability in our region, as presented in our data set, will be a valuable asset for future climate scenarios models and assessing an important contribution to better evaluate the consequences of different scenarios of climate change.

BIBLIOGRAPHY

Affolter, S., Häuselmann, A.D., Fleitmann, D., Leuenberger, M., Breecker, D., in review. Triple isotope (δD, δ^{18}O, δ^{17}O) study on precipitation, drip water and speleothem fluid inclusions for a central European cave (NW Switzerland). Quaternary Science Reviews.

Allen, J. R., Long, A. J., Ottley, C. J., Pearson, D. G., and Huntley, B., 2007. Holocene climate variability in northernmost Europe. Quaternary Science Reviews, 26(9), 1432-1453.

Bond, G., Kromer, B., Beer, J., Muscheler, R., Evans, M.N., Showers, W., Hoffmann, S., Lotti-Bond, R., Hajdas, I., Bonani, G., 2001. Persistent solar influence on north Atlantic climate during the Holocene. Science 294, 2130-2136.

Breitenbach, S.F.M., Rehfeld, K., Goswami, B., Baldini, J.U.L., Ridley, H.E., Kennett, D.J., Prufer, K.M., Aquino, V.V., Asmerom, Y., Polyak, V.J., Cheng, H., Kurths, J., Marwan, N., 2012. COnstructing Proxy Records from Age models (COPRA). Clim. Past 8, 1765-1779.

Büntgen, U., Tegel, W., Nicolussi, K., McCormick, M., Frank, D., Trouet, V., Kaplan, J., Herzig, F., Heussner, K and Esper, J., 2011. 2500 years of European climate variability and human susceptibility. Science, 331(6017), 578-582.

Casty, C., Wanner, H., Luterbacher, J., Esper, J., Bohm, R., 2005. Temperature and precipitation variability in the european Alps since 1500. Int J Climatol 25, 1855-1880.

Cheng, H., Lawrence Edwards, R., Shen, C.-C., Polyak, V.J., Asmerom, Y., Woodhead, J., Hellstrom, J., Wang, Y., Kong, X., Spötl, C., Wang, X., Calvin Alexander Jr, E., 2013. Improvements in 230Th dating, 230Th and 234U half-life values, and U–Th isotopic measurements by multi-collector inductively coupled plasma mass spectrometry. Earth and Planetary Science Letters 371–372, 82-91.

Duplessy, J.C., Roche, D.M., Kageyama, M., 2007. The Deep Ocean During the Last Interglacial Period. Science 316, 89-91.

Edwards, R.L., Cheng, H., Wasserburg, G.J., 1987. U-238, U-234, Th-230, Th-232 systematics and the precise measurement of time over the past 500,000 years. Earth and Planetary Science Letters 81, 175-192.

Esper, J., Duethorn, E., Krusic, P. J., Timonen, M., and Büntgen, U. 2014. Northern European summer temperature variations over the Common Era from integrated tree-ring density records. Journal of Quaternary Science, 29(5), 487-494.

Fleitmann, D., Cheng, H., Badertscher, S., Edwards, R.L., Mudelsee, M., Gokturk, O.M., Fankhauser, A., Pickering, R., Raible, C.C., Matter, A., Kramers, J., Tuysuz, O., 2009. Timing and climatic impact of Greenland interstadials recorded in stalagmites from northern Turkey. Geophys Res Lett 36.

Fohlmeister, J., Schroder-Ritzrau, A., Scholz, D., Spotl, C., Riechelmann, D.F.C., Mudelsee, M., Wackerbarth, A., Gerdes, A., Riechelmann, S., Immenhauser, A., Richter, D.K., Mangini, A., 2012. Bunker Cave stalagmites: an archive for central European Holocene climate variability. Clim Past 8, 1751-1764.

Fohlmeister, J., Vollweiler, N., Spötl, C., Mangini, A., 2013. COMNISPA II: Update of a mid-European isotope climate record, 11 ka to present. The Holocene 23, 749-754.

Frisia, S., Borsato, A., Preto, N., McDermott, F., 2003. Late Holocene annual growth in three Alpine stalagmites records the influence of solar activity and the North Atlantic Oscillation on winter climate. Earth and Planetary Science Letters 216, 411-424.

Grant, K.M., Rohling, E.J., Bar-Matthews, M., Ayalon, A., Medina-Elizalde, M., Ramsey, C.B., Satow, C., Roberts, A.P., 2012. Rapid coupling between ice volume and polar temperature over the past 150,000 years. Nature 491, 744-747.

Hasenfratz, A., 2012. Temperature reconstruction over the past two millenia based on stalagmite δ18O record from the Jura Swiss Mountains, Institute of Geological Sciences. Bern University, p. 79.

Hasenfratz, A., Fleitmann, D., Häuselmann, A.D., Lehner, F., Cheng, H., Edwards, R.L., Leuenberger, M., Affolter, S., Raible, C.C., Breitenbach, S.F.M., Luterbacher, J., in prep. Central European temperature variations over the past two millennia based on a stalagmite oxygen isotope record from the Swiss Jura Mountains.

Häuselmann, A.D., Affolter, S., Tabersky, D., Schmassmann, S., Breitenbach, S.F.M., Cheng, H., Edwards, R.L., Leuenberger, M., Vogel, N., Günther, D., Kiefer, R., Haug, G., Jeannin, P.-Y., Fleitmann, D., in prep. Late Glacial environmental and temperature reconstruction in Central Europe: a multi-proxy and multi-techniques approach on speleothems from Milandre Cave (Swiss Jura Mts.).

Jeannin, P.-Y., Grasso, A.D., 1995a. Estimation des infiltrations efficaces journalières sur le bassin karstique de la Milandrine (Ajoie, JU, Suisse). Bulletin d'Hydrogéologie 14, 83–93.

Jeannin, P.-Y., Grasso, A.D., 1995b. Recharge respective des volumes de roche peu perméable et des conduits karstiques, rôle de l'épikarst. Bulletin du Centre d'Hydrogéologie 14, 95–111.

Joerin, U.E., Stocker, T.F., Schlüchter, C., 2006. Multicentury glacier fluctuations in the Swiss Alps during the Holocene. The Holocene 16, 697-704.

Jones, P.D., Mann, M.E., 2004. Climate over past millennia. Reviews of Geophysics 42, 1-42

Kern, Z., Kohán, B., Leuenberger, M., 2014. Precipitation isoscape of high reliefs: interpolation scheme designed and tested for monthly resolved precipitation oxygen isotope records of an Alpine domain. Atmos. Chem. Phys. 14, 1897-1907.

Luterbacher, J., Dietrich, D., Xoplaki, E., Grosjean, M., Wanner, H., 2004. European seasonal and annual temperature variability, trends, and extremes since 1500. Science 303, 1499-1503.

Mangini, A., Spötl, C., Verdes, P., 2005. Reconstruction of temperature in the Central Alps during the past 2000 yr from a δ 18 O stalagmite record. Earth and Planetary Science Letters 235, 741-751.

Mangini, A., Verdes, P., Spotl, C., Scholz, D., Vollweiler, N., Kromer, B., 2007. Persistent influence of the North Atlantic hydrography on central European winter temperature during the last 9000 years. Geophys Res Lett 34.

Niggemann, S., Mangini, A., Richter, D.K., Wurth, G., 2003. A paleoclimate record of the last 17,600 years in stalagmites from the B7 cave, Sauerland, Germany. Quaternary Science Reviews 22, 555-567.

Perrin, J., 2003. A conceptual model of flow and transport in a karst aquifer based on spatial and temporal variations of natural tracers. PhD Thesis, University of Neuchâtel, Switzerland.

Perrin, J., Jeannin, P.-Y., Zwahlen F., 2003a. Epikarst storage in a karst aquifer: a conceptual model based on isotopic data, Milandre test site, Switzerland. Journal of Hydrology 279, 106–124.

Perrin, J., Jeannin, P.-Y., Zwahlen F., 2003b. Implications of the spatial variability of infiltration-water chemistry for the investigation of a karst aquifer: a field study at Milandre test site, Swiss Jura. Hydrogeology Journal 11, 673–686.

Perrin, J., Kopp, L., 2005. Hétérogéné des écoulements dans la zone non saturée d'un aquifère karstique (site de Milandre, Jura suisse). Bulletin d'hydrogéologie 21, 33–58.

Renssen, H., Goosse, H., Muscheler, R., 2006. Coupled climate model simulation of Holocene cooling events: oceanic feedback amplifies solar forcing. Clim Past 2, 79-90.

Rozanski, K., Araguasaraguas, L., Gonfiantini, R., 1992. Relation between Long-Term Trends of O-18 Isotope Composition of Precipitation and Climate. Science 258, 981-985.

Rozanski, K., Johnsen, S.J., Schotterer, U., Thompson, L.G., 1997. Reconstruction of past climates from stable isotope records of palaeo-precipitation preserved in continental archives. Hydrolog Sci J 42, 725-745.

Shennan, S., Downey, S. S., Timpson, A., Edinborough, K., Colledge, S., Kerig, T., and Thomas, M. G. 2013. Regional population collapse followed initial agriculture booms in mid-Holocene Europe. Nature Communications, 4.

Schmassmann, S., 2010. Speleothem-based climate and environmental reconstruction: A pilot study in the Swiss Jura Mountains, Institute for Geological Sciences. University of Bern, p. 149.

Schürch, M., Kozel, R., Schotterer, U., Tripet, J.-P., 2003. Observation of isotopes in the water cycle—the Swiss National Network (NISOT). Env Geol 45, 1-11.

Shtober-Zisu, N., Schwarcz, H.P., Chow, T., Omelon, C.R., Southam, G., 2014. Caves in caves: evolution of post-depositional macroholes in stalagmites. International Journal of Speleology 43, 9.

Sodemann, H., Zubler, E., 2010. Seasonal and inter-annual variability of the moisture sources for Alpine precipitation during 1995-2002. Int J Climatol 30, 947-961.

Solomina, O.N., Bradley, R.S., Hodgson, D.A., Ivy-Ochs, S., Jomelli, V., Mackintosh, A.N., Nesje, A., Owen, L.A., Wanner, H., Wiles, G.C., 2015. Holocene glacier fluctuations. Quaternary Science Reviews 111, 9-34.

Wanner, H., Solomina, O., Grosjean, M., Ritz, S.P., Jetel, M., 2011. Structure and origin of Holocene cold events. Quaternary Science Reviews 30, 3109-3123.

Wirth, S. B., Glur, L., Gilli, A., and Anselmetti, F. S. , 2013. Holocene flood frequency across the Central Alps–solar forcing and evidence for variations in North Atlantic atmospheric circulation. Quaternary Science Reviews, 80, 112-128.

Xoplaki, E., Luterbacher, J., Paeth, H., Dietrich, D., Steiner, N., Grosjean, M., Wanner, H., 2005. European spring and autumn temperature variability and change of extremes over the last half millennium. Geophys Res Lett 32.

CHAPTER 6.

CONCLUSIONS AND OUTLOOK

The most important goal of the STALCLIM project was to use and develop the potential of speleothems as paleoclimate and paleoenvironmental archives by coordinating and combining a series of state-of-the-art methods in speleothems proxies. Two different cave settings and time scales were studied, and relative to each cave, we have used speleothems to reconstruct low- to high- frequency climate and environment variability.

Schafsloch Cave, from where sample MF3 was collected, is located in a high alpine setting sensitive to variations in climate and atmospheric circulation. A considerable effort was put into dating, analysing the chemical composition of calcite, and observing the petrography and layer boundaries. Between 130.1 ± 0.4 and 225.8 ± 2.3 ka BP the cave aquifer was influenced not only by changes in temperature and precipitation, but also by the dynamic of a small glacier present above the cave. This detailed study has provided valuable new information on i) the quantitative temperature variations and water availability over glacial-interglacial intervals, and ii) the evolution of a small glacier body intermittently present above the Schafsloch Cave, despite the relatively few precisely dated samples covering the time interval of interest. Changing isotopic composition of the sample suggests possible changes in air mass pathways that may trigger changes in climate. The importance of orbital parameters (summer insolation budget, sustained by increase seasonality) in the major climate shifts during the studied interval is highlighted. Our results place the timing of the penultimate deglaciation at around 131.8 ± 0.6 ka BP, in good agreement with precisely-dated records from North America and Europe, and 2.8 ± 0.7 ka earlier than recorded in Asian monsoon regions. We therefore support the notion that the Asian monsoon system and ITCZ responded largely to wintertime cold anomalies in the North Atlantic and Eurasia.

At the global scale, the scientific community continues to debate the role of internal (changes in the AMOC, rise in the CO_2 concentration) and external factors (insolation, obliquity) in triggering major climate events. This study shows that high-resolution independently-dated records, such as speleothems, represent a key asset in trying to decouple the regional and global impact of these factors over long-term intervals.

Open questions remain regarding the evidence for a “mystery warm interval” during the full glacial stage of MIS 6, which suggests a complete meltdown of the glacier, together with at least two other partial retreat phases. More high resolution data covering MIS 6 in Europe is required in order to improve our understanding on this particular topic.

Interpretation of trace element concentration in speleothem calcite remains a challenge, and even more so if one wants to understand their pattern in a highly-dynamic glacial setting and in subglacial water, for which few modern analogues exist. In the future, details analyses of ratios of Mg and Sr isotopes and the type of organic matter incorporated in the sample (as changes in its content were observed at times when the glacier was present above the cave) can enhance our understanding of the landscape evolution in response to climate change in these high alpine environments. Nevertheless, comparing and building a data sets of chemical (isotopic, trace elements) and biological (organic matter, microbial mats) properties of calcite formed under warm-based glaciers, may advance our understanding in quantifying chemical composition of meltwater and biologic evolution at the base of the glacier.

In the second half of the thesis a multi-proxy, multi-method approach was used to reconstruct in detailed climate and vegetation variability in the Swiss Jura Mountains, together with a new high resolution cold-season temperature change and environment evolution at the Milandre cave site for the last 14 550 y BP. Timing of the chronozones during Holocene-Late Glacial intervals shows very good agreement with regional terrestrial $\delta^{18}O$ records. Vegetation responded almost immediately to major changes in temperature. Over Bølling and Allerød intervals mean AWT fluctuate between 5.0-5.5°C. A 1.2° C gradual cooling marks the transition into the YD, and a 1.4 °C warming marks the transition into the Holocene. The first part of the YD, between 12 750 -12 030 y BP, was colder and drier compared to the second part, between 12 030 - 11 653 y BP. During the Holocene, AWS temperature varies between 4.8 to 6.9 °C, with a mean of 5.9°C. An increase in vegetation density and soil formation are observed between 4 700 - 5 717 y BP and 498 - 975 y BP.

The Milandre record highlights the teleconnections between the climate in Switzerland and the sea-ice-atmosphere system of the North Atlantic Ocean. The isotopic data have been combined with external datasets, particularly concerning the long-term evolution of meteoric precipitation patterns, temperature and $\delta^{18}O$ composition at the sites. The establishment of wetter conditions at this cave site (46°N) after 12 100 ± 100 y BP, is most likely the result of the gradual northward retreat of the polar front and subsequent increased moisture delivery into Western Europe. We also present evidence that the source of the moisture in the Swiss Jura Mountains did not experience major changes over the last 14 550 y BP.

One of the main objectives of this thesis was to develop long and continuous records of climate change in Switzerland. We are confident that the new isotopic and temperature reconstructions based on speleothem-proxies from the Milandre Cave site (Swiss Jura Mountains) will be an important asset in addressing current research topics in the North Atlantic region, such as North Atlantic Oscillation variability, temperature seasonality, and the nature and structure of cold and warm periods in Central Europe.

In addition to the two sites that comprise the main focus of this thesis, lower resolution isotopic and dating analyses were also performed on several other samples from the Jura Mountains and the Swiss Alps (please refer to Table 1.1). More detailed investigation of these samples is recommended with regard to climate variability in Switzerland during the Holocene, the last glacial interval and MIS 5.

ACKNOWLEDGEMENTS

Four years ago, when I started my scientific and personal journey in the STALCLIM project, seems like another lifetime. Presenting this thesis would have been impossible without the support and effort of several people and organizations, to whom I will like to present my deepest gratitude.

Thank you, Mulțumesc, Un grand merci, Danke, Merci viü mau, Efharisto …

prof. dr. Dominik Fleitmann, my main supervisor
... for giving me the possibility to perform science in your group
… for your patience and support during all the ups and downs of the project
… for coping with the distance and my stubbornness during the last two years

prof. dr. Markus Leuenberger, my co-supervisor
… for accepting to co-supervise my work and for his support during the last year
… for your continuous interest in the speleothem sciences

prof. dr. Christoph Spötl
… for kindly agreeing to be the external referee of this thesis and for adapting to the limited time provided for that

prof. dr. Flavio Anselmetti
… for accepting to chair my PhD defence

prof. dr. Hai Cheng and prof. dr. Larry Edwards
… for performing the ^{230}Th analysis, your collaboration and fruitful discussions

dr. Sally Lowick and dr. Philipp Häuselmann
… for proofing the English language of this thesis

Dominik, Seraina, Igor and Gaby
… for training and assistance in the laboratory methods and procedures

Gina and Adam
… for your interest in speleothem sciences and your help in the lab and field campaigns

Stephane and Daniel
… for your friendship and support
… for building together memories and experiences, both in science and general aspects of life

Sebastian, Nadia and Yves
... sharing your knowledge, help in the field, and for really helpful comments and suggestions

Thomas, Dorian, Sally, Marius, Kelly Ann, Marina and Andrei
… for all the chocolate and coffee time together and for coping with my high energy and bothering

prof. dr. Karl Ramseyer, prof. dr. Klaus Mezger, and Sigrid Zimmermann
… for all the administrative and advising support

Cave Protection and Scientific Commissions of the Swiss Speleological Society
… for allowing us to collect speleothems in Swiss caves and for their support

Höhlen-Gruppe Ybrig (HGY), Spéléo-Club Jura (SCJ), SGH Bern, SGH Interlaken, Höhlenclub Alpstein (HCA), Spéléo-Club de Cheseaux (SCC), Groupe d`Exploration aux Fées (GEF), Ostschweizerische Gesellschaft für Höhlenforschung (OGH) and Swiss Institute for Speleology and Karstology (SISKA)
… for providing us with samples, valuable field work support and fruitful discussions

OCCR and CUSO doctoral schools
… for organizing our continuous formation classes, firld trips, and young researchers meetings

The community of Cave and Speleothem sciences
… for being a great motivation and kindly replying to any requests and questions over the last years

Swiss National Founds
… for funding the Sinergia STALCLIM project

And last but not least

A huge list of friends, from the caving community and not only (you all know who you are)
… for giving me a reality check and understanding my absence and low energy sometimes

Urs and Margaretha
… for their love, support and patience in coping with two researchers in the family

Mama, tata, mami, liana, gelu, paul, amalia
… for your great support, love, patience and help, from the moment I arrived in this colorful world until now
… for spending so much time in Switzerland and keeping me free of loads of family responsibilities
… vă iubesc și nu exista cuvinte să vă mulțumesc îndeajuns

Philipp
… for continuously being an example in scientific ethics and perseverance
… for understanding my absence, late return home and moody mornings
… for being there anytime for everything

Thomas Emil Gottlieb
… for your great joy and hugs every time I return home, and not only
... for providing enough distraction from this thesis and constantly reminding me what is really important in life

DEDICATED TO

M.SC. SILVIA SCHMASSMANN

YOUNG SPELEOTHEM RESEARCHER AND CAVE EXPLORER

(18.01.1982 – 30.12.2013)

... FOR HER INITIAL STUDY OF SEDIMENTS AND SPELEOTHEMS FROM MILANDRE CAVE AND, IN THE SAME TIME, FOR HER HARD WORK IN THE EXPLORATION AND PROTECTION OF THE UNDERGROUND ENVIRONMENT

APPENDIX

A. DATA

For all practical purposes, for all the samples presented in table supplementary data can be found on the CD enclosed and consists of the following files:

1. Stable isotopes analysis performed at the Institute of Geological Sciences, Bern University
2. ^{230}Th ages measured at the department of Geography and Geophysics, University of Minnesota, USA
3. ^{230}Th ages measured at the Institute of Geological Sciences, Bern University, Switzerland

B. MANUSCRIPTS

Except the manuscripts presented as chapters in this thesis, our research group prepares for publication two papers, which are found in the following pages:

S. Affolter, A. D. Häuselmann, D. Fleitmann, Ph. Häuselmann and M. Leuenberger (submitted in revised form) Triple isotope (δD, $\delta^{17}O$, $\delta^{18}O$) study on precipitation, drip water and speleothem fluid inclusions for a western central European cave (NW Switzerland)

A. Hasenfratz, D. Fleitmann, A.D. Häuselmann, F. Lehner, H. Cheng, R. L. Edwards, M. Leuenberger, C. C. Raible, S.F.M. Breitenbach, J. Luterbacher (in prep.) Central European temperature variations over the past two millennia based on a stalagmite oxygen isotope record from the Swiss Jura Mountains

Triple isotope (δD, $\delta^{17}O$, $\delta^{18}O$) study on precipitation, drip water and speleothem fluid inclusions for a western central European cave (NW Switzerland)

Stéphane Affolter[1,3*], Anamaria D. Häuselmann[2,3], Dominik Fleitmann[4,3], Philipp Häuselmann[5] and Markus Leuenberger[1,3]

[1] Climate and Environmental Physics, Physics Institute, University of Bern, 3012 Bern, Switzerland

[2] Institute of Geological Sciences, University of Bern, 3012 Bern, Switzerland
[3] Oeschger Center for Climate Change Research, University of Bern, 3012 Bern, Switzerland
[4] Department of Archaeology, School of Archaeology, Geography and Environmental Sciences and Centre for Past Climate Change, University of Reading, Whiteknights, PO Box 227, Reading RG6 6AB, UK
[5] Swiss Institute for Speleology and Karst Studies, 2301 La Chaux-de-Fonds, Switzerland

*corresponding author: affolter@climate.unibe.ch

Abstract

Water isotopes are powerful tracers of the hydrological cycle and they have been extensively used for paleoclimate reconstruction. The traditional δD and $\delta^{18}O$ are namely known to provide information on past precipitation, temperature and atmospheric circulation variations. More recently, the use of $^{17}O_{excess}$ parameter derived from precise measurement of $\delta^{17}O$ and $\delta^{18}O$ gives new insight in tracing the hydrological cycle. Debated and not yet fully understood, $^{17}O_{excess}$ could provide, as d-excess, additional information on the atmospheric conditions at the moisture source in parallel to transport processes as well as site effects. In this paper, we investigate the climate signal transmission in water stable isotopes (δD, $\delta^{17}O$ and $\delta^{18}O$) from precipitation to cave drip water and finally to speleothem fluid inclusions for Milandre cave in northwestern Switzerland. A two year-long daily resolved precipitation isotope record above the cave has been established and was compared to collected cave drip water (3 months average resolution) and modern as well as early Holocene speleothem fluid inclusions (multidecadal resolution). Amount weighted mean δD, $\delta^{18}O$ and $\delta^{17}O$ are -71.0‰, -9.9‰, -5.2‰ for isotope compositions of precipitation, -60.3‰, -8.7‰, -4.6‰ for cave drip water and -61.3‰, -8.3‰, -4.7‰ for the fluid inclusions, respectively. Secondary order proxies have also been derived in precipitation and drip water and present similar values with 18 per meg for $^{17}O_{excess}$ whereas d-excess is 1.5‰ more negative in drip water. For fluid inclusions, their interpretation relies on the instrumental precision. Results show that the atmospheric signal is shifted towards enriched values in the drip water and fluid inclusions (δ of ~ + 10‰ for δD). A weak seasonality is still visible in the drip water isotope signal but shifted by around 8 – 10 months (groundwater residence time) when compared to the precipitation. Moreover, we carried out the first $\delta^{17}O$ measurement in speleothem fluid inclusions, as well as the first comparison of the $\delta^{17}O$ behaviour from the meteoric water to the fluid inclusions entrapment in speleothems. This study on precipitation, drip water and fluid inclusions will be used as a speleothem proxy calibration for Milandre cave in order to reconstruct paleotemperatures and moisture source variations for western central Europe.

1. Introduction

Water isotopes (hereafter discussed as $\delta^{18}O_p$) in precipitation rely on the moist air masses history through moisture source, atmospheric circulation and evaporation/condensation processes. On a regional scale $\delta^{18}O_p$ varies in function of surface air temperature, amount of precipitation, moisture source origin and rainout effect (Rozanski et al., 1992; Araguas-Araguas et al., 2000). Speleothems are now widely used for continental paleoclimate reconstructions. Understanding the key processes that govern cave climate and hydrology one has to know the boundary conditions, i.e. atmospheric meteorological conditions, evapotranspiration by plants at the surface and processes in the soil and in the transition zone. Only with these prerequisites speleothem data can be interpreted in terms of climate and hydrology (Riechelmann et al., 2011). Cave monitoring studies constitute a new standard for the interpretation of speleothem proxies and characterising the relationship between water isotopes of precipitation and cave drip water is becoming routine in caves worldwide (Cruz et al., 2005; Moerman et al., 2010; Cuthbert et al., 2014; Genty et al., 2014).

Stalagmites in particular allow the reconstruction of climate for long time intervals throughout the Quaternary (Cheng et al., 2009; Fleitmann et al., 2009; Meckler et al., 2012). They can be precisely dated using laminae counting (Fleitmann et al., 2004; Shen et al., 2013; Duan et al., 2015) or more commonly by Uranium-Thorium series analyses (Cheng et al., 2013) and they can provide information on past climate change at high resolution (Henderson, 2006).

Most of the paleoclimate reconstructions are based now on calcite geochemistry (Shakun et al., 2007). Routinely measured are $\delta^{18}O_c$ and $\delta^{13}C$ for calcite, which are respectively proxies for moisture supply (Burns et al., 2001; Fleitmann et al., 2003; Kennett et al., 2012; Vaks et al., 2013; Luetscher et al., 2015) and vegetation dynamics (Genty et al., 2010; Rudzka et al., 2011; Blyth et al., 2013) above the cave. Although widely used, $\delta^{18}O_c$ is influenced by different processes above and in the cave environment such as temperature and humidity driven isotope fractionation of the atmospheric water cycle, fractionation associated with the biospheric exchanges, equilibrium and kinetic fractionation between calcite and soil/karst waters during the passage from the surface into the cave. These effects make the interpretation of $\delta^{18}O_c$ difficult (Lachniet, 2009).

Fluid inclusions represent past drip water and are consequently relics of past precipitation above the cave at the time when fluid inclusions were closed (Schwarcz et al., 1976). Hence, they can be used as a direct proxy for paleotemperature or moisture history (Fleitmann et al., 2003; van Breukelen et al., 2008; Griffiths et al., 2010). Based on the correlation between mean annual temperature and mean annual $\delta^{18}O_p$ on a global scale (Dansgaard, 1964) past temperature can thus be reconstructed using for instance the relationship that exists for calcite precipitation at equilibrium (Kim and O`Neil, 1997). However, one has to consider that the seasonal distribution of precipitation is a key factor that could easily yield misleading temperature estimates for the past. Moreover, most cave carbonates are not deposited in oxygen equilibrium with their parent drip waters (McDermott et al., 2006). Thus, it was observed that temperatures calculated on modern speleothems using an empirical relationship (Craig, 1965) were closer to corresponding cave air temperatures. More recently, a new empirical calibration based on several caves data already takes a mean disequilibrium into account (Tremaine et al., 2011) and seems to provide reliable temperature estimates. A multi-proxy method comparison paper (Meckler et al., in review) shows the potential of speleothems for paleotemperature reconstructions by comparing the results of four different paleothermometers that are (i) speleothem fluid inclusions (Dublyansky and Spotl, 2009; Affolter et al., 2014), (ii) liquid-vapour homogenization of fluid inclusions (Kruger et al., 2011), (iii) noble gases concentration in stalagmite water (Vogel et al., 2013), and (iv) clumped isotopes (Meckler et al., 2014). With this objective in mind it is thus important to monitor the isotope proxies from the precipitation falling above the cave to evaluate if the isotopic composition of cave drip and speleothem fluid inclusion water is comparable. So far, most investigations study the relationship between precipitations and drip water, while in this study we additionally investigate the climate signal transmission to speleothem fluid inclusions. Recent developments in speleothem fluid inclusion measurement techniques allow the measurement of both δD_{fi} and $\delta^{18}O_{fi}$ on a single sample (Arienzo et al., 2013; Affolter et al., 2014). We provide here an extension of the method by measuring $\delta^{17}O_{fi}$ in fluid inclusion water offering new horizons for paleoclimate research based on speleothems. $\delta^{17}O$ measurements on water samples were so far achieved using CoF_3 fluorination of water (Landais et al., 2012a), but a more recent laser absorption spectroscopy based technique allows now fast and simple triple isotope measurements on water samples (Steig et al., 2014).

Secondary order proxies d-excess and $^{17}O_{excess}$ can be calculated from the triple isotope measurements on water aliquots. Deuterium excess is obtained from hydrogen (δD) and oxygen ($\delta^{18}O$) isotopes values and is defined as $d = \delta D - 8 \times \delta^{18}O$ (Dansgaard, 1964). It carries information about the ocean surface conditions, namely it is used to characterise the disequilibrium conditions at the moisture source. It is mainly dependent on sea surface temperature, normalised relative humidity and wind speed at the moisture source (Jouzel and Merlivat, 1984; Uemura et al., 2008) but is also dependent on local factors such as recycling of local moisture. Similarly to d-excess, $^{17}O_{excess}$ is calculated (see section 3.3) from small variations in oxygen isotopes ($\delta^{17}O$ and $\delta^{18}O$) and it corresponds to the deviation from the line of 0.528 corresponding to meteoric waters (Luz and Barkan, 2010). It constitutes a promising, but debated parameter to provide additional information on the water cycle (Winkler et al., 2012; Schoenemann et al., 2014; Li et al., 2015). The $^{17}O_{excess}$ corresponds to an indicator of evaporation condition at the moisture source (Angert et al., 2004; Barkan and Luz, 2007) and it has been so far mostly studied in the Polar Regions (Landais et al., 2008; Landais et al., 2012b; Schoenemann et al., 2014) and poorly in the lower latitudes (Landais et al., 2010; Luz and Barkan, 2010). Over the ocean, $^{17}O_{excess}$ is negatively correlated with the normalised relative humidity (Uemura et al., 2010). A direct link with the relative humidity was observed in coastal area of Antarctica (Winkler et al., 2012) but Schoenemann et al., (2014) showed that in Antarctica, $^{17}O_{excess}$ has a strong dependence on the atmospheric temperature during transport due to the temperature dependence of supersaturation that overwhelm any information about the relative humidity. $^{17}O_{excess}$ can also be influenced by processes of the terrestrial biosphere (Landais et al., 2007). Local conditions may also influence $^{17}O_{excess}$ (Winkler et al., 2012; Steen-Larsen et al., 2014; Li et al., 2015).

In Switzerland, isotopes in precipitations have been surveyed for decades within the isotope network ISOT by the Climate and Environmental Physics at the University of Bern (CEP) financially supported by the Swiss Federal Office for the Environment (FOEN). (Schurch et al., 2003) summarises part of this work for a west-east transect across Switzerland for three distinct areas representing the Jura Mountains (La Brévine station), the Swiss Plateau (Bern station) and the Southern Alps (Locarno station). The study performed at the Mormont station (Fig. 1) constitutes a prolongation of this transect up to the Tabular Jura that constitutes a flat Plateau to the NW of the last elevation of the Jura Mountains and provides additional information on $\delta^{18}O$ and δD behaviour preventing the rainout effect that may occur when moisture encounters the first escarpment of the Jura Mountains. The link between $\delta^{18}O$ in precipitation and cave waters has already been studied in Milandre cave (Perrin et al., 2003a).

In this paper, we present an overview of the hydrogen (δD) and oxygen ($\delta^{18}O$ and for the first time $\delta^{17}O$ in drip water and speleothem fluid inclusions) isotope signal transfer in water for a karst system in the Jura Mountains. We investigate the isotopic evolution from precipitation to cave drip water and its final enclosure into the speleothem fluid inclusions, and discuss the preservation of the climate signal. Based on these investigations, we conclude that stalagmites from Milandre cave are well suited for future paleoclimate reconstructions.

2. Site settings

Milandre cave (47.4855° N / 7.0161° E, elevation 373 m a.s.l.) is located in Boncourt (45 km westward of Basel, NW Switzerland) (Fig. 1). Geologically, the cave is part of a karst aquifer belonging to the Jura Mountains geological structure, more precisely it is located in the Tabular Jura unit that is made of subhorizontal Mesozoic limestones overlying Oxfordian marls. Milandre aquifer consists of a few metres thick soil and epikarst that overlie the unsaturated zone of the karst and eventually the phreatic zone (Perrin et al., 2003b).

The cave section shown on Fig. 2 represents approximately one third of the total network. Cave galleries develop mostly along fractures oriented north/south on a horizontal distance of 2.7 km with a total of 10.5 km of galleries and an overall positive elevation of 135 metres. The 4.633 km long Milandrine River flows in the lower part of the caves system which drains a surface catchment area of around 13 km^2 that is at a mean elevation of 500 m a.s.l. (Perrin, 2003; Perrin et al., 2007). The Milandrine flows directly into the Allaine River after passing a major siphon located at the natural resurgence. Except for this first natural entrance, the cave has a second natural access 30 metres above the siphon. A tunnel to access the former show cave has been built close to the natural entrance to facilitate access for visitors, but in the seventies the exploitation was stopped due to major flooding. The former show cave (200 metres long) is connected at its end to a well preserved fossil gallery called *Galerie des Fistuleuses* (literally “soda straws gallery”) via a second man-made access tunnel (15 metres long) excavated by the Jura caving club and opened in March 1968. A metallic door was placed in this connecting tunnel to preserve the cave site. This entrance remains closed, except for safety reasons when CO_2 concentration levels are too high to allow scientific trips. Land use above the cave is nowadays mainly constituted of forests, pastures and isolated individual constructions, especially above the downstream parts including the monitoring site. An extended description of the hydrological settings (Perrin et al., 2003a), of epikarst storage characteristics (Perrin et al., 2003b) and hydraulics aspects of Milandre cave system (Jeannin, 1996) allow a good understanding of the system.

Our monitoring study focuses on the *Galerie des Fistuleuses* where most of the stalagmites were collected. Furthermore, it has the main advantage of being easily accessible and that the cave climate is not disturbed when the doors remain closed. A detailed topographic map and an extended description are available in (Gigon and Wenger, 1986).

Milandre cave is influenced by the climate conditions prevailing over the study site which are representative for central/western Europe. Annual repartition of moisture fluxes for the northern Swiss Alps has been estimated by (Sodemann and Zubler, 2010) and gives the following results: ~39.5% from North Atlantic sectors, ~23% from Mediterranean area, ~21% from Europe continental source and ~16.5% from Northern Europe. Moreover, the source of precipitation suggests a principal continental contribution for the summer months whereas during winter continental contribution is low and the North Atlantic represents the major input. Contribution of moisture fluxes coming from the Mediterranean occurs mostly in winter, spring and autumn. For our study site we can expect similar conditions.

Mean annual precipitation recorded at Fahy station (Fig. 1) over the period 1960-2011 averages 1055 mm. An increase of 40 mm between the periods 1960-1990 and 1990-2011 is observed. Moreover, seasonal variability is well visible with significantly lower average precipitation amounts (monthly average of 74 mm) in winter (December-January-February, DJF), highest precipitation amount (101 mm) in summer (June-July-August, JJA) and intermediate values (89 mm) in March-April-May (MAM) and September-October-November (SON). Mean annual temperature at Fahy station (2 m above surface) over the last five decades shows maximum mean temperatures in August with 17.2°C and minimum in January with 0.4°C for an overall average air temperature of 8.6°C. It is worth noting that averaged temperatures between the period 1960-1990 and 1990-2011 increase from respectively 8.1°C to 9.2°C showing a significant warming of the Jura Plateau region. Temperature in the soil (5 cm depth) is also recorded at the station and gives mean annual values of 10.3°C between 1990 and 2011 that is 1.1°C more than the surface temperature.

Correlation maps with a spatial resolution of 0.5° x 0.5° and centred on 48°N 7°E were realised using the KNMI Climate Explorer (http://climexp.knmi.nl/) and the CRU TS 3.22 datasets for temperature and precipitation (Harris et al., 2014) to investigate the relationship of different climate parameters for NW Switzerland based on available temperature and precipitation (Fahy station, time series 1990-2011) and $\delta^{18}O_p$ (Basel CEP station, time series 1986-2010). According to the approach of

(Rozanski et al., 1992), seasonality of time series was removed beforehand. For Fahy station, spatial correlation maps with the CRU TS gridded data indicates that the mean annual temperature and precipitation are representative for central/western Europe, including Switzerland, France (eastern, centre and north), Germany and Belgium. Indeed, local temperature in Fahy station and European temperature are significantly correlated ($r > 0.80$) for most of central Europe. A similar observation made with the amount of precipitation leads to significant correlation ($r > 0.60$) for central/western Europe (Fig. 3b). Correlation maps realised between $\delta^{18}Op$ in Basel CEP station and temperature show significant correlation ($r = 0.60$, Fig. 3c) with central/western Europe, e.g. Germany, France and Belgium, whereas no correlation is observed with the amount of precipitation (Fig. 3d).

3. Methodology

3.1. Monitoring

A cave monitoring campaign was carried out in the *Galerie des Fistuleuses* between November 2011 and June 2014. Continuous and spot measurements of cave temperature, drip rate, relative humidity and air P_{CO2} measurements were conducted. Cave air temperature was measured every 15 minutes since October 2012 using a UTL-3 Scientific Dataloggers (GEOTEST, Zollikofen and Snow and Avalanche Research SFL, Davos, Switzerland) at an accuracy of 0.1°C. A Stalagmate Plus Mk2b (Driptych, United Kingdom) was used to monitor drip rates using an acoustic technique (drops per hour) at the M6 site since June 2012 (Collister and Mattey, 2008). The device was placed in an open pot connected to a one litre glass vial through an outlet tube to collect the water in glass bottles which were replaced around every three months (Fig. 2).

In the *Galerie des Fistuleuses*, spot measurements show air flow lower than 100 l/s (Testo 405-V1 device), humidity rate of 100% (Aspirationspsychrometer Hänni device) and P_{CO2} ranging from 0.30 to 1.41% (continuous (CORA device) and spot (Dräger X-am 5600 device) measurements from 2008 to 2014). Occasionally, the P_{CO2} concentration in the gallery can rise up to values of around 4%, especially during late autumn and early spring, as a result of processes that still need to be investigated.

Water samples were collected for geochemical analysis at different drip sites where stalagmites were taken (Table 1) to better understand isotope behaviour occurring between precipitation, drip water and its enclosure in speleothem fluid inclusions. The survey includes four drip sites for water isotopes (M4, M6, M9 and Fi-2) and three cave locations for temperature (including M2, M4, M6, M8, M9 and Fi-2). M6, M8, M9 and Fi-2 are located in the same cave chamber (refer to Fig. 2 for site positions).

Temperature and drip loggers were installed in the chamber where M6, M8 and M9 stalagmites were collected, approximately 300 metres after the end of the show cave (Fig. 2). A drip logger instrument was placed at the exact location where water was dripping from a soda straw on M6 stalagmite (from a height of ~2 metres). Stalagmite M8 grew close to M6 but was not active when removed. Finally, waters from the three drip sites (M6, Fi-2 and M9 which are 0.5 and 5 metres away from M6, respectively) were collected and analysed to estimate the homogeneity of the drip water chemistry.

3.2. Water isotope monitoring program

Data are based on two meteorological stations from the MeteoSwiss network. Precipitation samples and daily amount data were obtained from Mormont station (n° 534, 47.44 N / 7.04 E, altitude 540 m a.s.l.). The precipitation collection campaign was carried between March 2012 and July 2014, and a total of 274 precipitation events were recorded at 8 a.m. local time in an open gauge and stored in 100, 200 or 500 ml sealed glass bottles depending on the precipitation size. One must keep in mind that when collecting in an open gauge, evaporation occurring throughout the day could lead to a fractionation of the precipitation water, especially during the summer. The automated Fahy station (n° 500 , 47.42 N / 6.94 E, altitude 596 m a.s.l), located 7 km away from Mormont station, has provided daily data of precipitation amounts, mean relative humidity, mean soil and air temperatures since 1960. Both stations are located close to Milandre Cave (Fig. 1) and are therefore used as reference sites.

Cave water samples were obtained from five drip sites corresponding to the sample locations M2, M4, M6, M9 and Fi-2 between November 2010 and June 2014, and are further named “downstream” drip waters. Moreover, additional waters from one secondary intermediate flow tributary of Milandrine River (EN) and three additional percolation samples (ST, VI and GO) with approximately five or six orders of magnitude higher flow than M6 were collected in the upstream part of the cave (Perrin et al., 2003a) and are further called “upstream” cave waters.

3.2.1 Isotope measurements

Water isotope analyses of precipitation and cave waters were performed at the CEP (University of Bern) using a Picarro L2140-i wavelength-scanned cavity ring-down spectroscopy (WS-CRDS) instrument (Picarro Inc., Sunnyvale, CA, USA). For precipitation and drip water analysis, aliquots of water are filled in 2 ml glass vials and sealed with rubber/aluminium caps. The vials are then placed in a PAL COMBI-xt autosampler (CTC Analytics AG, Zwingen, Switzerland) connected to the Picarro L1102-i for δD and $\delta^{18}O$ and L2140-i for additional $\delta^{17}O$ values. Water is then injected using a syringe five or six times directly into the vaporisation unit of the analyser and the three first values are discarded due to memory effect. Reproducibility of measurements is typically 0.1‰ for $\delta^{18}O$ and $\delta^{17}O$ and 0.5‰ to 1‰ for δD.

For fluid inclusions, we used a new online method based on a Picarro L1102-i WS-CRDS instrument (Affolter et al., 2014) that allows measuring both δD and $\delta^{18}O$ isotopes on a single speleothem sample with precisions better than 0.4‰ for $\delta^{18}O$ and 1.5‰ for δD. Furthermore, accuracy and precision of the new method were also successfully assessed through an inter-laboratory comparison with the CF-IRMS method (Meckler et al., in review). The only modification made to the line is the replacement of the stainless steel capillary connecting the peristaltic pump to the dripping device by a glass capillary (0.18 mm inner diameter). Significant improvement was made on the measurement protocol with a reduction of time from 5 to 2 hours (90 minutes to recover the background condition stability and 20 to 40 minutes for the sample measurement itself mainly depending on the amount of released water) for one speleothem sample measurement, allowing up to five sample measurements per day. To perform $\delta^{17}O$ measurements in speleothem fluid inclusions, the line was connected to a Picarro L2140-i that is able to measure $\delta^{17}O$ in addition to $\delta^{18}O$ and δD. The instrument performance was assessed using the same approach as described in (Affolter et al., 2014). The precision of $\delta^{17}O$ measurements for stalagmite water samples is 0.3‰. Table 2 summarises the precision of the different water isotope measurements. In this study, blocks of calcite of around 0.5 grams were crushed releasing ~0.6 ml of water for fluid inclusions analysis of recent samples (M6), whereas blocks of ~1.5 grams where necessary for early Holocene (M8) samples to provide ~0.5 ml. It is worth mentioning that Holocene values are given here only for a first preliminary comparison to present conditions. For isotope analysis of the calcite ($\delta^{18}O_c$), the samples were measured using a Finnigan Delta V Advantage mass spectrometer equipped with an automated carbonate preparation system (Gas Bench II) at the Institute of Geological Sciences, University of Bern, Switzerland. 150-200 micrograms of sample were analysed and results are reported relative to the international Vienna Peedee Belemnite (VPDB) standard. The analytical error for $\delta^{18}O_c$ is 0.07‰ VPDB (1σ) (Fleitmann et al., 2009)..

3.2.2 $^{17}O_{excess}$ calibration

The $^{17}O_{excess}$ measurements made at Bern were calibrated using four internal water standards that themselves were analysed at the *Laboratoire des Sciences du Climat et de l'Environnement* in Paris with the method of CoF_3 fluorination of water to produce pure oxygen that is eventually analysed by dual inlet-IRMS (Landais et al., 2012b). Due to really small differences in $^{17}O_{excess}$, values are given in per meg (10^{-6}). Corresponding $\delta^{17}O$ values were calculated using Eq. 2 based on the relationship of (Luz and Barkan, 2010) (Eq. 1):

$$^{17}O\_excess = ln(\delta^{17}O+1)-0.528 \times (\delta^{18}O\ +1) \qquad Eq.\ 1$$

and consequently:

$$\delta^{17}O(‰)=((e^{(\delta 17O\text{-}excess/1000+0.528 \times ln\ (\delta 18O)/1000\ +\ 1)})-1)\ \times 1000 \qquad Eq.\ 2$$

Table 2 summarises the isotopic values of different internal standard waters used in this study. We experienced discrepancies between values obtained for $^{17}O_{excess}$ based on the CoF3 method performed at Paris, our own less-precise equilibration method ((Elsig, 2008 #1618)) and the high-precision laser-based cavity ring-down measurements. A detailed comparison of the three different methods will be presented in a separate publication. The values presented in this study are based on the four laboratory internal water standards that themselves were calibrated to the international scale by measuring V-SMOW, V-SLAP and V-GISP using the Picarro L2140-i instrument.

4. Results and discussion

4.1 M6 drip discharge

Drip rates between 2012 and 2014 at the M6 site are highly variable and range from 11 drops/hour (October 2012, 2013 and 2014) up to 278 drops/hour (February 2013). A seasonal pattern is clearly visible with the highest drip rates during the winter months (DJF) and the lowest during summer and autumn. Nearby Fi-2 drip site was checked at a three months interval and shows that drip rate was five times higher (with a similar seasonality as at M6) which emphasizes the variability in cave environment and the need of local monitoring. Nevertheless, isotope values for both drip locations are similar (Table 3). Drip rate depends on the aquifer recharge, i.e. on the amount of precipitation above the cave. The comparison between drip rate and precipitation is given in Fig. 4 and shows that both are closely related. Lowest drip rates in summer means that the overlying reservoir is draining out, as the aquifer is less recharged in summer mainly due to increased evapotranspiration (Fig. 1).

However, fairly high precipitation in autumn and winter recharges the aquifer and drip rates are increasing steadily, indicating that cold season precipitation (roughly from September to May) contribute to groundwater replenishment above Milandre cave.

We investigated the relationship between heavy rainfall events and cave drip rates in order to evaluate the response time. During summer when the reservoir is at its lowest level a two day-long precipitation event starting on 23.08.2013 (51.1 mm in total) showed only a slight response in drip discharge two days later (from 28 to 30 drops/hour). On 28.07.2013, a precipitation event (26.5 mm) showed no corresponding signal in the drip discharge but rather a continuous decrease of values. In spring, two consecutive days of precipitation (39.1 mm in total) produced a peak in drip rate (from 64 to 112 drops/hour) around five days later. Another two-day long event starting on 26.04.2013 (total 34.2 mm) gave a response six days later with an increase from 60 to 97 drops/hour. During winter months, an intense precipitation period between 24.12.2013 and 28.12.2013 (85.2 mm in total) led to an increase from 41 to 103 drops/hour around six days later. Overall, drip rates respond within 2-6 days to major precipitation events and drip rate is much more reactive in intensity during colder months (30-60 drops/hour) compared to summer (~ 0-2 drops/hour). Indeed, heavy rainfall events in summer seems to produce no or only slight responses in the drip discharge, which can be explained by the fact that the water is evaporated at the surface and used by vegetation and only lastly for refilling of the soil and epikarst.

While drip loggers count the total number of drops that fall from the roof in the cave, the drops are collected in a bottle for subsequent analysis of water isotopes. Knowing the collected water amount between two visits and the total drip amount over the same period, we estimated drop size diameter on two consecutive 3 month intervals between July 2013 and January 2013. We obtained similar results with respectively drop sizes diameters of 2.769 mm (91855 drops, 1021 grams of water collected) and 2.763 mm (89755 drops, 990.8 grams) for an averaged drop volume of 11.08 mm^3 (or ml). This would correspond to a mean discharge of 0.13 ml/s.

4.2 Mean annual surface and cave temperatures

Comparison between cave, soil and atmospheric temperature is shown in Fig. 5 to determine if the cave temperature corresponds to the mean temperature at the surface (Luetscher and Jeannin, 2004). A temperature logger was placed at the M6 drip site location and has recorded cave temperatures from 24th October 2012 and is still running. A one year average (October 2012 - October 2013) shows a mean annual temperature in the cave of 9.8 ± 0.2°C with minimum and maximum temperatures of 9.0°C and 10.2°C, where extremes could probably be due to the opening of the door connecting the show cave and the *Galerie des Fistuleuses* to allow cave CO_2 concentrations to decrease. However, observations document that this has only a minor effect on temperature. For the same period, surface mean annual temperature at Fahy station recorded an average temperature of 8.5°C, slightly colder ($\delta T = -1.3$ °C) than mean cave temperature. The difference towards warmer temperatures in the cave can be explained by the 200 m elevation difference between the cave (~400 m a.s.l.) and Fahy station (~600 m a.s.l.). Note that earlier temperature monitoring performed between 2008 and 2010 in the same cave gallery (Schmassmann, 2010) showed consistent mean annual values of 9.6°C. Consequently, observations are similar over both monitoring periods and mean annual cave temperature corresponds to the mean annual surface temperature when taking the adiabatic gradient of ~0.0055°Cm^{-1} (Rolland, 2003) into account.

4.3 Comparison of water isotopes in precipitation, drip water and speleothem fluid inclusions

The potential of Milandre stalagmites can be estimated by comparing fluid inclusion water isotopes to that of the corresponding drip water and amount weighted precipitation. Table 3 summarises δD, $\delta^{17}O$, $\delta^{18}O$ stable isotopes results and associated secondary order proxies d-excess (d) and $^{17}O_{excess}$ (D17) performed in this study. In total 274 analyses of precipitation, 22 "downstream" drip waters, 32 "upstream" cave waters and 8 fluid inclusions (including 4 without $\delta^{17}O$) were performed.

Isotopes in drip water are integrated over a long period of time (see Section 4.8) and consequently precipitation values must be given in mean weighted delta value form using Eq. 3 to allow comparison with cave drip isotope values:

$$\delta i_{\text{mean weighted}} = \left(\textstyle\sum_i \delta_{(i \times ni)}\right) / \left(\textstyle\sum_i n_i\right) \qquad \textit{Eq. 3}$$

where δ_i is the daily precipitation isotope value and n_i the daily amount of precipitation. Mean weighted values are given in Table 3. It is noteworthy that a net recharge weighting does not alter the data significantly. Isotope values are always given in brackets in this specific order (δD; $\delta^{18}O$; $\delta^{17}O$). Values are sometimes given for seasons: winter (DJF), spring (MAM), summer (JJA) and autumn (SON).

4.3.1 Isotopes in precipitation

Precipitation above Milandre catchment area shows δD_p and $\delta^{18}O_p$ values with a typical local signature comparable to values obtained for Switzerland (Perrin et al., 2003a; Schurch et al., 2003). Fig. 6 summarises all measurements of daily precipitation together with their respective $^{17}O_{excess}$ and d-excess, temperature and relative humidity for Mormont station.

Variability of isotope values in precipitation is high, with values ranging between -1.07‰ and -165.63‰ for δD_p, 3.36‰ and -21.75‰ for $\delta^{18}O_p$ and 1.79‰ and -11.49‰ for $\delta^{17}O_p$ with corresponding mean isotope composition between July 2012 and June 2014 of respectively (-64.97; -9.05; -4.78) ‰. Isotope values show a seasonal sensitivity with enriched values in JJA (-41.17; -6.03; -3.18) ‰ and depleted in DJF (-86.40; -11.82; -6.23) ‰ with corresponding amplitudes (45.2, 5.8; 3.1) ‰. Mormont shows large variations for two consecutive years with a shift of (7.31; 1.37; 0.71) ‰. However, an average of several years show significantly damped variations that do not exceed 0.5‰ in $\delta^{18}O_p$.

CEP stations values are given for comparison and correspond to the transect Basel-Bern-Locarno in Switzerland (Fig. 1 and Fig. 8b). Locarno is located on the southern side of the Alps and presents different climatic settings from Bern and Basel located on the northern side. Basel station is close to Mormont station and presents slightly more negative values of 0.2‰ and 2‰ for $\delta^{18}O_p$ and δD_p respectively.

4.3.2 Isotopes in cave waters

Drip waters show comparable values for all three isotopes between "downstream" drip sites and "upstream" cave waters with overall means of (-60.86 ±1.74; -8.76 ±0.25; -4.63 ±0.13) ‰. Slight differences may have to do with the heterogeneity of the sampling time and natural local variability.

In the monitored chamber, values for M6 (-60.33; -8.73; -4.60) ‰ are integrated over three months (around 1 litre sample), whereas spot values are given for Fi-2 (around 10 to 20 ml samples). They agree well in both δD and $\delta^{18}O$ isotope composition with shifts of 0.58‰ in δD and 0.06‰ in $\delta^{18}O$ over the two years. The overall isotope amplitude measured is 0.4‰ for $\delta^{18}O_{dw}$. A seasonal trend is visible but with two major differences compared to precipitation signal: (i) the signal amplitude is smoothed by a factor of ~25 and (ii) the signal is shifted of several months due to the residence time in the karst (see Section 4.8 for discussion).

In summary, waters sampled at from different cave sites show comparable means, amplitudes as well as standard deviations in their isotopic compositions implying that the precipitation waters are homogeneously mixed in the soil, epikarst and vadose zone above the cave before being transferred to the cave drip sites.

4.3.3 Isotopes in fluid inclusions

For fluid inclusions, results from modern active samples covering the last 40 years have already been partially published (Affolter et al., 2014) and additional measurements are given in Table 2. Speleothem fluid inclusion values for recent samples (-61.3; -8.3; -4.7) ‰ are similar for δD, $\delta^{18}O$ as well as $\delta^{17}O$ to the cave drip water suggesting that signal coming from the cave drip water is faithfully recorded in the speleothem fluid inclusion water and consequently, that ancient inclusions represent relics of past drip water. For early Holocene sample values are slightly more negative but still comparable to today's values.

4.4 Secondary parameters d-excess and $^{17}O_{excess}$ between precipitation and cave drip water

In the daily precipitation samples from Mormont, $^{17}O_{excess}$ values range from -26 to 72 per meg for a two years mean value of 18 per meg (idem for weighted mean) similar to the two years averaged drip water values of 18 and 19 per meg for the M6 and nearby Fi-2 drip sites in the monitored cave chamber. Mean seasonal values are 13 per meg (JJA), 17 per meg (SON), 25 per meg (DJF) and 19 per meg (MAM). During the monitoring period, $^{17}O_{excess}$ shows recurrent trends with rather stable winter values of 27 ±2 per meg (December 12 – April 13) and 25 ±4 per meg (November 13 – March 14) and minimum values of 3 per meg for both August 2012 and August 2013. The former may be explained by the rather constant moisture source originated from Atlantic Ocean during winter months (Sodemann and Zubler, 2010). Overall, $^{17}O_{excess}$ shows a monthly amplitude of 40 per meg which is comparable to observations made on a yearly basis at Vostok station in Antarctica (Landais et al., 2012a). In Fig. 6, $^{17}O_{excess}$ is anti-correlated to $\delta^{18}O$ and consequently with site temperature with more positive values in winter (40 per meg) and lower values in summer (0 per meg). Long term $^{17}O_{excess}$ time series records in precipitation are rare or even absent and this especially in low latitudes making the comparison difficult. Nevertheless, a few record are available but mainly in the Polar Regions and there, our observed anticorrelation between $\delta^{18}O$ and $^{17}O_{excess}$ is in opposition with the strong correlation observed on a limited number of events in Vostok solid precipitation that was explained by change in the kinetic vs. equilibrium fractionation proportion (Landais et al., 2012a), but similar to what was observed in a snow pit at the same station where the anticorrelation between $^{17}O_{excess}$ and $\delta^{18}O$ may be attributed to stratospheric influences (Winkler et al., 2012) . Furthermore, our measurements are in agreement with a few measurements in Greenland described in (Landais et al., 2012b). Additionally, in the African monsoon precipitation, (Landais et al., 2010) show also an anticorrelation between δD and $^{17}O_{excess}$ measured on a very limited amount of precipitation events.

The relationship between ln ($\delta^{18}O/1000+1$) versus ln($\delta^{17}O/1000+1$) can help to understand the principle behind the anticorrelation and seasonal variations in $^{17}O_{excess}$ by variations in kinetic fractionation. The fractionation factor $a_{equilibrium}$ (slope) for vapour-liquid water is 0.529 (Barkan and Luz, 2005), whereas the diffusion fractionation (kinetic) factor for water vapour is 0.518 (Barkan and Luz, 2007). Thus, the slope determined in meteoric water is a combination of both equilibrium and kinetic fractionation and the corresponding GMWL for oxygen isotopes has a slope of 0.528 (Luz and Barkan, 2010). In this study based on a two years record, the averaged a_{mean} is 0.5271 (see section 4.7.2) and presents seasonal variations. The fractionation factor is lower in summer (0.5255) than in winter (0.5271), whereas it is 0.5283 and 0.5274 for spring and autumn respectively. It is interesting to see that the a_{mean} corresponds to a_{winter}. It is then possible to formulate an explanation for the anticorrelation between $\delta^{18}O$ and $^{17}O_{excess}$ values by seasonal variations in the kinetic fractionation. Indeed, replacing the fractionation factor a in Eq. 1 for summer (low value) will decrease the $^{17}O_{excess}$ values, whereas it is the opposite for winter. Spring values show also a higher $^{17}O_{excess}$ than autumn (Fig. 6) but very close to the mean observed value for precipitation. This might indicate that the mean $^{17}O_{excess}$ value of about 20 per meg observed in our precipitation may correspond to a mean source effect corresponding, after (Uemura et al., 2010) to a normalized humidity of around 65%, which is, however, rather low compared to measured conditions over the Atlantic region even assuming an sea-air temperature difference of 0.5 to 1 +°C (Singh et al., 2005). Mechanisms responsible to explain these variations should be further studied and include kinetic fractionation during evaporation at the source, during transport, during cloud processes including supersaturation and finally process at the site of precipitation. These mechanisms are complex and involve several meteorological parameters such as humidity conditions, temperature, pressure pattern driving wind fields and strengths, condensation nuclei concentration and its specificity.

To better understand factors influencing $^{17}O_{excess}$ parameter at the study site, we evaluate its sensitivity to temperature and relative humidity both at the condensation site and at the main moisture source locations. We used the relative humidity and temperature data from the M6 buoy in the North Atlantic (Irish Weather Buoy Network, 53.07°N/15.88°W, see Fig. 3 for approximate location) located at a distance of roughly 1800 km to determine if any influence of moisture source coming from the Atlantic can be detected in this remote continental location. Based on a 31 days running average, we compare firstly $^{17}O_{excess}$ with the temperature or relative humidity. We find that $^{17}O_{excess}$ anti-correlates both with temperature at the condensation site ($R^2 = 0.36$) and with sea surface temperature ($R^2 = 0.60$). For the relative humidity, $^{17}O_{excess}$ anticorrelates for the Atlantic ($R^2 = 0.22$) but no correlation is observed with local relative humidity ($R^2 = 0.02$) indicating an influence of both temperature and relative humidity of the moisture source. A multiple regression of $^{17}O_{excess}$ with the relative humidity and the temperature at Fahy Meteoswiss station gives a correlation of 0.41 (R^2). Adding the relative humidity of the Atlantic source region to the regression analyses, the correlation coefficient increases to 0.61 (R^2), no further improvement is observed when adding the Atlantic source temperature at M6 (0.62). Note, even if the monthly running average may introduce an artificially high correlation, this indicates that oceanic condition at the source (M6 buoy) has an influence on $^{17}O_{excess}$ data in NW Switzerland. Further investigations should be made to try to disentangle the influence of individual parameter on the $^{17}O_{excess}$ parameter. It is nonetheless worth mentioning that the high correlation with the study site may be the reflection of seasonal covariation of temperature ($R^2 = 0.72$) between the oceanic source and the condensation site, whereas the correlation is low between the respective relative humidity ($R^2 = 0.14$).

Local d-excess shows seasonal fluctuations ranging between -27.96‰ and 21.95‰ around a mean value of 7.41‰ and presents lower d-excess during the summer (~4.7‰) and higher values during the winter (~10.6‰). Overall, d-excess shows a seasonal amplitude of 8‰. Differences can be explained by the origin of moisture during the summer that is mainly continental and probably with local secondary evaporation, whereas during winter it is mainly provided by the Atlantic Ocean (Sodemann and Zubler, 2010). Schotterer et al., (2000) assigned these variations to evaporation conditions at the moisture source, to evaporation of falling rain-drop and evaporation of local soil moisture. Averaged local weighted d-excess is 8.1‰ in precipitation (7.1‰ in summer and 8.1‰ in winter) and slightly lower compared to drip waters with values ranging between 8.9‰ (M6) and 9.5‰ (Fi-2) for the monitored cave chamber. The 1‰ difference between precipitation and drip water is probably due to the buffering in the karst system resulting from the mixing and residence time and consequently the unequal reservoir filling with more water supplies from the cold season.

In summary, $^{17}O_{excess}$ signal is kept in the drip water whereas d-excess is ~1‰ depleted. That means that sufficient analytical precision in speleothem fluid inclusion measurements should allow retrieving climate information from both $^{17}O_{excess}$ and d-excess from this cave.

4.5 Summary for the monitored chamber

Table 4 summarises the delta values and secondary proxies d-excess and $^{17}O_{excess}$ that are of interest for the monitored cave chamber (M6, Fi-2 and M9). The difference between the Mormont weighted mean and the drip water is discussed in Section 4.8. It is worth mentioning here that if the isotope values are weighted using the net recharge (rain – evapotranspiration) at Fahy station, then values (-73.30‰, -10.20‰ and -5.38‰ for δD, $\delta^{18}O$ and $\delta^{17}O$, respectively) are still close to the precipitation amount weighted. Drip water and sub-recent speleothem fluid inclusion values are similar for δD, whereas for $\delta^{18}O$ and $\delta^{17}O$ values are slightly more negative by 0.4‰ and 0.1‰ respectively but still within the method uncertainty. Nevertheless, the two recent sample measurements made with the Picarro L2140-i show identical values (-60.2; -8.6; -4.7) ‰ as M6 drip site. Thus, no significant differences are found between speleothem fluid inclusion water and modern drip water. Early Holocene values show slightly more negative values. $^{17}O_{excess}$ shows the same value in the cave and at the surface while d-excess is 1‰ more positive at surface. In fluid inclusions, $^{17}O_{excess}$ is potentially preserved and thus, it would be possible to derive together with the use of the carbon isotope additional information on past biospheric activity (Landais et al., 2007) or past hydrological changes (Schoenemann et al., 2014).

Theoretical values for modern speleothem calcite determined using the relationship of (Friedman and O'Neil, 1977) are not far from the $\delta^{18}O_c$ measured values (6.5‰). Indeed, a calculated $\delta^{18}O_c$ value of -7.27‰ is obtained (offset of ~0.8‰) when using the two year $\delta^{18}O$ averaged drip water isotope value of -8.7‰ and cave temperature of 9.8°C. By doing the same exercise using the most recent empirical relationship based on a large set of cave studies that already take into account a "mean" disequilibrium inherently present in cave environment (Tremaine et al., 2011), a theoretical $\delta^{18}O_c$ value of -6.85‰ is obtained that is even closer to the measured value meaning that $\delta^{18}O_c$ precipitates in disequilibrium. It is interesting to note that in B7 cave in east Germany (Niggemann et al., 2003) located around 450 km northward from Milandre cave $\delta^{18}O$ values of drip water (-8.4‰) and corresponding calcite (-6.3‰) are similar to those observed in Milandre cave.

Good agreement between drip water and the recent fluid inclusion isotope compositions confirms that the cave signal is preserved in speleothems. Nevertheless, hydrogen isotope values seem to be a more conservative proxy for paleoclimate reconstructions than corresponding oxygen, probably because hydrogen has no reservoir for isotope exchange during the transfer in the karst whereas oxygen may exchange continuously with the host calcite of the surrounding rock formation. During isotope measurements, mixing and storage of the isotopes in the soil and epikarst will allow recovering the decadal mean when measuring speleothem fluid inclusions and the annual mean for $\delta^{18}O$ of the calcite, or potentially seasonal variations. For fluid inclusions this is not an issue since the thickness of samples allows only reconstructions of decadal integrated values in this cave. Indeed, slabs up to 5 mm thick are required for fluid inclusion analysis and consequently the time resolution is dependent on the stalagmite growth speed. For example, the modern part of M6 stalagmite required with an annual growth rate 0.1 mm (laminae counting; Häuselmann et al., 2013) would correspond to a resolution of 40-50 years for fluid inclusion measurements done on a 5 mm slab.

4.6 Factors influencing isotope ratios and relationship to climate

In order to identify the forcing factors of isotope variability, we investigated relationships between atmospheric parameters and isotope values. Correlations (R^2), respectively slopes, are always given in brackets and in this specific order (δD; $\delta^{18}O$; $\delta^{17}O$), respectively (d-excess; $^{17}O_{excess}$) for secondary order proxies.

Correlations of water isotopes in precipitations with daily average temperature are lower (0.28; 0.36: 0.30) than for monthly mean precipitation (0.75; 0.73; 0.73) showing clearly the temperature dependence of the site. Corresponding slopes on a monthly basis (3.26; 0.39; 0.22 ‰ / 1°C) are lower than the 0.56‰ / 1°C for $\delta^{18}O$ observed for the region of Bern during the period 1994 – 2001 (Schurch et al., 2003), but in accordance to the values determined in Basel of 0.34‰ / 1°C for the period 1986 – 2010 which indicates that Basel CEP station is more representative for the Milandre cave area compared to Bern. Low correlations are observed for d-excess and $^{17}O_{excess}$ with local temperature on a daily basis (0.04; 0.06) as well as on a monthly basis (0.03; 0.20).

Relative humidity at the precipitation site shows low correlation for all isotopes (0.04; 0.12; 0.04) and a better correlation with monthly mean relative humidity (0.15; 0.17; 0.17). Secondary proxies have no significant correlation both on a daily (0.00; 0.01) and monthly basis (0.08, 0.01). Precipitation amount shows no correlation with all three isotopes both on a daily and on a monthly basis. The d-excess and $^{17}O_{excess}$ show insignificant correlation on a daily (0.09; 0.05) and monthly basis (0.15; 0.07).

Seasonality of stable isotopes in precipitation for Switzerland was shown to be correlated to temperature and water vapour pressure with lower values in winter corresponds to depleted isotope values (Schurch et al., 2003) which is confirmed by our observations as water isotopes in precipitation are best correlated with temperature at the condensation site and consequently the dominant effect (Fig. 7 and 3c). When values are integrated on a monthly basis, all three isotopes react in the same way to temperature (~73%) and to relative humidity (~17%), whereas on a daily basis relationships are less robust. The best correlation for $^{17}O_{excess}$ explains 20% of its variation by site temperature. For d-excess a low correlation of 15% is observed with the monthly amount of precipitation.

In Europe, several monitoring studies to understand the relationship between water isotopes in precipitation and corresponding drip waters were recently carried out. Approximately on a North South transect, in Han-sur-Lesse cave (Belgium), van Rampelbergh et al., 2014 found that the temperature effect has a clear influence on the regional water isotope composition in the precipitation with increasing values in summer, similar as observed in this study which is also corroborated with the spatial correlation maps observations (Fig. 3c). Moreover, the water isotope composition of the drip water is constant suggesting a good mixing and a long residence time in the epikarst. Nevertheless, the temperature is not always the driving parameter for $\delta^{18}O_p$; for instance in Villars cave (South France), (Genty et al., 2014) observed only a weak correlation between surface temperature and $\delta^{18}O_p$ mainly due to the interaction of different air masses coming from the Atlantic and the Mediterranean Sea. In Molinos cave (North East Spain), (Moreno et al., 2014) observed that temperature and amount of precipitation have an important effect on $\delta^{18}O_p$ but the source effect (North Atlantic or Western Mediterranean) is dominant on $\delta^{18}O_p$ due to the location of the cave between the two moisture sources that are North Atlantic and Western Mediterranean that have each a distinct $\delta^{18}O$ signature. These three European examples illustrate cave to cave variations in water isotope interpretation and thus, the uniqueness of each cave site and the need for specific cave monitoring.

Larger scale atmospheric effects can also have an influence on $\delta^{18}O_p$ of the study site. The link between $\delta^{18}O_p$ and the large scale atmospheric patterns such as the NAO for Europe has been investigated by Baldini et al., (2008) who observed that for central European mid-latitudes the NAO index is correlated to the winter $\delta^{18}O_p$ and was attributed to the strong control of air temperature on $\delta^{18}O_p$ (Baldini et al., 2008). The NAO is strongly correlated to temperature and precipitation over Europe (Hurrell and Van Loon, 1997) and consequently it has a direct influence on $\delta^{18}O_p$ through wind dominant patterns and consequently the amount of precipitation and temperature, and this especially in winter (Baldini et al., 2008). . Generally, isotopic values are depleted in winter compared to summer months, the influence of NAO on winter months may lead to an increase in precipitation with less negative values that will smooth the annual means. The influence of the North Atlantic Oscillation (NAO) on $\delta^{18}O_p$ in central Switzerland has been discussed by Teranes and McKenzie (2001). They present paleoclimate reconstructions using sediments of Lake Baldeggersee (central Switzerland, alt. 463 m a.s.l.) based on a modern calibration. The lake is located around 100 km eastward from Milandre cave and it was shown that $\delta^{18}O_c$ there is mainly driven by temperature but it is also suggested that the NAO may have a discernible influence on the isotopic composition of regional precipitation and that long term trend in the NAO index can explain $\delta^{18}O_c$ isotopic trends in lake sediments data (Teranes and McKenzie, 2001). Other observations linked the $\delta^{18}O$ of continental archives with changes in the NAO in central Europe, for alpine ice cores in the Swiss Alps (Schotterer et al., 2002), and even further East, in $\delta^{18}O_c$ from speleothem from Spannagel cave in Austria (Mangini et al., 2005). More recently, (Luetscher et al., 2015) interprets the isotopic composition in speleothems as a proxy for changes in the North Atlantic storm track during the Last Glacial Maximum in the Sieben Hengste cave systems (Swiss Alps). It is worth noting that for the last three examples, the link between archives and NAO or storm track is observed at high elevations in the Alps which could be due to higher sensitivity of continental archives to NAO index, as for instance suggested for lake sediments in the Western French Alps (Guyard et al., 2013). To have a closer look at the precipitation site data, we investigated the relationships between $\delta^{18}O_p$ and the NAO index both on a two years interval (daily event basis) at the study site and on a 25 years interval at the CEP station in Basel that recorded $\delta^{18}O_p$ since 1986 (monthly basis). Results indicate no correlation ($R^2=0.009$) at the study site between daily NAO index and daily $\delta^{18}O_p$ opposite to what was recently observed in NE Spain (Moreno et al., 2014). This observation seems coherent with regard to the relative distance of the Atlantic moisture source and to the multi-source of moisture air masses (Sodemann and Zubler, 2010). When looking at the correlation between monthly NAO index and $\delta^{18}O_p$ in Basel for the period 1986 – 2012, no correlation ($R^2=0.0002$) is observed on a monthly basis. For the summer months (JJA), no correlation is observed for both periods with $R^2 = 0.005$ and $R^2 = 0.016$ respectively. Three months seasonal mean show a correlation ($R^2=0.35$) for winter (DJF) and no correlation for summer months JJA ($R^2=0.004$). Teranes and McKenzie (2001) showed that isotope data in Bern and NAO index are in good agreement for the period 1972 – 1995. We observed indeed a high correlation between three months NAO index versus winter (DJF) $\delta^{18}O_p$ in Basel for the period 1986 – 1995 ($R^2 = 0.75$) in agreement with Baldini et al. (2008), whereas a lower correlation ($R^2=0.28$) is observed for the period 1995-2012. Further investigations would be necessary on Milandre speleothem isotope records to see if such an influence is also detected.

In summary, for NW Switzerland $\delta^{18}O_p$ is mainly controlled by the temperature at the condensation site (Schurch et al., 2003; this study). Correlation maps between $\delta^{18}O_p$ and temperature (Fig. 3c) show a significant correlation for central/western Europe and isotopes are related to temperature both on a short (2 years) and on a long interval (25 years). Together with the temperature effect, a discernible influence of large scale atmospheric effects (NAO) on $\delta^{18}O_p$ is expected (Teranes and McKenzie, 2001) which will mainly have an influence on winter moisture source conditions. A good correlation is observed between the NAO index and the DJF months at the study site but no correlation is seen on a daily precipitation basis. Finally, for the precipitation amount, no significant correlation is observed either at the study site location on a two year time scale or when comparing with the 25 years CEP Basel station record (Fig. 3c)

4.7 Local meteoric water lines

4.7.1 Local meteoric water line from $\delta^{18}O$ and δD

The local meteoric water line (LMWL) has been determined for NW Switzerland using the relationship between δD and $\delta^{18}O$ on daily precipitation samples collected between March 2012 and March 2014. The least square regression equation corresponds to $\delta D = 7.92 \times \delta^{18}O + 7.26$ ($R^2 = 0.98$) which is close to the Global Meteoric Water Line (GMWL, $\delta D = 8 \times \delta^{18}O + 10$). In addition, winter ($\delta D = 8.21 \times \delta^{18}O + 10.62$, $R^2 = 0.98$) and summer ($\delta D = 7.62 \times \delta^{18}O + 4.74$, $R^2 = 0.95$) meteoric water lines are shown in Fig. 8. Lower d-excess (4.74‰) and a slightly lower slope indicate evaporation probably mainly occurring in the open gauge used for collection.

Fig. 8 (left panel) summarises all precipitation isotope values produced in this study, whereas Fig. 8 (right panel) shows cave and fluid inclusion waters along with the LMWL and GMWL. Cave waters are close to the LMWL and shifted following the LMWL to more positive values. Eventually, the LMWL will be used for future paleotemperature calculations from speleothem fluid inclusions (e.g. Kim and O`Neil, 1997; Tremaine et al., 2011).

4.7.2 Local meteoric water line from $\delta^{18}O$and $\delta^{17}O$

Relationship between $\delta^{17}O$ and $\delta^{18}O$ in meteoric waters from NW Switzerland is presented in Fig. 9 together with the relationship for drip waters and specific monitored site location. The slope that relate the local liquid water and vapour at equilibrium (LMWL for oxygen) presents a slope of 0.527 similar to the GMWL for oxygen defined by Luz and Barkan (2010) of 0.528. In cave waters slight variations are observed with a lower slope of 0.518 measured on 40 samples only, but integrated over two years. The cave slope corresponds to the values of terrestrial biospheric exchange (respiration) of Luz and Barkan (2005) with a slope of 0.5179 ±0.0006 and leaf transpiration slope of Landais et al. (2007).

4.8 Estimation of water transfer time between surface and cave

The transfer time for water infiltrating the soil and epikarst above the cave and its corresponding exit in the M6 soda straw inside the cave was estimated. The estimation of residence time (t) of water in the aquifer for M6 drip site was based on isotope delay between precipitation and drip water. First series of measurements performed with Picarro L1102-i and performed after each field sampling at M6 and Fi-2 drip sites allowed the estimation of a 0.4‰ amplitude (Fig. 10). Re-measurements using a Picarro L2140-i made one to three years after the water sampling do not show a clear seasonality any more in drip water maybe due to sample alteration during storage. Nevertheless, a variation of 0.4‰ in the drip water was used to estimate the residence time of water in the epikarst.

Based on isotope signal transmission through the epikarst, hydrogen (δD) and oxygen ($\delta^{18}O$) signals are shifted compared to the precipitation signal suggesting a residence time of precipitation waters in the epikarst of around 8 – 10 months. Moreover, the signal is smoothed by a factor of 25. The attenuation is a function of the residence time of the water in the bedrock. As the mean values in drip water are highly smoothed, drip water must represent an integrated surface precipitation close to one year. This suggests that a residence time of 8 – 10 months seems to be possible.

This estimate is corroborated with simple model estimation by comparing the signal amplitude and shift in precipitation and cave water. To estimate the residence time, the seasonal variations have to be taken into account. During the summer, water will preferentially be used by vegetation or evaporated and only partly be stored in the reservoir, whereas during the winter precipitation is infiltrating in the aquifer exhibiting more negative isotope values. Thus, a clear asymmetry between winter and summer infiltration occurs (Fig. 1) and leads to more negative values that are in contrast with the measurements that requires further explanation, which is given the next paragraph. The contribution of different seasonal drip water has to be taken into account and consequently weighted. Eventually, a 10 months mixing associated to a monthly weighted drip rate is able to explain the amplitude smoothing and the temporal shift of the signal in cave drip water. To further investigate the residence time issue, tritium isotope measurements on the collected cave water samples could be performed (Kluge et al., 2010). However, precision may not be sufficient to solve the issue completely.

After crossing the aquifer, the smoothed $\delta^{18}O$ isotope signal exiting in the cave is 1‰ more positive than in precipitation. This enrichment cannot be explained by isotope variation in precipitation alone, as precipitation values are stable in the range of 0.5‰ within the monitoring time interval. Instead, the enrichment observed in both δD and $\delta^{18}O$ isotopes may be due to recycled condensed water inside the aquifer (Luo et al., 2013), but in Milandre cave, evapotranspiration occurring at the surface prior to infiltration is probably sufficient to explain this enrichment. Evaporation processes at the surface will tend to evaporate preferentially lighter water molecules meaning that the heavier ones will infiltrate the aquifer, which leads to isotope enrichment. Already less than 15% evaporated water accounts for the observed isotopic enhancement.

Epikarst storage in Milandre karst aquifer (Perrin et al., 2003b) and infiltration of meteoric waters for the corresponding catchment area (Perrin et al., 2003a) have been carefully described and can be summarised as following: soil and epikarst act as an important groundwater storage of the karst system and/or water circulates slowly in the unsaturated zone. The transit time is long enough for the water to reach equilibrium with calcite and water chemistry is mainly driven by mixing of water derived from different infiltration zones in the epikarst (Williams, 2008). Moreover, Perrin et al. (2003b) observed stable δ^{18}O values of 9.15 ± 0.21‰ between June 1999 and July 2000 for waters coming from 15 cave sites. Isotope values showed low variability in time and location, so he defines δ^{18}O as a conservative tracer for precipitation flowing out of the cave at Saivu spring (Fig. 1). In this study, δ^{18}O "upstream" cave waters are on average ~0.3‰ more positive (-8.83 ± 0.27‰). This enrichment agrees with the trend observed in precipitation from Basel and Bern CEP stations of 0.02‰ year m^{-1}. Indeed, multiplying the trend by 14 years leads to an enrichment of 0.28‰ in precipitation close to the observations made in Milandre cave.

5. Conclusions

Oxygen (δ^{17}O, δ^{18}O) and hydrogen (δD) isotope evolution recorded during a two year monitoring period in precipitation, drip water and speleothem fluid inclusions for Milandre cave (NW Switzerland) is presented. Seasonal variations are visible in precipitation with more enriched values in summer and depleted in winter. Water isotopes in NW Switzerland precipitation are mainly controlled by air temperature ($R^2 = 0.73$) on a monthly basis. A low correlation ($R^2 = 0.13$) is observed with local relative humidity, but no correlation is observed with the amount of precipitation. Preliminary observations suggest that influence of large scale atmospheric effects such as NAO on $\delta^{18}O_p$ occurs mainly during winter months.

Isotope values are enriched by around 10‰ for δD and 1.2‰ for δ^{18}O in drip water compared to weighted precipitation values which can be explained by evaporative processes at the surface prior to infiltration in the aquifer. Nevertheless, the isotope signal is smoothed to a high degree due to mixing in the soil and epikarst and of residence time of around 8 – 10 months in the aquifer above the cave. The climatic signal is shifted towards more positive values in drip water and hardly show any seasonality (annual amplitude of 0.4‰) smoothed by a factor of ~25 compared to precipitation (annual amplitude of 10‰). Analyses of M6 and M8 stalagmite fluid inclusions coming from the monitored cave chamber showed that the mean annual drip water signal is preserved after its enclosure in speleothem calcite for recent samples allowing speleothem based paleoclimate reconstruction in Milandre cave. The cave located at the border between France and Switzerland presents climate conditions representative for central/western Europe.

After a few adaptations of our measuring line, we successfully performed, for the first time, δ^{17}O measurements of fluid inclusion water together with δD and δ^{18}O on a single speleothem sample. This analytical advance may allow expanding the speleothem based paleoclimate reconstruction possibilities to the $^{17}O_{excess}$ parameter as it has already been done for ice cores (Winkler et al., 2012).

In this study, we showed for the first time that the δ^{17}O signal is preserved between precipitation and cave water with the two year monitoring. The secondary parameter $^{17}O_{excess}$ shows equivalent averaged values of 18 per meg in both precipitation and drip water. We have shown that $^{17}O_{excess}$ results measured in fluid inclusions are roughly comparable to surface precipitation. Extended instrument calibration, as well as the use of several replicates may help obtaining more robust values. These results are promising and retrieving past information about the moisture source based on speleothem fluid inclusions is potentially achievable but more has to be learned. Analytical precision in $\delta^{18}O_{fi}$ and $\delta^{17}O_{fi}$ measurements is the key to detecting precise variations in $^{17}O_{excess}$.

Investigations of geochemical parameters, the understanding of processes as well as cave accessibility and speleothem richness and preservation allow us to define Milandre cave as a good candidate for paleoclimate reconstructions.

Acknowledgments

We warmly thank Mrs. Anne Forster for sampling daily precipitation water at Mormont MeteoSwiss station. We would also like to thank Pierre-Xavier Meury (Speleo-Club Jura) for field work support in Milandre cave, Peter Nyfeler (Climate and Environmental Physic in Bern) for helpful technical assistance and Sebastian Breitenbach for his valuable comments. We thank MeteoSwiss for their scientific support and for providing meteorological data. We acknowledge three anonymous reviewers for their comments that improved the quality of the manuscript. This study is part of "STALCLIM" and "STALCLIM 2", Sinergia projects financed through the Swiss National Science Foundation (grant no. CRSI22-132646/1).

References

Affolter, S., Fleitmann, D., Leuenberger, M., 2014. New online method for water isotope analysis of speleothem fluid inclusions using laser absorption spectroscopy (WS-CRDS). Clim. Past 10, 1291-1304.

Angert, A., Cappa, C.D., DePaolo, D.J., 2004. Kinetic O-17 effects in the hydrologic cycle: Indirect evidence and implications. Geochim Cosmochim Ac 68, 3487-3495.

Araguas-Araguas, L., Froehlich, K., Rozanski, K., 2000. Deuterium and oxygen-18 isotope composition of precipitation and atmospheric moisture. Hydrol Process 14, 1341-1355.

Arienzo, M.M., Swart, P.K., Vonhof, H.B., 2013. Measurement of δ18O and δ2H values of fluid inclusion water in speleothems using cavity ring-down spectroscopy compared with isotope ratio mass spectrometry. Rapid Commun Mass Sp 27, 2616-2624.

Baldini, L.M., McDermott, F., Foley, A.M., Baldini, J.U.L., 2008. Spatial variability in the European winter precipitation delta(18)O-NAO relationship: Implications for reconstructing NAO-mode climate variability in the Holocene. Geophys Res Lett 35.

Barkan, E., Luz, B., 2005. High precision measurements of O-17/O-16 and O-18/O-16 ratios in H2O. Rapid Commun Mass Sp 19, 3737-3742.

Barkan, E., Luz, B., 2007. Diffusivity fractionations of (H2O)-O-16/(H2O)-O-17 and (H2O)-O-16/(H2O)-O-18 in air and their implications for isotope hydrology. Rapid Commun Mass Sp 21, 2999-3005.

Blyth, A.J., Smith, C.I., Drysdale, R.N., 2013. A new perspective on the delta C-13 signal preserved in speleothems using LC-IRMS analysis of bulk organic matter and compound specific stable isotope analysis. Quaternary Sci Rev 75, 143-149.

Burns, S.J., Fleitmann, D., Matter, A., Neff, U., Mangini, A., 2001. Speleothem evidence from Oman for continental pluvial events during interglacial periods. Geology 29, 623-626.

Cheng, H., Edwards, R.L., Broecker, W.S., Denton, G.H., Kong, X.G., Wang, Y.J., Zhang, R., Wang, X.F., 2009. Ice Age Terminations. Science 326, 248-252.

Cheng, H., Edwards, R.L., Shen, C.C., Polyak, V.J., Asmerom, Y., Woodhead, J., Hellstrom, J., Wang, Y.J., Kong, X.G., Spotl, C., Wang, X.F., Alexander, E.C., 2013. Improvements in Th-230 dating, Th-230 and U-234 half-life values, and U-Th isotopic measurements by multi-collector inductively coupled plasma mass spectrometry. Earth Planet Sc Lett 371, 82-91.

Collister, C., Mattey, D., 2008. Controls on water drop volume at speleothem drip sites: An experimental study. Journal of Hydrology 358, 259-267.

Craig, H., 1965. The measurement of oxygen isotope paleotemperatures. Stable isotopes in oceanographic studies and palaeotemperatures 23, pp. 166–182.

Cruz, F.W., Karmann, I., Viana, O., Burns, S.J., Ferrari, J.A., Vuille, M., Sial, A.N., Moreira, M.Z., 2005. Stable isotope study of cave percolation waters in subtropical Brazil: Implications for paleoclimate inferences from speleothems. Chem Geol 220, 245-262.

Cuthbert, M.O., Baker, A., Jex, C.N., Graham, P.W., Treble, P.C., Andersen, M.S., Ian Acworth, R., 2014. Drip water isotopes in semi-arid karst: Implications for speleothem paleoclimatology. Earth Planet Sc Lett 395, 194-204.

Dansgaard, W., 1964. Stable Isotopes in Precipitation. Tellus 16, 436-468.

Duan, F.C., Wu, J.Y., Wang, Y.J., Edwards, R.L., Cheng, H., Kong, X.G., Zhang, W.H., 2015. A 3000-yr annually laminated stalagmite record of the Last Glacial Maximum from Hulu Cave, China. Quaternary Res 83, 360-369.

Dublyansky, Y.V., Spotl, C., 2009. Hydrogen and oxygen isotopes of water from inclusions in minerals: design of a new crushing system and on-line continuous-flow isotope ratio mass spectrometric analysis. Rapid Commun Mass Sp 23, 2605-2613.

Fleitmann, D., Burns, S.J., Neff, U., Mangini, A., Matter, A., 2003. Changing moisture sources over the last 330,000 years in Northern Oman from fluid-inclusion evidence in speleothems. Quaternary Res 60, 223-232.

Fleitmann, D., Burns, S.J., Neff, U., Mudelsee, M., Mangini, A., Matter, A., 2004. Palaeoclimatic interpretation of high-resolution oxygen isotope profiles derived from annually laminated speleothems from Southern Oman. Quaternary Sci Rev 23, 935-945.

Fleitmann, D., Cheng, H., Badertscher, S., Edwards, R.L., Mudelsee, M., Gokturk, O.M., Fankhauser, A., Pickering, R., Raible, C.C., Matter, A., Kramers, J., Tuysuz, O., 2009. Timing and climatic impact of Greenland interstadials recorded in stalagmites from northern Turkey. Geophys Res Lett 36.

Friedman, I., O'Neil, J.R., 1977. Compilation of Stable Isotope Fractionation Factors of Geochemical Interest. In: Fleischer, M. (Ed.), Data of Geochemistry, 6th edition.: U.S. Geol. Survey Prof. Paper 440-KK, pp. 1-12.

Genty, D., Combourieu-Nebout, N., Peyron, O., Blamart, D., Wainer, K., Mansuri, F., Ghaleb, B., Isabello, L., Dormoy, I., von Grafenstein, U., Bonelli, S., Landais, A., Brauer, A., 2010. Isotopic characterization of rapid climatic events during OIS3 and OIS4 in Villars Cave stalagmites (SW-France) and correlation with Atlantic and Mediterranean pollen records. Quaternary Sci Rev 29, 2799-2820.

Genty, D., Labuhn, I., Hoffmann, G., Danis, P.A., Mestre, O., Bourges, F., Wainer, K., Massault, M., Van Exter, S., Regnier, E., Orengo, P., Falourd, S., Minster, B., 2014. Rainfall and cave water isotopic relationships in two South-France sites. Geochim Cosmochim Ac 131, 323-343.

Gigon, R., Wenger, R., 1986. Inventaire Spéléologique de la Suisse. II. Canton du Jura. Commission Spéléologique de la Société helvétique des Sciences Naturelles. Porrentruy, Switzerland.

Griffiths, M.L., Drysdale, R.N., Vonhof, H.B., Gagan, M.K., Zhao, J.X., Ayliffe, L.K., Hantoro, W.S., Hellstrom, J.C., Cartwright, I., Frisia, S., Suwargadi, B.W., 2010. Younger Dryas-Holocene temperature and rainfall history of southern Indonesia from delta O-18 in speleothem calcite and fluid inclusions. Earth Planet Sc Lett 295, 30-36.

Guyard, H., Chapron, E., St-Onge, G., Labrie, J., 2013. Late-Holocene NAO and oceanic forcing on high-altitude proglacial sedimentation (Lake Bramant, Western French Alps). Holocene 23, 1163-1172.

Harris, I., Jones, P.D., Osborn, T.J., Lister, D.H., 2014. Updated high-resolution grids of monthly climatic observations – the CRU TS3.10 Dataset. Int J Climatol 34, 623-642.

Häuselmann, A.D., 2013. Younger Dryas and Holocene temperature variations recorded in stalagmites from Milandre cave, Switzerland. Isotopes of Carbon, Water, and Geotracers in Paleoclimate Research, 26 – 28 August 2013, Bern, Switzerland.

Henderson, G.M., 2006. Climate - Caving in to new chronologies. Science 313, 620-622.

Hurrell, J., Van Loon, H., 1997. Decadal Variations in Climate Associated with the North Atlantic Oscillation, In: Diaz, H., Beniston, M., Bradley, R. (Eds.), Climatic Change at High Elevation Sites. Springer Netherlands, pp. 69-94.

Jeannin, P.Y., 1996. PhD Thesis, CHYN, University of Neuchâtel, Switzerland.

Jouzel, J., Merlivat, L., 1984. Deuterium and O-18 in Precipitation - Modeling of the Isotopic Effects during Snow Formation. J Geophys Res-Atmos 89, 1749-1757.

Kennett, D.J., Breitenbach, S.F.M., Aquino, V.V., Asmerom, Y., Awe, J., Baldini, J.U.L., Bartlein, P., Culleton, B.J., Ebert, C., Jazwa, C., Macri, M.J., Marwan, N., Polyak, V., Prufer, K.M., Ridley, H.E., Sodemann, H., Winterhalder, B., Haug, G.H., 2012. Development and Disintegration of Maya Political Systems in Response to Climate Change. Science 338, 788-791.

Kim, S.T., ONeil, J.R., 1997. Equilibrium and nonequilibrium oxygen isotope effects in synthetic carbonates. Geochim Cosmochim Ac 61, 3461-3475.

Kluge, T., Riechelmann, D.F.C., Wieser, M., Spotl, C., Sultenfuss, J., Schroder-Ritzrau, A., Niggemann, S., Aeschbach-Hertig, W., 2010. Dating cave drip water by tritium. J Hydrol 394, 396-406.

Kruger, Y., Marti, D., Staub, R.H., Fleitmann, D., Frenz, M., 2011. Liquid-vapour homogenisation of fluid inclusions in stalagmites: Evaluation of a new thermometer for palaeoclimate research. Chem Geol 289, 39-47.

Lachniet, M.S., 2009. Climatic and environmental controls on speleothem oxygen-isotope values. Quaternary Sci Rev 28, 412-432.

Landais, A., Barkan, E., Luz, B., 2008. Record of delta O-18 and O-17-excess in ice from Vostok Antarctica during the last 150,000 years. Geophys Res Lett 35.

Landais, A., Ekaykin, A., Barkan, E., Winkler, R., Luz, B., 2012a. Seasonal variations of O-17-excess and d-excess in snow precipitation at Vostok station, East Antarctica. J Glaciol 58, 725-733.

Landais, A., Risi, C., Bony, S., Vimeux, F., Descroix, L., Falourd, S., Bouygues, A., 2010. Combined measurements of O-17(excess) and d-excess in African monsoon precipitation: Implications for evaluating convective parameterizations. Earth Planet Sc Lett 298, 104-112.

Landais, A., Steen-Larsen, H.C., Guillevic, M., Masson-Delmotte, V., Vinther, B., Winkler, R., 2012b. Triple isotopic composition of oxygen in surface snow and water vapor at NEEM (Greenland). Geochim Cosmochim Ac 77, 304-316.

Landais, A., Yakir, D., Barkan, E., Luz, B., 2007. The Triple Isotopic Composition of Oxygen in Leaf Water and Its Implications for Quantifying Biosphere Productivity, In: Todd, E.D., Rolf, T.W.S. (Eds.), Terrestrial Ecology. Elsevier, pp. 111-125.

Li, S., Levin, N.E., Chesson, L.A., 2015. Continental scale variation in 17O-excess of meteoric waters in the United States. Geochim Cosmochim Ac 164, 110-126.

Luetscher, M., Boch, R., Sodemann, H., Spotl, C., Cheng, H., Edwards, R.L., Frisia, S., Hof, F., Muller, W., 2015. North Atlantic storm track changes during the Last Glacial Maximum recorded by Alpine speleothems. Nat Commun 6.

Luetscher, M., Jeannin, P.Y., 2004. Temperature distribution in karst systems: the role of air and water fluxes. Terra Nova 16, 344-350.

Luo, W.J., Wang, S.J., Xie, X.N., 2013. A comparative study on the stable isotopes from precipitation to speleothem in four caves of Guizhou, China. Chem Erde-Geochem 73, 205-215.

Luz, B., Barkan, E., 2005. The isotopic ratios 17O/16O and 18O/16O in molecular oxygen and their significance in biogeochemistry. Geochim Cosmochim Ac 69, 1099-1110.

Luz, B., Barkan, E., 2010. Variations of O-17/O-16 and O-18/O-16 in meteoric waters. Geochim Cosmochim Ac 74, 6276-6286.

Mangini, A., Spotl, C., Verdes, P., 2005. Reconstruction of temperature in the Central Alps during the past 2000 yr from a delta O-18 stalagmite record. Earth Planet Sc Lett 235, 741-751.

McDermott, F., Schwarcz, H., Rower, P.J., 2006. Isotopes in Speleothems, In: Leng, M.J. (Ed.), Isotopes in Paleoenvironmental Research. Springer, The Netherlands.

Meckler, A.N., Affolter, S., Dublyanski, Y.V., Krüger, Y., Vogel, N., Bernasconi, S.M., Frenz, M., Kipfer, R., Leuenberger, M., Spötl, C., Carolin, S., Cobb, K.M., Moerman, J., Adkins, J.F., Fleitmann, D., in review. Glacial-interglacial temperature change in the tropical West Pacific: A comparison of stalagmite-based paleo-thermometers. Quaternary Sci Rev, submitted.

Meckler, A.N., Clarkson, M.O., Cobb, K.M., Sodemann, H., Adkins, J.F., 2012. Interglacial Hydroclimate in the Tropical West Pacific Through the Late Pleistocene. Science 336, 1301-1304.

Meckler, A.N., Ziegler, M., Millan, M.I., Breitenbach, S.F.M., Bernasconi, S.M., 2014. Long-term performance of the Kiel carbonate device with a new correction scheme for clumped isotope measurements. Rapid Commun Mass Sp 28, 1705-1715.

Moerman, J.L., Cobb, K.M., Kollmeyer, R., Clark, B., Tuen, A.A., 2010. Climatic influences on daily rainwater delta O-18 and delta D timeseries in Northern Borneo. Geochim Cosmochim Ac 74, A716-A716.

Moreno, A., Sancho, C., Bartolome, M., Oliva-Urcia, B., Delgado-Huertas, A., Estrela, M.J., Corell, D., Lopez-Moreno, J.I., Cacho, I., 2014. Climate controls on rainfall isotopes and their effects on cave drip water and speleothem growth: the case of Molinos cave (Teruel, NE Spain). Clim Dynam 43, 221-241.

Niggemann, S., Mangini, A., Richter, D.K., Wurth, G., 2003. A paleoclimate record of the last 17,600 years in stalagmites from the B7 cave, Sauerland, Germany. Quaternary Sci Rev 22, 555-567.

Perrin, J., 2003. A conceptual model of flow and transport in a karst aquifer based on spatial and temporal variations of natural tracers. PhD Thesis, CHYN, University of Neuchâtel, Switzerland.

Perrin, J., Jeannin, P.Y., Cornaton, F., 2007. The role of tributary mixing in chemical variations at a karst spring, Milandre, Switzerland. J Hydrol 332, 158-173.

Perrin, J., Jeannin, P.Y., Zwahlen, F., 2003a. Implications of the spatial variability of infiltration-water chemistry for the investigation of a karst aquifer: a field study at Milandre test site, Swiss Jura. Hydrogeol J 11, 673-686.

Perrin, K., Jeannin, P.Y., Zwahlen, F., 2003b. Epikarst storage in a karst aquifer: a conceptual model based on isotopic data, Milandre test site, Switzerland. J Hydrol 279, 106-124.

Riechelmann, D.F.C., Schroder-Ritzrau, A., Scholz, D., Fohlmeister, J., Spotl, C., Richter, D.K., Mangini, A., 2011. Monitoring Bunker Cave (NW Germany): A prerequisite to interpret geochemical proxy data of speleothems from this site. J Hydrol 409, 682-695.

Rolland, C., 2003. Spatial and seasonal variations of air temperature lapse rates in Alpine regions. J Climate 16, 1032-1046.

Rozanski, K., Araguasaraguas, L., Gonfiantini, R., 1992. Relation between Long-Term Trends of O-18 Isotope Composition of Precipitation and Climate. Science 258, 981-985.

Rudzka, D., McDermott, F., Baldini, L.M., Fleitmann, D., Moreno, A., Stoll, H., 2011. The coupled delta C-13-radiocarbon systematics of three Late Glacial/early Holocene speleothems; insights into soil and cave processes at climatic transitions. Geochim Cosmochim Ac 75, 4321-4339.

Schmassmann, S., 2010. Master Thesis, Geological Institute, University of Bern, Switzerland.

Schoenemann, S.W., Steig, E.J., Ding, Q.H., Markle, B.R., Schauer, A.J., 2014. Triple water-isotopologue record from WAIS Divide, Antarctica: Controls on glacial-interglacial changes in O-17(excess) of precipitation. J Geophys Res-Atmos 119, 8741-8763.

Schotterer, U., Stichler, W., Graf, W., Buerki, H.-U., Gourcy, L., Ginot, P., Huber, T., 2002. Stable isotopes in alpine ice cores: Do they record climate variability?

Schotterer, U., Stocker, T., Bürki, H., Hunziker, J., Kozel, R., Grasso, D.A., Tripet, J.P., 2000. Das Schweizer Isotopen-Messnetz. Trends 1992-1999. Gas, Wasser, Abwasser, 733-741.

Schurch, M., Kozel, R., Schotterer, U., Tripet, J.P., 2003. Observation of isotopes in the water cycle - the Swiss National Network (NISOT). Environ Geol 45, 1-11.

Schwarcz, H.P., Harmon, R.S., Thompson, P., Ford, D.C., 1976. Stable Isotope Studies of Fluid Inclusions in Speleothems and Their Paleoclimatic Significance. Geochim Cosmochim Ac 40, 657-665.

Shakun, J.D., Burns, S.J., Fleitmann, D., Kramers, J., Matter, A., Al-Subary, A., 2007. A high-resolution, absolute-dated deglacial speleothem record of Indian Ocean climate from Socotra Island, Yemen. Earth Planet Sc Lett 259, 442-456.

Shen, C.C., Lin, K., Duan, W.H., Jiang, X.Y., Partin, J.W., Edwards, R.L., Cheng, H., Tan, M., 2013. Testing the annual nature of speleothem banding. Sci Rep-Uk 3.

Singh, R., Kishtawal, C.M., Joshi, P.C., 2005. Estimation of monthly mean air-sea temperature difference from satellite observations using genetic algorithm. Geophys Res Lett 32.

Sodemann, H., Zubler, E., 2010. Seasonal and inter-annual variability of the moisture sources for Alpine precipitation during 1995-2002. Int J Climatol 30, 947-961.

Steen-Larsen, H.C., Masson-Delmotte, V., Hirabayashi, M., Winkler, R., Satow, K., Prie, F., Bayou, N., Brun, E., Cuffey, K.M., Dahl-Jensen, D., Dumont, M., Guillevic, M., Kipfstuhl, S., Landais, A., Popp, T., Risi, C., Steffen, K., Stenni, B., Sveinbjornsdottir, A.E., 2014. What controls the isotopic composition of Greenland surface snow? Clim Past 10, 377-392.

Steig, E.J., Gkinis, V., Schauer, A.J., Schoenemann, S.W., Samek, K., Hoffnagle, J., Dennis, K.J., Tan, S.M., 2014. Calibrated high-precision O-17-excess measurements using cavity ring-down spectroscopy with laser-current-tuned cavity resonance. Atmos Meas Tech 7, 2421-2435.

Teranes, J.L., McKenzie, J.A., 2001. Lacustrine oxygen isotope record of 20(th)-century climate change in central Europe: evaluation of climatic controls on oxygen isotopes in precipitation. J Paleolimnol 26, 131-146.

Tremaine, D.M., Froelich, P.N., Wang, Y., 2011. Speleothem calcite farmed in situ: Modern calibration of delta O-18 and delta C-13 paleoclimate proxies in a continuously-monitored natural cave system. Geochim Cosmochim Ac 75, 4929-4950.

Uemura, R., Barkan, E., Abe, O., Luz, B., 2010. Triple isotope composition of oxygen in atmospheric water vapor. Geophys Res Lett 37.

Uemura, R., Matsui, Y., Yoshimura, K., Motoyama, H., Yoshida, N., 2008. Evidence of deuterium excess in water vapor as an indicator of ocean surface conditions. J Geophys Res-Atmos 113.

Vaks, A., Gutareva, O.S., Breitenbach, S.F.M., Avirmed, E., Mason, A.J., Thomas, A.L., Osinzev, A.V., Kononov, A.M., Henderson, G.M., 2013. Speleothems Reveal 500,000-Year History of Siberian Permafrost. Science 340, 183-186.

van Breukelen, M.R., Vonhof, H.B., Hellstrom, J.C., Wester, W.C.G., Kroon, D., 2008. Fossil dripwater in stalagmites reveals Holocene temperature and rainfall variation in Amazonia. Earth Planet Sc Lett 275, 54-60.

Van Rampelbergh, M., Verheyden, S., Allan, M., Quinif, Y., Keppens, E., Claeys, P., 2014. Monitoring of a fast-growing speleothem site from the Han-sur-Lesse cave, Belgium, indicates equilibrium deposition of the seasonal delta O-18 and delta C-13 signals in the calcite. Clim Past 10, 1871-1885.

Vogel, N., Brennwald, M.S., Fleitmann, D., Wieler, R., Maden, C., Susli, A., Kipfer, R., 2013. A combined vacuum crushing and sieving (CVCS) system designed to determine noble gas paleotemperatures from stalagmite samples. Geochem Geophy Geosy 14, 2432-2444.

Williams, P.W., 2008. The role of the epikarst in karst and cave hydrogeology: a review. Int J Speleol 37, 1-10.

Winkler, R., Landais, A., Sodemann, H., Dumbgen, L., Prie, F., Masson-Delmotte, V., Stenni, B., Jouzel, J., 2012. Deglaciation records of O-17-excess in East Antarctica: reliable reconstruction of oceanic normalized relative humidity from coastal sites. Clim Past 8, 1-16.

Table 1: List of collected stalagmites in Milandre cave and related monitored parameters. The isotope parameters are for drip water.

Name	**Stalagmite**	**Active**	**Collection**	**Location**	**Monitored parameters at location**
M2	yes	yes	2007	Gal. des Fistuleuses	Cave T
M4	yes	yes	2007	Show cave	Cave T, δD, $\delta^{18}O$, $\delta^{17}O$
M6	yes	yes	2011	Gal. des Fistuleuses	Cave T, drip discharge, δD, $\delta^{18}O$, $\delta^{17}O$
M8	yes	no	2011	Gal. des Fistuleuses (next to M6)	Cave T
M9	yes	yes	2014	Gal. des Fistuleuses (5 m from M6)	Cave T, δD, $\delta^{18}O$, $\delta^{17}O$
Fi-2	no	yes	growing	Gal. des Fistuleuses (1 m from M6)	Cave T, δD, $\delta^{18}O$, $\delta^{17}O$

Table 2: (a) Overview of internal standard waters used in this study. Measured values with corresponding uncertainties are given for the isotopes. Secondary order parameters are calculated from these values. (b) Overview of standard deviations (SD) for measurements performed on precipitation, drip water and speleothem fluid inclusion samples for two different instruments (Picarro L1102-i and L2140-i).

	δD (‰)	**δ^{18}O (‰)**	**δ^{17}O (‰)**		**^{17}Oexcess (per meg)**	**d-excess (‰)**
(a) Standard						
Meerwasser	-1.24 ±0.5	-0.044 ±0.05		-3		1.59
ST-08	-77.46 ±0.5	-10.79 ±0.05	-5.74 ±0.05		19	8.86
Dye-III	-210.23 ±0.5	-27.21 ±0.05				7.45
Eiswasser	-274.09 ±0.5	-35.29 ±0.05	-18.77 ±0.05		-8	8.23
Bern-SLAP	-262.96 ±0.5	-55.21 ±0.05	-29.14 ±0.05		412	178.72
Dome-C	-428.26 ±0.5	-54.18 ±0.05	-28.92 ±0.05			5.18
(b) Standard deviation						
SD water	0.5	0.1	0.1		10	0.5
SD extracted water (L1102-i)	1.5	0.4				1.6
SD extracted water (L2140-i)	1.4	0.2	0.3	3	60	1.5

Table 3: Summary of water isotope measurements for precipitations, cave waters and speleothem fluid inclusions along with standard deviations between measurements (analytical error for speleothem). *Based on monthly mean values. *2 See text for discussion on 17Oexcess measurement precision.

Sample	**Time interval**	**n**	**δD (‰)**	**SD (‰)**	**δ18O (‰)**	**SD (‰)**	**δ17O (‰)**	**SD (‰)**	**D17 (per meg)**	**SD (per meg)**	**d (‰)**	**SD (‰)**
Precipitation stations												
Basel CEP*	July 12 - June 13		-70.33	26.24	-9.88	3.27					8.71	1.04
Bern CEP*	July 12 - June 13		-78.86	29.67	-11.05	3.54					9.56	2.25
Locarno CEP*	July 12 - June 13		-61.20	28.57	-9.07	3.52					11.4	2.83
Mormont	July 12 - June 13	149	-68.30	34.77	-9.68	4.32	-5.10	2.29	19	14	9.10	4.72
Mormont	July 13 - June 14	125	-60.99	31.33	-8.31	4.05	-4.39	2.15	16	17	5.51	6.28
Mormont	July 12 - June 14	274	-64.97	33.38	-9.05	4.25	-4.78	2.25	18	15	7.47	5.76
Mor. weighted	July 12 - June 13	id.	-73.91	id.	-10.43	id.	-5.50	id.	19	id.	9.52	id.
Mor. weighted	July 13 - June 14	id.	-67.13	id.	-9.17	id.	-4.83	id.	17	id.	6.16	id.
Mor. weighted	July 12 - June 14	id.	-71.03	id.	-9.89	id.	-5.22	id.	18	id.	8.10	id.
« Downstream » drip waters												
M6	June 12 - June 14	7	-60.33	1.62	-8.73	0.13	-4.60	0.07	18	9	9.52	0.69
Fi-2	June 12 - June 14	7	-61.69	2.31	-8.83	0.25	-4.65	0.13	19	12	8.93	0.96
M9	Oct. 13 - June 14	3	-58.77	1.65	-8.37	0.44	-4.42	0.23	14	5	8.21	1.90
M4	June 13 - Jan.14	2	-62.11	1.02	-9.00	0.11	-4.74	0.05	24	7	9.85	0.15
M2	Jan. 13 - Jan. 14	1	-58.49		-8.62		-4.56		-1		10.45	
« Upstream» cave waters												
EN	Sept. 12 - April 14	8	-63.29	1.97	-9.04	0.23	-4.78	0.11	8	11	9.06	0.70
GO	Sept. 12 - April 14	8	-61.77	1.25	-8.94	0.12	-4.72	0.06	12	10	9.76	0.68
ST	Sept. 12 - April 14	8	-62.22	2.20	-8.92	0.25	-4.72	0.12	5	14	9.17	0.60
VI	Sept. 12 - April 14	8	-59.06	0.98	-8.43	0.23	-4.45	0.12	8	9	8.40	2.53
Speleothem fluid inclusions												
M6 top 4	0-40 years	1	-60.1	1.5	-8.9	0.4	-4.8	0.3	36	360*2	11.1	1.5
M6 top 5	0-40 years	1	-60.3	1.5	-8.3	0.4	-4.7	0.3	-15	360*2	6.1	1.5
M8-4	Early Holocene	1	-63.0	1.5	-9.4	0.4					12.2	1.6
M8-4bis	Early Holocene	1	-61.6	1.5	-9.8	0.4	-5.2	0.3	127	360	16.8	1.5
M8-5	Early Holocene	1	-62.3	1.5	-7.5	0.4					2.3	1.6
M8-5bis	Early Holocene	1	-63.1	1.5	-8.0	0.4	-4.4	0.3	23	360	0.9	1.5
M8-6	Early Holocene	1	-65.7	1.5	-7.7	0.4					4.1	1.6
M8-6bis	Early Holocene	1	-65.6	1.5	-10.3	0.4	-5.6	0.3	39	360	16.8	1.5

Table 4. Water isotope comparison between precipitations, drip water and speleothem fluid inclusions at M6 drip site. Refer to Table 3 for reproducibility. For recent speleothem samples standard deviations between replicates are 0.5‰, 1.4‰ and 0.1‰ for respectively δD, $\delta^{18}O$ and $\delta^{17}O$. * Measured with Picarro L2140-i.

Water type	**Time period**	**n**	**δD** **(‰)**	**$\delta^{18}O$** **(‰)**	**$\delta^{17}O$** **(‰)**	**D17** **(per meg)**	**d** **(‰)**
Precipitation station							
Mormont weighted	July 12 - June 14	274	-71.0	-9.9	-5.2	18	8.1
Cave drip waters							
M6	June 12 - June 14	7	-60.3	-8.7	-4.6	18	9.5
Fi-2	June 12 - June 14	7	-61.7	-8.8	-4.7	19	8.9
Speleothems							
Fluid inclusions	0-40 years	4/2*	-61.3	-8.3	-4.7*	10*	8.6
Fluid inclusions	Early Holocene	6/3*	-63.6	-8.8	-5.0*		
Speleothem calcite	0-40 years	1		-6.5			
Speleothem calcite	Early Holocene	3		-6.6			

FIGURE CAPTIONS

Figure 1: (a) Milandre cave location (46 km eastward of Basel) with MeteoSwiss stations Le Mormont and Fahy (stars). Isotope network stations (Basel, Bern and Locarno) run by the Climate and Environmental Physics at the University of Bern are displayed in the upper right figure. (b) Annual climatology at MeteoSwiss station Fahy. Mean values for each month (period 1981-2013) are given for precipitation, temperature, relative humidity and water balance (rain – evapotranspiration). In July, evapotranspiration is larger than the amount of precipitation.

Figure 2: Topographic map of the downstream part of Milandre cave with locations of collected stalagmites (M1 to M9) as well as drip sites (M2, M4, M6, M9 and Fi-2). The cave continues on 3.7 km to reach the artificial Maira pit (modified from (Gigon and Wenger, 1986). The Galerie des Fistuleuses corresponds to a 400 metres long oval-shaped tube with an average height of three metres interrupted by two crawling sections. It is part of an upper level of fossil galleries located approximately 30 metres above the active Milandrine River. To access the upstream part of the cave a 20 metres high pit called Puits du Maira ("Maira pit", Fig. 1) was excavated and inaugurated in 1974. This new excavation allows speleologists to go across the cave. The pictures show the cave chamber with (a) M8 and M6 stalagmites before being removed. (b) General view with M6 and Fi-2 drip sites after removal of stalagmites. (c) Drip logger and water collection system for M6 dripping site.

Figure 3: Spatial correlation maps for MeteoSwiss Fahy station (star, plots a and b) and CEP Basel (star, plots c and d). Different coefficient correlation r ranges are given for temperature (0 to 1) and precipitation (-1 to 1) maps. (a) Correlation of temperature in Fahy MeteoSwiss station versus European temperatures for the period 1990 – 2011. (b) Idem for precipitation amount against European precipitation amount. (c and d) Correlation between δ^{18}Op in Basel CEP station with (c) European temperatures and (d) amount of precipitation for the period 1982 – 2010. The blue dot represents the approximate location of M6 buoy.

Figure 4: Daily and monthly precipitation at Mormont MeteoSwiss station between January 2012 and July 2014 and response of the cave system at M6 drip site. Winter seasons (DJF) are highlighted in grey.

Figure 5: Cave air temperature is included between mean air temperature and soil temperature when compared to Fahy station (~200 metres higher than the monitored cave chamber). Small variations in cave air temperature are probably due to the opening of the doors to ventilate the cave for CO_2 dissipation. Winter seasons (DJF) are highlighted in grey.

Figure 6: Water stable isotope measurements and corresponding monthly means (black lines, 31 days running average for the relative humidity and temperature) in precipitation from Mormont station together with temperature and relative humidity from Fahy station. Winter seasons (DJF) are highlighted in grey.

Figure 7: Relationship between daily δ^{18}O and temperature for Mormont MeteoSwiss station. Daily precipitation values (blue dots) show a lower correlation than monthly mean values (black squares).

Figure 8: (Left panel) Local meteoric water line from δD and δ^{18}O in precipitation for Mormont station. Winter (DJF) and Summer (JJA) meteoric water line and associated regression based on two seasons. (Right panel) Zoom that summarises mean isotope values from this study plotted together with the local meteoric water line and the dashed global meteoric water line.

Figure 9: Local meteoric water line from δ^{17}O and δ^{18}O in precipitation (black dots) for Mormont station and for drip waters (red dots).

Figure 10: Relationship between δ^{18}O in precipitation and in M6 drip site. Winter seasons (DJF) are highlighted in grey.

FIGURE 1

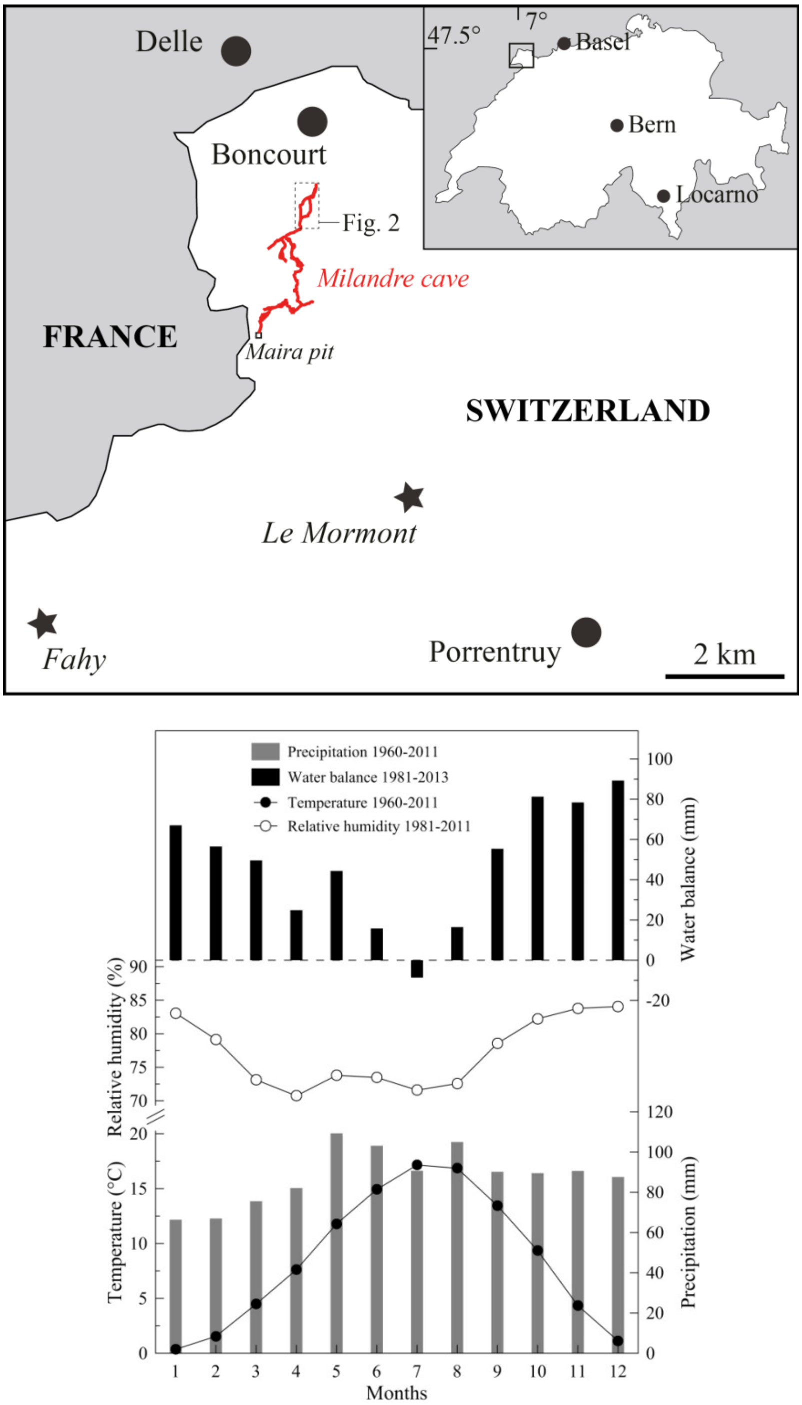
Delle
Boncourt
Fig. 2
Milandre cave
Maira pit
FRANCE
SWITZERLAND
Le Mormont
Fahy
Porrentruy
2 km
47.5°
7°
Basel
Bern
Locarno
Precipitation 1960-2011
Water balance 1981-2013
Temperature 1960-2011
Relative humidity 1981-2011
Water balance (mm)
100
80
60
40
20
0
-20
Relative humidity (%)
90
85
80
75
70
Temperature (°C)
20
15
10
5
0
Precipitation (mm)
120
100
80
60
40
20
0
1
2
3
4
5
6
7
8
9
10
11
12
Months

FIGURE 2

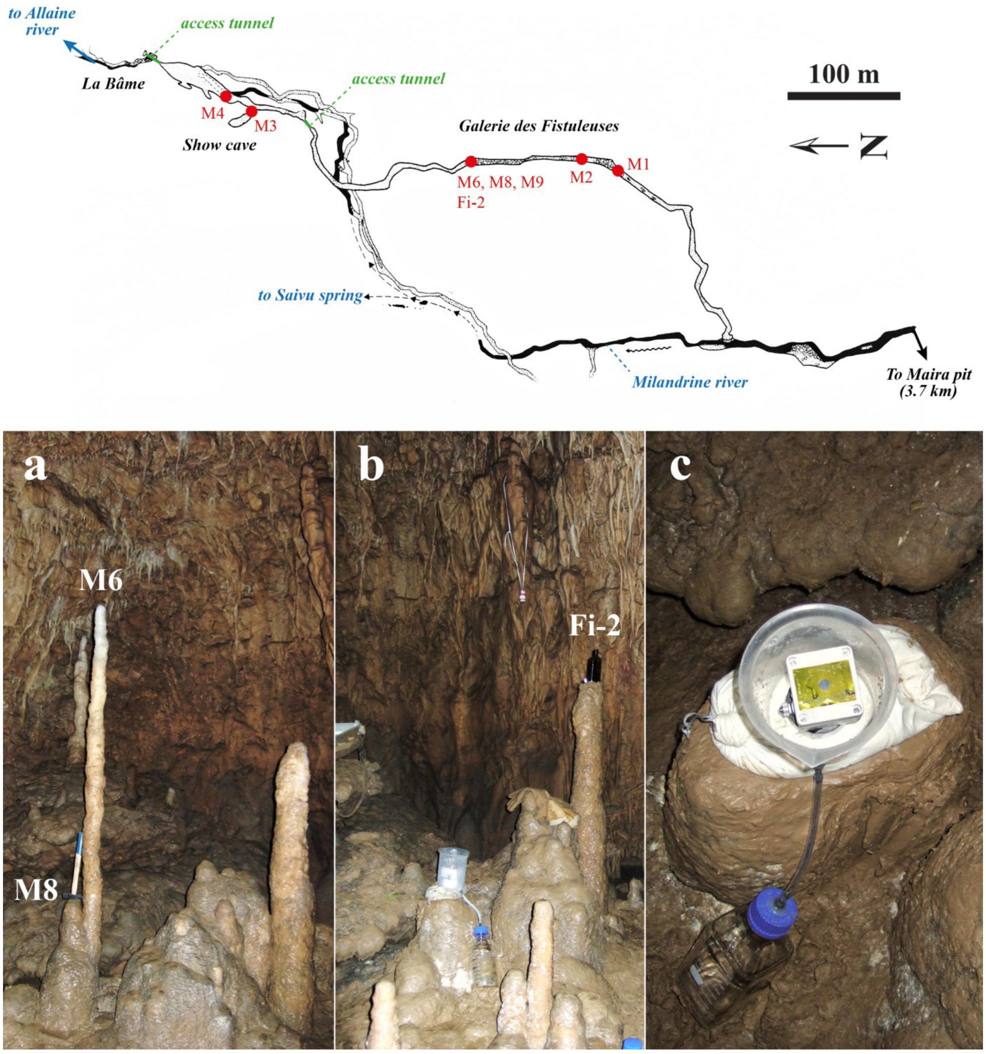
to Allaine river
access tunnel
La Bâme
access tunnel
100 m
M4
M3
Show cave
Galerie des Fistuleuses
N
M6, M8, M9
Fi-2
M2
M1
to Saivu spring
Milandrine river
To Maira pit (3.7 km)
a
M6
M8
b
Fi-2
c

FIGURE 3

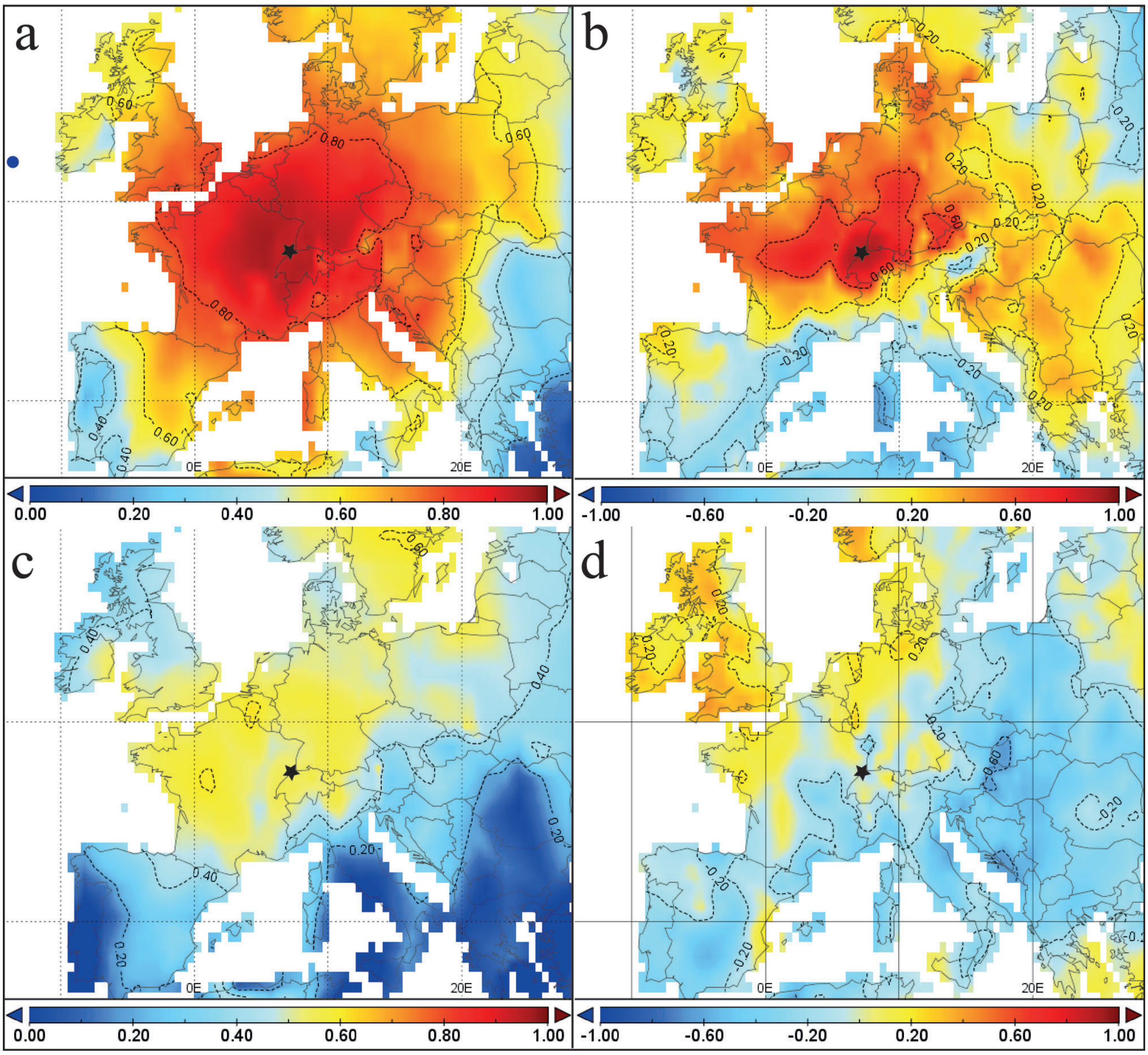
a
b
c
d
0.80
0.60
0.40
0.20
-0.20
0E
20E
0.00
0.20
0.40
0.60
0.80
1.00
-1.00
-0.60
-0.20
0.20
0.60
1.00

FIGURE 4

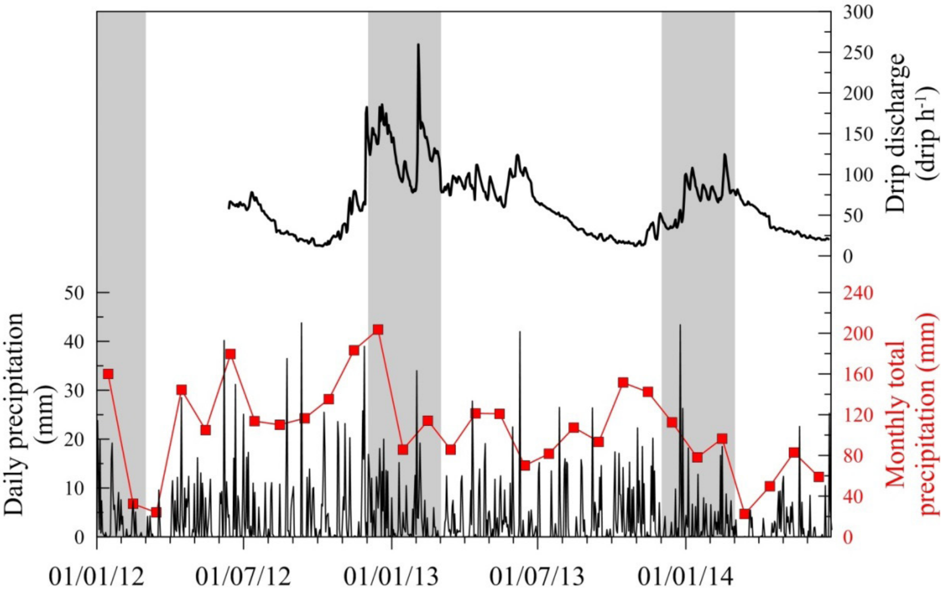

FIGURE 5

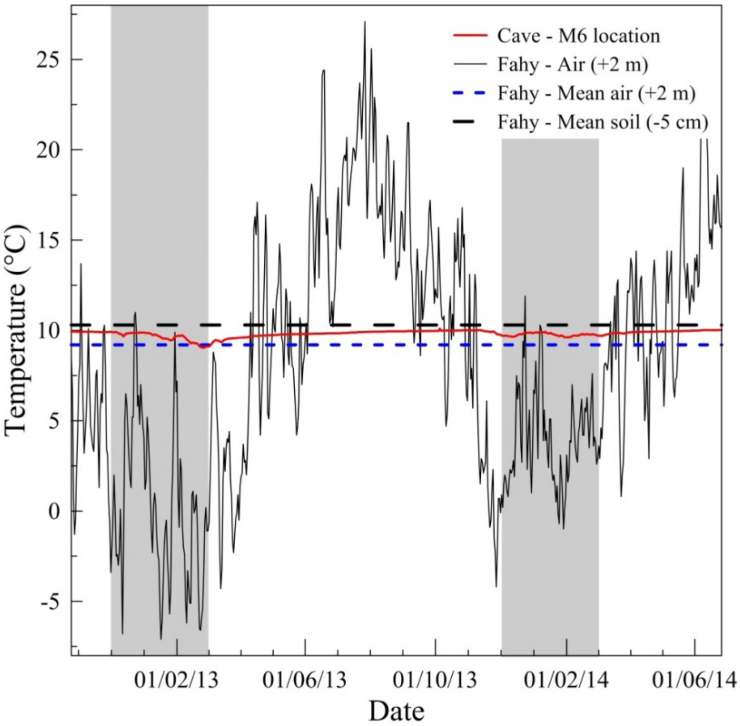

FIGURE 6

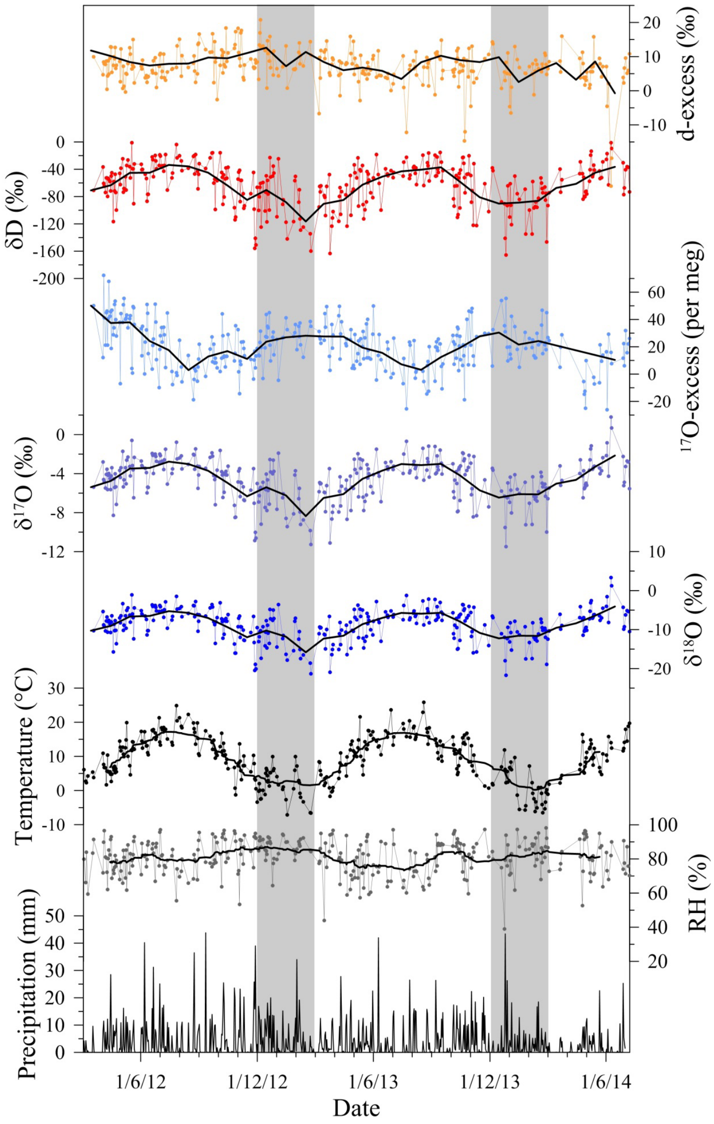

FIGURE 7

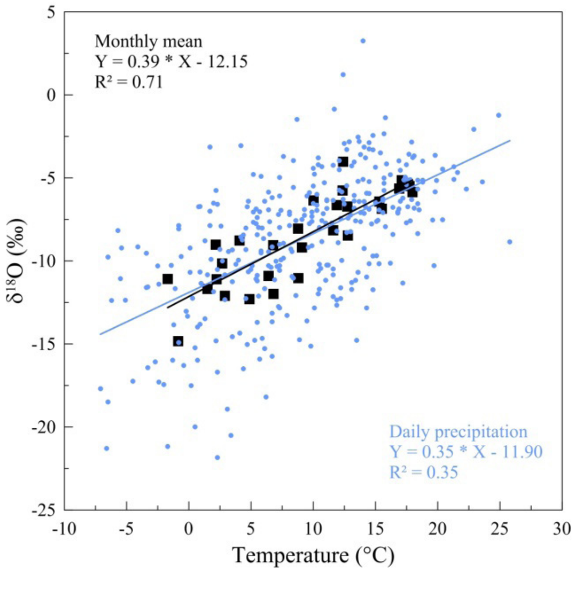

FIGURE 8

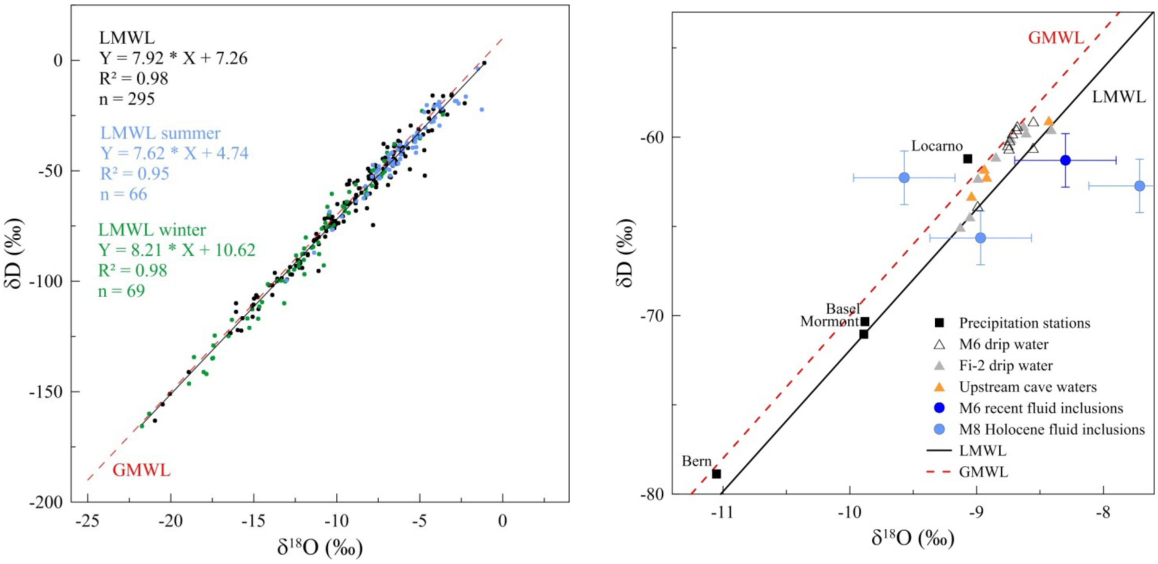

FIGURE 9

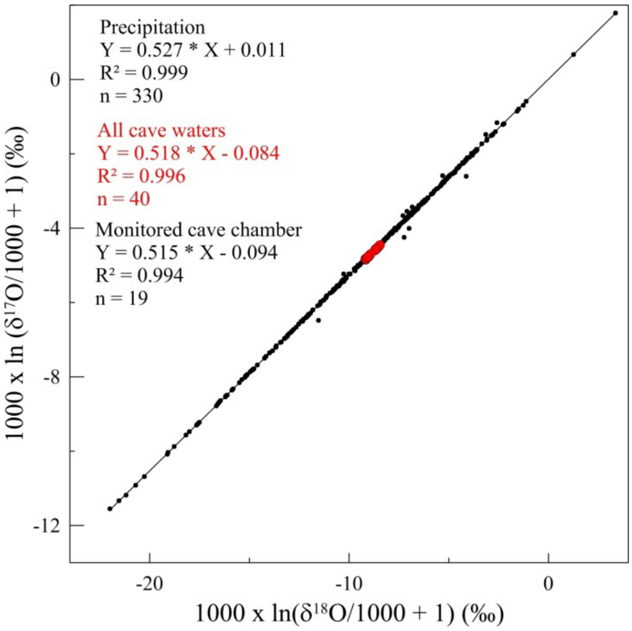

FIGURE 10

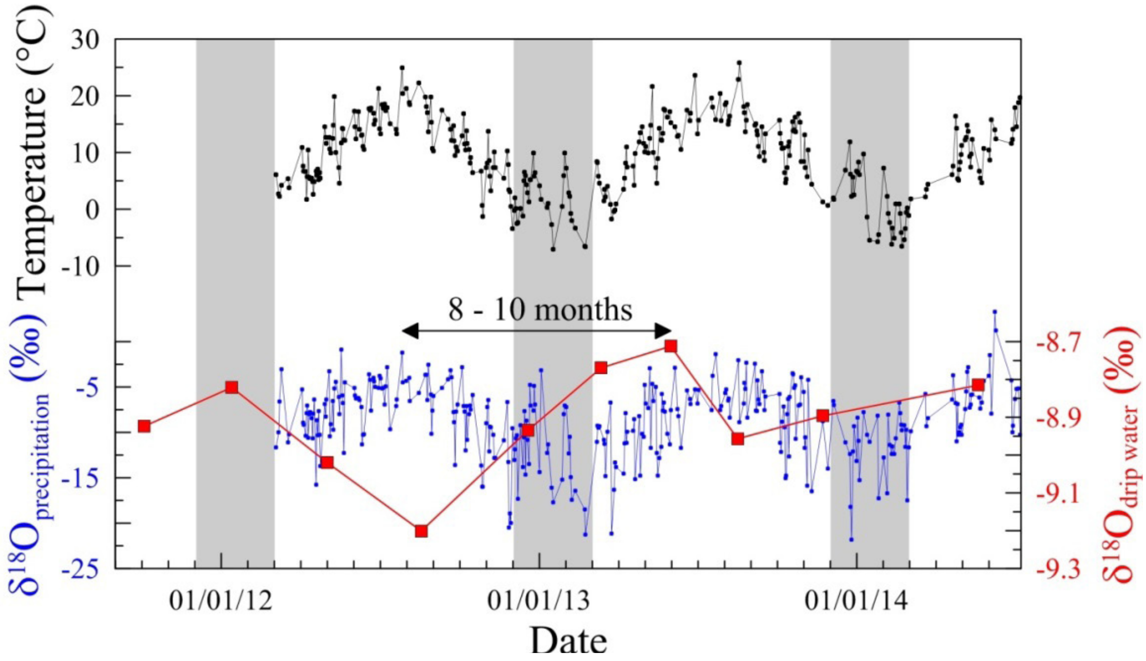
Temperature (°C)
30
20
10
0
-10
8 - 10 months
$\delta^{18}O_{precipitation}$ (‰)
-5
-15
-25
$\delta^{18}O_{drip\ water}$ (‰)
-8.7
-8.9
-9.1
-9.3
01/01/12
01/01/13
01/01/14
Date

Central European temperature variations over the past two millennia based on a stalagmite oxygen isotope record from the Swiss Jura Mountains

A. Hasenfratz[a, b, *1*], D. Fleitmann[a, b, □], A. Häuselmann[a, b], F. Lehner[b, c], H. Cheng[d, e], R. L. Edwards[d], M. Leuenberger[b, c], C. C. Raible[b, c], S.F.M. Breitenbach[f], J. Luterbacher[g]

[a] Institute of Geological Sciences, University of Bern, Baltzerstrasse 1-3, Bern 3012, Switzerland
[b] Oeschger Centre for Climate Change Research, University of Bern, Zähringerstrasse 25, Bern 3012, Switzerland
[c] Climate and Environmental Physics, Institute of Physics, University of Bern, Sidlerstrasse 5, Bern 3012, Switzerland
[d] Department of Geology and Geophysics, University of Minnesota, Minnesota 55455, USA
[e] Institute of Global Environmental Change, Xi'an Jiaotong University, Xi'an 710049, China
[f] Geological Institute, Department of Earth Sciences, ETH Zürich, Sonneggstrasse 5, Zürich 8092, Switzerland
[g] Justus-Liebig University of Giessen, Department of Geography, Senckenbergstr. 1, Giessen 35390, Germany

Keywords: Switzerland, Milandre Cave, temperature reconstruction, Holocene, stalagmite/speleothem, oxygen isotopes ($\delta^{18}O$)

Abstract

Central European temperature reconstructions covering the last two millennia are almost entirely based on tree rings and lake sediments. As a result, these temperature reconstructions are seasonally biased and reflect summer rather than mean annual air or cold season temperatures. To fill this gap of knowledge, we reconstructed a highly resolved 2000 year-long speleothem-based oxygen isotope ($\delta^{18}O$) record from Milandre Cave in the Swiss Jura Mountains. Climate in this region is strongly influenced by westerly air masses, making Milandre Cave an ideal site to record climate variability in the North Atlantic and European realm. $\delta^{18}O$ variations observed in the stalagmite are attributed to fluctuations in cold season temperature as the aquifer is recharged predominantly between autumn and spring. Calibration using historical temperature unveils temperature variations of nearly 2°C within the past two millennia, with a temperature difference between the warmest decade of the Medieval Climate Anomaly (950–1250 AD) and the coldest decade of the Little Ice Age (1400–1700 AD) amounting to ~1.8°C. Modeled cold season temperatures for the past millennium compare remarkably well with our reconstruction, and confirm the importance of both, solar forcing and internal variability, in driving Central European climate.

1. Introduction

Quantitative climate reconstructions covering the last two millennia are in increasingly high demand to assess the sensitivity of the climate system to anthropogenic and natural forcing and to establish firm links between climatic and societial changes (PAGES, 2009). The '2k-Network' of the IGBP Past Global Changes (PAGES) is aimed at integrating new and existing paleoclimate data, with the goal of generating a global array of regional syntheses of climate variability for the last 2000 years. The rather stable boundary conditions of the climate system during this period (Jones and Mann, 2004; Wanner et al., 2008) allow to study the causes and nature of annual to multi-decadal natural climate variability. It is therefore not surprising that numerous temperature reconstructions covering the last one or two millennia were developed (PAGES 2k Consortium, 2013, and references therein). Yet, most of these reconstructions are based on tree rings and lake sediments and thus biased towards warm season rather than cold season or annual temperatures (e.g., Büntgen et al., 2011; Larocque-Tobler et al., 2012). Thus, paleoclimate records providing information on cold season or mean annual air temperatures are now in high demand by the paleoclimate community.

Central European speleothems are paleoclimate archives with the potential to supply well-dated, highly resolved, and continuous paleoclimate records, which allow reconstructing temperature during the cold season (Mangini et al., 2005; Fohlmeister et al., 2012). Reduced effective infiltration into the karstic aquifer during summer (e.g., Perrin and Kopp, 2005; Wackerbarth et al., 2010) increases the proportion of autumn, winter and spring (AWS hereinafter) precipitation participating in the deposition of speleothem calcite and results in a cold season bias of its oxygen isotopic composition ($\delta^{18}O$). Here, we present a biannually resolved AWS temperature reconstruction spanning two millennia that is derived from a stalagmite collected in Milandre Cave, Swiss Jura Mountains, in western Central Europe. Stalagmite $\delta^{18}O$ values are calibrated against regional historical temperature reconstructions to develop a transfer function to calculate absolute AWS temperatures. This record is then compared to various regional to hemispheric climate reconstructions to enhance our understanding of the climate

---

[*] Corresponding author. Present address: Institute of Geology, ETH Zürich, Sonneggstrasse 5, Zürich 8092, Switzerland. Tel.: +41 44 632 69 75.
E-mail address: adam.hasenfratz@erdw.ethz.ch (A. Hasenfratz)

variability in Central Europe and the North Atlantic-European realm. The Milandre Cave temperature time series is compared to an ensemble of model simulations covering the past millennium to examine the influence of external forcing and internal variability on mid-European AWS temperatures.

2. Milandre Cave: climate and environmental setting

Milandre Cave (47.47°N, 7.02°E, ~500 m asl) is located in the Swiss Jura Mountains (Fig. 1), a region with a semi-continental climate. The prevailing westerly winds transport maritime air to the area and account for year-round precipitation, leading to precipitation of up to 1054 mm yr^{-1}. Accordingly, the moisture in the region is dominated by North Atlantic sources, with occasional contributions from land-recycled moisture during summer (Sodemann and Zubler, 2010). Monthly precipitation averages range from 110 mm in May to 74 mm in January. Mean annual temperature is around 9°C, with mean winter and summer temperatures of 1.1°C and 16.4°C, respectively (meteorological data encompass the period 1960–2011 AD, and are from the nearby weather station Fahy belonging to the Swiss national weather service MeteoSwiss).

The Milandre Cave system encompasses more than 10 km and is part of a karstic aquifer that lies within layers of chalky Rauracian limestone. These are directly underlain by marls that act as an aquiclude (Kovàcs and Jeannin, 2003). Bedrock thickness above the active part of the karst system varies between 30 and 80 m. There are three known entrances to the cave system, an artificial one at the upstream part of the cave system and two entrances at the downstream part. The latter two are both natural, but were enlarged by speleologists to access the deeper part of Milandre Cave (Gigon and Wenger, 1986). Land use involves pasture, forestry, arable land and some small settlements (Jeannin, 1996; Perrin et al., 2003a). Thickness of prevailing silty loam soils does not exceed a few meters, and infiltration to the aquifer is mainly diffuse through the soil zone (Perrin et al., 2007). The aquifer is drained by a well-developed karstic network consisting of the Milandrine underground river and its tributaries, with a catchment area of ~13 km^2 (Jeannin, 1996).

Stalagmite M6 was collected in the fossil gallery *'Galerie des Fistuleuses'* (see Fig. 1), situated in a remote part of Milandre Cave, approximately 30 m above the active part and 200 m south of the northern entrance. This part of the cave can be accessed by a 15 m long tunnel, which was mined in 1967 AD. Cave air temperature is 9.9°C and constant throughout the year (±0.1 °C; monitored in 2012 and 2013), which is close to mean annual air temperature in this region.

Over the last two decades, investigations of the study site provided deep insights into the functioning of the Milandre karst system (e.g., Jeannin, 1996; Perrin, 2003; Perrin et al., 2007; Savoy, 2007), which is essential to reliably interpret proxy records of speleothems.

3. Materials and methods

3.1 . Speleothem description

The candlestick-shaped stalagmite M6 is 182 cm tall and decreases continuously in diameter from about 20 cm at the base to about 5 cm at the top (Fig. 2). M6 developed on the top of a large base stalagmite in an area where it remained unaffected by occasional floodings. The stalagmite was active when collected in autumn 2011, and consists of whitish calcite with no visible organic inclusions and no signs of discontinuities. M6 was fed by a 22 cm soda straw, and the recent fall height amounted to ~1 m. Drip rates at the sampling location vary seasonally between 20 and 200 drips per minute (approx. 0.8 and 8 ml min^{-1}) in summer and winter, respectively (monitored between June 2012 and January 2013). For this study, only the top 52 cm of M6 were analyzed.

A large part of the stalagmite shows couplets of white and porous, and thinner translucent and dense laminae. While the white laminae often show distinct thinning towards the flanks, the translucent laminae exhibit a rather constant thickness. The thickness of the lamina couplets generally decreases with depth, for which reason couplets are increasingly harder to identify in the older portion of the stalagmite.

3.2. Dating and stable isotope analysis

The chronology of stalagmite M6 is based on Uranium-series ages (^{230}Th hereinafter) and annual lamina counting. ^{230}Th dating was performed on a multi-collector inductively coupled plasma mass spectrometer (Thermo-Finnigan Neptune) at the Minnesota Isotope Laboratory, University of Minnesota, USA. For the measurements, calcite samples of ~200 mg were collected with a standard dentist drill along the central growth axis. Detailed information on analytical procedures is provided in Fleitmann et al. (2009).

Continuous lamina counting was only possible for the upper 20.5 cm. Counting was conducted on high-resolution scans (4800 dpi) along the central growth axis of the stalagmite.

Stable isotope sampling was conducted along the growth axis using an electronically controlled micromill, at 0.1 mm increments on the top 4.4 cm, and at 0.5 mm increments from 4.5 to 50 cm depth of the stalagmite (150 µg sample weight).

The higher resolved section of the time series was downsampled to 0.5 mm resolution using the linear integration interpolation function in the AnalySeries software (Paillard et al., 1996). Measurements were performed on a Finnigan Delta V Advantage mass spectrometer equipped with an automated carbonate preparation system (Gas Bench II) at the Institute of Geological Sciences, University of Bern, Switzerland. External precision of $\delta^{18}O$ analyses, upon which the focus is held in this study, is 0.08‰ (1σ error). All $\delta^{18}O$ are reported in permil (‰) relative to the international Vienna Pee Dee Belemnite (VPDB) carbonate standard, unless stated otherwise. Further details on the methodology are provided in Fleitmann et al. (2009).

4. Results

The ^{230}Th-dating results for the uppermost 52 cm of stalagmite M6 are provided in Table 1. All ^{230}Th ages are in stratigraphic order, with the deepest sample providing an age of 2077±95 yr BP. The uppermost date at 1.2 cm from the stalagmite top has an age of 41±97 yr BP and thus provides further evidence that M6 was actively growing when collected. Unfortunately, very low concentrations of Uranium (~0.05 ppm) and presence of detrital Th result in rather high chronological uncertainties.

The chronology of M6 was improved by counting annual couplets in the upper part, where the ^{230}Th ages were disregarded, and by using the COPRA algorithm (Breitenbach et al., 2012) in the bottom part to establish proxy confidence limits. The resulting median of the 1000 Monte Carlo simulations and its 95% confidence interval represent a robust age model for the bottom part (Fig. 3). As it was not trivial to distinguish between annual and subannual laminae, a conservative uncertainty of 10% of the absolute age was assigned to the lamina chronology. The lamina counts follow the radiometric age model very well and confirm that the couplets are annual in origin. Moreover, they reduce the age uncertainties significantly. In general, growth rates are very high within the top 52 cm and range from 0.14 to 0.50 mm per year.

The oxygen isotope profile (0–50 cm, 1345 values) extends back to 11 BC and its resolution varies between subannual and 4 years (Fig. 6B). $\delta^{18}O$ values vary between -5.36 and -8.37‰ around a mean of -6.76‰. Superimposed on the long-term trends distinct short-term variations of 1 to 2‰ are observed.

5. Discussion

5.1. Paleoclimatic significance of stalagmite $\delta^{18}O$ values

Detailed understanding of the modern water-carbonate system in Milandre Cave is essential to reduce uncertainties associated with the interpretation of stalagmite $\delta^{18}O$ values. This implies that changes in $\delta^{18}O$ of water along the pathway from precipitation to speleothem calcite must be traced. The following paragraphs provide information on aquifer recharge conditions above Milandre Cave and the principal factors influencing $\delta^{18}O$ values in precipitation, cave drip water and stalagmite calcite.

5.1.1. Modern climate-precipitation $\delta^{18}O$ relationship in Switzerland

To determine the climatic factors governing $\delta^{18}O$ of precipitation ($\delta^{18}O_p$), we examined the $\delta^{18}O_p$ time series from Bern (70 km southwest of Milandre Cave), one of the longest in Central Europe (Schürch et al., 2003). Monthly $\delta^{18}O_p$ values in Bern (1971–2010 AD) are positively correlated with local temperature ($r=0.41$; $p<0.05$; both time series were deseasonalized), with maximum and minimum $\delta^{18}O_p$ values measured in summer and winter, respectively (Fig. 4). A weekly resolved $\delta^{18}O_p$ time series above Milandre Cave, measured from September 1999 to January 2002 (Perrin et al., 2003a), is in good agreement with the $\delta^{18}O_p$ record from Bern, indicating that the latter record is a valid approximation for variations in $\delta^{18}O_p$ above the cave.

The increase of precipitation-weighted $\delta^{18}O_p$ with mean annual temperature (MAT), the so-called 'temperature effect' (Dansgaard, 1964), amounts to 0.52‰ per 1°C in Bern, which is in good agreement with observed T-$\delta^{18}O_p$ relationships in the Greater Alpine Region (0.48–0.65‰ per 1°C; Rozanski et al., 1993; Schotterer et al., 2000; 2010) and Europe (0.59±0.09‰ per 1°C; McDermott et al., 1999). Important for this study, precipitation-weighted $\delta^{18}O_p$ in Bern and MAT averaged over the northwestern Alps (Auer et al., 2007) are significantly correlated ($r=0.48$; $p<0.05$).

An additional comparison between $\delta^{18}O_p$ values at Bern and gridded temperature data between 1971 and 2009 AD (CRU TS 3.10; Mitchell and Jones, 2005) reveals highest correlations in regions situated to the west of Switzerland (Fig. 4C), underlining the important role of the westerlies in transporting moisture to Central Europe. This assumption is also supported by isobaric back trajectories, which reveal that the vast majority of the moist air masses associated with heavy precipitation events in western Switzerland (Valais) originate from the North Atlantic (Horton et al., 2012).

Overall, air temperature seems to be the primary parameter influencing $\delta^{18}O_p$ above Milandre Cave (Siegenthaler and Oeschger, 1980; Schotterer et al., 2000; Schürch et al., 2003; Schotterer et al., 2010).

5.1.2. Groundwater recharge above Milandre Cave

The timing and amount of recharge to the karst aquifer above Milandre Cave is an important control on drip water $\delta^{18}O$ ($\delta^{18}O_{dw}$) values. Daily effective infiltration amounts from 1981 to 2011 AD were calculated based on the approach by Jeannin and Grasso (1995a). As surface runoff is negligible above Milandre Cave (Perrin and Kopp, 2005), effective infiltration I_{eff} can be expressed as where P refers to the amount of precipitation (mm), AET to actual evapotranspiration (mm), and ΔV_{soil} (mm) to variations in soil moisture. For the calculations of I_{eff}, daily precipitation data from the nearby (5 km) MeteoSwiss station Fahy were exploited. In order to calculate AET, potential evapotranspiration (PET) and precipitation are needed, whereas AET is subsequently required to estimate ΔV_{soil}. Although direct measurements of PET were performed at Fahy, they are only of limited use for this study as they were conducted solely for the growing season between 1988 and 1999 AD. However, MeteoSwiss additionally provides estimates of PET for Fahy by applying an empirical approach developed for grassland in Switzerland (Primault, 1962). Because of the high correlation between measured and estimated values ($r=0.91$, $n=72$, $p<0.05$) for PET, MeteoSwiss PET estimates for Fahy are well suited to calculate AET above Milandre Cave.

AET is limited either by the energy available, which is expressed as PET, or by the availability of water (the sum of the daily precipitation amount and the soil water content), for which case AET is lower than PET. Hence, daily values of AET are obtained by taking the minimum value of the two. Importantly, the maximum soil water storage capacity has a large influence on AET and consequently on effective infiltration. When, for instance, the soil stock is incomplete, net precipitation (adjusted for evapotranspiration) first fills the soil before the aquifer is recharged. As defined by Jeannin and Grasso (1995a), a field capacity of 140 mm, a value typical for silty loam, was used. In addition, the daily uptake capacity of the soil was limited to 10 mm of water (Jeannin and Grasso, 1995a), i.e., precipitation exceeding this threshold is directly infiltrated and percolated through the soil zone, independent of the actual soil humidity.

Calculated effective infiltration between 1981 and 2011 AD above Milandre Cave (Fig. 5) indicates that effective infiltration peaks in winter when AET is lowest and soils are saturated. As one would expect, high evapotranspiration in summer leads to soil moisture deficiency and recharge of the karst aquifer is generally low. Hence, a much smaller fraction of the summer precipitation (34%) is effectively infiltrated in comparison to winter precipitation (89%). Overall, 83% of total annual recharge occurrs in autumn, winter and spring (AWS). These results compare well with earlier attempts to estimate effective infiltration above Milandre Cave (Jeannin and Grasso, 1995a; Perrin and Kopp, 2005)

To test the accuracy of our calculations, monthly means for effective infiltration above Milandre Cave and discharge of the nearby river Allaine, measured in Boncourt, are compared (data available from www.bafu.admin.ch/hydrology; February 2013). One of the major tributaries of the Allaine is the Milandrine, the underground river of the Milandre Cave system. The strong correlation ($r=0.84$, $p<0.05$) between our calculated time series of effective infiltration above Milandre Cave and discharge of the Allaine adds confidence about the accuracy of our calculations (Fig. 5) as nearly every infiltration peak matches high riverine discharge.

5.1.3. Control on drip water $\delta^{18}O$

$\delta^{18}O_{dw}$ values are controlled by $\delta^{18}O$ of precipitation above the cave site, effective infiltration and various processes in the soil and epikarst (e.g., evaporation). As outlined above, air temperature exerts the strongest influence on $\delta^{18}O_p$ values above Milandre Cave. As only around 55% of total annual rainfall infiltrate into the soil and epikarst (see paragraph 5.1.2 for further details), $\delta^{18}O_{dw}$ values do not reflect the *annual average* isotopic composition of precipitation above Milandre Cave. Although precipitation amounts are higher during summer, the annual mean $\delta^{18}O$ of the seepage in Milandre Cave is slightly more negative than the mean $\delta^{18}O_p$ highlighting the importance of effective infiltration (Perrin et al., 2003a). Moreover, the $\delta^{18}O_{dw}$ signal shows strong buffering confirming the important role of the soil and the epikarst subsystems in mixing, storage and distribution of infiltrated waters (Perrin et al., 2003a; 2003b).

These results confirm observations that the karst aquifer is generally recharged during the cold season and drained in summer (Jeannin and Grasso, 1995a; Jeannin, 1996; Perrin et al., 2003a; Perrin and Kopp, 2005). Preliminary counts of drip rates at the sampling site of stalagmite M6 provide supporting evidence for this assumption, with drip rates being lowest towards the end of the summer (based on ongoing monitoring between June 2012 and January 2013 AD).

5.1.4. Control on stalagmite calcite $\delta^{18}O$

When speleothem calcite is deposited in isotopic equilibrium with parent drip water, calcite $\delta^{18}O$ ($\delta^{18}O_{ct}$) values are primarily influenced by two variables: the $\delta^{18}O$ value of drip water and cave air temperature (McDermott, 2004; Lachniet, 2009). By using modern $\delta^{18}O_{dw}$ values in Milandre Cave, we can test whether calcite was deposited in isotopic equilibrium. Given present-day $\delta^{18}O_{dw}$ of $-8.92\pm0.09‰_{VSMOW}$ and cave air temperatures of 9.9°C, the expected $\delta^{18}O_{ct}$ of $-6.51‰_{VPDB}$, calculated by applying the fractionation equation given in Coplen (2007), is close to the observed value at the tip of stalagmite M6 ($-6.23\pm0.08‰_{VPDB}$). This indicates that modern calcite is precipitated under conditions close to isotopic equilibrium.

Furthermore, to test whether calcite was deposited in isotopic equilibrium with its parent drip water, we applied the so-called "Hendy test" (Hendy, 1971). Measurements along five growth layers revealed no clear pattern in $\delta^{18}O$ (criterion 1), although variations at layer H2 and H3 exceed 0.5‰ (Fig. 6A). While the same two show a positive correlation between $\delta^{13}C$

and $\delta^{18}O$ ($p<0.05$) along their growth layers (criterion 2) suggesting possible kinetic effects, covariation between $\delta^{13}C$ and $\delta^{18}O$ along the growth axis (criterion 3) is weak ($r=0.24$, $p<0.05$). However, any variation towards the flanks of the stalagmite could also result from imprecise sampling, as the integration of different growth layers is practically almost unavoidable (Dorale and Liu, 2009). Moreover, there is increasing evidence that the "Hendy test" may not be a valid control to assess isotopic equilibrium close to the growth axis (e.g., Spötl and Mangini, 2002), where stable isotope profiles are commonly drilled. Instead, greatest confidence can be obtained by replication of $\delta^{18}O$ time series using contemporaneously deposited speleothems from the same or a nearby cave (Dorale and Liu, 2009; Lachniet, 2009). The annually laminated stalagmite M4, covering the past 185 years (Schmassmann, 2010), was retrieved from a cave passage nearby. It reproduces well within age errors (Fig. 6B) indicating that its evolution predominantly reflects a climatic signal.

The two influencing factors, $\delta^{18}O_{dw}$ and cave air temperature through its control on equilibrium fractionation, are expected to act against each other as long-term cooling of the surface climate leads to low $\delta^{18}O_{ct}$, whereas concomitant lower cave air temperatures favor the enrichment of ^{18}O in the calcite. In general, variations in $\delta^{18}O_{dw}$ of mid-latitude cave sites in Europe tend to outweigh the fractionation effect during calcite precipitation (Lachniet, 2009; McDermott et al., 2011). Furthermore, temperature-dependent variations in $\delta^{18}O_p$ (+0.52‰ $°C^{-1}$; see section 4.1) are expected to be larger in magnitude than those associated with variations in cave air temperature (-0.22‰ $°C^{-1}$ with temperatures of around 9°C; Kim and O'Neil et al., 1997), theoretically resulting in a present-day net relationship between $\delta^{18}O_{ct}$ and MAT of about 0.3‰ $°C^{-1}$.

In summary, we argue that changes in $\delta^{18}O_{ct}$ are closely related to changes in $\delta^{18}O_{dw}$, which is strongly influenced by temperature-controlled variations in $\delta^{18}O_p$. As stalagmite M6 captures a direct temperature signal inherent in $\delta^{18}O_p$, it is very well suited to capture variations in AWS temperature over the last two millennia in Central Europe. This is in contrast to two recently published Holocene speleothem $\delta^{18}O$ records from Central Europe both exhibiting an inverse $\delta^{18}O_p$-temperature relationship. In detail, $\delta^{18}O$ variations in stalagmites from Spannagel Cave, Austrian Alps, are suggested to reflect variations in the moisture source region (North Atlantic Ocean vs. the Mediterranean Sea) and/or variations in the seasonality of precipitation (Mangini et al., 2005), whereas at Bunker Cave in Western Germany, only the latter effect is expected to be primarily responsible for $\delta^{18}O_{ct}$ variations (Fohlmeister et al., 2012). However, the relationship between temperature and seasonality of precipitation on the one hand, and temperature and atmospheric processes on the other hand, are not stable through time (e.g., Casty et al., 2005).

5.2. Temperature calibration of calcite $\delta^{18}O$ values

Similar to previous attempts to reconstruct temperature from stalagmite $\delta^{18}O_{ct}$ values (Frisia et al., 2005; Mangini et al., 2005), gridded historical temperature data (Luterbacher et al., 2004; Xoplaki et al. 2005) were used for the calibration of the M6 $\delta^{18}O_{ct}$ values (Fig. 7). To account for the observed cold season bias of effective infiltration above Milandre Cave, the M6 $\delta^{18}O_{ct}$ record is calibrated against mean AWS temperature averaged over a broader region (45-49.5°N, 3-9°E) whose temperature exhibits high correlation to temperature and $\delta^{18}O_p$ at Bern (Fig. 4C). Before the calibration, the M6 $\delta^{18}O$ record was fine-tuned within age uncertainties to the temperature curve using AnalySeries (Paillard et al., 1996) (Fig.7A).

The period between 1680 and 1960 AD was selected as calibration period due to disturbance of cave climate after the mid 1960's when a tunnel was constructed (Gigon and Wenger, 1986), and increased uncertainties in the temperature reconstruction prior to 1680 AD (Luterbacher et al., 2004; Xoplaki et al., 2005). To develop a transfer function, we compared six intervals of different AWS temperatures with corresponding sections in the M6 $\delta^{18}O_{ct}$ record. The coldest interval occurred between about 1685 and 1700 AD coinciding with the late Maunder Minimum with mean cold season temperatures of 3.98±0.31°C. The calcite deposited during this time has the most negative $\delta^{18}O$ values of the past 500 years (-7.29±0.13‰) and delivers the first and lowest point on the calibration curve. The second point with a $\delta^{18}O$ value of -6.71±0.10‰ corresponds to the subsequent temperature peak around 1720 AD (4.56±0.19°C). A cold period around 1845 AD (4.26±0.17°C) corresponds with the last significant advance of Alpine glaciers (Böhm et al., 2001; Casty et al., 2005) and marks the third point on our calibration curve. The corresponding section of the stalagmite exhibits $\delta^{18}O$ values of -7.24±0.12‰. A second cold period at the end of the 19th century, when winters were identified as the coldest since 1760 AD in the European Alps (Böhm et al., 2001), delivers the fourth point of the transfer function. During this interval, regional temperature and M6 $\delta^{18}O_{ct}$ values averaged 4.42±0.22°C and -7.00±0.17‰, respectively. The fifth and highest point marks the period between 1920 and 1960 AD, before the greenhouse gas-induced sharp temperature rise, where constantly high $\delta^{18}O$ values of -6.47±0.06‰ correspond to temperatures which are 0.31°C higher than in the average calibration period. The last point of the transfer function averages a relatively stable period between 1755 and 1825 AD, when temperature and $\delta^{18}O_{ct}$ amounted to 4.56±0.01°C and -6.79±0.07‰, respectively. The linear fit applied to these calibration points represents the transfer function (see Fig. 7B).

The transfer function exhibits a slope of 0.87‰ $°C^{-1}$ and reflects the positive correlation between $\delta^{18}O_p$ and temperature in the mid-latitudes. However, the net slope between $\delta^{18}O_{ct}$ and temperature should be considerably lower at around 0.3‰ $°C^{-1}$ (see paragraph 5.1.4). Similarly, also Frisia et al. (2005) have observed a significantly higher temperature effect than expected in a stalagmite from the southeastern Alps. The amplified sensitivity of $\delta^{18}O_{ct}$ to temperature is remarkable as karst aquifers are generally associated with attenuation rather than amplification of the isotopic signal (Yonge et al., 1985; Perrin et al., 2003a; 2003b). Furthermore, as calcite was deposited close to isotopic equilibrium with parent drip water, strong kinetic fractionation effects can be ruled out. Although the reason for this discrepancy remains unknown, the close correspondence between historical temperature and $\delta^{18}O_{ct}$ over the past 500 years (Fig. 8) and the good fit of the linear model defining the transfer function (r^2=0.92) appears to confirm the reliability of the postulated $\delta^{18}O_{ct}$-temperature relationship.

5.3. Temperature variability during the past two millennia

The M6 AWS temperature reconstruction (hereafter referred to as M6T) corresponds remarkably well to regional AWS temperature reconstructions derived from documentary and historical evidence for the region represented by the speleothem proxy (Luterbacher et al., 2004; Xoplaki et al., 2005) and for the Swiss Mittelland (Pfister, 1993), also beyond the calibration period back to 1500 AD (Fig. 8). In the following, the M6T reconstruction is compared to other temperature records of Central Europe and the North Atlantic-European realm. Although comparing records representing different seasons may lead to misinterpretations and can be of somewhat limited informative value, we are convinced that such comparisons help to elucidate the seasonal discrepancies in the temperature evolution.

The M6T record over the last millennium documents generally higher and lower temperatures during the MCA (950–1250 AD) and LIA (1400–1700 AD; as defined by Mann et al., 2009), respectively, a temperature pattern that is in good agreement with numerous climate archives from the North Atlantic realm (Graham et al., 2011, and references therein). Lowest temperatures within the last millennium are observed around 1450 AD, with temperatures well below the ones recorded during the Late Maunder Minimum around 1700 AD. An increase in the relative importance of winter precipitation recharging the aquifer as cause for this distinct minimum in $\delta^{18}O$ is rather unlikely as summer precipitation in the Swiss Jura Mountains was reconstructed above-average during this period (Magny et al., 2011). Moreover, winter and summer proxy evidence from the Jura Mountains and the European Alps confirm that the mid-15th century was at least as cold as the late 17th century (Mangini et al., 2005; Millet et al., 2009; Larocque-Tobler et al., 2010; Magny et al., 2011; Larocque-Tobler et al., 2012).

Although most of the records in the North Atlantic-European realm show a prolonged warm phase during the MCA, there are notable differences in timing, duration and magnitude of the warming. The maximum in the M6T record at around 1125 AD corresponds well to single-proxy and multi-proxy reconstructions from the European Alps (Mangini et al., 2005; Millet et al., 2009, Büntgen et al., 2011; Trachsel et al., 2012), and to a reconstructed retreat of the Great Aletsch glacier around the first quarter of the 13th century (Holzhauser et al., 2005) considering its response time of 50 to 100 years (Häberli and Holzhauser, 2003). However, the timing of temperature maxima in individual records is not synchronous, which is most likely related to a spatially heterogeneous medieval warming (e.g., Jansen et al., 2007; Diaz et al., 2011), chronological uncertainties of the proxy records, and, most importantly, different seasonal temperature.

The average AWS temperature difference between the LIA and the MCA amounts to 0.48°C in the M6T record, an estimate that is at the lower end of the (summer-biased) MAT difference suggested for the Greater Alpine Region (0.45-0.60°C), calculated by Mann et al. (2009). The difference between decadal minimum AWS temperature during the LIA and decadal maximum AWS temperature during the MCA (determined by applying 11-yr running averages) is about 1.8°C, which is comparable to the annual SST difference recorded in the North Atlantic off Iceland (~1.5°C; Sicre et al., 2011) and the cold season temperature difference attained in the record of the Austrian Alps (~1.7°C; Mangini et al., 2005), but significantly lower than observed in the Central European summer temperature reconstruction (3.0°C; Büntgen et al., 2011). The good correspondence to the difference obtained in the cold season temperature record from the Austrian Alps suggests that the calibration is also robust beyond the calibration period, and that summer temperatures reacted more sensitively to the MCA-LIA climate transition.

Between 700 and 900 AD, average temperatures in the M6T record are almost as low as in the 15th century, and clearly lower than for the average LIA. Temperature minima during this interval are also recorded at regional scale (Mangini et al., 2005; Sicre et al., 2011), but temperatures in these reconstructions remained higher than during the LIA. Apart from a short-term cold period in the third century, relatively high temperatures are observed between 0 and 700 AD. Remarkably, the peak warmth at around 550 AD corresponds well with a winter temperature maximum observed in the Austrian Alps (Mangini et al., 2005). However, this contrasts summer-biased climate records from Central Europe, which recorded a period of climate deterioration between about 400 and 700 AD (e.g., Holzhauser et al., 2005; Millet et al., 2009; Büntgen et al., 2011). These discrepancies between winter-sensitive and summer-sensitive proxies may indicate seasonally differing temperature evolution during this period.

In the pre-industrial Holocene, changes in solar activity can be considered as an important climate forcing factor (see Gray et al., 2010 for a review). The correlation between reconstructed solar activity (Steinhilber et al., 2009) (Fig. 8B) and the M6T record is weak ($r=0.17$, $p<0.05$). However, most of the prominent grand minima (Usoskin et al., 2007) and maxima correspond well with short-term (multi-decadal) temperature fluctuations. A temperature depression around 710 AD coincides with one of the major solar minima. A period of high solar activity between the Oort and Wolf Minimum, also referred to as the Medieval Maximum of sunspot activity (Eddy, 1977), coincides with the well-defined temperature peak in the M6T record at around 1125 AD. Solar activity is generally low during the LIA, coinciding with low temperatures in the temperature reconstruction. The Spörer Minimum defines a long-lasting period (1390–1550 AD) of very low solar activity, corresponding well to the coldest period in M6T. During the Maunder Minimum (1650–1725 AD) reconstructed AWS temperatures show a distinct negative anomaly despite the relatively moderate change in solar irradiance. This confirms the hypothesis that a negative North Atlantic Oscillation (NAO) could have contributed to substantial winter cooling in Central Europe (Wanner et al., 2000; Shindell et al., 2001; Luterbacher et al., 2001; Mangini et al., 2005, Spangehl et al., 2010). These observations indicate that temperature variations in Central Europe are partly but not exclusively driven by changes in solar irradiance, an observation that is in agreement with previous results on Holocene archives from Central Europe (Niggemann et al., 2003a; 2003b; Mangini et al., 2005; Büntgen et al., 2006; Trachsel et al., 2010; Magny et al., 2011).

The interpretation of volcanic forcing (Fig. 8A) in European paleoclimate records is more complex and spatially and seasonally heterogeneous. Whereas winter-biased continental proxies from Central Europe are expected to record a warming following single volcanic eruptions (Fischer et al., 2007; Zanchettin et al., 2013), a cumulative effect of large volcanic eruptions on climate during certain periods may result in a temperature drop in Europe as global-scale cooling outweighs the regional winter warming effect (e.g., Hegerl et al., 2011). Periods of intensified volcanic activity and decreased solar activity during the 12th and 13th century, together with sea ice-ocean-atmosphere feedbacks, may have contributed to the initiation of the LIA (Miller et al., 2012; Lehner et al., 2013). During the LIA, decreased solar forcing and enhanced volcanic forcing are thought to have contributed to the prolonged cooling (Shindell et al., 2003). Several tropical eruptions during the second half of the 15th century, for instance, may have amplified the impact of the Spörer Minimum leading to the observed temperature minimum in our and other temperature reconstructions.

In addition to natural forcing, internal variability may play an important role in determining climate change, particularly at regional scale (Goosse et al., 2006). General circulation models (GCM) can assist in estimating how much the climate might have been expected to change given the reconstructed forcings in the past, and correspondingly, how much variability might be expected to have arisen from internal variability (Jones and Mann, 2004, Goosse et al., 2005). Thus, comparison between model simulations and the reconstructed temperature may further help to assess the impact of external forcing.

5.3. Inferences from model simulations

Two ensembles of transient simulations were carried out, resulting in monthly temperature estimates for the period 1149–2098 AD (Fig. 9). The simulations were conducted with a coupled GCM, the Community Climate System Model version 3 (CCSM3), which consists of four components: the atmosphere, the ocean, the sea ice, and the land surface (Collins et al., 2006). The time-varying external forcing applied is composed of solar and volcanic forcing, and greenhouse gas concentrations (Hofer et al., 2011). For further information on the climate model the reader is referred to Collins et al. (2006), detailed information about the forcing datasets are provided in Hofer et al. (2011) and Lehner et al. (2012a).

An ensemble of four transient simulations was run from 1500 to 2098 AD using the low-resolution CCSM3, which uses a horizontal atmosphere/land surface grid of approximately 3.75° by 3.75° (Lehner et al., 2012a). Furthermore, an ensemble of six simulations was carried out for the time period 1149–1499 AD using the medium-resolution version resulting in a resolution of about 2.8° by 2.8° (Lehner et al., 2012b). The simulated AWS temperature was averaged over 2x2 grid boxes centered as close to the study site as allowed by the resolution of the model (see Fig. 9D).

On average, between 1149 and 1960 AD, simulated AWS temperatures are about 0.1°C lower than the reconstructed ones (Fig. 9C). This is a remarkably small difference, considering the different regions for which temperature was simulated/reconstructed, and the uncertainties in simulation and reconstruction. Except for the second half of the 20th century, when the greenhouse gas-induced warming is not recorded in stalagmite M6 (likely due to a disturbance of the cave climate), the reconstructed temperature is in good agreement with the ensemble mean. Because of relatively high solar activity, temperatures in the model simulations for the period 1150–1350 AD are generally warmer than during the subsequent LIA when solar forcing was lower. Moreover, the prominent solar minima are also evident in the simulations. Fig. 9B shows the temperature evolution of one selected member of each ensemble in detail. They are in relatively good agreement with our temperature reconstruction besides an apparent offset in the period 1100–1500 AD perhaps related to a systematic bias of the M6 age model in this time interval. Importantly, the ensemble mean allows a more robust interpretation as single members represent only one realization of the possible responses. Indeed, most of the higher-frequency variations of the different ensemble members are relatively heterogeneous, indicating the range of natural variability inherent in the system (Fig. 9A).

In order to address the sensitivity to solar forcing, the M6T record is also compared to the "low solar" CCSM version 4 simulation by Landrum et al. (2013), consisting of a lower magnitude of the solar forcing in comparison to the "medium solar" simulations presented above (Hofer et al., 2011; see Ammann et al., 2007 for the classification of the solar forcing). The long-term trend of decreasing AWS temperatures during the pre-industrial period of the last millennium and the cold spell during the Spörer Minimum are similarly evident in Landrum et al. (2013), even though the temperature decrease during the LIA is less pronounced. Again, higher frequency variations observed in the temperature reconstruction are not reproduced by the simulation, and are possibly dominated by internal variability.

In summary, the long-term temperature trend and the magnitudes of the transient model simulations compare well with the speleothem $\delta^{18}O$-inferred temperature, and confirm that low-frequency variations in solar activity had considerable influence on Central European climate (e.g., Crowley, 2000; Bauer et al., 2003; Goosse et al., 2005; Fernández-Donado et al., 2013). On decadal scales, however, natural variability of the climate system seems to mask the higher frequency variations in solar forcing (e.g., Goosse et al., 2006). Furthermore, rapid transitions, as observed in the aftermath of the MCA, have been suggested to be not solely controlled by simple modifications in radiative forcing, but also by internal variability and feedback mechanisms in the atmosphere or ocean (Wanner et al., 2011, Lehner et al., 2013). Internally generated changes in the NAO or the Atlantic Meridional Overturning Circulation, for instance, are well known to play a determinant role in controlling Central European climate variability (Graham et al., 2011).

5.5. Influence of the North Atlantic Oscillation

The NAO is the dominant mode of atmospheric winter circulation over the North Atlantic and Europe and is characterized by a meridional gradient in the distribution of atmospheric mass over the North Atlantic (Hurrell, 1995; Wanner et al., 2001). While NAO-induced variations in precipitation are well observed over northern and southern Europe, NAO variability in Central Europe is best captured in winter temperature and winter temperature-sensitive $\delta^{18}O_p$ time series (Wanner et al., 2003; Baldini et al., 2008; Field, 2010; Langebroek et al., 2011; Fohlmeister et al., 2012). It was shown that correlation between winter temperature in Central Europe and the Alps and the winter NAO index is relatively high for the observational era (Wanner et al., 2003; Casty et al., 2005). Moreover, results of Langebroek et al. (2011) suggest that Central European $\delta^{18}O_p$, as reflected in the stalagmite M6T record, may be even stronger related to atmospheric circulation. This is also confirmed by the good correspondence ($r=0.40$, $p<0.05$) between precipitation-weighted $\delta^{18}O_p$ above Milandre Cave and the winter NAO index (Fig. 4B). Hence, low-frequency temporal variations in cold season-biased $\delta^{18}O_{ct}$-inferred temperature can potentially be used to trace the influence of large-scale changes in atmospheric circulation on Central European climate beyond the instrumental period.

Until today, several NAO reconstructions have been published (summarized by Pinto and Raible, 2012). The longest NAO reconstruction dates back to 1049 AD (Trouet et al., 2009), and uses a speleothem-based precipitation proxy from Scotland (Proctor et al., 2000) and a tree ring-based drought proxy from Morocco (Esper et al., 2007) to account for pressure-induced hydrological changes at both centers of action of the NAO. The M6T record and the proxy-based NAO reconstruction reveal some similar low-frequency patterns over the last millennium (Fig. 10). The persistent positive NAO phase during the MCA, associated with stronger westerlies during the winter season, would provide a dynamical explanation for the observed warmth in our record during medieval times (Trouet et al., 2009). However, the timing of the phase change varies in the two records, and also the short-term fluctuations in our speleothem record do not coincide with the rather stable NAO reconstruction during the MCA. Moreover, the M6 AWS temperature record fails to verify against shorter NAO reconstructions (Luterbacher et al., 2002; Cook et al., 2003) and the longest instrumental winter NAO index (Jones et al., 1997). Furthermore, one single proxy is unlikely to reflect this complex climatic phenomenon reliably due to its susceptibility to spatial changes of the NAO centers of action, which may result in changes of the winter storm tracks and in an inadequate reflection of the NAO signal (Raible et al., 2006; Lehner et al., 2012b). Instead, the NAO variability within the past two millennia is probably best captured by applying a multi-proxy approach. The combination of the two paleorecords used by Trouet et al. (2009) with additional NAO-sensitive proxies in the North Atlantic realm may significantly improve the reconstruction, whose robustness has been questioned recently (Lehner et al., 2012b).

6. Conclusions and Outlook

The temporally high resolved speleothem $\delta^{18}O$ record from the Swiss Jura Mountains captures variations in AWS temperatures representative for supra-regional climate. The reliability of the two millennia spanning temperature reconstruction is confirmed by the good correspondence to historical temperature reconstructions for the last 500 years. Whereas the lowest temperatures are found during the 8th and 15th century, temperatures at the MCA peak at around 1125 AD were reconstructed to be the highest within the past 2000 years. However, temperatures during the second half of the 20th century are not comparable to the rest of the reconstruction owing to an apparent bias possibly due to the disturbance of cave climate. Comparison to a solar proxy and model simulations indicate that temperature variability is affected by changes in solar forcing, but internal variability plays an important role on decadal scale.

The so far deepest radiometric age in stalagmite M6 (at a depth of 143 cm from totally 182 cm) yields an age of almost 14 ka BP. As there is no sign of any hiatus, the stalagmite provides an invaluable archive for a continuous sub-decadally resolved paleotemperature record back to the last deglaciation.

Acknowledgments

This study was carried out in the framework of the Sinergia project "STALCLIM" funded by the Swiss National Science Foundation (SNSF; grant no. CRSI22-132646/1 to DF). We thank Philipp Häuselmann for his support during the fieldworks at Milandre Cave, and the Spéléo-Club Jura for their collaboration. FL is supported by the National Centre of Competence in Research (NCCR) Climate funded by SNSF. CCR is supported by the Sinergia project FUPSOL of the SNSF (130642). JL acknowledges support from the DFG Project PRIME 2 (PRecipitation In past Millennia in Europe, extension back to Roman time) within the Priority Program 'INTERDYNAMIK', from DFG Project "Historical Climatology of the Middle East based on Arabic sources back to AD 800", and from EU/FP7 project ACQWA (NO212250). The model simulations were performed at the Swiss National Supercomputing Centre (CSCS).

References

Ammann, C.M., Joos, F., Schimel, D.S., Otto-Bliesner, B.L., Tomas, R.A., 2007. Solar influence on climate during the past millennium. Results from transient simulations with the NCAR Climate System Model. Proceedings of the National Academy of Sciences 104, 3713–3718.

Auer, I., Böhm, R., Jurkovic, A., Lipa, W., Orlik, A., Potzmann, R., Schöner, W., Ungersböck, M., Matulla, C., Briffa, K., Jones, P., Efthymiadis, D., Brunetti, M., Nanni, T., Maugeri, M., Mercalli, L., Mestre, O., Moisselin, J.-M., Begert, M., Müller-Westermeier, G., Kveton, V., Bochnicek, O., Stastny, P., Lapin, M., Szalai, S., Szentimrey, T., Cegnar, T., Dolinar, M., Gajic-Capka, M., Zaninovic, K., Majstorovic, Z., Nieplova, E, 2007. HISTALP - historical instrumental climatological surface time series of the Greater Alpine Region. International Journal of Climatology 27, 17–46.

Baldini, L.M., McDermott, F., Foley, A.M., Baldini, J.U.L, 2008. Spatial variability in the European winter precipitation δ^{18}O-NAO relationship: Implications for reconstructing NAO-mode climate variability in the Holocene. Geophysical Research Letters 35, L04709.

Bauer, E., Claussen, M., Brovkin, V., Hünerbein, A., 2003. Assessing climate forcings of the Earth system for the past millennium. Geophysical Research Letters 30, 1276, doi:10.1029/2002GL016639.

Böhm, R., Auer, I., Brunetti, M., Maugeri, M., Nanni, T., Schöner, W., 2001. Regional temperature variability in the European Alps: 1760–1998 from homogenized instrumental time series. International Journal of Climatology 21, 1779–1801.

Breitenbach, S.F.M, Rehfeld, K., Goswami, B., Baldini, J.U.L., Ridley, H.E., Kennett, D.J., Prufer, K.M., Aquino, V.V., Asmerom, Y., Polyak, V.J., Cheng, H., Kurths, J., Marwan, N., 2012. COnstructing Proxy Records from Age Models (COPRA). Climate of the Past 8, 1765–1779.

Büntgen, U., Frank, D.C., Nievergelt, D., Esper, J., 2006. Summer temperature variations in the European Alps, AD 755–2004. Journal of Climate 19, 5606–5623.

Büntgen, U., Tegel, W., Nicolussi, K., McCormick, M., Frank, D., Trouet, V., Kaplan, J.O., Herzig, F., Heussner, K.U., Wanner, H., Luterbacher, J., Esper J., 2011. 2500 years of European climate variability and human susceptibility. Science 331, 578–582.

Casty C., Wanner H., Luterbacher J., Esper J., Böhm R., 2005. Temperature and precipitation variability in the European Alps since 1500. International Journal of Climatology 25, 1855–1880.

Collins, W.D., Bitz, C.M., Blackmon, M.L., Bonan, G.B., Bretherton, C.S., Carton, J.A., Chang, P., Doney, S.C., Hack, J.J., Henderson, T.B., Kiehl, J.T., Large, W.G., McKenna, D.S., Santer, B.D., Smith, R.D, 2006. The community climate system model version 3 (CCSM3). Journal of Climate 19, 2122–2143.

Coplen T.B., 2007. Calibration of the calcite-water oxygen-isotope geothermometer at Devils Hole, Nevada, a natural laboratory. Geochimica et Cosmochimica Acta 71, 3948–3957.

Cook E.R. 2003. Multi-proxy reconstructions of the North Atlantic Oscillation (NAO) index: A critical review and a new well-verified winter NAO index reconstruction back to AD 1400. In: Hurrell, J.W., et al. (Eds.), The North Atlantic Oscillation: Climatic Significance and Environmental Impact, Geophysical Monograph, volume 134, American Geophysical Union, Washington D.C., pp. 63–79.

Crowley, T.J., 2000. Causes of climate change over the past 1000 years. Science, 289, 270–277.

Dansgaard, W., 1964. Stable isotopes in precipitation. Tellus 16, 436–468.

Diaz, H.F., Trigo, R., Hughes, M.K., Mann, M.E., Xoplaki, E., Barriopedro, D., 2011. Spatial and temporal characteristics of climate in Medieval times revisited. Bulletin of the American Meteorological Society 92, 1487–1500.

Dorale, J.A., Liu, Z., 2009. Limitations of Hendy test criteria in judging the paleoclimatic suitability of speleothems and the need for replication. Journal of Cave and Karst Studies 71, 73–80.

Eddy, J.A., 1977. Climate and the changing sun. Climatic Change 1, 173–190.

Esper, J., Frank, D.C., Büntgen, U., Verstege, A., Luterbacher, J., Xoplaki, E., 2007. Long-term drought severity variations in Morocco. Geophysical Research Letters 34, L17702.

Fernández-Donado, L., González-Rouco, J.F., Raible, C.C., Ammann, C.M., Barriopedro, D., García-Bustamente, E., Jungclaus, J.H., Lorenz, S.J., Luterbacher, J., Phipps, S.J., Servonnat, J., Swingedouw, D., Tett, S.F.B., Wagner, S., Yiou, P., Zorita, E., 2013. Large-scale temperature response to external forcing in simulations and reconstructions of the last millennium. Climate of the Past 9, 393-421.

Field R.D., 2010. Observed and modeled controls on precipitation δ^{18}O over Europe: From local temperature to the Northern Annular Mode.

Journal of Geophysical Research 115, D12101.

Fischer, E.M., Luterbacher, J., Zorita, E., Tett, S.F.B., Casty, C, Wanner, H., 2007. European climate response to tropical volcanic eruptions over the last half millennium. Geophysical Research Letters 34, L05707.

Fleitmann, D., Cheng, H., Badertscher, S., Edwards, R.L., Mudelsee, M., Göktürk, O.M., Fankhauser, A., Pickering, R., Raible, C.C., Matter, A., Kramers, J., Tüysüz, O., 2009. Timing and climatic impact of Greenland interstadials recorded in stalagmites from northern Turkey. Geophysical Research Letters 36, L19707.

Fohlmeister, J., Schröder-Ritzrau, A., Scholz, D., Spötl, C., Riechelmann, D.F.C., Mudelsee, M., Wackerbarth, A., Gerdes, A., Riechelmann, S., Immenhauser, A., Richter, D.K., Mangini, A, 2012. Bunker Cave stalagmites: an archive for central European Holocene climate variability. Climate of the Past Discussions 8, 1687–1720.

Frisia, S., Borsato, A., Spötl, C., Villa, I.M., Cucchi, F., 2005. Climate variability in the SE Alps of Italy over the past 17 000 years reconstructed from a stalagmite record. Boreas 34, 445–455.

Gigon, R., Wenger, R., 1986. Inventaire spéléologique de la Suisse, canton du Jura. Commission Spéléologie de la Sociéte helvétique des sciences naturelles, Porrentruy.

Goosse, H., Renssen, H., Timmermann, A., Bradley, R.S., 2005. Internal and forced climate variability during the last millennium: a model-data comparison using ensemble simulations. Quaternary Science Reviews 24, 1345–1360.

Goosse, H., Renssen, H., Timmermann, A., Bradley, R.S., M.E. Mann, 2006. Using paleoclimate proxy-data to select optimal realisations in an ensemble of simulations of the climate of the past millennium. Climate Dynamics 27, 165–184.

Graham, N.E., Ammann, C.M., Fleitmann, D., Cobb, K.M., Luterbacher, J., 2011. Support for global climate reorganization during the Medieval Climate Anomaly. Climate dynamics 37, 1217–1245.

Gray, L.J., Beer, J., Geller, M., Haigh, J., Lockwood, M., Matthes, K., Cubach, U., Fleitmann, D., Harrison, G., Hood, L., Luterbacher, J., Marsh, N., Shindell, D., van Geel, B., White, W., 2010. Solar influences on climate. Reviews of Reophysics 48, RG4001.

Häberli W., Holzhauser H., 2003. Alpine glacier mass changes during the past two millennia. PAGES News 11, 13–15.

Hegerl, G., Luterbacher, J., Gonzàlez-Rouco, F.J., Crowley, T., Xoplaki, E., 2011. Influence of human and natural forcing on European seasonal temperatures. Nature Geoscience 4, 99–103.

Hendy, C.H., 1971. The isotopic geochemistry of speleothems–i. the calculation of the effects of different modes of formation on the isotopic composition of speleothems and their applicability as palaeoclimatic indicators. Geochimica et Cosmochimica Acta 35, 801–824.

Hofer, D., Raible, C.C., Stocker, T.F., 2011. Variation of the Atlantic meridional overturning circulation in control and transient simulations of the last millennium. Climate of the Past 7, 133–150.

Holzhauser, H., Magny, M., Zumbühl, H.J., 2005. Glacier and lake-level variations in west-central Europe over the last 3500 years. The Holocene 15, 789–801.

Horton, P., Jaboyedoff, M., Metzger, R., Obled, C., Marty R., 2012. Spatial relationship between the atmospheric circulation and the precipitation measured in the western Swiss Alps by means of the analogue method. Natural Hazards and Earth System Sciences 12, 777–784.

Hurrell J.W., 1995. Decadal trends in the North Atlantic Oscillation: regional temperatures and precipitation. Science 269, 676–679.

Jansen, E., Overpeck, J., Briffa, K.R., Duplessy, J.-C., Joos, F., Masson-Delmotte, V., Olago, D., Otto-Bliesner, B., Peltier, W.R., Rahmstorf, S., Ramesh, R., Raynaud, D., Rind, D., Solomina, O., Villalba, R., Zhang, D., 2007. Palaeoclimate. In: Solomon, S., Qin, D., Manning, M., Chen, Z., Marquis, M., Averyt, K.B., Tignor, M., Miller, H.L. (Eds.), Climate Change 2007: The Physical Science Basis. Contribution of Working Group I to the Fourth Assessment Report of the Intergovernmental Panel on Climate Change. Cambridge University Press, Cambridge, United Kingdom and New York, NY, pp. 433–497.

Jeannin, P.-Y., 1996. Structure et comportement hydraulique des aquifères karstiques. PhD Thesis, University of Neuchâtel, Switzerland.

Jeannin, P.-Y., Grasso, A.D., 1995a. Estimation des infiltrations efficaces journalières sur le bassin karstique de la Milandrine (Ajoie, JU, Suisse). Bulletin d'Hydrogéologie 14, 83–93.

Jeannin, P.-Y., Grasso, A.D., 1995b. Recharge respective des volumes de roche peu perméable et des conduits karstiques, rôle de l'épikarst. Bulletin du Centre d'Hydrogéologie 14, 95–111.

Jones, P.D., Mann, M.E., 2004. Climate over past millennia. Reviews of Geophysics, 42, 1–42.

Jones, P.D., Jonsson, T., Wheeler, D., 1997. Extension to the North Atlantic Oscillation using early instrumental pressure obervations from Gibraltar and south-west Iceland. International Journal of Climatology 17, 1433–1450.

Kim, S.T., O'Neil, J.R., 1997. Equilibrium and nonequilibrium oxygen isotope effects in synthetic carbonates. Geochimica et Cosmochimica Acta 61, 3461–3475.

Kovàcs, A., Jeannin, P.-Y., 2003. Hydrogeological overview of the Bure plateau, Ajoie, Switzerland. Eclogae Geologicae Helvetiae 96, 367–380.

Lachniet, M.S., 2009. Climatic and environmental controls on speleothem oxygen–isotope values. Quaternary Science Reviews 28, 412–432.

Landrum, L., Otto-Bliesner, B.L., Wahl, E.R., Conley, A., Lawrence, P.J., Rosenbloom, N., Teng, H., 2013. Last Millennium Climate and its variability in CCSM4. Journal of Climate 26, 1085–1111.

Langebroek, P.M., Werner, M., Lohmann, G., 2011. Climate information imprinted in oxygen-isotopic composition of precipitation in Europe. Earth and Planetary Science Letters 311, 144–154.

Larocque-Tobler, I., Grosjean, M., Heiri, O., Trachsel, M., Kamenik, C., 2010. Thousand years of climate change reconstructed from chironomid subfossils preserved in varved lake Silvaplana, Engadine, Switzerland. Quaternary Science Reviews 29, 1940–1949.

Larocque-Tobler, I., Stewart, M.M., Quinlan, R., Trachsel, M., Kamenik, C., Grosjean, M., 2012. A last millennium temperature reconstruction using chironomids preserved in sediments of anoxic Seebergsee (Switzerland): consensus at local, regional and Central European scales. Quaternary Science Reviews 41, 49–56.

Lehner, F., Raible, C.C., Hofer, D., Stocker, T.F., 2012a. The freshwater balance of polar regions in transient simulations from 1500 to 2100

AD using a comprehensive coupled climate model. Climate Dynamics 39, 347–363.

Lehner, F., Raible, C.C., Stocker, T.F., 2012b. Testing the robustness of a precipitation proxy-based North Atlantic Oscillation reconstruction. Quaternary Science Reviews 45, 85–94.

Lehner, F., Born, A., Raible, C., Stocker, T., 2013. Amplified inception of European Little Ice Age by sea ice-ocean-atmosphere feedbacks. Journal of Climate. doi:10.1175/JCLI-D-12-00690.1, in press.

Luterbacher, J., Rickli, R., Xoplaki, E., Tinguely, C., Beck, C., Pfister, C., Wanner H., 2001. The Late Maunder Minimum (1675–1715) - A key period for studying decadal scale climatic change in Europe. Climatic Change 49, 441–462.

Luterbacher, J., Xoplaki, E., Dietrich, D., Jones, P.D., Davies, T.D., Portis, D., Gonzalez-Rouco, J.F., Von Storch, H., Gyalistras, D., Casty, C., Wanner, H., 2002. Extending North Atlantic oscillation reconstructions back to 1500. Atmospheric Science Letters 2, 114–124.

Luterbacher, J., Dietrich, D., Xoplaki, E., Grosjean, M., Wanner, H., 2004. European seasonal and annual temperature variability, trends, and extremes since 1500. Science 303, 1499–1503.

Magny, M., Peyron, O., Gauthier, E., Vannière, B., Millet, L., Vermot-Desroches, B., 2011. Quantitative estimates of temperature and precipitation changes over the last millennium from pollen and lake-level data at Lake Joux, Swiss Jura Mountains. Quaternary Research 75, 45–54.

Mangini, A., Spötl, C., Verdes, P., 2005. Reconstruction of temperature in the Central Alps during the past 2000 yr from a $\delta^{18}O$ stalagmite record. Earth and Planetary Science Letters 235, 741–751.

Mann, M.E., Zhang, Z., Rutherford, S., Bradley, R.S., Hughes, M.K., Shindell, D., Ammann, C., Faluvegi, G., Ni, F., 2009. Global signatures and dynamical origins of the Little Ice Age and the Medieval Climate Anomaly. Science 326, 1256–1260.

McDermott, F., 2004. Paleo-climate reconstruction from stable isotope variations in speleothems: a review. Quaternary Science Reviews 23: 901–918.

McDermott, F., Frisia, S., Huang, Y., Longinelli, A., Spiro, B., Heaton, T.H.E., Hawkesworth, C.J., Borsato, A., Keppens, E., Fairchild, I.J., van der Borg, K., Verheyden, S., Selmo, E., 1999. Holocene climate variability in Europe: Evidence from $\delta^{18}O$, textural and extension-rate variations in three speleothems. Quaternary Science Reviews 18, 1021–1038.

McDermott, F., Atkinson, T.C., Fairchild, I.J., Baldini, L.M., Mattey, D.P., 2011. A first evaluation of the spatial gradients in $\delta^{18}O$ recorded by European Holocene speleothems. Global and Planetary Change 79, 257–287.

Millet, L., Arnaud, F., Heiri, O., Magny, M., Verneaux, V., Desmet, M., 2009. Late-Holocene summer temperature reconstruction from chironomid assemblages of Lake Anterne, northern French Alps. The Holocene 19, 317–328.

Miller, G.H., Geirsdottir, A., Zhong, Y., Larsen, D.J., Otto-Bliesner, B.L., Holland, M.M., Bailey, D.A., Refsnide, K.A., Lehman, S.J., Southon, J.R., Anderson, C., Björnsson, H., Thordarson, T., 2012. Abrupt onset of the Little Ice Age triggered by volcanism and sustained by sea-ice/ocean feedbacks. Geophysical Research Letters 39, L02708.

Mitchell T.D., Jones P.D., 2005. An improved method of constructing a database of monthly climate observations and associated high-resolution grids. International Journal of Climatology 25, 693–712.

Niggemann, S., Mangini, A., Mudelsee, M., Richter, D.K., Wurth, G., 2003a. Sub-Milankovitch climatic cycles in Holocene stalagmites from Sauerland, Germany. Earth and Planetary Science Letters 216, 539–547.

Niggemann, S., Mangini, A., Richter, D.K., Wurth G., 2003b. A paleoclimate record of the last 17,600 years in stalagmites from the B7 cave, Sauerland, Germany. Quaternary Science Reviews 22, 555–567.

PAGES, 2009. Science Plan and Implementation Strategy. IGBP Report No. 57. IGBP Secretariat, Stockholm.

PAGES 2k Consortium, 2013. Continental-scale temperature variability during the past two millennia. Nature Geoscience 6, 339–346.

Paillard, D., Labeyrie, L., Yiou, P., 1996. Macintosh program performs time-series analysis. Eos Transaction American Geophysical Union 77, 379.

Perrin, J., 2003. A conceptual model of flow and transport in a karst aquifer based on spatial and temporal variations of natural tracers. PhD Thesis, University of Neuchâtel, Switzerland.

Perrin, J., Kopp, L., 2005. Hétérogéné des écoulements dans la zone non saturée d'un aquifère karstique (site de Milandre, Jura suisse). Bulletin d'hydrogéologie 21, 33–58.

Perrin, J., Jeannin, P.-Y., Zwahlen F., 2003a. Epikarst storage in a karst aquifer: a conceptual model based on isotopic data, Milandre test site, Switzerland. Journal of Hydrology 279, 106–124.

Perrin, J., Jeannin, P.-Y., Zwahlen F., 2003b. Implications of the spatial variability of infiltration-water chemistry for the investigation of a karst aquifer: a field study at Milandre test site, Swiss Jura. Hydrogeology Journal 11, 673–686.

Perrin, J., Jeannin, P.-Y., Cornaton, F., 2007. The role of tributary mixing in chemical variations at a karst spring, Milandre, Switzerland. Journal of Hydrology 332, 158–173.

Pfister, C., 1993. Historical weather indices from Switzerland. In: IGBP PAGES/World Data Center-A for Paleoclimatology Data Contribution Series No. 93–027. NOAA/NGDC Paleoclimatology Program, Boulder CO, USA.

Pinto J.G., Raible C.C., 2012. Past and recent changes in the North Atlantic oscillation. Wiley Interdisciplinary Reviews: Climate Change 3, 79–90.

Primault B., 1962. Du calcul de l'évapotranspiration. Theoretical and Applied Climatology 12, 124–150.

Proctor, C.J., Baker, A., Barnes, W.L., Gilmour, M.A., 2000. A thousand year speleothem proxy record of North Atlantic climate from Scotland. Climate Dynamics 16, 815–820.

Raible, C.C., Casty, C., Luterbacher, J., Pauling, A., Esper, J., Frank, D.C., Büntgen, U. Rösch, A.C., Wild, M., Tschuck, P., Vidale, P.-L., Schär, C., Wanner, H., 2006: Climate Variability - Observations, Reconstructions and Model Simulations, Climate Change 79, 9–29.

Rozanski, K., Araguas-Araguas, L., Gonfiantini R., 1993. Isotopic patterns in modern global precipitation. Climate Change in Continental Isotope Records 78, 1–36.

Savoy, L., 2007. Use of natural and artificial reactive tracers to investigate the transfer of solutes in karst systems. PhD Thesis, University of Neuchâtel, Switzerland.

Schmassmann, S., 2010. Speleothem-based climate and environmental reconstruction: A pilot study in the Swiss Jura Mountains. Master Thesis, University of Bern, Switzerland.

Schotterer, U., Stocker, T., Bürki, H., Hunziker, J., Kozel, R., Grasso, D.A., Tripet J.P., 2000. Das Schweizer Isotopen-Messnetz: Trends 1992-1999. Gas, Wasser, Abwasser 80, 733–741.

Schotterer, U., Schürch, M., Rickli, R., Stichler, W., 2010. Wasserisotope in der Schweiz: Neue Ergebnisse und Erfahrungen aus dem nationalen Messnetz ISOT. Gas, Wasser, Abwasser 90, 1073–1081.

Schürch, M., Kozel, R., Schotterer, U., Tripet, J.P., 2003. Observation of isotopes in the water cycle - the Swiss National Network (NISOT). Environmental Geology 45, 1–11.

Shindell, D.T., Schmidt, G.A., Mann, M.E., Rind, D., Waple, A., 2001. Solar forcing of regional climate change during the Maunder Minimum. Science 294, 2149–2152.

Shindell, D.T., Schmidt, G.A., Miller, R.L., Mann, M.E., 2003. Volcanic and solar forcing of climate change during the preindustrial era. Journal of Climate 16, 4094–4107.

Sicre, M.A., Hall, I.R., Mignot, J., Khodri, M., Ezat, U., Truong, M.X., Eiriksson, J., Knudsen, K.L., 2011. Sea surface temperature variability in the subpolar Atlantic over the last two millennia. Paleoceanography 26, PA4218.

Siegenthaler, U. Oeschger, H., 1980. Correlation of ^{18}O in precipitation with temperature and altitude. Nature 285, 314–317.

Sodemann, H., Zubler, E., 2010. Seasonal and inter-annual variability oft he moisture sources for Alpine precipitation during 1995–2002. International Journal of Climatology 30, 947–961.

Spangehl,T., Cubasch, U., Raible, C. C., Langematz, U., Schimanke, S., Koerper, J., Hofer, D., 2010. Transient climate simulations from the Maunder Minimum to present day: the role of the stratosphere. Journal of Geophysical Research 115, doi:10.1029/2009JD012358.

Spötl, C., Mangini, A., 2002. Stalagmite from the Austrian Alps reveals Dansgaard–Oeschger events during isotope stage 3: Implications for the absolute chronology of Greenland ice cores. Earth and Planetary Science Letters 203, 507–518.

Steinhilber, F., Beer, J., Fröhlich, C., 2009. Total solar irradiance during the Holocene. Geophysical Research Letters 36, L19704.

Trachsel, M., Grosjean, M., Larocque-Tobler, I., Schwikowski, M., Blass, A., Sturm, M., 2010. Quantitative summer temperature reconstruction derived from a combined biogenic Si and chironomid record from varved sediments of Lake Silvaplana (south-eastern Swiss Alps) back to AD 1177. Quaternary Science Reviews 29, 2719–2730.

Trachsel, M., Kamenik, C., Grosjean, M., McCarroll, D., Moberg, A., Bràzdil, R., Büntgen, U., Dobrovolny, P., Esper, J., Frank, D.C., Friedrich, M., Glaser, R., Larocque-Tobler, I., Nicolussi, K., Riemann, D., 2012. Multi-archive summer temperature reconstruction for the European Alps, AD 1053–1996. Quaternary Science Reviews 46, 66–79.

Trouet, V., Esper, J., Graham, N.E., Baker, A., Scourse, J.D., Frank, D.C., 2009. Persistent positive North Atlantic Oscillation mode dominated the medieval climate anomaly. Science 324, 78–80.

Usoskin, I.G., Solanki, S.K., Kovaltsov, G.A., 2007. Grand minima and maxima of solar activity: new observational constraints. Astronomy and Astrophysics 471, 301–309.

Wackerbarth, A., Scholz, D., Fohlmeister, J., Mangini, A., 2010. Modelling the δ^{18}O value of cave drip water and speleothem calcite. Earth and Planetary Science Letters 299, 387–397.

Wanner, H., Holzhauser, H., Pfister, C., Zumbühl H.P., 2000. Die Klimavariabilität im europäischen Alpenraum auf der Zeitskala von Jahren bis Jahrhunderten. Erdkunde 54, 62–69.

Wanner, H., Brönnimann, S., Casty, C., Gyalistras, D., Luterbacher, J., Schmutz, C., Stephenson, D.B., Xoplaki, E., 2001. North Atlantic Oscillation – concepts and studies. Surveys in Geophysics 22, 321–382.

Wanner, H., Luterbacher, J., Casty, C., Böhm, R., Xoplaki, E., 2003. Variabilität von Temperatur und Niederschlag in deneuropäischen Alpen seit 1500. In: Jeanneret, F., Wastl- Walter, D., Wiesmann, U., Schwyn, M. (Eds.), Welt der Alpen - Gebirge der Welt, Haupt, Bern, Switzerland, 61–76.

Wanner, H., Beer, J., Bütikofer, J., Crowley, T.J., Cubasch, U., Flückiger, J., Goosse, H., Grosjean, M., Joos, F., Kaplan, J.O., Küttel, M., Müller, S.A., Prentice, I.C., Solomina, O., Stocker, T.F., Tarasov, P., Wagner, M., Widmann, M., 2008. Mid- to Late Holocene climate change: an overview. Quaternary Science Reviews 27, 1791–1828.

Wanner, H., Solomina, C., Grosjean, M., Ritz, S.P., Jetel, 2011. Structure and origin of Holocene cold events. Quaternary Science Reviews 30, 3109–3123.

Xoplaki, E., Luterbacher, J., Paeth, H., Dietrich, D., Steiner, N., Grosjean, M., Wanner, H., 2005. European spring and autumn temperature variability and change of extremes over the last half millennium. Geophysical Research Letters 32, L15713.

Yonge, C.J., Ford, D.C., Gray, J., Schwarcz, H.P., 1985. Stable isotope studies of cave seepage water. Chemical Geology 58, 97–105.

Zanchettin, D., Timmreck, C., Bothe, O., Lorenz, S., Hegerl, L., Graf, H.-F., Luterbacher, J., Jungclaus, J.H., 2013. Delayed winter warming: a decadal dynamical response to strong tropical volcanic eruptions. Geophysical Research Letters 40, 204–209.

FIGURE CAPTIONS

Figure 1. Location map of Milandre Cave, situated south of the village Boncourt in the Jura Mountains in Central Europe. Subfigure **A** and **B** are from *Atlas der Schweiz*, version 3.0, and subfigure **C** was modified after Perrin et al. (2003a).

Figure 2. Stalagmite M6 from Milandre Cave. This study focuses on the top part of the stalagmite (white frame). Red circles represent locations of dated samples (see Table 1). Section A (blue square) displays a zone with high growth rate where the lamina couplets are well visible.

Figure 3. Age model of stalagmite M6 (0-52 cm). The bottom part is based on seven ^{230}Th ages (black squares with 2σ error; Table 1) that have been used to perform a Monte Carlo (MC) simulation using the COPRA algorithm (Breitenbach et al., 2012). The resulting median (black line) is shown with its 95% uncertainty range (dark gray area). The top part relies on annual lamina counts (red), shown with an assumed 10% counting uncertainty range. The six topmost ^{230}Th ages (white squares), and the associated MC-generated median (dashed line) incl. its 95% confidence level (light gray area) were discarded for the age model due to their high uncertainties relative to the lamina chronology.

Figure 4. Modern relationship between climate and precipitation δ^{18}O (1971–2010 AD). **A** Monthly δ^{18}O in Bern (black) compared to monthly precipitation-weighted δ^{18}O above Milandre Cave (blue; Perrin et al., 2003a) and to monthly temperature in Bern (red). **B** Comparison of annual precipitation-weighted δ^{18}O (black) to mean annual temperature (MAT) in Bern (red), and to the winter NAO index (orange; www.cpc.ncep.noaa.gov). **C** Cross-correlation of monthly deseasonalized temperature and monthly precipitation in NW Switzerland (47.25–47.75°N, 6.75–7.25°E; small black square) to monthly gridded deseasonalized temperature and precipitation in Europe (CRU TS 3.10 at 0.5° resolution; Mitchell and Jones, 2005), and correlation of monthly precipitation-weighted and deseasonalized δ^{18}O in Bern (black circle) to monthly gridded deseasonalized temperature in Europe. The area specified in the maps (45.0–49.5°N, 3.0–9.0°E) is suggested to be representative for the $\delta^{18}O_p$-temperature relationship observed in NW Switzerland. Correlation analysis was performed on the KNMI climate explorer website (climexp.knmi.nl).

Figure 5. Estimated effective infiltration at Milandre Cave (1981–2011 AD). Estimation was carried out using precipitation data (blue) from the MeteoSwiss weather station Fahy, and estimates of actual evapotranspiration (AET) and soil moisture. Monthly discharge amounts of the Allaine (black), measured at the village Boncourt, correspond well with the estimates of effective infiltration (red) confirming the model output. The yellow columns mark the winter seasons.

Figure 6. A «Hendy test» results along six different growth layers in stalagmite M6, including correlation analysis between δ^{18}O and δ^{13}C along the central growth axis. **B** Replication of δ^{18}O between the high-resolution records of stalagmites M6 and M4, sampled in the downstream part of Milandre Cave. The median of the M6 δ^{18}O record and its 95% confidence bounds are shown as black line and as gray area, respectively.

Figure 7. A Comparison of M6 δ^{18}O to regional autumn to spring (AWS) temperatures derived from historical reconstructions (Luterbacher et al., 2004; Xoplaki et al., 2005). Before calibration, the speleothem oxygen record was fine-tuned to the historical temperature reconstructions. 'R.a.' stands for 'running average'. **B** The transfer function between δ^{18}O and regional historical temperature has been constructed from six intervals between 1685 and 1960. The dashed lines and the error bars represent the upper and lower 95% confidence limits for the linear fit and the six calibration points, respectively.

Figure 7 (updated). A Comparison of M6 δ^{18}O (5-years running mean) to regional autumn to spring (AWS) temperatures derived from historical reconstructions (9 year running mean, Luterbacher et al., 2004; Xoplaki et al., 2005) between 1730 and 2011 CE. Before calibration, the speleothem oxygen record was fine-tuned to the historical temperature reconstruction. **B.** The transfre function between δ^{18}O and the regional historical reconstructions has been constructed with data between 1730 and 1960 CE.

Figure 8. Temperature variability over the past two millennia. **A** Optical depth changes in the visible band due to volcanic aerosols (Crowley, 2000; Hofer et al., 2011) **B** Ice core based reconstruction of total solar irradiance anomaly with reference to (wrt) 1986 AD. (Steinhilber et al., 2009). The yellow bars denote the five grand solar minima of the past 2000 years (Usoskin et al., 2007) **C** δ^{18}O-inferred Central European autumn to spring (AWS) temperature (T; 13-sample running average (r.a.) in black) incl. the median (dashed black line) and its 95% confidence limits (gray area). **D** AWS T (25-yr r.a.) averaged over a region indicated by the black square in Fig. 9 (historical; Luterbacher et al., 2004; Xoplaki et al., 2005). **E** Switzerland AWS T (17-yr r.a.; documentary; Pfister, 1993) **F** Austrian Alps winter T (9-sample r.a.; speleothem; Mangini et al., 2005). **G** Central European summer T anomaly wrt 1901–2000 AD (25-yr r.a.; tree-ring width; Büntgen et al., 2011). **H** European Alps summer T anomaly wrt 1901–2000 AD (multi-archive; Trachsel et al., 2012).

Figure 9. Comparison of autumn to spring (AWS) temperature in two ensemble simulations, consisting of six members for 1149–1499 AD (orange; medium-resolution CCSM3) and of four members for 1500–2098 AD (red; low-resolution CCSM3; 2012–2098 AD is not shown), to the M6 δ^{18}O-inferred temperature reconstruction (black). **A** The brown curves are the raw data of the simulation, and the colored and black lines represent 13-yr and 13-sample running averages (r.a.), respectively. The median T uncertainty and its 95% confidence bounds are shown as black dashed line and as gray area. **B** M6 AWS temperature

(same curves as in A) compared to selected members (13-yr r.a.). **C** M6 AWS temperature (same curves as in A) compared to the ensemble mean of the two CCSM3 simulations, and to the CCSM4 "low" solar temperature simulation by Landrum et al. (2013) in blue. **D** Map showing the areas over which the simulated temperature was averaged, and the region represented by the M6 temperature record, respectively.

Figure 10. Reconstructed M6 autumn to spring (AWS) temperature (13-sample running average (r.a.) in black, median temperature and its 95% confidence bounds as black dashed line and gray area, respectively) compared to the instrumental winter NAO index from Jones et al. (1997) (31-yr r.a.), representing the pressure difference between Gibraltar and Iceland, and to the reconstructed winter NAO from Luterbacher et al. (2002) (31-yr r.a.) and Trouet et al. (2009).

FIGURE 1.

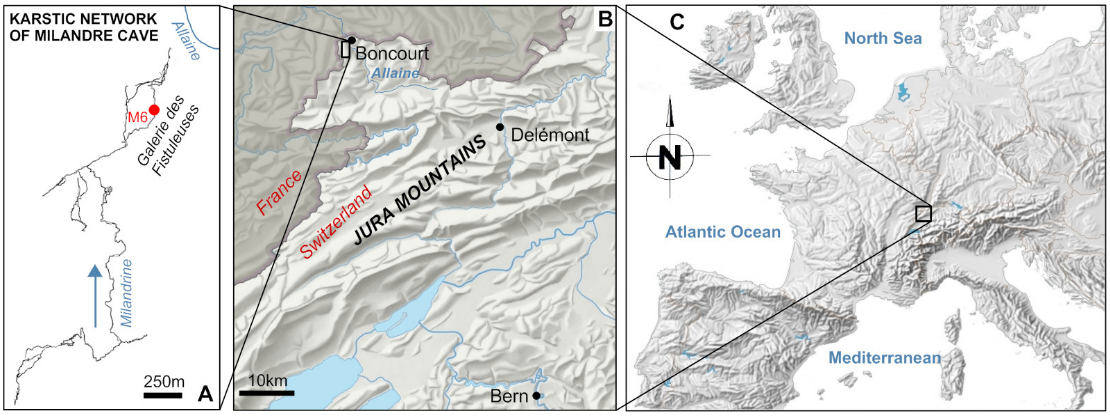

FIGURE 3.

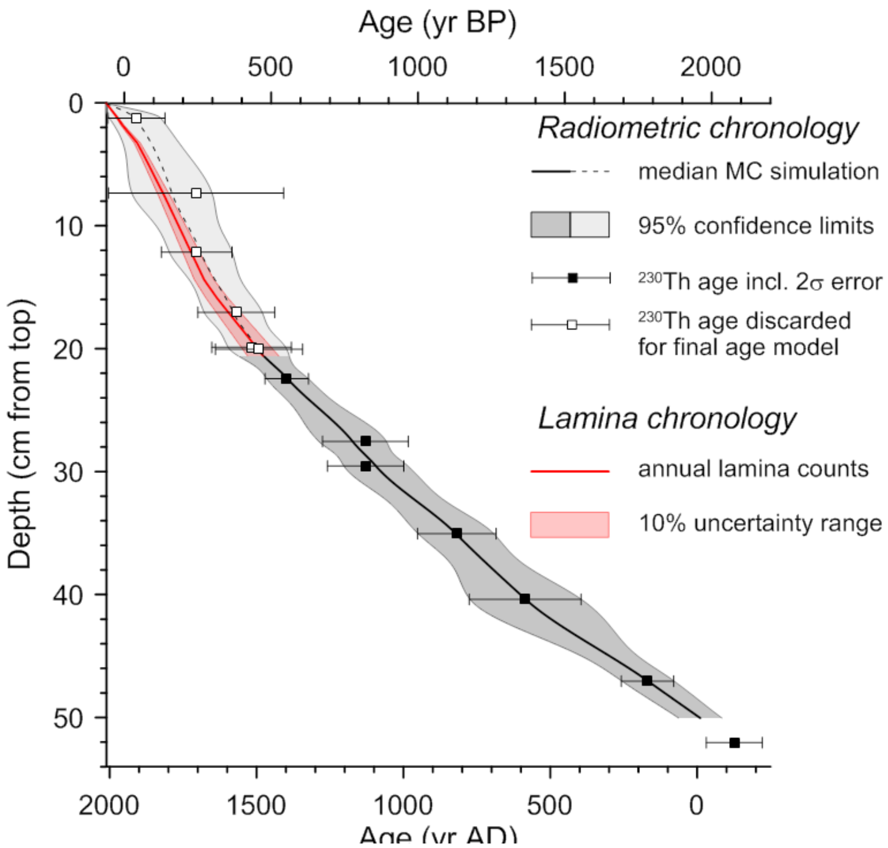

FIGURE 2.

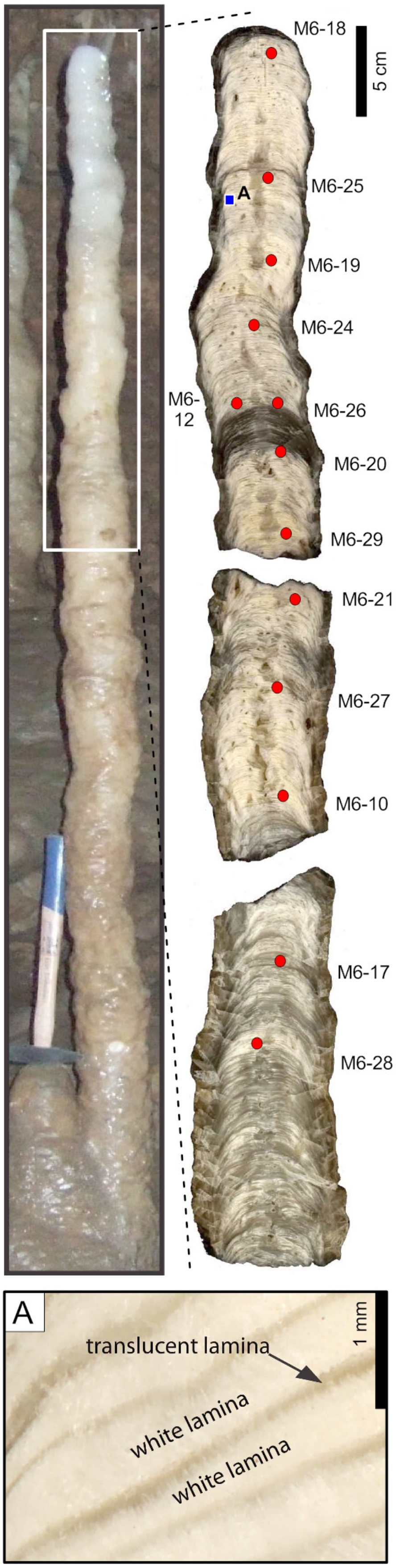
M6-18
5 cm
M6-25
A
M6-19
M6-24
M6-12
M6-26
M6-20
M6-29
M6-21
M6-27
M6-10
M6-17
M6-28
A
translucent lamina
1 mm
white lamina
white lamina

FIGURE 4.

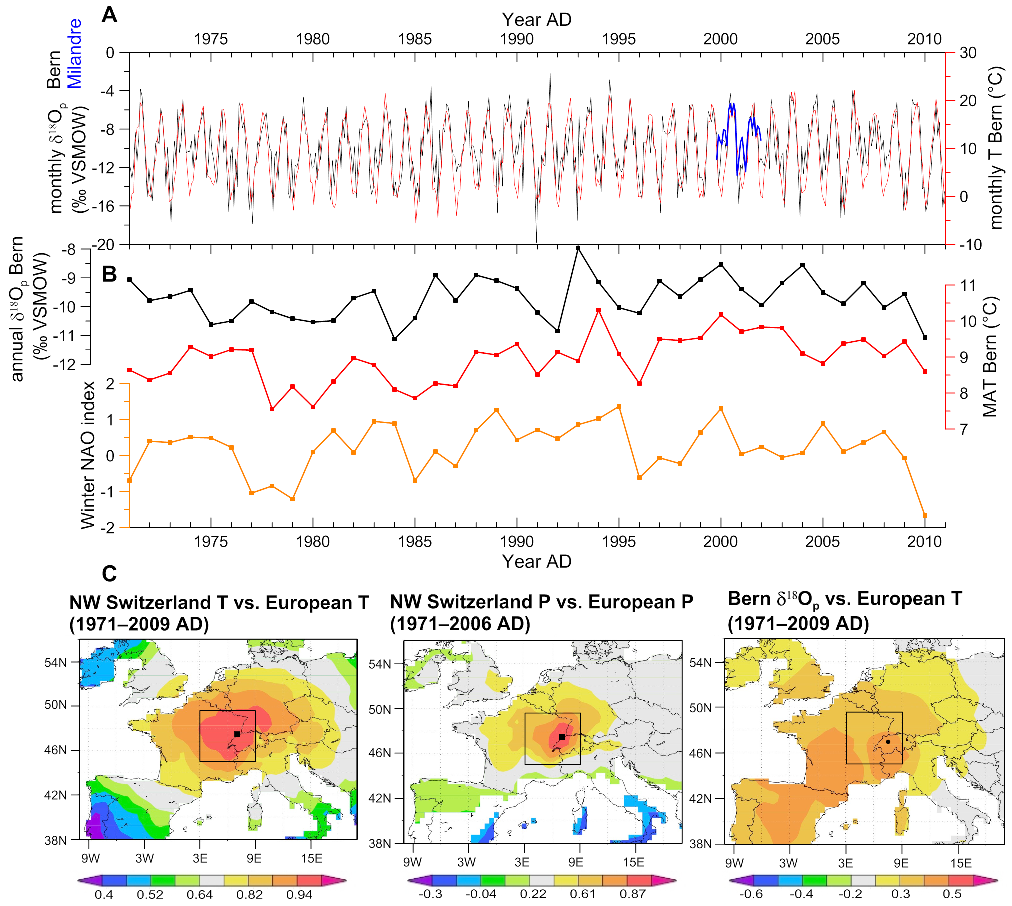

FIGURE 5.

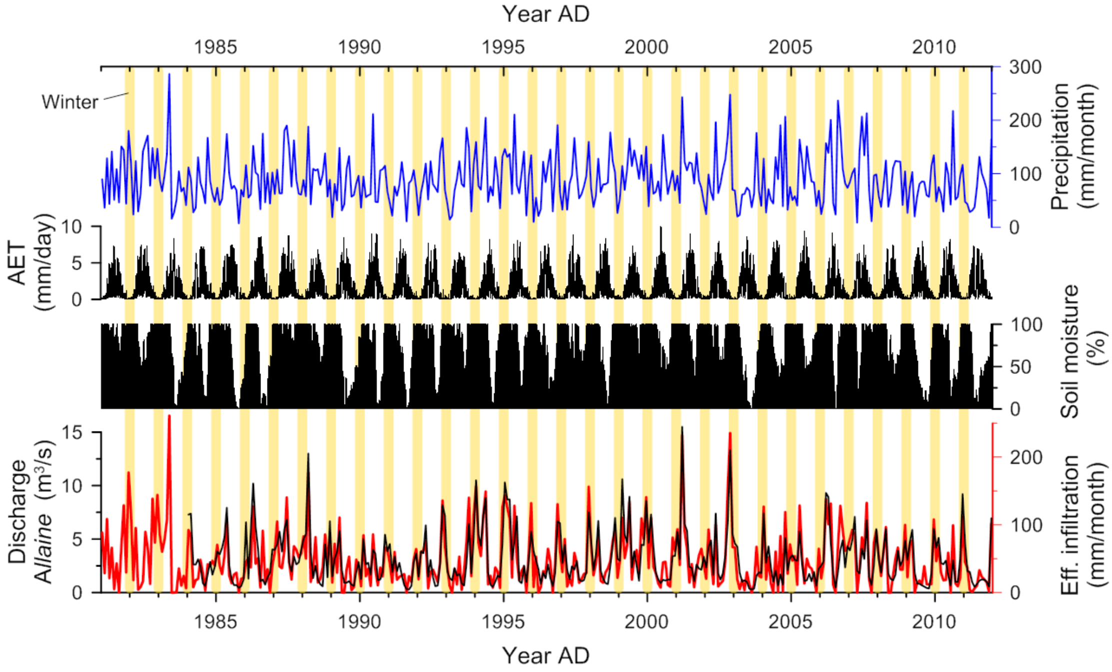

FIGURE 6.

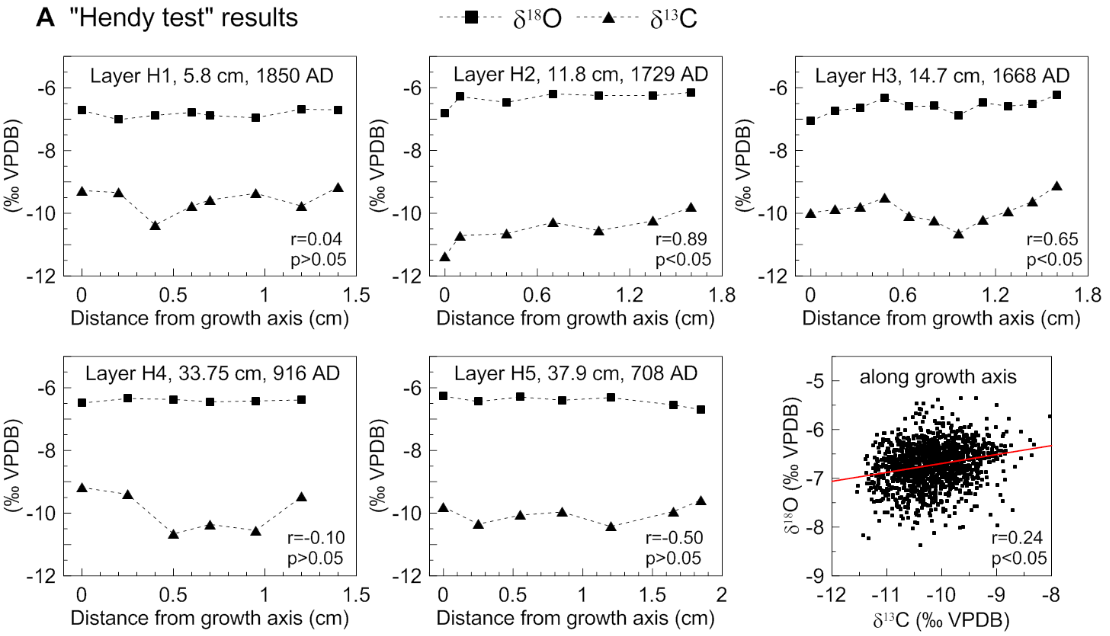
A "Hendy test" results

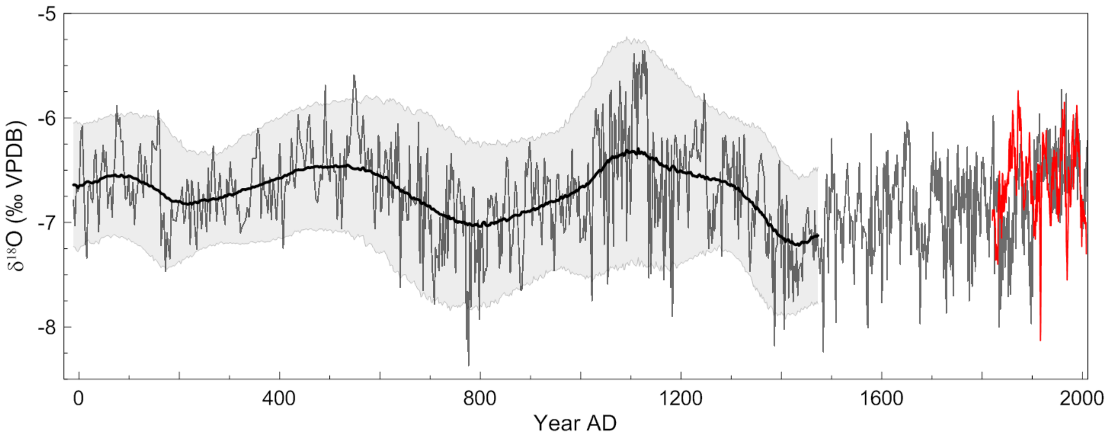
B Replication of δ18O between **M6** and **M4**

FIGURE 7.

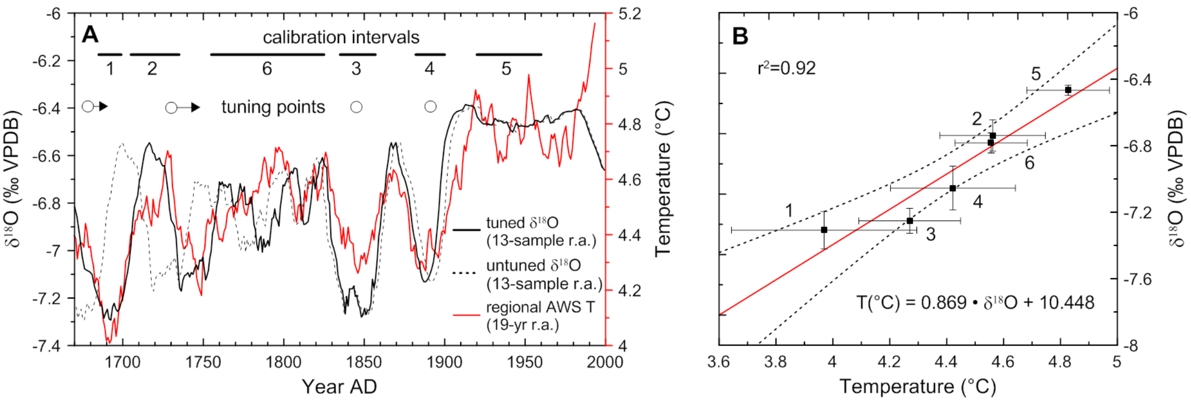

FIGURE 7 (updated).

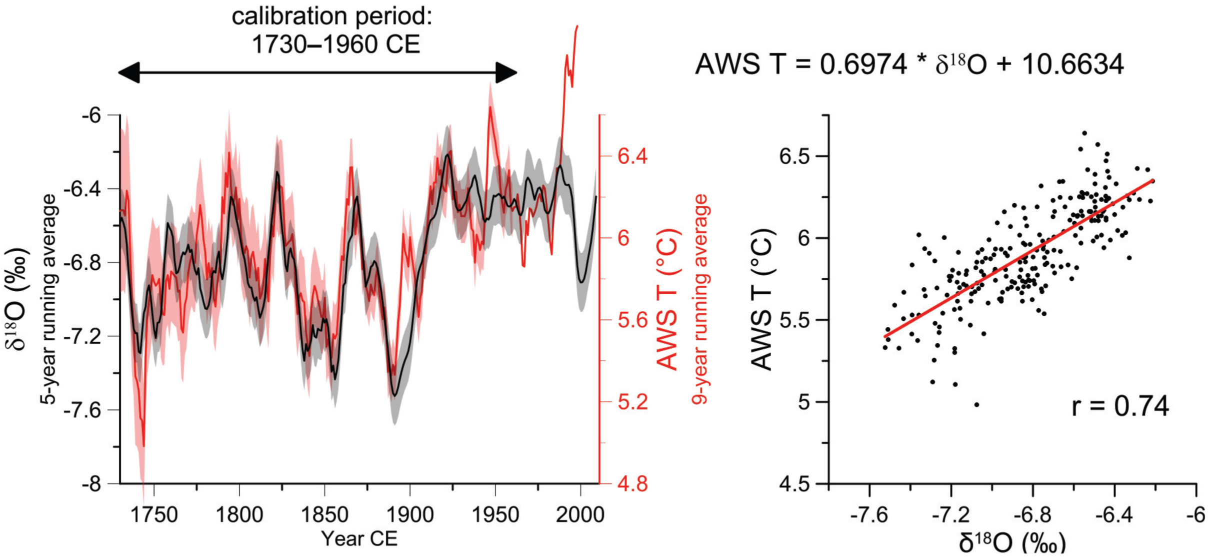

FIGURE 8.

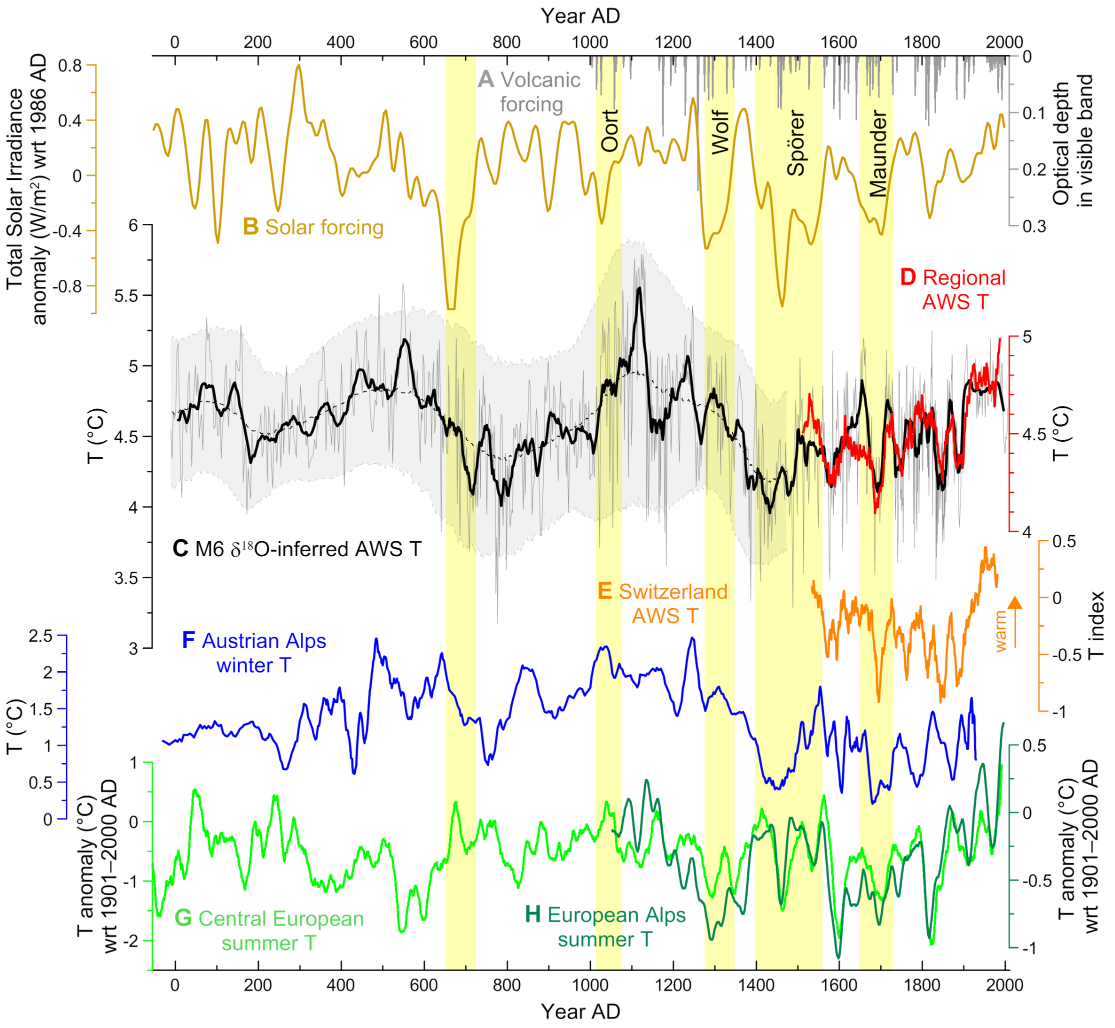

FIGURE 9.

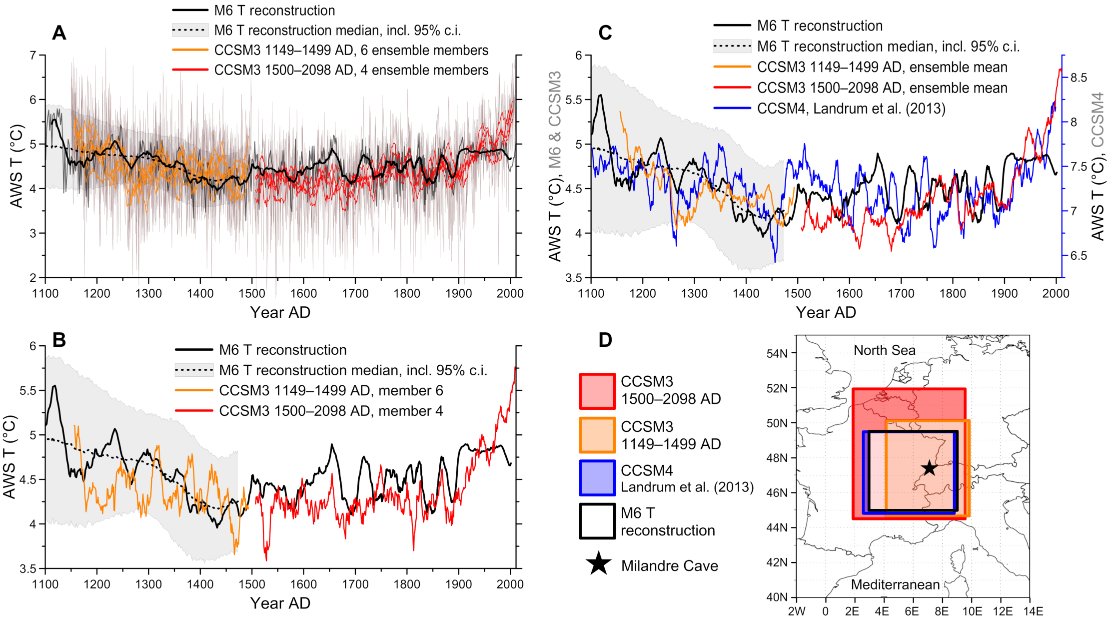

FIGURE 10.

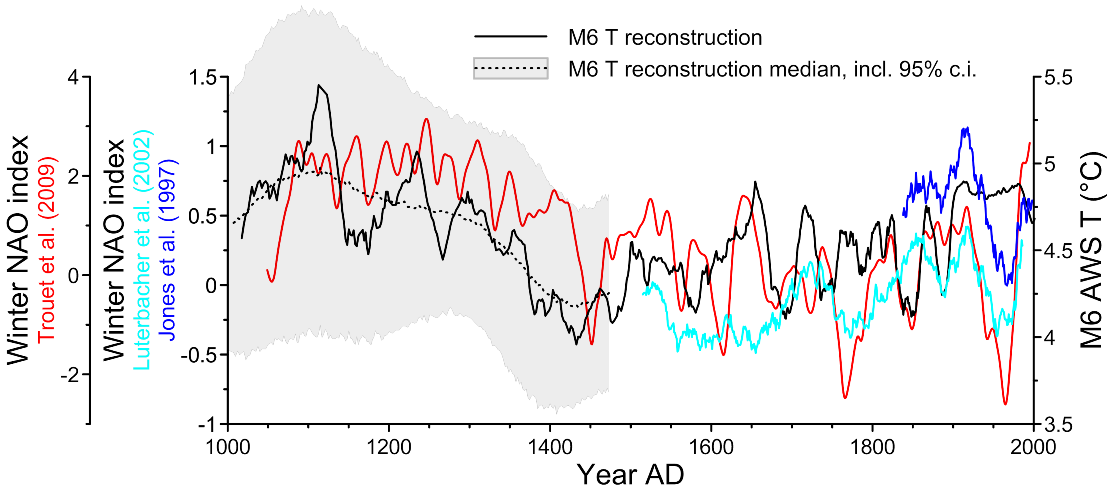
M6 T reconstruction
M6 T reconstruction median, incl. 95% c.i.
Winter NAO index
Trouet et al. (2009)
Winter NAO index
Luterbacher et al. (2002)
Jones et al. (1997)
M6 AWS T (°C)
Year AD
4
2
0
-2
1.5
1
0.5
0
-0.5
-1
5.5
5
4.5
4
3.5
1000
1200
1400
1600
1800
2000

Erklärung

gemäss Art. 28 Abs. 2 RSL 05

Name/Vorname: Häuselmann Anamaria Diana

Matrikelnummer: 07-103-237

Studiengang: Klimawissenschaften

Bachelor ☐ Master ☐ Dissertation ☐

Titel der Arbeit: Late Quaternary and Holocene paleoclimate and paleoenvironmental reconstruction – a multi-proxy approach on Swiss speleothems

Leiter der Arbeit: Prof. Dr. Dominik Fleitmann

Ich erkläre hiermit, dass ich diese Arbeit selbständig verfasst und keine anderen als die angegebenen Quellen benutzt habe. Alle Stellen, die wörtlich oder sinngemäss aus Quellen entnommen wurden, habe ich als solche gekennzeichnet. Mir ist bekannt, dass andernfalls der Senat gemäss Artikel 36 Absatz 1 Buchstabe o des Gesetzes vom 5. September 1996 über die Universität zum Entzug des auf Grund dieser Arbeit verliehenen Titels berechtigt ist.

…………………..…………………..

Ort/Datum

………………………………………

Unterschrift

Häuselmann Anamaria Diana

Date of birth: 23. 01. 1982 in Bistrita (Romania)

EDUCATION

2011-2015: Dissertation at the Institute of Geological Sciences and Oeschger Centre for Climate Change Research, University of Bern, Switzerland

PhD thesis: Late Quaternary and Holocene paleoclimate and paleoenvironmental reconstruction – a multi-proxy approach on Swiss speleothems

Supervisors: Prof.Dr. Dominik Fleitmann and Prof.Dr. Markus Leuenberger

2007-2010: Major in Pure and Applied Quaternary Sciences at the Institute of Geological Sciences, University of Bern

Master Thesis: Evaluation of geomorphological process rates by combining modern river sediment loads and spatially distributed rainfall data - A study in the catchment of Emme River, Canton of Bern (CH)

Supervisors: Prof.Dr. Fritz Schlunegger and Dr. Oliver Kracht

2002- 2007: Diploma in Engineering Geologyat the Babes-Bolyai University Cluj Napoca, Faculty of Biology and Geology, specialization Technical Geology, module Mineralogy

Diploma Thesis: Speleogenesis and Sedimentary Deposits in Cioclovina Cave, Sureanu Mts., Romania

Supervisors: Prof. Dr. Bogdan Onac and Dr. Philipp Häuselmann

1996-2000: Grigore Silasi High School Beclean, specialization accounting-banking

1992-1996: Secundary School, Beclean pe Somes, Romania

1988-1992: Primary School, Beclean pe Somes, Romania

LANGUAGES

Romanian: mother language	French: medium level
English: advanced level	German: medium level

AWARDS

2013 Best Scientific Poster Prize, International Congress of Speleology, Brno

2013 Young Researcher Prize of the Scientific Commission for Speleology of SSS/SGH and ScNat (co-prize)